SURFACE CONJUGATION OF UPCONVERSION NANOPARTICLES VIA SUPRAMOLECULAR HOST-GUEST SELF-ASSEMBLY

UTS
UNIVERSITY OF TECHNOLOGY SYDNEY

Yulong Sun

Supervised by

Dr Joshua Chou (Principal Supervisor)

Dr Xiaoxue Xu (Co-Supervisor)

A/Prof Alison T Ung (Co-Supervisor)

School of Life Sciences

Faculty of Science

University of Technology Sydney

This dissertation is submitted for the degree of Doctor of Philosophy

December 2018

In loving memory of my grandfather, Mr. Jingzhi Fu (1937-2017)

To my grandmother, my mother, my father, and all of friends

CERTIFICATE OF ORIGINAL AUTHORSHIP

I, Yulong Sun declare that this thesis, is submitted in fulfilment of the requirements for the award of Doctor of Philosophy, in the School of Life Sciences, Faculty of Science at the University of Technology Sydney.

This thesis is wholly my own work unless otherwise reference or acknowledged. In addition, I certify that all information sources and literature used are indicated in the thesis.

Yulong Sun

Signature:

Date: 30 August 2018

ABSTRACT

Surface Conjugation of Upconversion Nanoparticles *via* Supramolecular Host-Guest Self-Assembly

Yulong Sun

Surface functionalization and conjugation hold the key to driving many purpose-synthesized nanoparticles into real-world applications. Lanthanide (Ln) ions doped upconversion nanoparticle (UCNP) is a good example: while it delivers a great promise as molecular probes, sensors, drug carriers and light transducers for a library of application in the area of biological and physical science. However, the hydrophobic surface of UCNPs, sometimes, is one of the main challenges for further applications, especially in natural science. It remains a bottleneck for the community to explore practical strategies to functionalize the UCNPs surfaces for hydrophilicity conversion and further bioconjugation to meet many cellular and molecular specific needs.

Supramolecular self-assembly is one of the leading topics in supramolecular chemistry. It is a process in which disordered molecular building blocks are specifically re-ordered and also a phenomenon where the components of a system assemble themselves spontaneously *via* interaction to form a larger functional unit. In the view of thermodynamics, self-assembly is an equilibrium process where the assembled components are in equilibrium with the individual components. In other words, it is driven by the minimization of Gibbs free energy. Compared with molecular chemistry, self-assembly, as the most critical component of the assembled method, was formed by intermolecular forces.

This thesis shows a new surface conjugation approach for UCNP modification *via* supramolecular host-guest interactions leading as-made oleic acid (OA) stabilized UCNPs (OA-UCNPs) from hydrophobic into hydrophilic. At the same time, the modified

host molecules on the surface of UCNPs can provide a considerable number of cavities, which can form the host-guest interaction with a series of molecules, such as anti-cancer drugs, biomolecules, and inorganic materials. The advantage of the modification approach is no further reaction formed for conjugation, which hugely increases the binding amounts and also shows the excellent binding behaviour by using the different binding systems.

This thesis is aiming to conduct studies of:

(i) the investigation of the surface of OA-UCNPs (in **Chapter 3**)

   To convert UCNPs with high efficiency and yield, the original cover needs to be investigated. We predict and proof the binding strength and binding mode between an OA and two ß-NaYF$_4$ crystal surfaces of UCNPs.

(ii) the binding behaviours of different organically functional groups (**Chapter 4**)

   Compared with the original of OA from the surface of UCNPs, we also choose several organic molecules which hold different functional groups. We discuss the effect of different functional groups and, most importantly, the binding mode and binding behaviour on the surface of UCNPs.

(iii) the investigation of binding behaviours of macrocycles on the surface of UCNPs and their applications in binding with organic molecules, biomolecules, and inorganic materials (**Chapter 4** ~ **Chapter 6**).

   We raise and design a new approach to convert the surface of UCNPs with different kinds of macrocycles. Then, we provide three applications in the areas of drug delivery, cell targeting, and energy transfer.

The thesis is organized as follows:

There are four main parts of the thesis, which includes:

- **Part I** Background

In this part, I introduce some basic information about supramolecular chemistry and UCNPs. The section of supramolecular chemistry consists of the concepts of supramolecular chemistry, supramolecular interactions, the selectivity of supramolecular chemistry, host-guest chemistry, self-assembly, and the current development of supramolecular chemistry. In the section of UCNPs, I start from the mechanism of upconversion to show the advantage of the upconversion materials, then display the synthetic methods of UCNPs for the further discussion on the surface modifications.

- **Part II** Literature Review: the surface modification and conjugation of UCNPs.

In this part, the surface modified approaches are sorted by the different supramolecular interactions. Except for the surface modification criteria, this review also gives a summary of surface conjugation of UCNP *via* supramolecular interactions with organic molecules and inorganic nanoparticles.

- **Part III** The original surface of OA-UCNPs

This part shows the synthesis and characterization of OA-UCNPs, and also the binding behaviour of OA on two kind crystal surfaces of UCNPs. This part also provides significant evidence to increase the efficiency of ligand exchange and surface binding.

- **Part IV** The applications of macrocycles modified UCNPs

This part includes three kinds of applications: molecular conjugation, biomolecular conjugation, and inorganic nanoparticle conjugation. All of these designs are based on the supramolecular host-guest interactions. In these chapters, we use two kinds of macrocycle to modify the surface of UCNPs for conjugating different types of organic molecules or inorganic materials, which showed in the following figure.
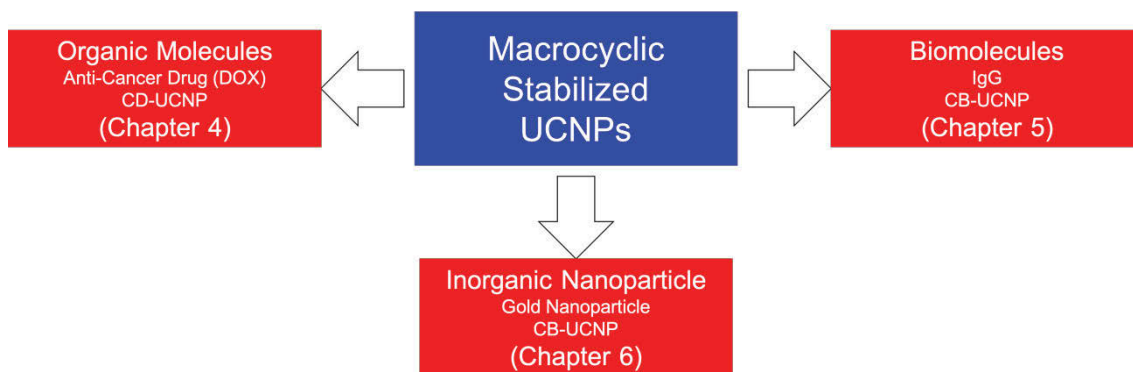
In **Chapter 4**, we conjugate anti-cancer drug, Doxorubicin Hydrochlorate (DOX), on the surface of UCNPs to test the bioavailability of DOX-loaded cyclodextrin-stabilized UCNPs (CD-UCNP). **Chapter 5** shows the binding properties of cucurbit[7]uril-stabilized UCNPs (CB-UCNP) with biomolecules, Immunoglobulin G, for cell targeting. The physical effect of UCNPs with AuNPs is investigated by the same binding approach, which explained in **Chapter 6**.

ACKNOWLEDGEMENTS

microscopic perspective. And also thank Alison for the great help on organic chemistry. More importantly, every time I chat with Alsion, I have a feeling at home. I am very fortunate to have these three as my supervisors. In these few years, they are more than just my supervisors, more like my best friend.

Much of the work described in this thesis cannot be completed so smoothly without the help of the kind people around me in the lab: Dr Wenjing Zhang for the great support on nanoparticles; Dr Joshua Chou for helping and teaching me on cell study; Baoming Wang for the cell imaging test and warm discussion; Dr Helen Xu for the material analysis and characterization; Yingzhu Zhou for the optical test; and Dr Olga Shimoni for the analysis of protein conjugation. Besides, I would like to thank my lab mates, Jiayan Liao, Bo Shao, Alex Gee, Matthew Cappadona, Christian Clarke, and Iurii Bodachivskyi for the support and encouragement. I also would like to thank all the members from Advanced Tissue Regeneration & Drug Delivery Group and Institute for Biomedical Materials and Devices for their great suggestion and discussion: Prof Dayong Jin, Dr Fan Wang, Dr Jinghua Fang, Dr Lu Liu, Zhiguang Zhou, Ming Guan, Chao Mi, Hao He, Dr Ying Wang, Anantdeep Kaur, Huan Wu, Yuan Liu, Dr Peter Su, Dr Laixu Gao, Guochen Bao, and Dr Joris Goudsmits. I am particularly grateful for the lab and technical assistance given by Dr Linda Xiao, Dr Ronald Shimmon, and Katie McBean.

In addition, I would like to thank my friends when I live in Sydney: Sheran Li, a knowledgeable person, for her warm sharing, great help and useful suggestions; Steven Vasilescu, my first Australian friend, for teaching me many useful English words which we could not learn from textbook; Jen Ming and Shilun Feng, the cute couple, for their positive life style; Jim Li, the non-economically suitable warm man, for his kindness, sharpness, and helpfulness; Wenjing Zhang, the sunflower, for bringing us the joy and special brain circuit; Yingzhu Zhou and Baoming Wang in "3A on the way" group for their help, encouragement and support in those days; Yibin Wei and Xiaoteng Jia in

CONTENTS

LIST OF TABLES

LIST OF FIGURES

LIST OF ABBREVIATIONS AND ACRONYMS

3D: Three Dimensional

Ad: Amantadine Hydrochloride

ATR: Attenuated Total Reflectance

AuNP: Gold Nanoparticle

BB[n]: Bambus[n]uril

BSA: Bovine Serum Albumin

C[n]A: Calix[n]arene

CB[7]: Cucurbit[7]uril

CB[n]: Cucurbit[n]uril

CB-UCNP: Cucurbit[7]uril Stabilized Upconversion Nanoparticle

CB-UCNP@IgG-ADC: N-1-Adamantanecarboxyl Immunoglobulin G Self-Assembled on the Surface of Cucurbit[7]uril Stabilized Upconversion Nanoparticle

CD: Cyclodextrin

CD-UCNP: Cyclodextrin Stabilized Upconversion Nanoparticle

CD-UCNPs-DOX: Doxorubicin Loaded Cyclodextrin Stabilized Upconversion Nanoparticle

CTAB: Cetyltrimethylammonium Bromide

DAPI: 2-(4-Amidinophenyl)-6-Indolecarbamidine Dihydrochloride

DLS: Dynamic Light Scattering

DMEM: Dulbecco's Modified Eagle's Medium

DMSO: Methyl Sulfoxide

DOX: Doxorubicin Hydrochlorate

DTGA: Differential Thermogravimetric Analysis

EDC: N-(3-Dimethylaminopropyl)-N′-Ethylcarbodiimide Hydrochloride

ErCl$_3$·6H$_2$O: Erbium (III) Chloride Hexahydrate

ESA: Excited State Absorption

EtOH: Ethanol

ETU: Energy Transfer Upconversion

FBS: Fetal Bovine Serum

FRET: Förster Resonance Energy Transfer

FT-IR: Fourier-Transform Infrared

HAuCl$_4$: Chloroauric Acid

IgG: Immunoglobulin G

IgG-ADC: N-1-Adamantanecarboxyl-IgG

ITC: Isothermal Titration Calorimetry

Ln: Lanthanide

Ln-UCNC: Lanthanide Doped Upconversion Nanocrystal

Ln-UCNP: Lanthanide Doped Upconversion Nanoparticle

L-Phe: L-Phenylalanine

L-Phe-AuNP: L-Phenylalanine Reduced Gold Nanoparticle

NH$_4$F: Ammonium Fluoride

MIM: Mechanically Interlocked Molecules

MTT: Thiazolyl Blue Tetrazolium Bromide

NMR: Nuclear Magnetic Resonance

NOBF$_4$: Nitrosyl Tetrafluoroborate

OA: Oleic Acid

OA-UCNP: Oleic Acid Stabilized Upconversion Nanoparticle

ODE: 1-Octadecene

OM: Oleylamine

PA: Photon Avalanche

P[n]A: Pillar[n]arene

PAH: Poly(Allylamine Hydrochloride)

PEG: Poly(Ethylene Glycol)

Phalloidin-FITC: Phalloidin-Fluorescein Isothiocyanate Labelled

PLNP: Persistent Luminescence Nanoparticle

PMPD: Poly(m-Phenylenediamine)

QD: Quantum Dots

SA: Sodium 1-Adamantanecarboxylate

SDP: Sodium Dodecyl Phosphate

SDS: Sodium Dodecyl Sulphate

TEM: Transmission Electron Microscopy

TGA: Thermogravimetric Analysis

THF: Tetrahydrofuran

UCNP: Upconversion Nanoparticle

UCNP-COOH: Direct Carboxyl-Modified Upconversion Nanoparticle

UV-vis: Ultraviolet Visible

XPS: X-Ray Photoelectron Spectra

XRD: X-Ray Diffraction

YbCl$_3$·6H$_2$O: Ytterbium (III) Chloride Hexahydrate

YCl$_3$·6H$_2$O: Yttrium (III) Chloride Hexahydrate

α-CD: α-Cyclodextrin

α-CD-COONa: Carboxylic α-Cyclodextrin Sodium Salt

α-CD-COOH-UCNP-DOX: Doxorubicin Loaded Carboxylic α-Cyclodextrin Stabilized Upconversion Nanoparticle

β-CD: β-Cyclodextrin

β-CD-COOH: Carboxylic β-Cyclodextrin

β-CD-COONa: Carboxylic β-Cyclodextrin Sodium Salt

β-CD-COOH-UCNP-DOX: Doxorubicin Loaded Carboxylic β-Cyclodextrin Stabilized Upconversion Nanoparticle

β-CD-PO$_3$Na$_2$: Phosphoric β-Cyclodextrin Sodium Salt

β-CD-PO$_3$Na$_2$-UCNP-DOX: Doxorubicin Loaded Phosphoric β-Cyclodextrin Stabilized Upconversion Nanoparticle

β-CD-SO₃Na: Sulfonic β-Cyclodextrin Sodium Salt

β-CD-SO₃Na-UCNP-DOX: Doxorubicin Loaded Sulfonic β-Cyclodextrin Stabilized Upconversion Nanoparticle

γ-CD: γ-Cyclodextrin

γ-CD-COONa: Carboxylic γ-Cyclodextrin Sodium Salt

γ-CD-COOH-UCNP-DOX: Doxorubicin Loaded Carboxylic γ-Cyclodextrin Stabilized Upconversion Nanoparticle

1 When Supramolecular Chemistry Meets Upconversion Nanoparticles: major concepts of supramolecular chemistry and upconversion nanoparticles

This chapter aims to briefly introduce the terms, definitions, and concepts of supramolecular chemistry and upconversion nanoparticles (UCNPs).

I acknowledge all the colleagues for supporting me on this section.

INTRODUCTION

In the last several decades, supramolecular chemistry, as an essential chemical tool, has been applied to a variety of nanomaterials, such as gold nanoparticles (AuNPs) (Hazarika, Ceyhan & Niemeyer 2004; Jing et al. 2008; Kaminker et al. 2010; Li et al. 2013; Niemeyer, Ceyhan & Hazarika 2003; Tang et al. 2012), quantum dots (QDs) (Chen et al. 2013; Dorokhin et al. 2010; Li et al. 2013; Medintz et al. 2005), graphene (Ciesielski et al. 2014; Ciesielski & Samori 2016; Ge et al. 2015; Haar et al. 2015; Liu, Chen & Jiang 2011; Qi et al. 2015; Samanta et al. 2012; Wang, Chen, et al. 2015). This supramolecular modification successfully enabled the improved nanomaterials to surface properties, such as surface hydrophilicity, energy, charge, and functional groups. This thesis focuses on the self-assembly properties of UCNPs (Idris et al. 2015). The chapter will introduce the basic concepts of supramolecular chemistry and UCNPs.

SUPRAMOLECULAR CHEMISTRY

1.1 What is Supramolecular Chemistry?

To answer this question, we have to go back to the development of supramolecular chemistry. In 1873, Johannes Diderik van der Waals firstly raised the existence of intermolecular forces (Tang & Toennies 2010; Valderrama 2010). This is the first that a person posed a force between molecules. Almost a century later, in the 1960s, the breakthrough was achieved by Charles J. Pedersen who synthesized the crown ethers (Pedersen, 1967; Izatt 2007, 2017). After this significant work, other researchers such as Donald J. Cram (Cram and Cram, 1978; Hawthorne 2001; Sherman 2007) and Jean-Marie Lehn (Lehn, 1995; Goodman 2007) started their research in synthesizing receptors with

high selectivity. In 1987, the Nobel Prize in Chemistry was awarded jointly to Donald J. Cram, Jean-Marie Lehn, and Charles J. Pedersen "*for their development and use of molecules with structure-specific interactions of high selectivity*." (Hirsch 2015)

The event is regarded as a milestone in the development of supramolecular chemistry. In 1995, Jean-Marie Lehn published a book named "Supramolecular Chemistry" to introduce the definition of supramolecular chemistry (Lehn, 1995). The definition was given in 1978:

> *Just as there is a field of molecular chemistry based on the covalent bond, there is a field of supramolecular chemistry, the chemistry of molecular assemblies and of the intermolecular bond.*

In the book, chemistry was separated into two parts: molecular chemistry and supramolecular chemistry **(Figure 1-1)**. Molecular chemistry focuses on the chemical (covalent) bond between atoms. However, supramolecular chemistry is **beyond molecular chemistry** which is based on the interactions between different molecules or different parts of a molecule (Lehn 1995). The key to the difference between them is if there is a new chemical bond formed.

In 2009, another book, "Supramolecular Chemistry" written by Prof Jonathan Steed from Durham University, gave a more detailed definition of supramolecular chemistry.

> *Supramolecular Chemistry: The study of systems involving aggregates of molecules or ions held together by non-covalent interactions, such as electrostatic interactions, hydrogen bonding, dispersion interactions and solvophobic effects.* (Steed & Atwood 2009)
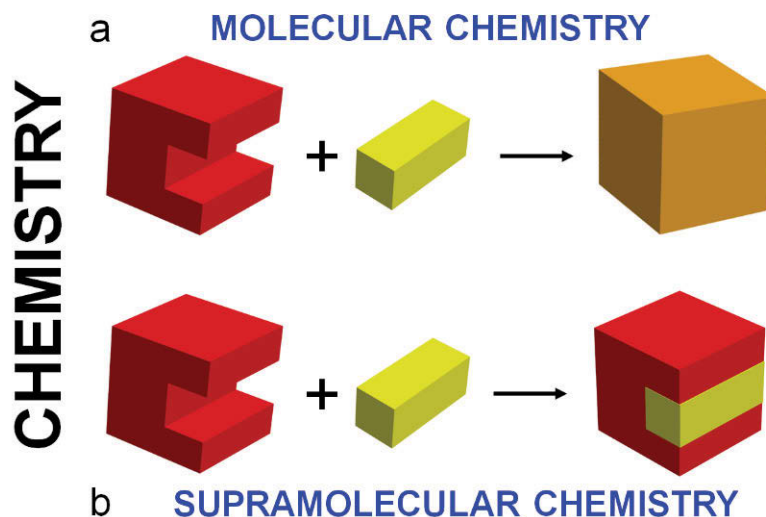
Figure 1-1. The difference between (a). molecular (traditional) chemistry and (b). supramolecular chemistry.

In 2016, the big breakthrough was achieved by Nobel Prize in Chemistry which was awarded jointly to Jean-Pierre Sauvage, Sir J. Fraser Stoddart and Bernard L. Feringa "*for the design and synthesis of molecular machines.*" (Feu et al. 2017; Jayaraman 2017) Combining the two Nobel Prizes, another definition of supramolecular chemistry could be raised only based on the words from the two Nobel Prizes.

> *Supramolecular Chemistry is the molecules with structure-specific interactions of high selectivity and the movement on-demand in a molecular machine.*

Gernerally, supramolecular chemistry can be classified into two broad categories: host-guest chemistry and self-assembly, which is based on the size and shape of building blocks (molecules) (Steed & Atwood 2009). If the size of a molecule is significantly larger than the other molecule and can take the smaller one into the larger molecule is called "host" molecule, the small one is its guest. The definitions of host and guest were given by Donald Cram, who said:

The host component is defined as an organic molecule or ion whose binding sites converge in the complex. The guest component is any molecule or ion whose binding sites diverge in the complex. (Cram 1986)

The "binding sites" in the definition is a part of the host and guest that can form the interaction between the two molecules from the difference in charge, size, and geometry. Jonathan Steed defined the host-guest chemistry, which is "*The study of large 'host' molecules that are capable of enclosing smaller 'guest' molecules via non-covalent interactions.*" (Steed & Atwood 2009) **(Figure 1-2)**
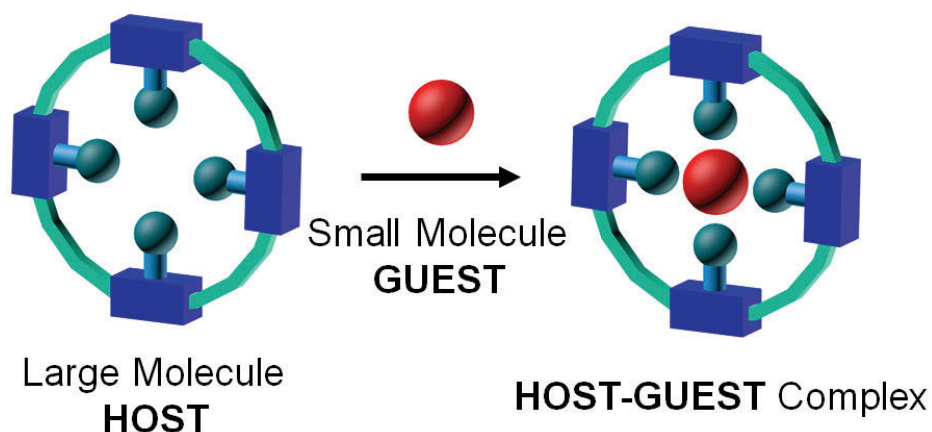
Figure 1-2. Host-guest based supramolecular system from molecular building blocks.

Contrary to the host-guest chemistry, when the size of the molecules is similar, no one acts as a host for others, the non-covalent binding of two or more molecules is termed self-assembly. There is also a definition of self-assembly was given by Jonathan Steed, which is *The spontaneous and reversible association of two and more components to form a larger, non-covalently bound aggregate.* (Steed & Atwood 2009) (**Figure 1-3**)
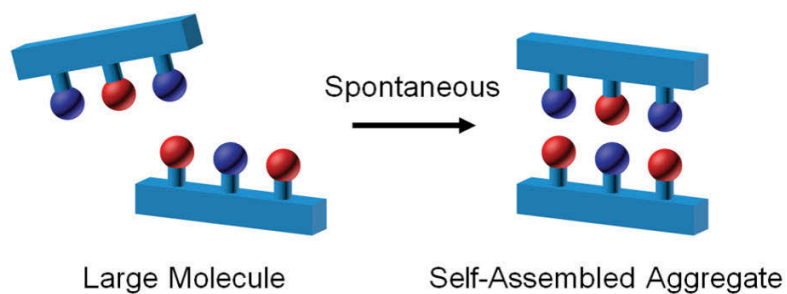
Figure 1-3. Self-assembled based supramolecular system from molecular building blocks.

1.2 Supramolecular Interactions

Supramolecular Interactions (Non-covalent interactions) can hold components together in supramolecular systems. Usually, non-covalent interactions, range from 2 kJ mol^{-1} to 300 kJ mol^{-1}, are considerably weaker than the covalent bonds which can vary from 150 kJ mol^{-1} to 450 kJ mol^{-1}. However, a supramolecular system usually has multi-binding sites, which are used in a co-operative manner to form a stable supramolecular complex. **Figure 1-4** shows the summary of binding strengths in various non-covalent interactions. (Steed and Atwood, 2009)
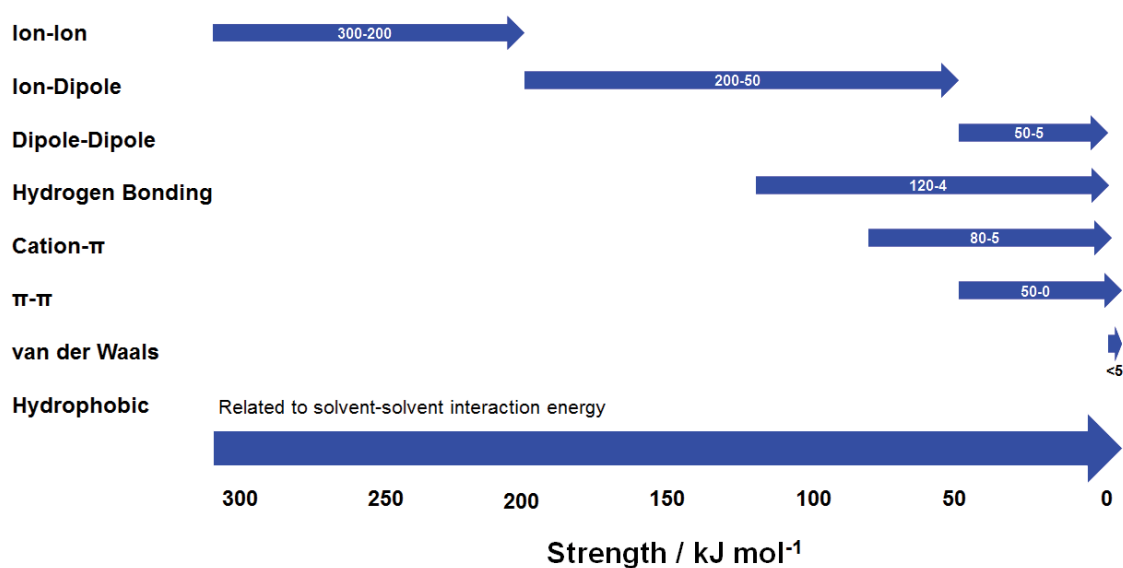
Figure 1-4. The summary of supramolecular interactions.

1.2.1 Ionic and Dipolar Interactions

There are three categories of ionic and dipolar interactions: (i) ion-ion interactions, (ii) ion-dipole interactions, and (iii) dipole-dipole interactions. All of them are based on the coulombic attraction between opposite charges, which shown in **Figure 1-5**.
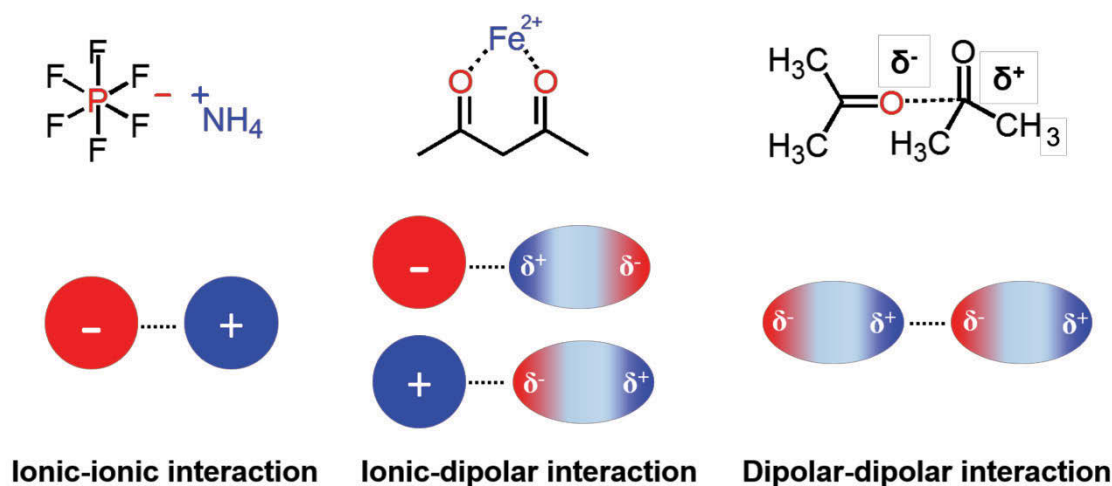
Figure 1-5. Examples and mechanisms of electrostatic interactions: ion-ion interaction (left), ion-dipole interaction (middle), and dipole-dipole interaction (right).

1.2.1.1 Ion-ion interactions

This ion-ion interaction is the strongest interaction in non-covalent interactions, which is comparable with parts of covalent bonds. Usually, ion-ion interaction is non-directional, and that interaction can occur in any orientation (**Figure 1-5**).

1.2.1.2 Ion-dipolar interactions

This interaction has orientation-dependent aspect requiring two entities to be aligned, so this interaction would be in an optimal direction (**Figure 1-5**). However, the strength of the interaction is weaker than ionic-ionic interaction (50-200 kJ mol^{-1}).

1.2.1.3 Dipolar-dipolar interactions

The dipole-dipole interaction is similar to ion-dipolar interaction (**Figure 1-5**), but the strength is the weakest among the ionic and dipolar interaction (5-50 kJ mol^{-1}).

1.2.2 Hydrogen Bond

Hydrogen bond is a particular kind of dipole-dipole interaction between a proton donor and a proton acceptor (Jeffrey, 1997). Due to the high directionality and specific binding strength, hydrogen bond is regarded as one of the most critical non-covalent bonds in supramolecular systems. In a supramolecular system, building blocks usually can form several hydrogen bonds because they process some donors and acceptors within the molecules. The donors in hydrogen bonds are groups with a hydrogen atom which is attached to an electronegative atom, such as nitrogen, oxygen, and fluoride. The electronegative atom can form a dipole in the chemical bond to make the hydrogen atom with a partial positive charge. On the other hand, acceptors in the hydrogen bonds are dipoles with electron-withdrawing atoms which can form the interaction with the positive hydrogen atom from the donor. **Figure 1-6** shows the typical binding behaviour of hydrogen bond between a carboxyl accepter and a secondary amine donor and the standard binding mode between an acceptor and a donor in a hydrogen bond.
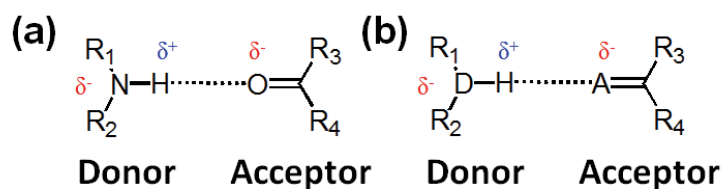
Figure 1-6. The typical binding behaviour of hydrogen bond between a carboxyl accepter and a secondary amine donor (a) and the standard binding mode between an acceptor and a donor in a hydrogen bond (b).

Typically, the strength of hydrogen bonds ranges from 4 to 120 kJ mol^{-1} depending on the types of donors and acceptors and also the geometry that hydrogen bond adopts in a binding pair. Various kinds of donors or acceptors process the partial charges, the significant differences in charges can increase the binding strength of hydrogen bonds. Primary hydrogen-bonding interactions are a direct interaction between an acceptor-donor pair, which has been shown in **Figure 1-6**. Besides, the secondary hydrogen-bonding interactions with the neighbouring groups have to be considered as well. Their charges can also either increase or decrease the binding strength by the attraction between opposite charges or repulsion between like charges. **Figure 1-7** shows two typical effects of the adjacent donors or acceptors.
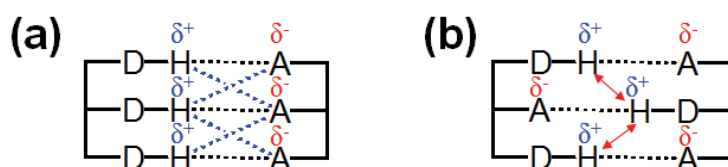
Figure 1-7. Two common primary hydrogen bond (black dashed line) modes of (a) all acceptors molecule to all donor molecules (DDD and AAA) and (b) two mixed donor/acceptor molecules (DAD and ADA). Secondary hydrogen interactions (blue hashed line) providing attractions between adjacent groups in DDD and AAA arrays, and the repulsions (red two direction angle) from DAD and ADA arrays.

Another typical example shown in **Figure 1-8** is hydrogen bonds between base-pairs in DNA. The total hydrogen bonds combine two/three primary hydrogen bonds, the attraction/repulsion from neighbouring atoms.
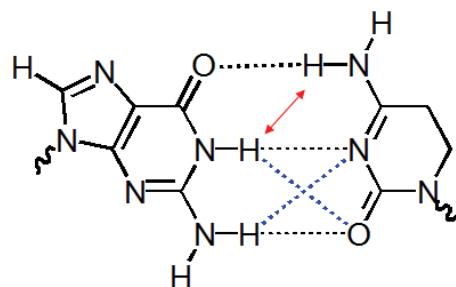
Figure 1-8. The hydrogen bonds between base-pairs (Guanine and Cytosine) in DNA.

1.2.3 π-Interactions

Two types of π-Interactions are found in supramolecular interactions, namely (i) cation-π interactions and (ii) π-π interactions. Many examples are well-known in the field of organometallic chemistry. There are two main π-π interactions are face-to-face interactions and edge-to-face interactions. (**Figure 1-9**).
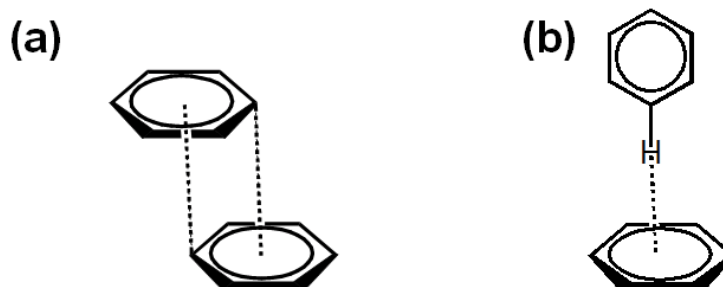
Figure 1-9. Two main π-π interactions: (a) face-to-face interactions, and (b) edge-to-face interactions.

The face-to-face interaction is a parallel ring system, separated by ca. 3.5 Å. This interaction is between the center of a ring and the corner of another. The edge-to-face interaction is a hydrogen atom from one ring forms an interaction with the center of another ring. These π-π interactions arise from the attraction between positive charge from o-framework of one conjugated system and the negative charge from a π-electron cloud of the other molecule.

A layer structure material named graphite is held together by face-to-face interactions. Another example can be found in nature is the double helix of DNA. The weak face-to-face interactions between base-pairs along the length of the double helix are responsible for the shape of DNA.

1.2.4 van der Waals Force

The interactions are dispersion effects that comprise two components, namely the London interaction and the exchange and repulsion interactions. Generally speaking, the van der Waals interactions are based on the electron distribution. **Figure 1-10** shows the van der Waals interaction between two atoms. Both nuclei of atoms are located at the right of atoms, so more positive charge distributes at the right part of atoms. The interaction can be formed between the positive side of one atom and the negative side of another.
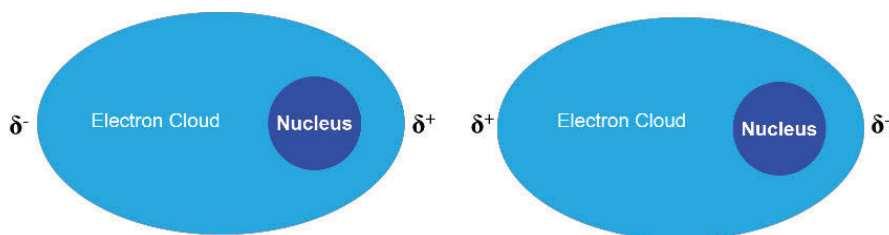
Figure 1-10. A van der Waals interaction between two atoms.

1.2.5 Hydrophobic Effects

Hydrophobic effects arise from the exclusion of non-polar groups or molecules from aqueous solution. In supramolecular chemistry, the hydrophobic interaction was paid much attention to the host-guest chemistry. Many organic molecules are hydrophobic which can be dissolved in water. However, when mixed with some water-soluble macrocycles, such as cyclodextrin (CD) or cucurbit[n]uril (CB[n]), these molecules can insert into the cavities of macrocycles to form the complexes. Hydrophobic effect is also significant in nature, which can push the formation of self-assembly of living cells or

amphiphilic structures. An example is shown in **Figure 1-11**, when two organic molecules are dispersed in an aqueous solution, they will automatically approach to lower the free energy, thereby forming a more stable structure.
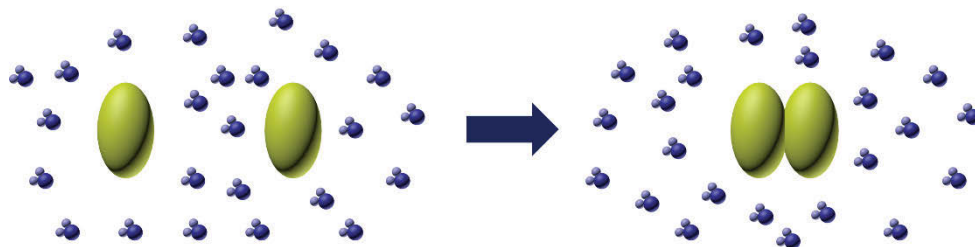
Figure 1-11. An example of the hydrophobic effect.

1.3 Selectivity

Generally, host molecules can provide appropriate binding sites for the guest molecules to bind with. For example, if host molecules process plenty of hydrogen bond donors, then ideally, the corresponding guest molecules should contain the same number of hydrogen bond acceptors. In this way, multiple interactions form between host and guest. A host that displays a preference for a particular guest or a library of guest molecules is said to show a degree of selectivity towards these species. Besides, selectivity can arise from some different factors, such as host-guest binding sites, host conformation and/or binding groups. The definition of selectivity (Steed and Atwood, 2009) is

> *the binding of one guest, or family of guests, significantly more strongly than others, by a host molecule. Selectivity is measured in terms of the ratio between equilibrium constants.*

1.3.1 The Mechanism and Factors of Selectivity

1.3.1.1 Lock-key principle

As key can open the door, supramolecular systems show the same phenomenon. The lock-key principle was raised by Emil Fisher in 1894, who worked on the binding of substrates by enzymes. He described that the enzyme as the lock and the substrate as the key. In principle, the key should have precisely the same shape and the size for the lock. However, in biological systems, the locks, enzymes, are highly flexible and conformationally dynamic in solution. To address the limitation, an interactive process mechanism for binding the substrate by an enzyme was raised by Daniel Koshland namely induced-fit, which is shown in **Figure 1-12** (This figure from the website: https://study.com/academy/lesson/induced-fit-enzyme-model-definition-theory-quiz.html). When a substrate is approaching, the enzyme will change the size of the cavity and the confirmation to fit the size of the substrate.
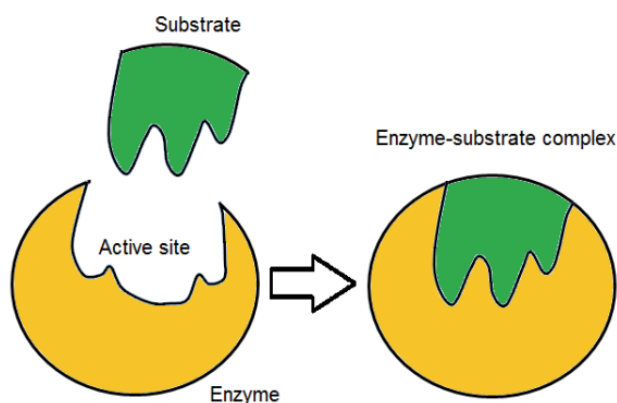
Figure 1-12. The induced-fit model of substrate binding.

1.3.1.2 Host-guest binding complementary

During the binding process, in biological systems, the size of enzymes is usually larger than its substrate. However, only a very small part of the enzyme, namely active site, is involved in the binding process. Normally, the active site of the enzyme has mutual

spatially and electronically complementary with the substrate. In short, both the host and the guest must have mutual spatially and electronically binding site to form a supramolecule.

1.3.1.3 Co-operativity of binding groups and the chelate effect

When a metal ion forms ion-dipole bonds with three bidentate ligands, the binding strength is much higher than six single unidentate ligands. An example to explain the co-operativity in the binding system is shown in **Figure 1-13**. The binding strength of Ni with three ethylenediamines is 10^8 times stronger than the one with six ammonia molecules. The definition of co-cooperativity is two or more binding sites acting in a concerted fashion to produce a combined interaction that is stronger than when the binding sites act independently of each other. The sites are co-operating with each other. In the case of binding two guests, co-operativity also represents the effect on the affinity of the host for one guest as a result of the binding of the other. The chelate effect is similar to co-operativity. The observation that multidentate ligands result in more stable complexes than comparable systems containing multiple unidentate ligands is a result of co-operativity between interacting sites.
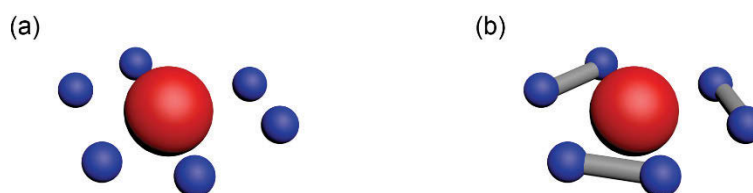
Figure 1-13. A model of ion surrounded by (a) six unidentate ammonia ligands and (b) three bidentate ethylenediamine ligands.

1.3.1.4 Preorganisation of host conformation

The preorganization means a host is preorganized when it requires a significant conformational change to bind a guest species. Based on that, the macrocyclic effect is raised. The host system that is preorganized into a sizeable cyclic shape could form more stable complexes as there is no energetically unfavorable change in conformation to bind a guest. An example is shown in **Figure 1-14**. After binding with the guest molecule, the confirmation of the host molecule will be changed to fit the guest.
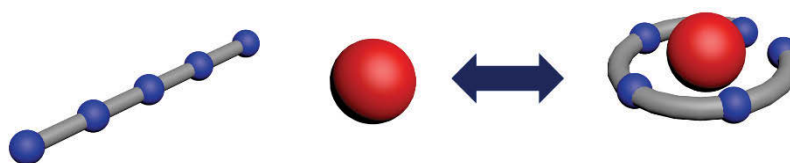
Figure 1-14. A model of preorganisation of host conformation.

1.3.2 Binding Constants

In supramolecular systems, the binding interaction between host molecules and guest molecules is an equilibrium process (**Equation 1-1**). The equilibrium constant for a binding process is called the binding constant or association constant. The definition of a binding constant is that: *the equilibrium constant for the interaction of a host with one or more guest. The binding constant provides a quantitative representation of the degree of association and is also called the association constant.*

$$Host + Guest \rightleftharpoons Host \cdot Guest \quad \text{(1-1)}$$
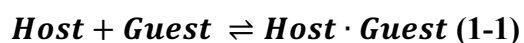
1.3.2.1 1:1 host-guest system

The binding constant is $\rightleftharpoons$calculated by **Equation 1-2**, using the concentrations of molecules at the equilibrium: host [H], guest [G] and the resulting complex [H·G]. The final value is K with the unit of mol/L or M^{-1}. The range of binding values has no

limitation, it can be from almost zero to very large. The methods of testing binding constants are titrations by Isothermal Titration Calorimetry (ITC), Nuclear Magnetic Resonance (NMR), Ultraviolet Visible (UV-vis) spectrum or fluorescence spectrum.

$$K = \frac{[H \cdot G]}{[H][G]} \ (1\text{-}2)$$

1.3.2.2 1:n host-guest system

In some cases, more than one guest molecule can bind with a host molecule which is 1:n host-guest system. Multiple equilibria of the binding type are described by stepwise binding constants for each guest as it binds, and the overall binding constant for the final complex is termed beta (β). The example of 1:3 complex process and calculation of multiple binding is shown below. For the stepwise binding constants (K_1, K_2, and K_3)

When a host molecule binds with the first guest molecule (**Equation 1-3 and 1-4**):
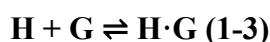
$$H + G \rightleftharpoons H \cdot G \ (1\text{-}3)$$

$$K_1 = \frac{[H \cdot G]}{[H][G]} \ (1\text{-}4)$$

When the 1:1 complex bonds with the second guest molecule (**Equation 1-5 and 1-6**):

$$HG + G \rightleftharpoons H \cdot G_2 \ (1\text{-}5)$$
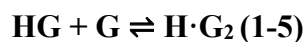
$$K_2 = \frac{[H \cdot G_2]}{[H \cdot G][G]} \ (1\text{-}6)$$

When the 1:2 complex bonds with the third guest molecule (**Equation 1-7 and 1-8**):

$$HG_2 + G \rightleftharpoons H \cdot G_3 \ (1\text{-}7)$$
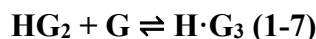
$$K_3 = \frac{[H \cdot G_3]}{[H \cdot G_2][G]} \ (1\text{-}8)$$

The overall binding constant for 1:3 host-guest binding (**Equation 1-9, 1-10 and 1-11**):

$$H + 3G \rightleftharpoons H \cdot G_3 \ (1\text{-}9)$$
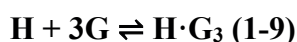
$$\boldsymbol{\beta_3} = \frac{[H \cdot G_3]}{[H][G]^3} \text{ (1-10)}$$

$$\boldsymbol{\beta_3} = \boldsymbol{K_1} \times \boldsymbol{K_2} \times \boldsymbol{K_3} \text{ (1-11)}$$

1.3.3 Kinetic and Thermodynamic Selectivity

1.3.3.1 Thermodynamic selectivity

The thermodynamic selectivity is the ratio of binding constants for a host binding two different guests, which is shown in **Equation 1-12**.

$$\boldsymbol{Selectivity} = \frac{K_{GUEST1}}{K_{GUEST2}} \text{ (1-12)}$$

1.3.3.2 Kinetic selectivity

Kinetic selectivity is based on a very different principle to thermodynamic selectivity, which is a time element involved. The transformed rate of competing substrates is the determining factor for kinetic selectivity. In nature, an enzyme or a catalyst is selective for the fastest-reacting substrate.

1.3.4 Solvent Effect

Before host molecules bind with guest molecules, both host and guest molecules absorb some solvent molecules on the surface. After forming the complex, these solvent molecules are getting free, and the entropy will increase. However, the increased entropy will affect the binding behaviour, which is called solvent effects. **Figure 1-15** shows the process of the effect of solvent molecules on the forming of a host-guest system. It can be understood that these solvent molecules can interact with the host and/or the guest molecule *via* supramolecular interactions. Some solvent molecules are able to inhibit the binding of host-guest, as the solvent dipole can strongly interact with a binding site, the formed the solvent-host or solvent-guest interactions are harder to break.
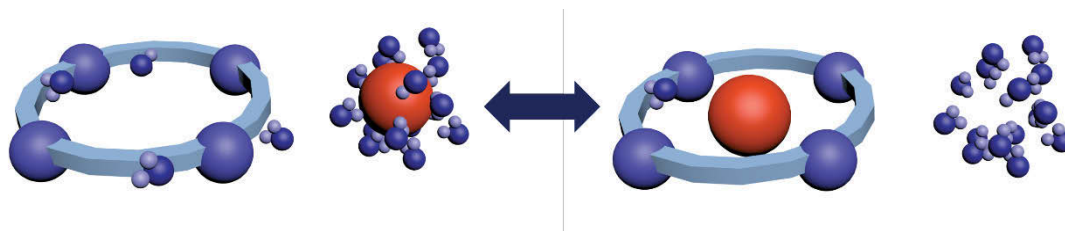
Figure 1-15. The process of the effect of solvent molecules on the formation of a host-guest system.

1.4 Host-Guest Chemistry

1.4.1 Guest

The definition of guest molecules in host-guest chemistry shows, in the complex, the smaller molecules are called guest molecules. It matches the size, the charge, and the shape to form the complexes with host molecules.

1.4.2 Hosts-Macrocycles

Host molecules usually are larger than a guest and can cover these particular guest molecules. There are several typical and famous macrocycles have been discovered and synthesized with a wide range of binding ability for numerous applications, such as crown ester, CD, "blue box", calix[n]arene (C[n]A), CB[n], pillar[n]arene (P[n]A), and bambus[n]uril (BB[n]). In this section, these advantages and disadvantages of each macrocycle are illustrated.

1.4.2.1 Crown ether

Crown ethers are cyclic molecules, which contain several ether groups, discovered by Charles Pedersen in 1967 (Pedersen, 1967). The structures of common crown ethers are shown in **Figure 1-16**. According to the different sizes, crown ethers can strongly bind

size-fit cations because of the ion-dipole interactions. An example of 18-crown-6 coordinating potassium is shown in **Figure 1-17**. Due to the hydrophobicity of most crown ethers, the resulting cations can transfer into nonpolar organic solvents.

Crown ether is a kind of cyclic organic molecules with several ether groups. The structure of common crown ethers is shown in **Figure 1-16**. Crown ether is synthesized by an organic chemist, Charles Pederson, who obtained the Nobel Prize in Chemistry in 1987 because of his significant contribution in supramolecular chemistry, especially in the foundation of crown ether.

The advantage of crown ethers is the high binding behaviour with cations, so they are usually used as phase transfer catalyst. Besides, 21- and 18-membered diazacrown ether derivatives exhibit excellent calcium and magnesium selectivity and are widely used in ion-selective electrodes. However, most of crown ethers are toxic which limits the development and applications.

Except for the common crown ether, sometimes, oxygens could be replaced by nitrogen to get the new types of molecules also provide numbers of dipole structures to recognize the cations.
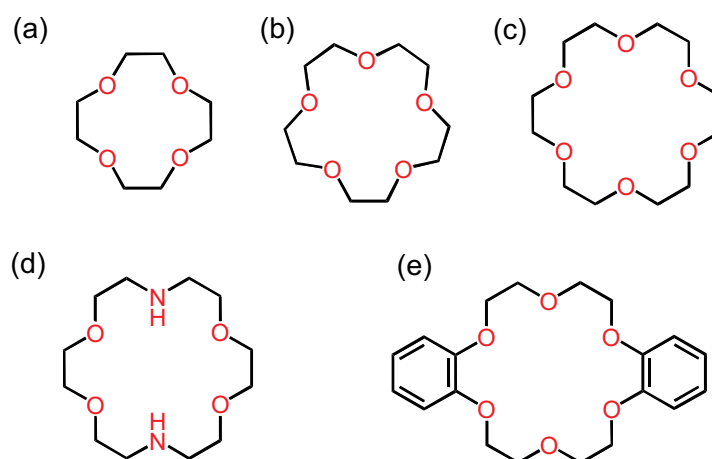
Figure 1-16. The molecular structures of several kinds of crown ethers: (a) 12-crown-4, (b) 15-crown-5, (c) 18-crown-6, (d) aza-18-crown-6, and (e) benzo-18-crown-6
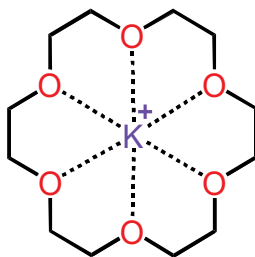
Figure 1-17. The complex of 18-crown-6 with potassium.

1.4.2.2 CDs

CDs are a library of compounds made of sugar units bound together as ring-shaped molecules. The common CDs include α-CD, β-CD, and γ-CD, which are shown in **Figure 1-18**. All kind of CDs are produced from enzymatic conversion, can be widely used in food, chemical industries, and drug delivery. As a ring structure, CDs provide inner hydrophobic cavities and hydrophilic outside surface. The typical structure entitles CDs unique preparty that can dissolve in water and also form complex with hydrophobic molecules. Therefore, CDs can be used for a series of applications, such as increasing bioavailability of hydrophobic drugs, cholesterol free products, and multifunctional dietary fibre.
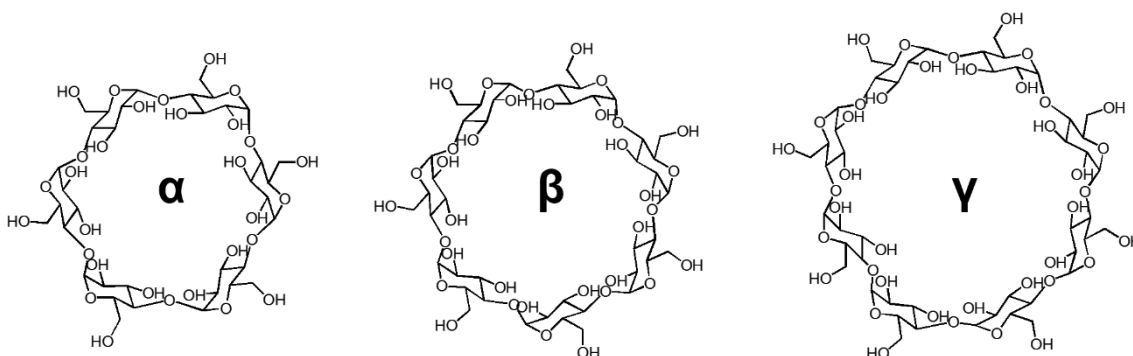
Figure 1-18. The structures of CDs (a) α-CD, (b) β-CD, and (c) γ-CD.

1.4.2.3 Cyclophane and "Blue Box"

Cyclophane is a polycyclic hydrocarbon type organic compound having one or more aromatic rings and one or more carbon chains or only one bond and is a kind of

Arylophane. An example of the most famous ring is cyclobis (paraquat-p-phenylene), commonly known as "blue box" (**Figure 1-19**). Due to its molecular structure, it can form one or more intermolecular forces with many small molecules and is widely used to discuss molecular mechanism and biological applications.
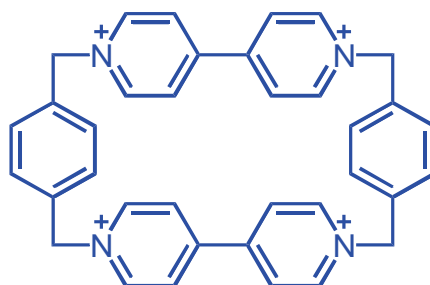
Figure 1-19. The structure of cyclobis(paraquat-p-phenylene) "Blue Box".

1.4.2.4 C[n]A

C[n]As are macrocycles based on the unit made of a phenol and an aldehyde. According to the numbers of the units, we usually can synthesize C[4]A and C[6]A. In C[4]A 4 up-down conformations exist: cone, partial cone, 1,2 alternate and 1,3 alternate (**Figure 1-20**). Much attention has also been paid to C[n]A because of their application of host-guest interaction, molecular self-assembly, and catalysis.

n=1 or 3
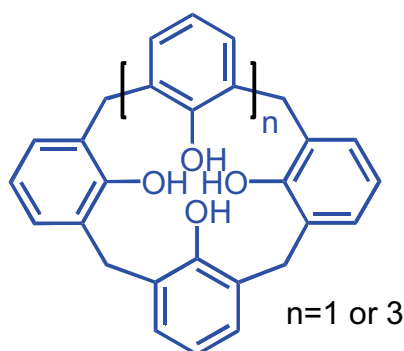
Figure 1-20. The structure of C[n]A.

1.4.2.5 CB[n]

The CB[n] molecule is a pumpkin-like cyclic compound. Its cavity is hydrophobic and open at both ends (**Figure 1-21**). The cavity is small at both ends and has a large middle to enclose organic molecules. The cavity is surrounded by a carbonyl group, and its openings at both ends are the same size, and the carbonyl groups at both ends form a bonding site with the cation, which enables it to pass through the hydrophobic action of the cavity, and the hydrogen bonding of the carbonyl group. To bond a metal ion or a charged portion of an organic molecule, the molecular structure of CB[n] is very rigid and cannot change shape to suit the guest molecule, so the coordination is accompanied by a strong specificity and extremely high association constant. However, it is difficult to introduce a functional group directly on the surface of the CB[n] relative to a host compound such as a crown ether, a CD or a C[n]A.

n=0,1,2,4......
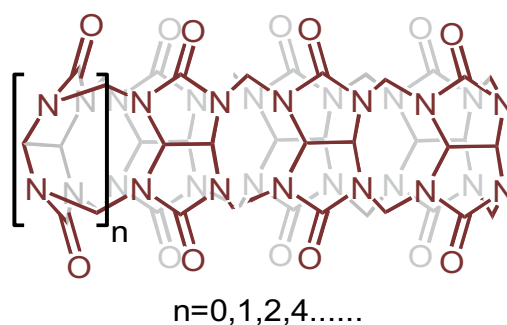
Figure 1-21. The structures of CB[n].

1.4.2.6 P[n]A

P[n]As are a new type of macrocycles made of hydroquinone units (5 to 10) connected in the para position. They are structurally similar to C[n]As that play an essential part in host-guest chemistry. The first P[n]A was reported in 2008 by Ogoshi research group (Ogoshi *et al.*, 2008). They used Lewis acid as a catalyst to obtain 1,4-Dimethoxypillar[5]arene (**Figure 1-22**).

R= OH or -OCH$_3$

n=1,2......
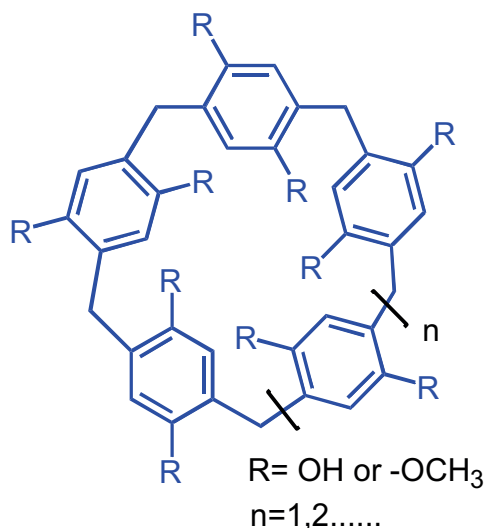
Figure 1-22. The structures of P[n]As.

After that, water-soluble P[5]As and P[6]As were synthesized to widen the applications of P[n]As. Currently, P[n]As ware widely used in biomedical applications such as drug delivery, chromatographic analysis, and bio-diagnostics. At the same time, P[n]A was also used for self-assembly to obtain the ordered structures.

1.4.2.7 BB[n]

Similar to CB[n], BB[n] is a new type of glycoluril-based macrocycles, whose synthesis was first reported in 2010 by the group of Dr Vladimir Sindelar (**Figure 1-23**) (Svec, Necas and Sindelar, 2010). Since then BB[n] has been investigated mainly due to its outstanding binding affinities towards anions in both organic solvents and water. As a new type of macrocycle, BB[n]s is at the beginning research stage on the synthesis and molecular recognition.
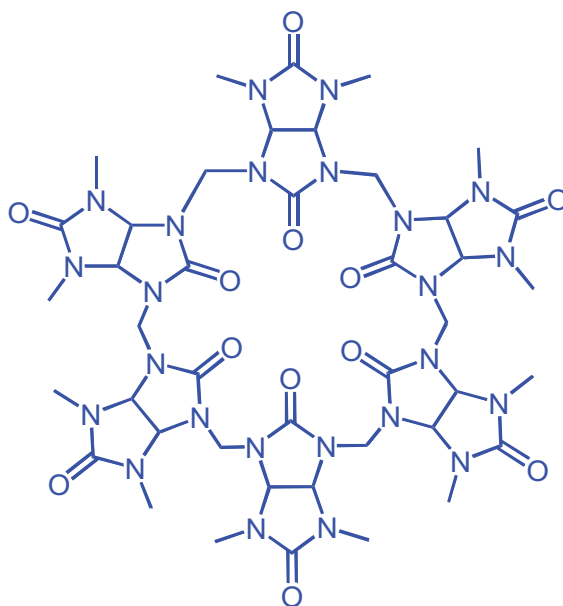
Figure 1-23. The structure of BB[6] and the synthetic method.

1.5 Self-Assembly

Self-assembly is a process of different building blocks arranging themselves from disordered to an ordered structure. The process is based on a library of supramolecular interactions, such as hydrogen bond, π interactions, van der Waals, and ion-dipole interactions (**Figure 1-24**). During the process, the system reduces the entropy and the free energy. Compared to host-guest interaction, self-assembly hardly recognises the size difference between interaction of two molecules. A definition of self-assembly was illustrated as follow:

> *The spontaneous and reversible association of molecular species to form larger, more complex supramolecular entities according to the intrinsic information contained in the components.*
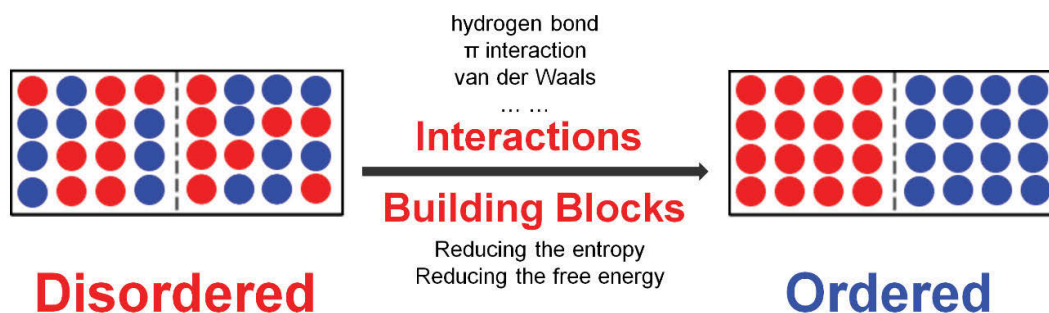
Figure 1-24. Schematic illustration of self-assembly.

According to the complexity of interactions in a system, self-assembly can be classified into single interaction self-assembly, multiple interaction self-assembly, multimediated assembly, unimultimediated assembly and hierarchical assembly.

1.6 Mechanically Interlocked Molecules (MIM)

MIM, as a particularly important concept in supramolecular chemistry, is of paramount importance in the field of topology. MIM is mainly made up of some molecules nested. Compared with previous connections between molecules, the formation of MIM does not depend on traditional covalent bonds, but on mechanical bonds. The essence of its mechanical bonds is the intermolecular interaction force, and it is also called supramolecular interaction. Dissociation of MIM occurs only when the covalent bond inside a component breaks. MIM is distinguished from traditional organic compounds, which belong to a new type of topology molecule.

1.6.1 Rotaxanes and Pureodorotaxanes

Rotaxane is a typical kind of MIMs formed by a ring of molecules on a dumbbell-shaped molecule (**Figure 1-25a**). The dumbbell-shaped molecule and the cyclic molecule have one or several intermolecular interactions (supramolecular interactions). When the dumbbell-shaped molecule lacks one (**Figure 1-25b**) or two stoppers (**Figure 1-25c**), it

is called a pseudorotaxane. When a dumbbell-shaped molecule has a plurality of cyclic molecules, it is called a polyrotaxane (**Figure 1-25d**).
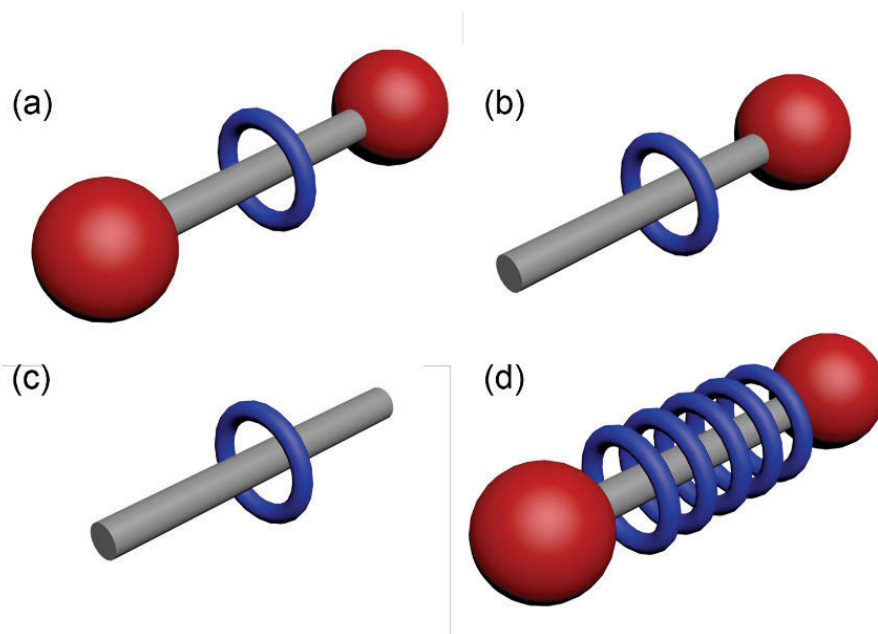
Figure 1-25. Some models of (a) rotaxane; (b) pseudorotaxane with one stopper; (c) pseudorotaxane without stoppers and (d) polyrotaxane.

1.6.2 Catenanes

Catenane is a MIM containing two or more interlocking macrocyclic molecules (**Figure 1-26**). These interlocked rings cannot be separated unless the covalent bond inside a ring molecule breaks. Common synthetic methods are divided into two methods: "statistical method" and template synthesis. The template synthesis is assembled by some molecules first, so that the molecules are in an appropriate configuration, which significantly improves the yield of the synthesis. Due to the inter-molecule rotation characteristics, hydrocarbons are widely used in molecular electronic devices and molecular sensors. (Gil-Ramírez, Leigh and Stephens, 2015; Erbas-Cakmak *et al.*, 2017; Zhang, August, *et al.*, 2018; Zhang, Stephens, *et al.*, 2018)
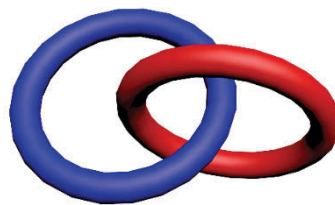
Figure 1-26. A model of typical Catenane.

1.7 Molecular Machine

Molecular machines are also known as nanomachines. Typically, it consists of three main elements: firstly, the components that make up the molecular device; secondly, these components have some interaction between one or several molecules or different parts of the same molecule; importantly, these interactions are subject to certain external forces or nanoscale molecular motion. In general, molecular systems with these three essential characteristics are called molecular machines.

In the past two decades, molecular machines have grown considerably. In 2016, the Royal Swedish Society awarded three scientists, Jean-Pierre Sauvage, Sir J. Fraser Stoddart and Bernard L. Feringa, the Nobel Prize in Chemistry, who have made outstanding contributions to the molecular machine field.

In general, molecular machines are divided into two broad categories: the first is a synthetic molecular machine; the other is a biological molecular machine. Artificial molecular machines are based on a wide range of chemical synthesis methods to synthesize MIM such as rotaxanes and catenanes. Common examples are a molecular switch/elevator (**Figure 1-27**).

Compared to synthetic molecular machines, biological molecular machines are mostly found in nature, especially in the fields of molecular biology and cell biology. A particularly famous example is the process of a ribosome translation which convert the

information of RNA to assemble a protein (**Figure 1-28**) (The figure from the website:

https://sciencing.com/role-ribosome-play-translation-4752555.html).
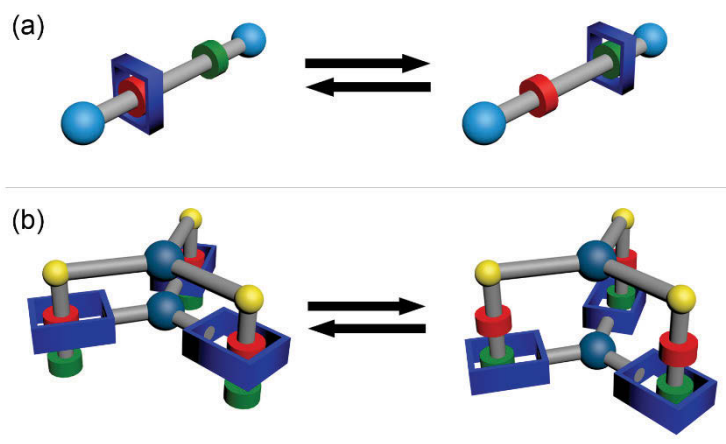
Figure 1-27. Some examples of synthetic molecular machines: (a) molecular motor, (b) molecular switch, and molecular shuttle.
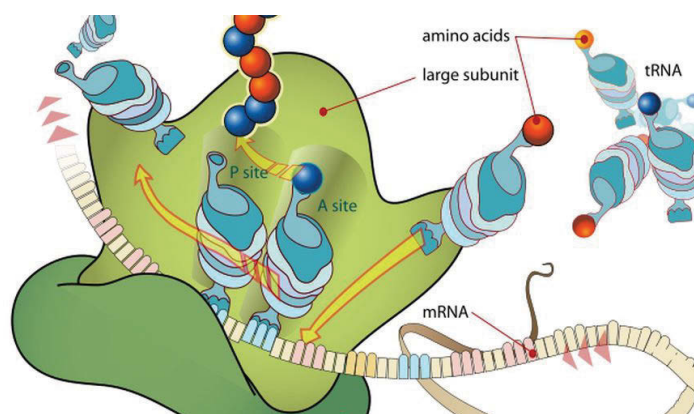
Figure 1-28. An example of biological molecular machines: ribosome's translation.

UPCONVERSION NANOPARTICLES

1.8 Introduction of UCNPs

Upconversion nanomaterials, converting infrared light at lower energy level into high energy visible and ultraviolet lights, are emerging as a new candidate for advanced biomedical and photonics applications, such as laser, solar cells, wave guides,

bioimaging, optical storage, security, and display devices. Lanthanide (Ln) doped upconversion nanocrystals (Ln-UCNCs) are dilute guest-host systems where trivalent Ln ions, acting as optically active sensitizers and activators, are dispersed as guests in an appropriate dielectric host lattice. Upconversion in Ln-UCNCs occurs through a series of photo-physical processes in which energy is absorbed and transferred by the 4fN electronic states of the Ln dopants whose configurations are often depicted as ladder-like manifolds.

1.8.1 Mechanism of Upconversion

There are three primary mechanisms in the upconversion luminescence: excited state absorption (ESA), photon avalanche (PA), and energy transfer upconversion (ETU). A specific case usually is recognized based on one of the mechanism or in combination.

1.8.1.1 ESA

ESA is based on multistep excitation by sequentially absorbing two or more photons from ground state to intermediate. When reaching the final excited state, the ion or electron will jump back to the ground state. **Figure 1-29** shows the ESA process that an ion or electron absorbs two photons, which wavelengths are ω1 and ω2, respectively. The electrons jump from ground state E0 to E2 in two steps and emit higher energy photon ω0 when drops back to the ground state.

1.8.1.2 PA

Compared with ETU, PA is a much more complicated process. A schematic illustration is shown in **Figure 1-30**. An electron is excited after absorbing excitation radiation (ω_1). However, sometimes, the absorbed energy cannot match the intermediate states. If the energy of absorption is higher than E_2, it will go down to the E_2 state. Then the electron will transfer parts of energy to another unit in the ground state, which results that two

electrons jump into another state (E_1) between E_2 and E_0. One of the electrons in the E_1 state can be excited to the E_3 state after absorbing the radiation (ω_1), which interacts with another E_0 electron to form three E_1 electrons. Then another electron in the E_1 state will excite into the E_3 state. After accumulation of the electrons in E_3, some electrons will go back from the E_3 state. The higher energy photons are emitted.
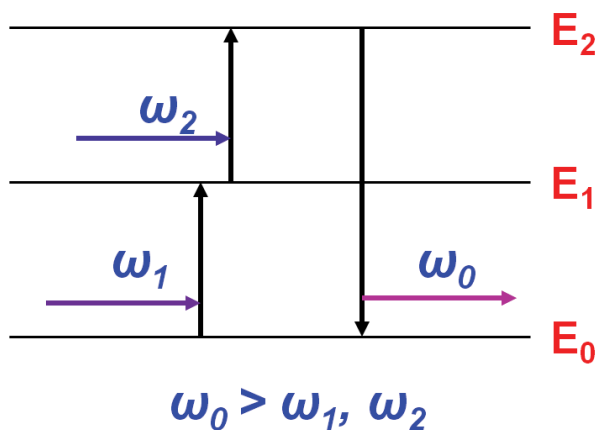
Figure 1-29. Scheme of ESA. An ion or electron at the ground stage absorbs two lower energy photons and emits a higher energy photon when jumping back to the ground state.
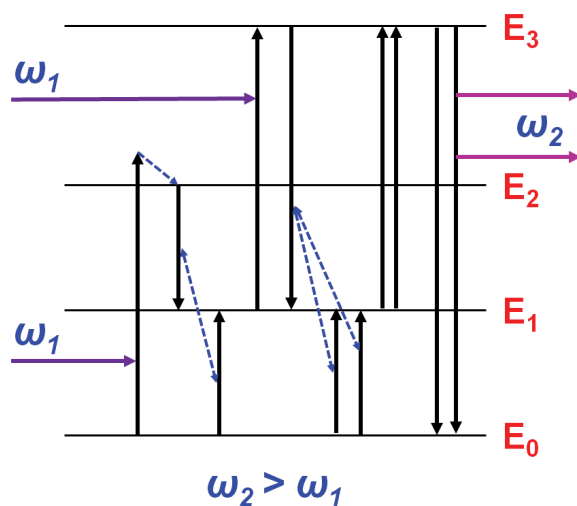
Figure 1-30. The scheme of PA.

1.8.1.3 ETU

In rare earth doped UCNP systems, ETU is the most efficient upconversion process. Two main situations are discussed and shown in **Figure 1-31**, which are (a) resonant non-radiative transfer and (b) phonon-assisted non-radiative transfer. There is a common condition for the two kinds of energy transfer to occur, that is, sensitizer and activator should be close enough. When the energy levels of the two active states are almost equal, the energy can be transferred from sensitizer to activator (**Figure 1-31a**). However, when there is a slight difference in energy between the two states, energy can still pass from sensitizer to activator under phonon-assisted conditions (**Figure 1-31b**).
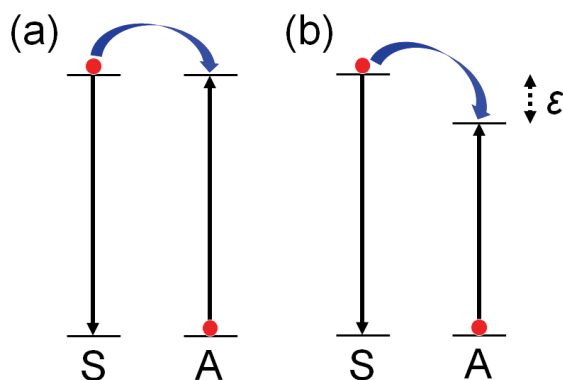
Figure 1-31. Energy transfer processes between two ions: (a) resonant non-radiative transfer; (b) phonon-assisted non-radiative transfer. (S: sensitizer, A: activator).

1.8.2 The Properties and Advantages of UCNPs

Compared to other luminescent materials, the most significant property of the up-conversion material is its anti-Stokes law. Traditionally, luminescent materials are stimulated with more intense light to produce relatively weaker light. For example, there are some luminescent materials producing visible light under the excitation of ultraviolet light, like QDs, fluorescence proteins. However, upconversion nanomaterials can convert

near-infrared light into visible light. In biological applications, this greatly diminishes the stimulation and auto-backgrounds of the organism by the excitation light.

1.9 Synthesis of Ln-Doped UCNPs

There are three conventional methods of the synthesis of UCNPs, i.e., thermal decomposition, hydrothermal synthesis, and ionothermal synthesis.

1.9.1 Thermal Decomposition Method

Thermal decomposition method generally comprises injecting a metal organic compound precursor into a high boiling organic solvent having a coordination property under anhydrous and oxygen-free conditions, and using the high temperature to make the precursor then rapidly decomposes and nucleates (Mai *et al.*, 2007).

Two kinds of nanocrystals (α-, β-) can be formed in different pathways. To synthesize α-NaYF$_4$ nanocrystals, the pathway includes four main stages (**Figure 1-32**), which are (1) nucleation in a delayed time; (2) size growth by monomer supply; (3) size shrinkage by dissolution; and (4) aggregation.
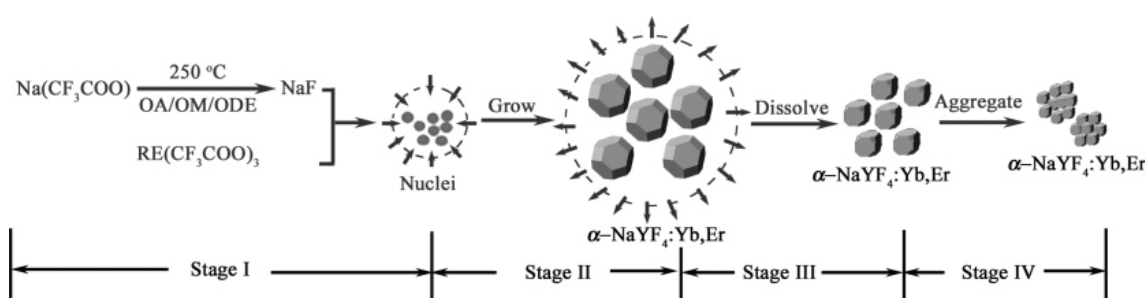
Figure 1-32. Schematic illustration of the growth stages of β-NaYF$_4$:Yb,Er nanocrystals via a delayed nucleation pathway. RE: Y, Yb, Er; OA: Oleic Acid; OM：Oleylamine. (Mai *et al.*, 2007)

Compared with α face crystal, β-nanocrystal shows a higher conversion ability with green emission 10 times stronger. There are three modes for the transition from α face to β face, which are based on the Ostwald-ripening promoted process, wherein the dissolution and recrystallization dominant. (**Figure 1-33**)
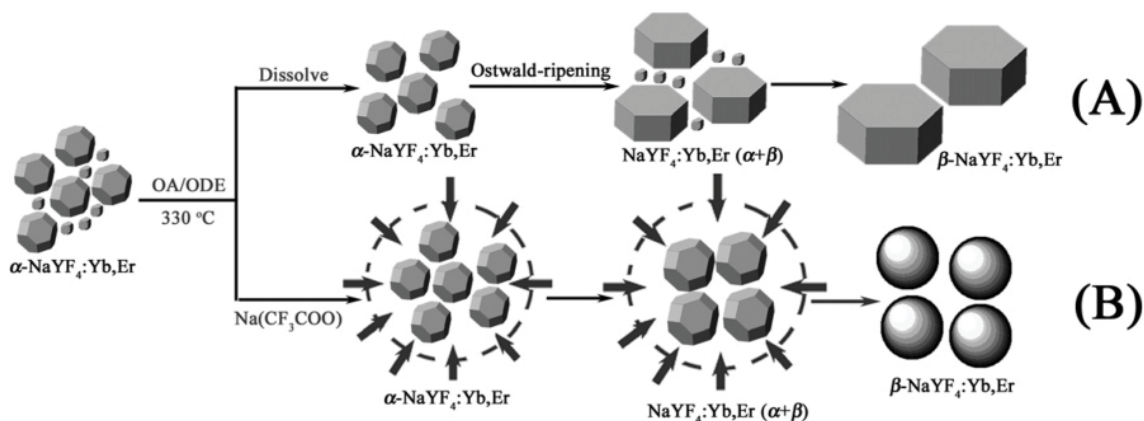
Figure 1-33. Schematic Illustration of the Growth Process of α-NaYF₄:Yb,Er Nanocrystals from β-NaYF₄:Yb,Er Monomers via a Delayed α→β Phase Transition. (Mai *et al.*, 2007)

1.9.2 Hydrothermal Synthesis Method

Hydrothermal synthesis is also a common synthetic approach, which can be processed under high pressures and temperatures. (Darani et al. 2015; Jiang, Qin & Zhou 2016; Li et al. 2017; Qiu et al. 2015; Wang & Cheng 2015; Zhang et al. 2016) Compared with the thermal decomposition method, hydrothermal synthesis is regarded as a relative mild approach which can react in a solution-based system at a lower temperature. There are different types of morphologies and architectures being made in this method. **Figure 1-34** shows the different kinds of upconversion nanocrystals which are synthesized via hydrothermal method. (Cao et al. 2011; Fan et al. 2006; Li et al. 2007; Yi et al. 2002; Zhang et al. 2007)
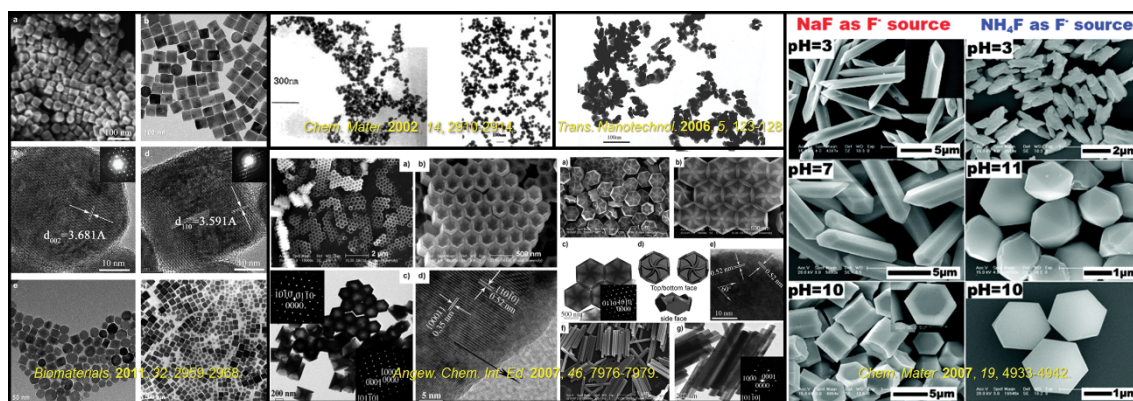
Figure 1-34. Nano/Microcrystals of upconversion materials by hydrothermal synthesis. (Cao et al. 2011; Fan et al. 2006; Li et al. 2007; Yi et al. 2002; Zhang et al. 2007)

1.9.3 Ionothermal Synthesis Method

In the last several decades, much attention has been paid to ionic liquid because of the low vapor pressure, non-flammability and chemical stability. (Hallett and Welton, 2011) A ionothermal synthetic approach of UCNPs based on an ionic liquid was raised because of the free reaction which means relatively the reaction is much softer. It can react under low temperature in a shorter time. In 2009, Liu and co-workers firstly synthesized water-soluble pure hexagonal-phase NaYF$_4$: Yb^{3+}, Er^{3+}/Tm^{3+}. (Liu et al. 2009) **Figure 1-35** shows the properties of morphology and upconversion luminescence spectra. However, this approach cannot be developed because the as-made materials process a low quality on the size distribution, uniformity and monodispersity compared with the other two methods.
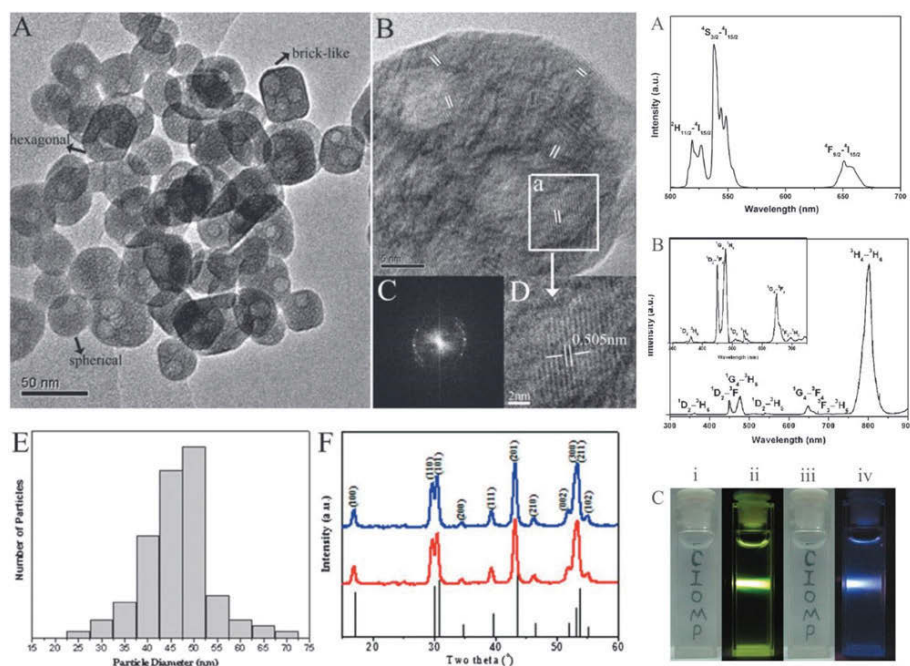
Figure 1-35. The ionothermal synthesis of hexagonal-phase NaYF₄: Yb³⁺, Er³⁺/Tm³⁺: the characterization and spectra. (Liu et al. 2009)

Therefore, the most widely used synthesis methods are still the thermal decomposition and hydrothermal synthesis, and most of these publications are still based on both two ways.

1.10 Conclusion

As the theoretical basis of the whole thesis, this chapter introduces the related concepts of supramolecular chemistry and the principle, properties and synthesis methods of upconversion materials. It has played a significant role and contribution to the elaboration of this thesis. At the same time, it also provides an essential basis for the discussion of related issues.

2 Literature Review: Supramolecular Interactions Induced Surface Modification and Conjugation of Upconversion Nanoparticles

2.1 Introduction

Surface functionalisation and bioconjugation hold the key to driving many purpose-synthesized inorganic nanoparticles into real-world applications. Ln ions doped UCNP is a good example (Zhou et al. 2015): while it delivers a great promise as molecular probes, sensors, drug carriers and light transducers for drug delivery (Shen, Zhao & Han 2013), light activated therapy (Idris et al. 2015), single molecular bio-sensing (Wang, Li & Zhang 2016), super-resolution nanoscopy (Liu, Lu, et al. 2017), and disease diagnostics (Huang et al. 2014).

However, the hydrophobic surface of UCNPs is one of the main challenges for biomedical applications. It remains a bottleneck challenge for the community to explore practical strategies to functionalize the UCNPs surfaces for hydrophilicity conversion and further bioconjugation to meet many cellular and molecular specific needs.

This review includes two parts:

1. Approaches of surface modification of UCNPs;
2. Self-assembled conjugation of UCNPs based on supramolecular interactions

2.2 Hydrophilic Modification Approaches on the Surface of UCNPs

2.2.1 Overview

In this section, we mainly divide the surface modification of UCNPs into four parts according to different mechanisms of supramolecular interaction: (1) ion-dipole interaction, also including hydrogen bond interaction; (2) hydrophobic effect; (3) *in situ* organic reactions; (4) the inorganic layer coating. Compared with other previous similar reviews, we have explored the essence of UCNP from a binding mechanism perspective.

On this basis, we can modify the surface of UCNPs effectively. **Figure 2-1** shows several major modification strategies of OA stabilized UCNPs (OA-UCNPs) based on binding mechanism (more details in **Chapter 3**).
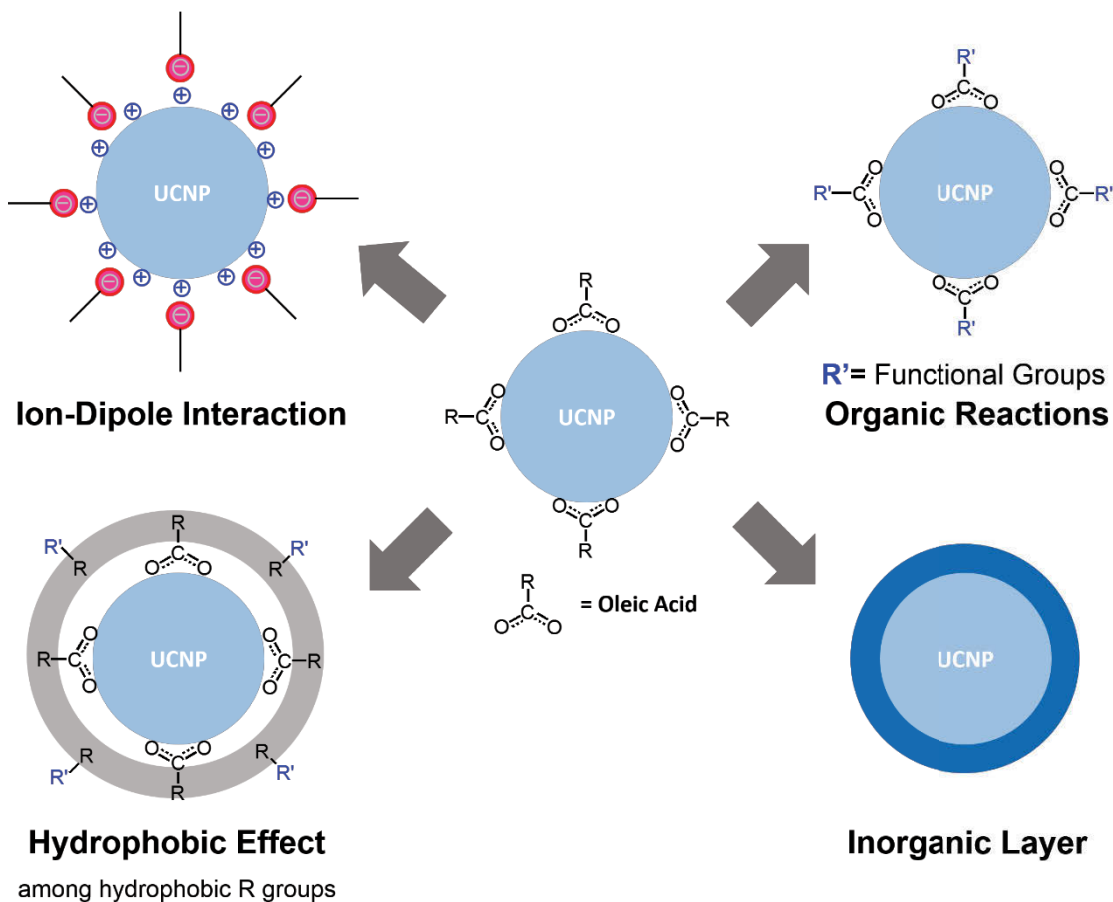
Figure 2-1. The overview of surface modification of UCNPs based on surface binding mechanism.

2.2.2 Ionic and Dipolar Interaction

As the strongest binding mode in supramolecular interactions, ionic and dipolar interactions (including ion-ion interaction, ion-dipole interaction, and dipole-dipole interaction) have become one of the most common modification methods on the surface of UCNPs. In general, the Y atoms on the surface of UCNPs has a certain positive charge due to the absence of three F atoms on the surface. Therefore, as long as the molecules modified have an electron-rich functional group, it is possible to form ion-dipole

interaction with Y atoms from the surface of UCNPs. Sometimes the strength of the modification depends on the number of oxygen (O) in the functional groups. There are two main approaches for modifying the surface of UCNPs comparing with the binding ability of carboxylate from OA molecules: one-step ligand exchange and two-step ligand exchange.

2.2.2.1 One-step ligand-exchanged approach

On the surface of OA-UCNPs, these carboxylate groups of OA molecules process two identical oxygen atoms (more details in **Chapter 3**) in total. In general, as long as the target functional group has more than two O atoms, the bonding ability of the functional group is stronger than the one of OA molecules, which is mainly because more O atoms provide more electrons and increase electron cloud density, which will have a stronger interaction with the Y atoms from the UCNPs. Therefore, the target molecules only need to be blended with OA-UCNP. The process is carried out under a certain temperature to weaken the interaction between OA and the UCNP surface. When a large amount of bare surface appears on the surface due to the dissociation of OA with Y atoms, the target molecules will be easy to connect to the surface of UCNP. Because of the stronger binding ability, only a very limited reverse reaction occurs, which means that it is difficult for OA to replace the target molecules. This method is called a one-step ligand-exchanged method.

An example shows the one-step ligand-exchanged method by using PEG-phosphate (Boyer et al. 2010; Sun et al. 2016). Compared with carboxylate, phosphate shows a higher electron cloud density, which means a stronger binding between the positive surface of UCNPs and phosphate terminal (**Figure 2-2**). Except for phosphate, other high electron cloud density functional groups also can process the properties, such as sulfonic and phosphoric groups (More details in **Chapter 4**). More examples are shown in **Table**

2-1 on **Page 43** (Dong et al. 2011; Gonzalez-Bejar et al. 2014; Liras et al. 2014; Nyk et al. 2008; Voliani et al. 2013; Zhang et al. 2009).
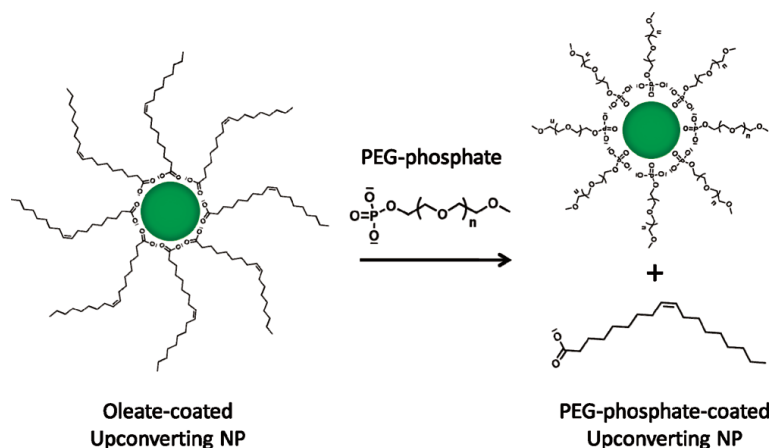
Figure 2-2. The ligand exchange reaction of OA-UCNP with PEG-phosphate. (Boyer et al. 2010)

2.2.2.2 Two-step ligand-exchanged approach

This method is mainly used as an alternative molecular binding ability is not strong enough to replace the OA out of the UCNP surface. For example, it is difficult to replace OA with a carboxylic acid-containing molecule, because of the similar binding abilities. Therefore, a two-step replacement method has been taken in this stage (Kong et al. 2017). First, the OA on the surface of the UCNPs were removed by using pickling, then the surface of the UCNP was completely exposed (Liu, Tan & Chen 2013; Ni et al. 2014; Wang, Wang, et al. 2013; Zhou, Noor & Krull 2014). After washed away the dissociated OA, the target molecule will be easily modified on the UCNP surface. The scheme of the two-step ligand-exchanged approach by using mild acid is shown in **Figure 2-3**. Similarly, nitrosyl tetrafluoroborate (NOBF$_4$) also can remove OA from the surface of UCNPs to form the ligand-free UCNPs. for further modification (**Figure 2-4**) (Esipova et al. 2012; Shen et al. 2013; Wang, Liu, et al. 2013; Yan et al. 2012). More examples are displayed in **Table 2-1** on **Page 43** (Wang et al. 2016; Esipova et al. 2012; Liu, Tan &

Chen 2013; Ni et al. 2014; Shen et al. 2013; Wang, Wang, et al. 2013; Wang, Liu, et al. 2013; Yan et al. 2012; Zhou, Noor & Krull 2014).
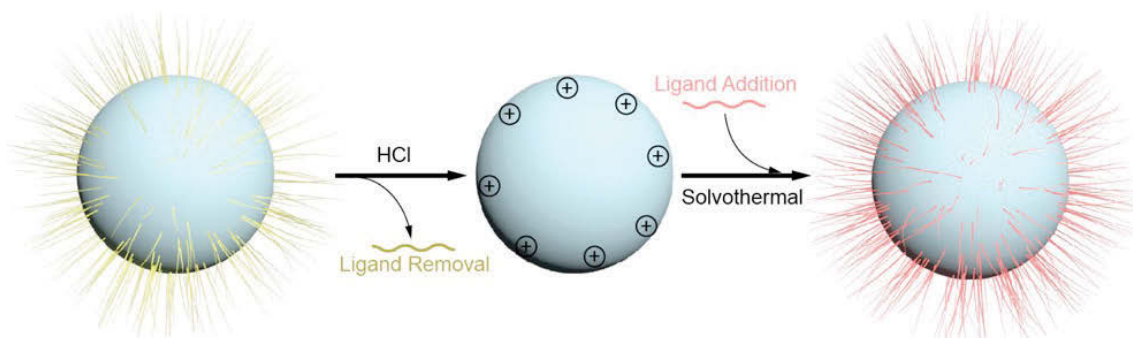
Figure 2-3. The two-step ligand-exchanged method on the surface of UCNPs by using acid.
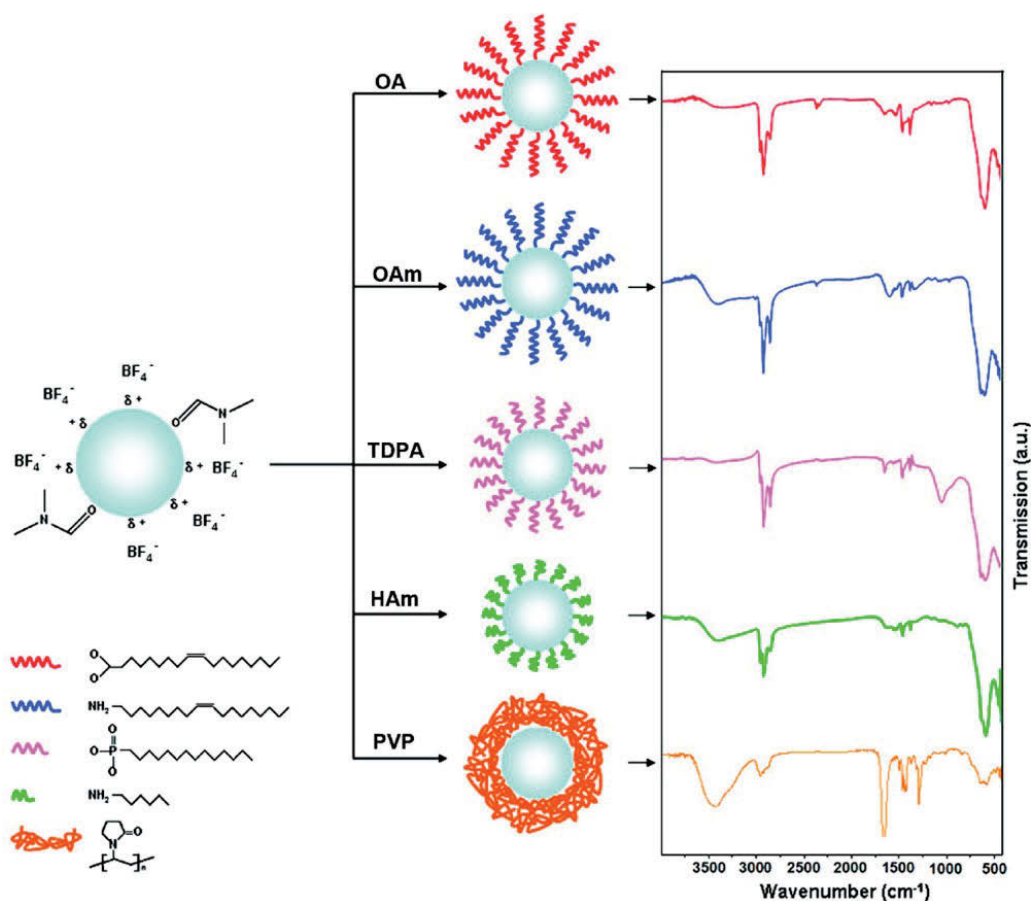
Figure 2-4. The two-step ligand-exchanged method on the surface of UCNPs by using NOBF₄. (Muhr et al. 2014)

2.2.2.3 Multiple site modification

When a host molecule binds several guest molecules, the binding constant of each molecule is K_1, K_2 …… K_n. Then the total binding constant (K_t) of the 1 : n binding system is $K_t = K_1 \times K_2 \times …… \times K_n$. (More details in Section 1.3.2 of **Chapter 1**).

It can be seen that a multiple binding mode is stronger than a binding mode of a single site. Therefore, many charged polymers, such as PAA, are used to modify the surface of UCNP. Compared to small molecules, these polymers have many repeating units that carry sites that bind to the surface of the UCNP, forming a multi-site binding mode. Therefore, this method is also widely used for surface replacement of UCNP. **Figure 2-5** shows the approach of replacement on the surface of UCNPs and several examples are displayed in **Table 2-1** on **Page 43** (Bogdan et al. 2010; Jin et al. 2015; Johnson et al. 2010; Naccache et al. 2009; Wang, Wu & Liu 2013; Xia et al. 2014; Xiong et al. 2010; Xu et al. 2017; Yi & Chow 2006).
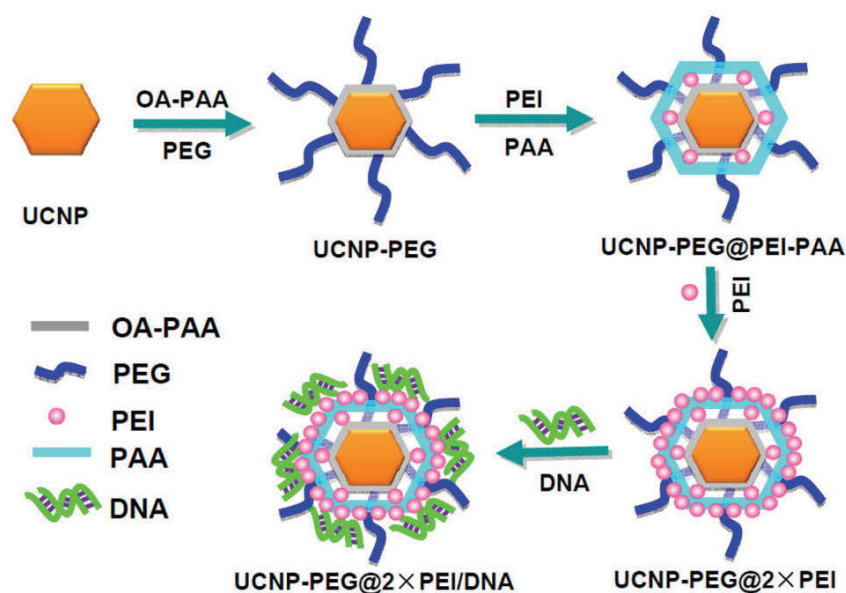
Figure 2-5. The ligand-exchanged method by using polymer. (He et al. 2013)

Similar to the replacement method of polymers, supramolecular macrocycles (Engel et al. 2018) and some small organic molecules with several functional groups (Cao et al.

2010) are also based on the multiple site binding. More details are shown in **Chapter 4**, **Chapter 5**, and **Chapter 6**.

2.2.2.4 Concentrations to ligand exchange

In addition to the influence of bonding ability, the concentration of the new ligand also affects the replacement of the ligand on the surface of the material to some extent. When the concentration of the new ligand increases, the collision probability of the new ligand with the UCNP surface increases, which improves the replacement efficiency to some extent. According to the reaction equilibrium theory, when the concentration of the reaction substrate is increased, the reaction proceeds more easily in the positive direction.

Table 2-1. Examples of ligand-exchange based on ion-dipole interactions on the surface of UCNPs.

Native Ligand	Method	New Ligand	Refs
OA	One-Step	PEG-Phosphate	(Boyer et al. 2010)
OM	One-step	Hexanedioic acid	(Zhang et al. 2009)
OA	One-step	Mercaptopropionic acid	(Nyk et al. 2008)
OM	One-step	Thioglycolic acid	(Dong et al. 2011)
OA	One-step	monothiolated heterobifunctional PEGs	(Gonzalez-Bejar et al. 2014; Liras et al. 2014; Voliani et al. 2013)
OA	Two-Step	Carboxylate-β-CD (β-CD-COO$^-$)	(Wang et al. 2016)
OA	Two-step	Polyallyamine	(Wang, Wang, et al. 2013)
OA	Two-step	Lysine	(Liu, Tan & Chen 2013)
OA	Two-step	HS-PEG-NH2	(Ni et al. 2014)

OA	Two-step	citrate	(Zhou, Noor & Krull 2014)
OA	Two-step	PAA	(Esipova et al. 2012; Shen et al. 2013; Wang, Liu, et al. 2013)
OA	Two-step	PVP	(Yan et al. 2012)
OA	Multiple Sites	PEI	(Wang, Wu & Liu 2013; Xu et al. 2017)
OM	Multiple Sites	β-CD-COOH*	(Engel et al. 2018)
OA	Multiple Sites	PAA	(Jin et al. 2015; Naccache et al. 2009; Xiong et al. 2010)
OA	Multiple Sites	Citrate	(Cao et al. 2010)
OM	Multiple Sites	PEG-carboxylate	(Yi & Chow 2006)
OA	Multiple Sites	Poly(amido amine)	(Bogdan et al. 2010)
OA	Multiple Sites	Poly(allyl amine)	(Xia et al. 2014)
OA	Multiple Sites	PVP	(Johnson et al. 2010)

*note: The structures may have a slight difference in β-CD-COOH.

2.2.3 Hydrophobic Effect

The OA molecule consists of two parts: one is the carboxylate bonded to the surface of the UCNP, and the other is the hydrophobic long chain (**Figure 2-6**). This hydrophobic long chain provides a hydrophobic environment for the UCNP surface. Therefore, long-chain hydrophobic structures with similar structures are easily intercalated into the UCNP surface due to hydrophobic interactions. If the other end of the inserted molecule carries

a hydrophilic group, the UCNP will be converted to hydrophilic. If this hydrophilic group
is chemically active, further modifications thus can be made.

The Cetyltrimethylammonium Bromide (CTAB) is an example. It has a hydrophilic end
and a hydrophobic long chain (**Figure 2-6**). Therefore, when CTAB is dispersed in the
dispersion of UCNP, CTAB will automatically intercalate to the surface of UCNP,
thereby allowing the quaternary ammonium salt portion to be exposed outside, thereby
converting UCNP into hydrophilic (**Figure 2-7**) (Cheng et al. 2015; Liu et al. 2011).
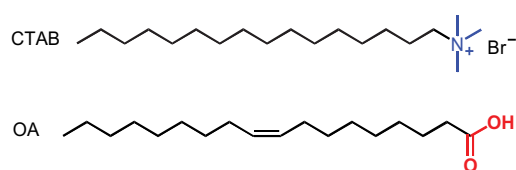
Figure 2-6. The structures of OA and CTAB.
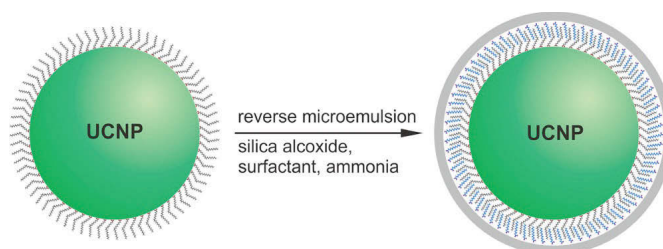
**Figure 2-7. The ligand-exchanged method by using hydrophobic effect. (Muhr et al.
2014)**

2.2.4 Organic Reactions on Original Ligand

After the synthesis of UCNPs, OA or OM are usually coated on the surface of
nanoparticles to stabilize the shape and properties of nanoparticles. Structurally, OA and
OM have a common feature, with a carbon-carbon double bond in the middle of the long
chain. Almost all in situ organic reactions are based on this carbon-carbon double bond.
First, the carbon-carbon double bond can be oxidized by the oxidizing agent. Due to the
use of different oxidizing agents, types of functional groups will be produced. In addition,
it is based on the Thiol-ene reaction, which is an organic reaction between a thiol and an

alkene, to form an alkyl sulfide. These methods based on original ligand reaction is summarized in **Table 2-2**.

Table 2-2. Examples of original ligand reaction.

Type	Reagent	Formation	refs
Oxidation	Lemieux-von Rudloff reagent	Aldehyde or ketone	(Chen et al. 2008)
Oxidation	ozone	Aldehyde or carboxylic acid	(Zhou et al. 2009)
Oxidation	3-chloroperoxy-benzoic acid	Epoxides	(Hu et al. 2008)
Click reaction	Thiol group	The functional group from the thiol molecule	(Sun et al. 2016)

2.2.5 Inorganic Coating

In addition to traditional organic chemistry methods, some inorganic materials are also used for surface modification of UCNP. By adopting a core-shell structure, UCNP is completely encapsulated in an inorganic structure that provides excellent protection for UCNP. However, the luminescence properties of the up-conversion may have an effect due to förster resonance energy transfer (FRET) or the like. **Table 2-3** shows the examples of inorganic coating.

Table 2-3. Examples of inorganic modification on the UCNPs.

Native ligand	Shell	refs
OA	SiO$_2$	(Cai et al. 2017; Hu et al. 2009; Jiang et al. 2015; Liu et al. 2014; Nguyen et al. 2016; Yang, Li, et al. 2014)
OA	Au	(Sudheendra et al. 2011; Zhang, Li, et al. 2010)
OM	Ag	(Dong et al. 2011)

2.3 Supramolecular Induced Organic-Inorganic Self-Assembly of UCNPs

2.3.1 Self-Assembly Based on Hydrophobic Effect

Hydrophobic effect is one of the most common methods for surface conjugations. Compared with some other methods, it shows several advantages; firstly, there is no more reaction needed to conjugate other molecules; secondly, the design of conjugation molecules is much easier. **Figure 2-8** shows an example of multiple conjugations (Cen et al. 2014). UCNPs were only mixed with all the target molecules. These molecules will automatically be inserted into the surface of nanoparticles.
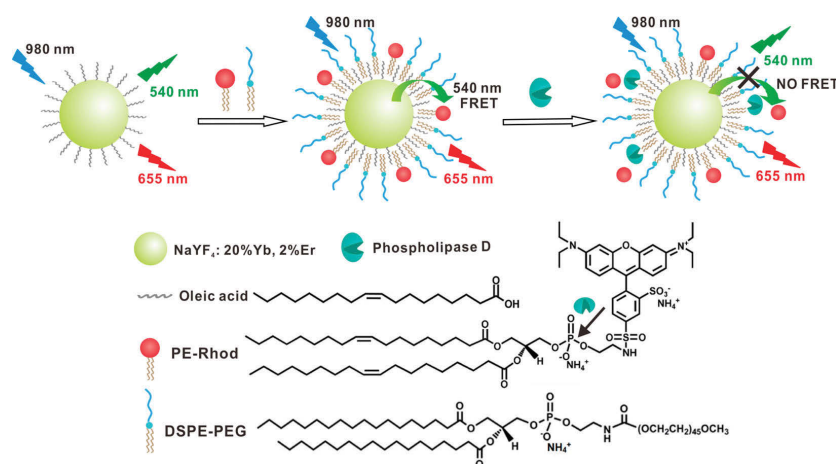
Figure 2-8. An example of surface conjugation by using hydrophobic interactions. (Cen et al. 2014)

In addition to this traditional mode of modification of the cuttings, polymer-assisted modes are also applied to the assembly of UCNPs and small molecules (**Figure 2-9**). In general, this polymer will have a hydrophobic interaction with both UCNP and organic molecules. With the aid of the polymer, small organic molecules are modified to the surface of the material (Zhao et al. 2017).
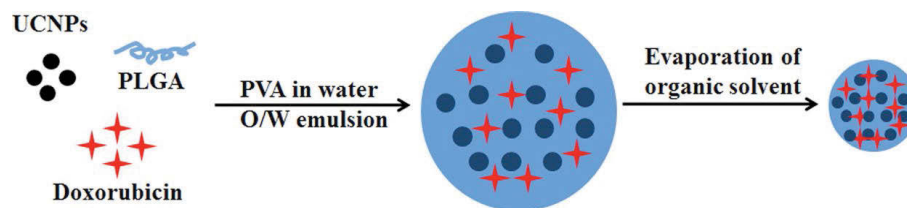
Figure 2-9. The polymer assisted self-assembly between UCNPs and DOX. (Zhao et al. 2017)

There is also an assembly method based on hydrophobic interactions that are primarily based on the interaction of the master. The host or guest molecule on the surface of the UCNP was modified to connect the other to the UCNP surface through host-guest interaction (Liu et al. 2010; Wang et al. 2016). Two typical examples were shown in **Figure 2-10** and **Figure 2-11**.
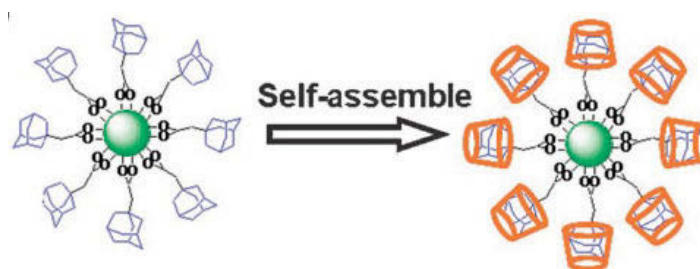
Figure 2-10. The host-guest (hydrophobic) interaction induced self-assembly system with guest modified UCNPs. (Liu et al. 2010)
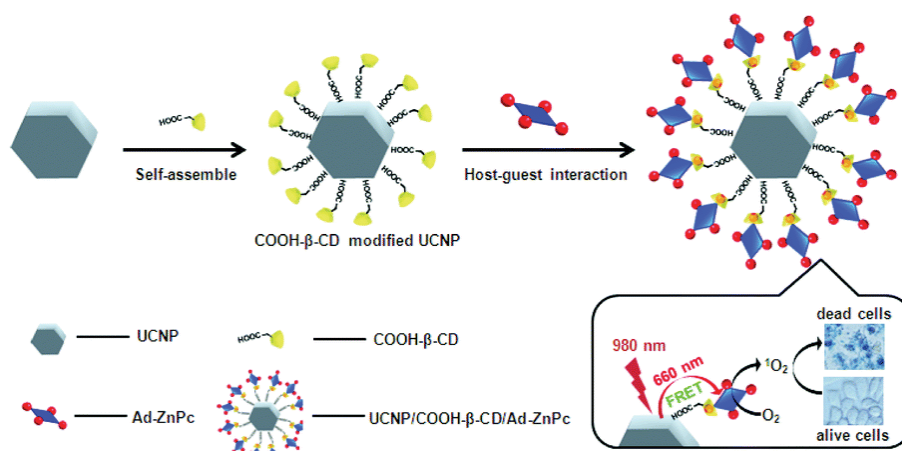
Figure 2-11. The host-guest (hydrophobic) interaction induced self-assembly system with host modified UCNPs. (Wang et al. 2016)

2.3.2 Self-Assembly Based on Ionic-Dipole Interaction

This interaction is based on different charges on the surface or the different density of electrons. A layer-by-layer system on the surface of UCNPs has been designed to achieve the molecular coating by ionic-dipole interaction (Wang *et al.*, 2013). By changing the pH, the amide bonds were broken. Obviously, the positive Poly(allylamine hydrochloride)- Poly(ethylene glycol) (PAH-PEG) layer was repulsed by the PAH layer on the top surface of UCNPs. (**Figure 2-12**) The pH sensitivity makes the materials not stable enough, but it also takes an advantage that some smart materials can be designed by the property.
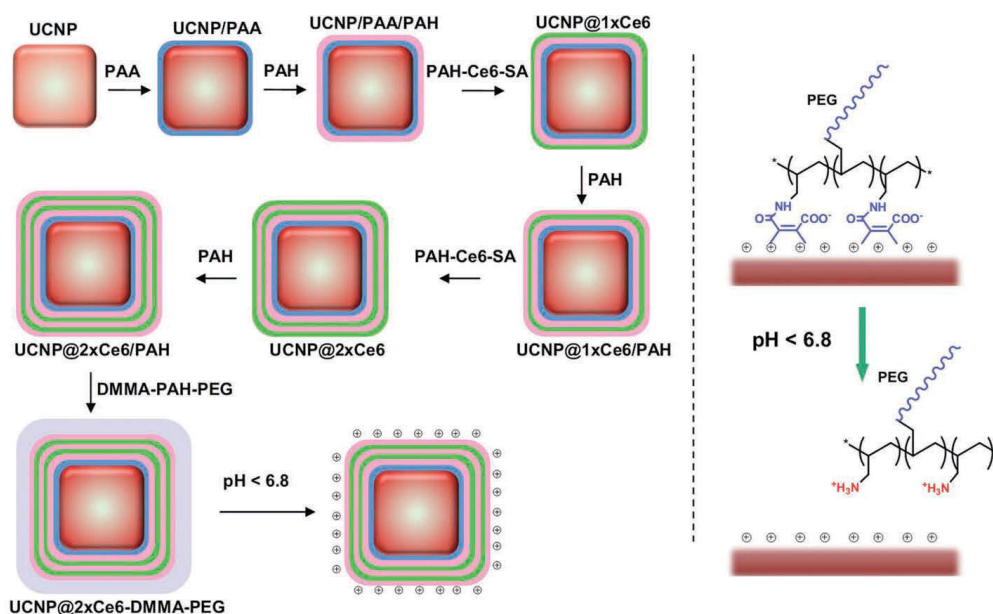
Figure 2-12. The Layer-by-Layer system on coating on the surface of UCNPs and the pH controlled method. (Wang *et al.*, 2013)

2.3.3 Self-Assembly Based on π Interaction

Compared with other methods, the conjugation based on π interaction is not that common. An example is reported by using the π-π stacking between UCNPs and poly(m-phenylenediamine) (PMPD) to build a biosensor(Wang, Wu & Liu 2013). To detect the target DNA, the probe DNA modified UCNPs were conjugated with PMPD by π-π

stacking because both of them get a large conjugate system. At the same time, PMPD can also form a FRET pair with UCNP. The emission of UCNPs will absorb by PDMA. When approaching the detection system, the target DNA will replace the PMPD and bind with probe DNA to recover the emission of UCNPs. The detection process is shown in **Figure 2-13**.
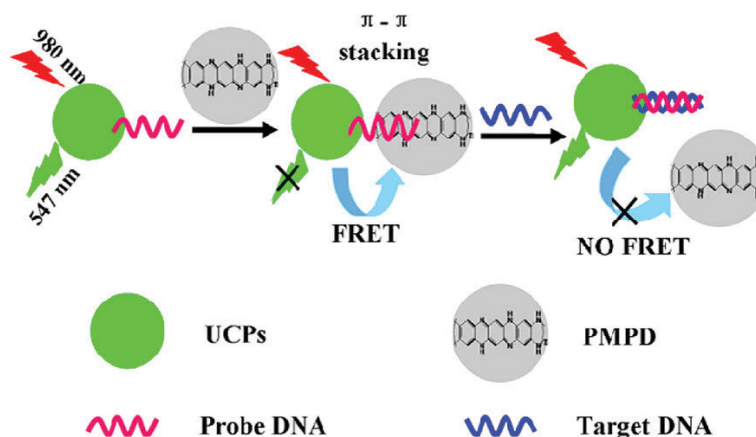
Figure 2-13. The UCNP sensor based on π-π interaction. (Wang, Wu & Liu 2013)

2.4 Supramolecular Induced Inorganic-Inorganic Self-Assembly of UCNPs

2.4.1 Inorganic-Inorganic Self-Assembly Based on Ion-Dipole Interaction

In the last section, a series of surface modification methods have been introduced for converting UCNPs from hydrophobic into hydrophilic. At the same time, UCNPs usually take some charges on the surface to increase water solubility. It is also because of the different charge of these surface that ion-dipole interaction can be formed to build a self-assembly system (Cheng et al. 2015; Xu et al. 2017). **Figure 2-14** showed an example of self-assembly between UCNPs and g-C$_3$N$_4$. By hydrophobic effect, CTAB molecules can insert into the surface of OA-UCNPs to positively charge the surface. Then ion-dipole interaction pushed CTAB inserted UCNPs self-assembled on negatively charged g-C$_3$N$_4$.
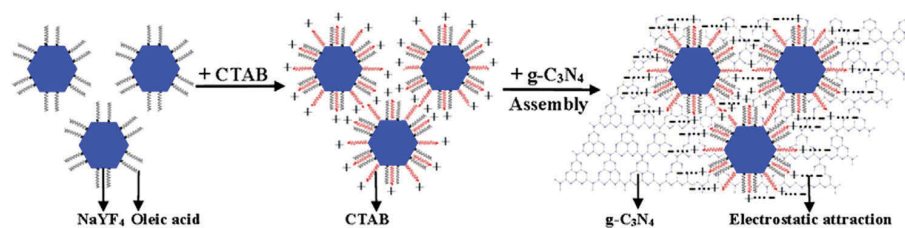
Figure 2-14. The self-assembly structure of UCNPs with g-C$_3$N$_4$ by ion-dipole interaction. (Cheng et al. 2015)

2.4.2 Inorganic-Inorganic Self-Assembly Based on Hydrophobic Effect

The as-made UCNPs usually stabilized with non-polar OA or OM molecules. When dispersed into a polar solvent, these nanoparticles will spontaneously aggregate in order to reduce the energy of the surface. The surface OA or OM molecules from different nanoparticles inserted each other to form a large conjugated system. (Bao et al. 2014; Liu, Ni, et al. 2016; Qiu et al. 2017; Song et al. 2017; Zhao et al. 2016) The process of self-assembly can be influenced due to the size of nanoparticles (Liu, Ni, et al. 2016) and some politic solution is also influenced the self-assembly (Liu, Ni, et al. 2016; Song et al. 2017). After mixed with surfactant or hydrophilic molecules, these nanoparticles will form a nanoparticle (Bao et al. 2014; Qiu et al. 2017; Zhao et al. 2016). An example of hybrid nanoclusters based on UCNPs and persistent luminescence nanoparticles (PLNPs) was shown in **Figure 2-15** (Qiu et al. 2017).
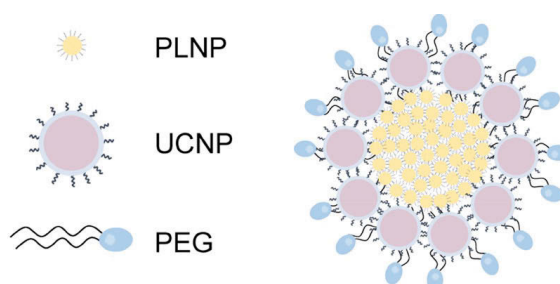
Figure 2-15. The self-assembly system between PLNPs and UCNPs because of hydrophobic effect. (Qiu et al. 2017)

2.4.3 Inorganic-Inorganic Self-Assembly Based on Hydrogen Bond

Hydrogen bond is a special type of ion-dipole interaction with direction. A typical example in nature is the hydrogen bonds between bases of DNA. An architecture between UCNPs and AuNPs has been reported by using hydrogen bonds between DNA (Sun et al. 2016). Firstly, two complementary DNA chains were modified onto two types of UCNPs, respectively. The self-assembled structure of UCNP dimer is shown in **Figure 2-16a**. Then, another pair of complementary DNA chain was future modified on the surface of UCNPs and AuNPs, which processes the architecture shown in **Figure 2-16b**. Compared with ion-dipole interaction, hydrogen bond induced self-assembly processes directionality and high selectivity. However, the binding ability is not high enough for building a self-assembly architecture. So, hydrogen bonds always appear in multiple binding systems.
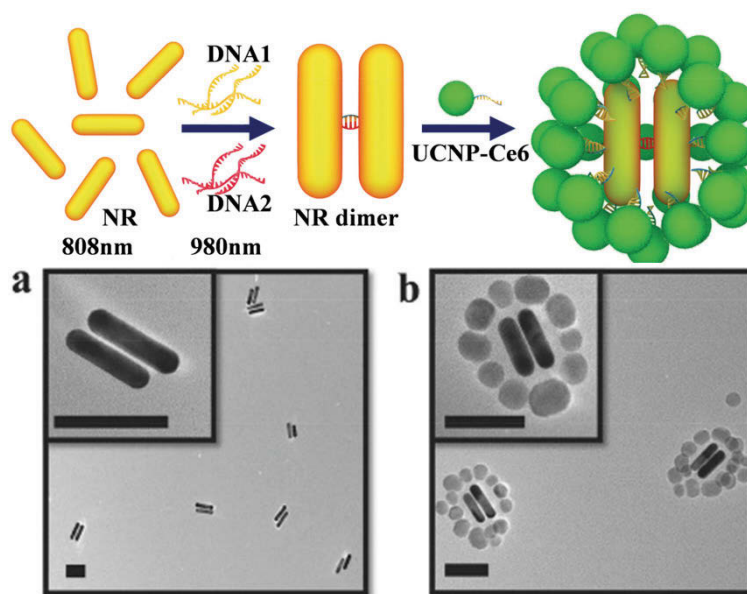
Figure 2-16. The self-assembled architectures between UCNPs and AuNPs by using hydrogen bonds. (Sun et al. 2016)

2.4.4 Inorganic-Inorganic Self-Assembly Based on Inorganic Assistance

Inorganic materials have also been used for the assistance of inorganic-inorganic self-assembly. Lv and his co-workers designed a self-assembly system (Lv et al. 2018) between Fe_3O_4 nanoparticles and UCNPs with the assistance from TiO_2 coating, which is shown in **Figure 2-17**.
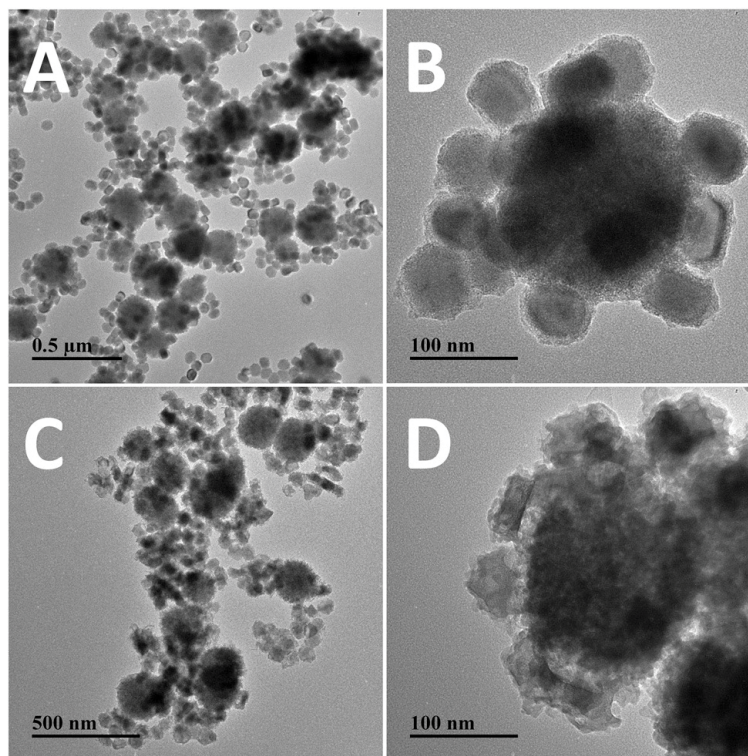
Figure 2-17. Transmission electron microscopy (TEM) images of TiO_2 composites assisted self-assembly structure between Fe_3O_4 nanoparticles and UCNPs. (Lv et al. 2018)

2.4.5 Inorganic-Inorganic Self-Assembly Based on Template Control

Self-assembly of template control is relatively simple compared to chemical interaction induced assembly. Only one condition is the size of nanoparticles can fit the structure of the template, then nanoparticles can "self-assemble" in order (Greybush et al. 2014; Zhang, Deng, et al. 2010). **Figure 2-18** showed an example of template-assisted self-

assembly for UCNPs and AuNPs. The relative distance between the two nanoparticles is only related to the template which does not require any modification.
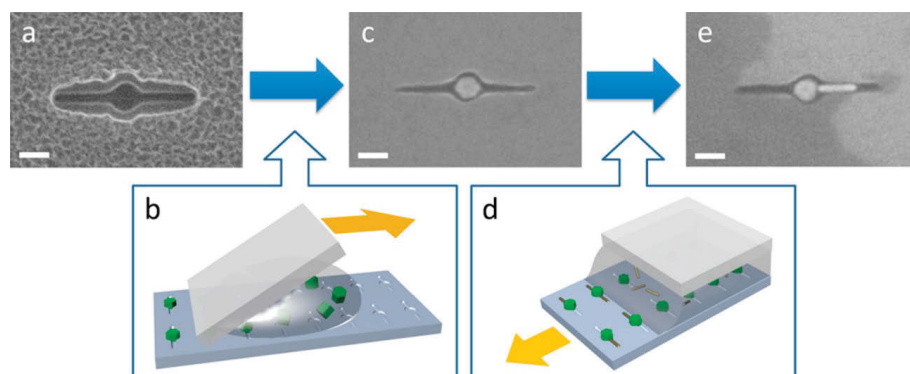
Figure 2-18. The process of template-assisted self-assembly between UCNPs and AuNPs. (Greybush et al. 2014)

3 THE SURFACE INVESTIGATION OF OLEIC ACID STABILIZED UPCONVERSION NANOPARTICLE

This chapter is based on the research described in the following publication:

Chem. Commun. **2018**, *54*, 3851-3854.

3.1 Introduction

From **Chapter 2**, we realized a tough problem of UCNPs is how to efficiently transfer and modify the surface into hydrophilic (Muhr et al. 2014). Normally, the as-made UCNPs are coated with OA to stable the surface (Lu et al. 2015). So, the nature of the interaction between the superficial atoms of UCNPs and OA molecules is significant to be investigated. In the hexagonal crystal, two kinds of surfaces are involved in the surface, which are {001} on the top and bottom, and {100} on the sides (**Figure 3-1**). The cell unit of β-NaYF₄ crystal shows each Yttrium (Y) atom connects with 9 Fluorine (F) atoms in **Figure 3-2**. However, on the surface of the crystal, the three on the top will be replaced by OA. It means these Y atoms on the surface of UCNPs show a particle positive charge (Liu, Xu, et al. 2016). The terminal of OA is carboxylate (dipolar) which can form ionic-dipolar interaction (**Chapter 1**) with the positive Y atom (ionic) on the surface. However, the specific binding mode and constant are unclear. It still keeps the difficulty of surface modification and ligand exchange. To solve the problem, in this chapter, we used several methods to characterise the surface of UCNPs and reveal the binding mode of OA on the surface of OA-UCNPs.
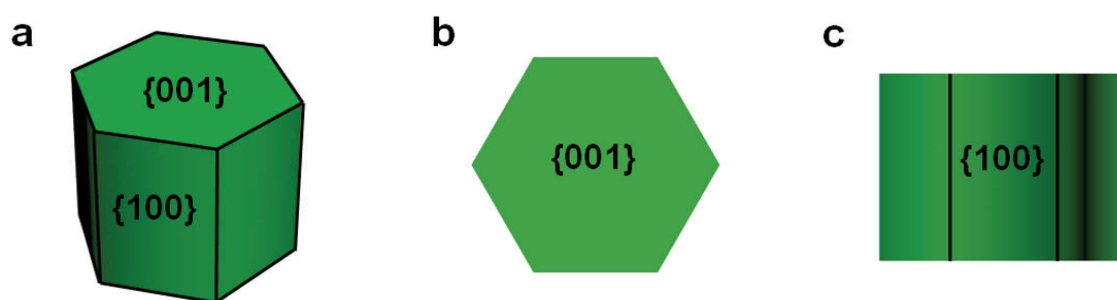
Figure 3-1. The hexagonal crystal of β-NaYF₄-based UCNPs: (a) the model of β-NaYF₄-based UCNPs; (b) the {001} crystal facet; (c) the {100} crystal facet.
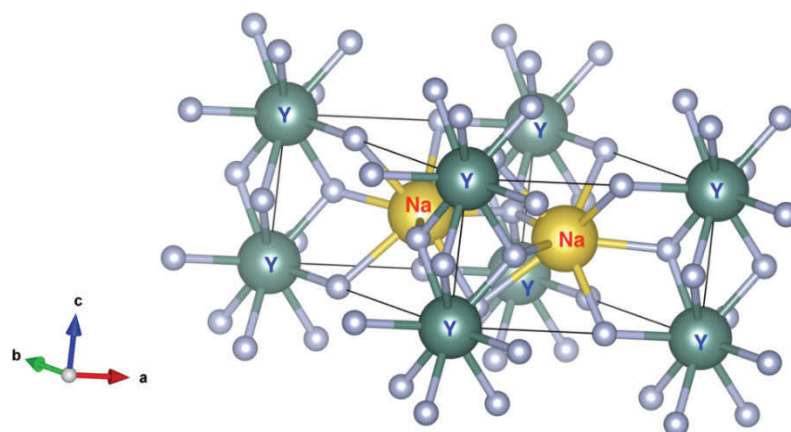
Figure 3-2. The crystal unit of hexagonal β-NaYF₄-based UCNP. The yellow dots stand for Sodium; the green dots stand for Yttrium. Note: these unmarked small grey dots are Fluorine.

3.2 Experimental Section

3.2.1 Materials

Yttrium(III) chloride hexahydrate (YCl$_3$·6H$_2$O), ytterbium(III) chloride hexahydrate (YbCl$_3$·6H$_2$O), erbium(III) chloride hexahydrate (ErCl$_3$·6H$_2$O), OA, 1-octadecene (ODE), ammonium fluoride (NH$_4$F) were purchased from Sigma-Aldrich. Methanol (MeOH), ethanol (EtOH), sodium hydroxide (NaOH) and cyclohexane were purchased from Chem Supply. All the starting materials and reagents were used as received. Unless otherwise noted, all reactions were performed under nitrogen atmosphere and in dry solvents.

3.2.2 Methods

All the details of materials characterisations are shown below.

3.2.2.1 Dynamic light scattering (DLS)

The particle size (DLS) was obtained using Zetasizer Nano ZS. The operating temperature is 25 °C. The concentrations of the testing solutions are prepared according to the guideline of Malvern.

3.2.2.2 Emission spectra

Emission spectra were carried out by our instrument, which is set-up by Mr. Chao Mi. The scheme of the instrument is shown in **Figure 3-3**. The testing range of wavelength is from 400 nm to 800 nm. (Chen et al. 2018)
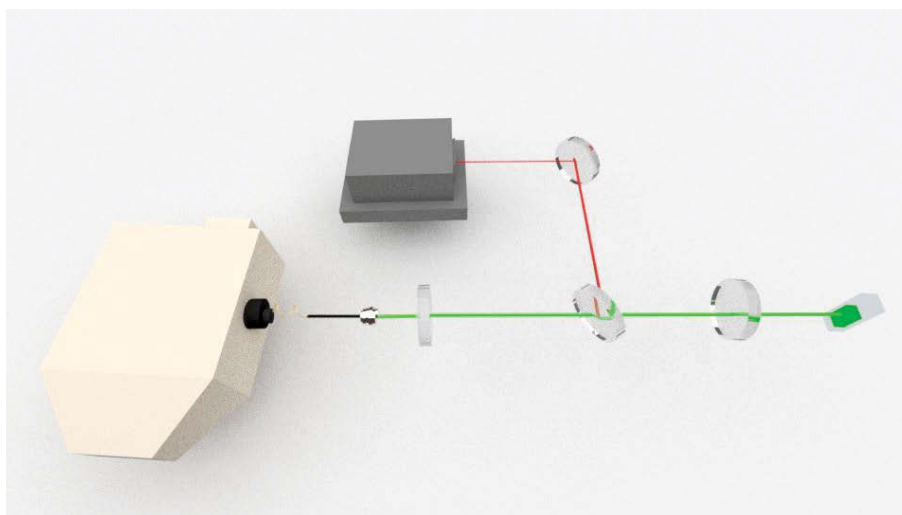
Figure 3-3. Schematic of the experimental configuration for measuring the emission of UCNPs under continuous-wave 980 nm diode laser.

3.2.2.3 Fourier-transform infrared (FT-IR) spectra

FT-IR spectra were recorded on a Nicolet 6700 spectrometer with attenuated total reflectance (ATR) method. The range of testing wavenumbers is from 4000 cm^{-1} to 500 cm^{-1}.

3.2.2.4 NMR Spectra

NMR spectra were recorded on an Agilent 500 MHz NMR spectrometer. The operating temperature is 25 °C.

3.2.2.5 Powder X-ray diffraction (XRD)

XRD measurements were carried out using a Bruker D8 Discover diffractometer. The radiation source was copper ($K\alpha = 1.39225$ Å).

3.2.2.6 Thermogravimetric analysis (TGA) and differential thermogravimetric analysis (DTGA)

TGA and DTGA were carried on a Simultaneous TG-DTA instrument S600 with a heating program consisting of a heating rate of 10 K/min from 373.15K to 1273.15 K under N_2.

3.2.2.7 TEM images

TEM images were collected on a FEI-Tecnai T20 instrument, employing an accelerating voltage of 200 kV.

3.2.2.8 X-ray photoelectron spectra (XPS)

XPS were tested by thermo ESCALAB250Xi X-ray photoelectron spectrometer from University of New South Wales.

3.2.3 Synthesis of Ln-UCNPs (NaYF$_4$: 20%Yb^{3+} / 2% Er^{3+})

The user-friendly synthesis method of the UCNPs (NaYF$_4$: 20%Yb^{3+} / 2% Er^{3+}) was modified from a previous report.(Lu et al. 2015) Generally, monodisperse NaYF$_4$:Yb, Er (78/20/2 mol%), YCl$_3$·6H$_2$O (0.78 mmol), YbCl$_3$·6H$_2$O (0.20 mmol), and ErCl$_3$·6H$_2$O (0.02 mmol) in 5 mL MeOH were added to a 50 mL flask containing 6 mL OA and 15 mL ODE. The mixture was slowly heated to 150 ℃ to get rid of H$_2$O and MeOH under argon atmosphere and maintained at 150 ℃ for about 30 min until a homogeneous transparent yellow solution was obtained. The system was then cooled down to room temperature with the flowing of argon. Then 10 mL MeOH solution of NH$_4$F (0.148 g, 4.0 mmol) and NaOH (0.10 g, 2.5 mmol) was added, and the solution was stirred at room

temperature for 1 h. The mixture was slowly heated to 110 °C to get rid of MeOH under argon atmosphere after MeOH evaporated, the solution was quickly heated to 300 °C and kept for 1.5 h before it was cooled down to room temperature.

After the reaction, the nanoparticles were washed with the mixture solution of EtOH / MeOH / OA / cyclohexane until the cyclohexane solution turned clear. Then the nanoparticles were dispersed and stored in cyclohexane.

3.3 Results and Discussion

3.3.1 Characterisations of OA-UCNPs.

As a type of outstanding optical nanoparticle, the emission is a fundamental property of UCNPs. **Figure 3-4a** shows the emission of the as-made OA-UCNPs (NaYF$_4$: 20% Yb^{3+} / 2% Er^{3+}). There are three main peaks in the spectrum, which are 520 nm, 540 nm and 650 nm, respectively. The energy level and the mechanism of the OA-UCNPs (NaYF$_4$: 20% Yb^{3+} / 2% Er^{3+}) is displayed in **Figure 3-4b**. (More details in **Chapter1**)
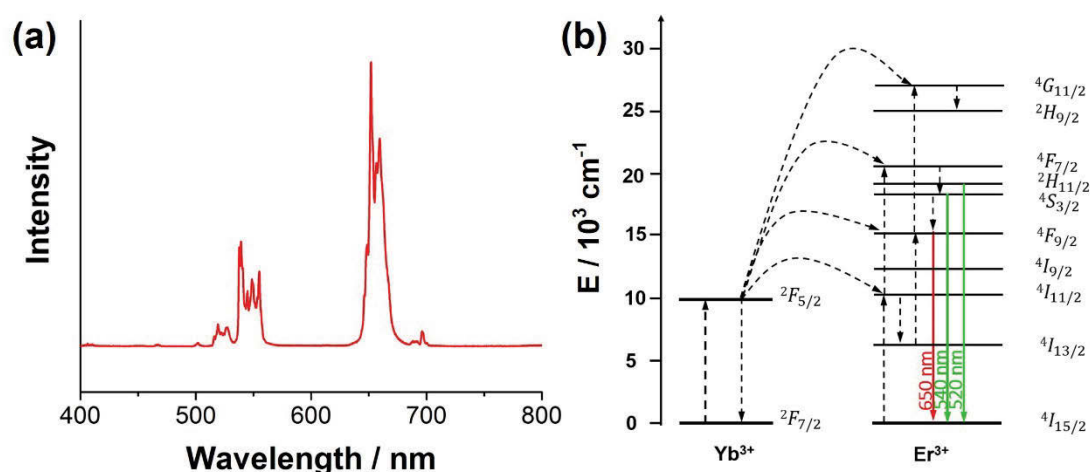
Figure 3-4. The optical properties of the OA-UCNPs (NaYF$_4$: 20% Yb^{3+} / 2% Er^{2+}): (a) the emission of the OA-UCNPs (NaYF$_4$: 20%Yb^{3+} / 2% Er^{3+}) and (b) the upconverting mechanism of the OA-UCNPs (NaYF$_4$: 20%Yb^{3+} / 2% Er^{3+}).

Figure 3-5 showed the XRD pattern of NaYF$_4$ nanocrystals co-doped with 20 % Yb^{3+} and 2% Er^{3+} (OA-UCNPs). Compared with the standard XRD patterns of hexagonal phase NaYF$_4$ (JCPDS: 00-016-0334) and NaYbF$_4$ (JCPDS: 00-027-1427), we confirmed that the nanoparticles we synthesised process the β-phase (hexagonal).
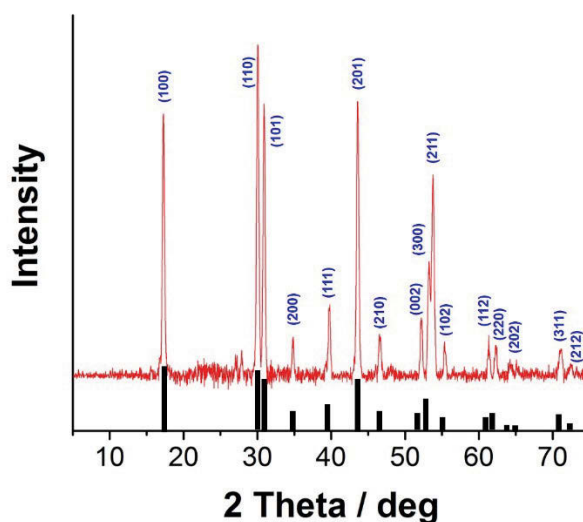
Figure 3-5. The XRD patterns of the OA-UCNPs (β-NaYF4: 2%Er^{3+} / 20%Yb^{3+} @ OA).

The NMR spectra were carried out to test the surface organic structure, which are shown in **Figure 3-6**. Compared with free OA (**Figure 3-6a**), the OA on the OA-UCNPs (**Figure 3-6b**) are settled at the same position of free OA. However, the peaks are getting broadly because of the effect of the surface metal of nanoparticles.

FT-IR spectra of free OA (red) and OA-UCNPs (blue) were shown in **Figure 3-7**. In the spectrum of free OA, the v_{st} (O-H) stretching from the carboxylic acid group was shown as a broad range from 3300 cm^{-1} to 2500 cm^{-1} because of the hydrogen bond. The range of C=O from COOH is from 1800 cm^{-1} to 1650 cm^{-1}. Specifically, when the COOH is connected with an aliphatic group, the typical range is from 1725 cm^{-1} to 1700 cm^{-1}. In **Figure 3-7**, the strong peak of v_{st} (C=O) stretching of OA was displayed at 1708 cm^{-1}, it also indicated that the COOH group was involved in the structure. In the spectrum of OA-UCNPs, the H-bonded broad peak (3300 cm^{-1} ~ 2500^{-1}) was disappeared, compared with

the free OA spectrum. The v_{st} (C=O) stretching was split into two peaks, and they shifted to 1547 cm^{-1} (asymmetric) to 1461 cm^{-1} (symmetric), respectively. It means the carboxylic acid groups in the OA had already changed to carboxylate (-COO$^-$) after modified on the surface of UCNPs rather than carboxylic acid (-COOH).
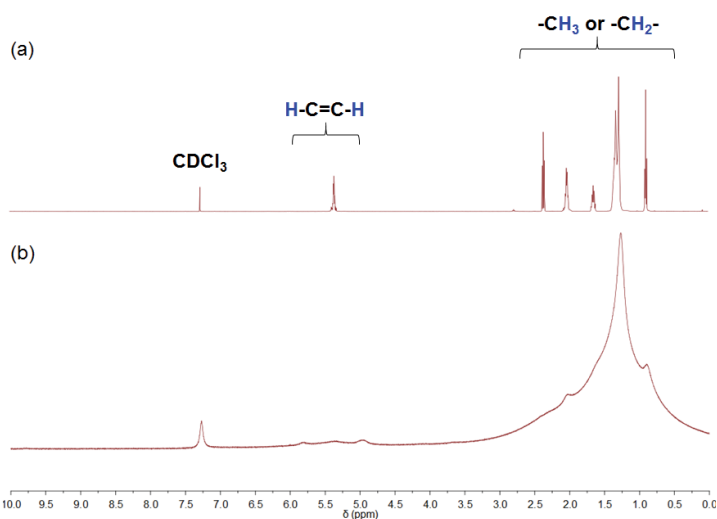
Figure 3-6. The ^{1}H NMR spectra (500 MHz) of (a) free OA molecules and (b) OA-UCNPs (NaYF$_4$: 20%Yb^{3+}/2%Er^{3+}@OA) in CDCl$_3$-d at 25 ºC.
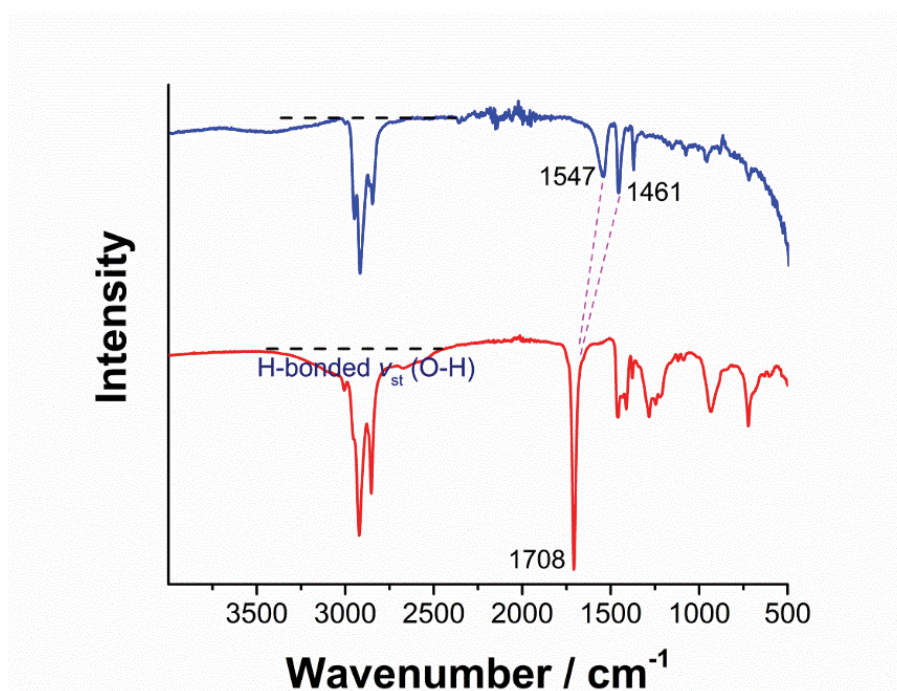
Figure 3-7. FT-IR spectra of OA (red) and OA-UCNPs (blue).

More details of the surface of OA-UCNPs is obtained from XPS. In the O1s region, only one O1s peak was shown in **Figure 3-8a**. It proves only one type of oxygen in the system. Further evidence illustrated both two carbon-oxygen bonds in the carboxylic group of OA were equalised after modified on the surface of $NaYF_4$ crystal because of resonance. In the C1s region (**Figure 3-8b**), the peak B also proves two carbon-oxygen bonds are the same because of resonance. As the same as FT-IR, it also means the formation of OA is carboxylate (-COO⁻) rather than carboxylic acid (-COOH). Besides, both of the oxygen atoms bond with the same Y atom.
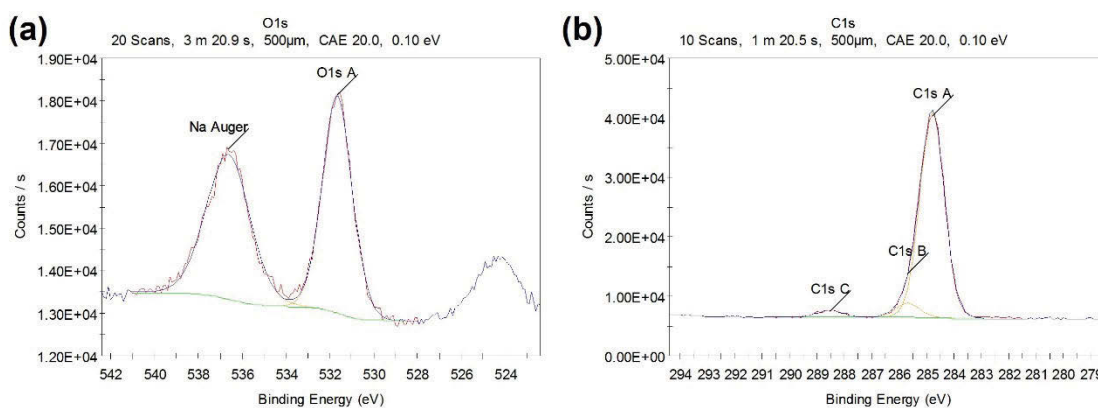
Figure 3-8. XPS Spectrum (a) O1s and (b) C1s of OA-UCNP.

The TGA and DTGA curves (**Figure 3-9a**) of free OA showed all the free OA could be removed before 300 °C and the weight loss temperature is 280 °C. After OA modified on the surface of bare UCNPs (**Figure 3-9b**), the temperature of removal is higher than free OA. It means that OA is binding on the surface of UCNPs.
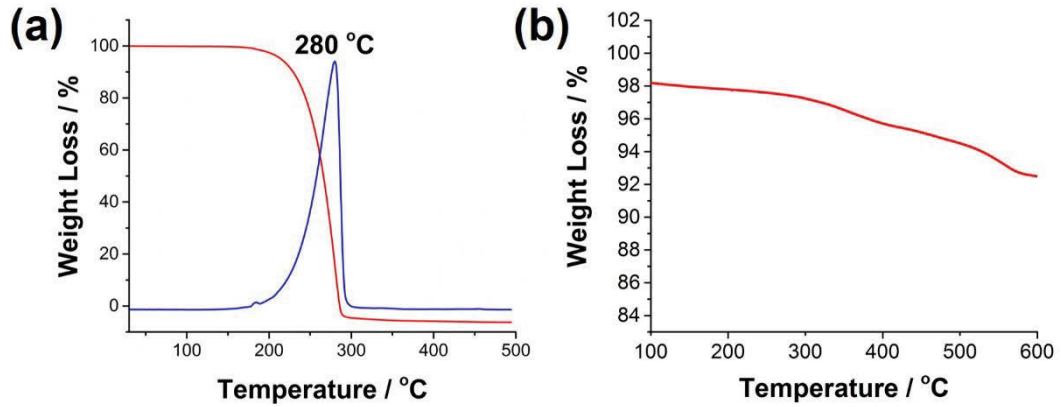
Figure 3-9. The TGA and DTGA curves: (a) the TGA (red) and DTGA (blue) of OA molecule, and (b) the TGA of OA-UCNPs.

3.3.2 Crystal Calculation.

Figure 3-10 shows β-NaYF$_4$ nanocrystal units which consist of the {001} facets at the ends and identical {100} facet around the cylinder sides. The Y^{3+} atoms form equilateral triangles with a length of 5.96 Å in the relaxed {001} surface, while rectangles are detected in the {100} surface with a shorter length of 3.53 Å.(Liu, Xu, et al. 2016)
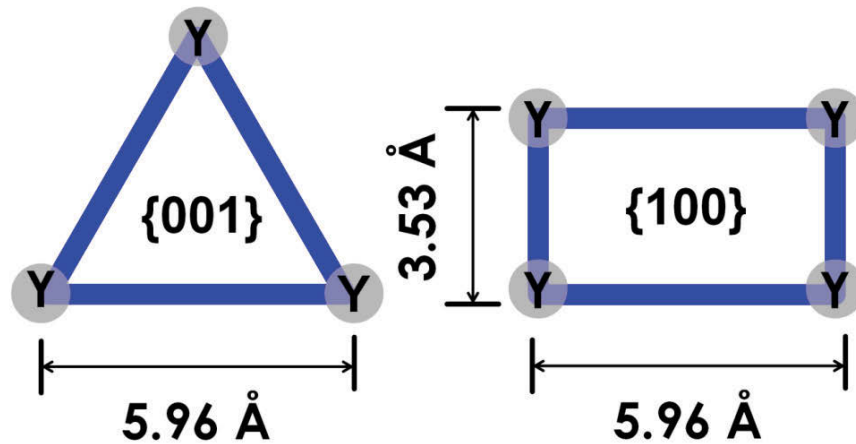
Figure 3-10. β-NaYF$_4$ nanocrystal units: the distance between two adjust Y^{3+} atoms is 5.96 Å in {001} facet (left); the two types of distances between two adjust Y^{3+} atoms are 5.96 Å and 3.53 Å/3.69 Å (right).

Figure 3-11a shows the structure of OA. According to the characterisation of OA-UCNP's surface, the form of OA is OA⁻ rather than OA. Due to the resonance of OA⁻ (**Figure 3-11b**), both of the C-O bonds are the same, 127 pm, and shown in **Figure 3-11c**. We predicted all the binding potentials which are shown in **Table 3-1** and **Table 3-2**.
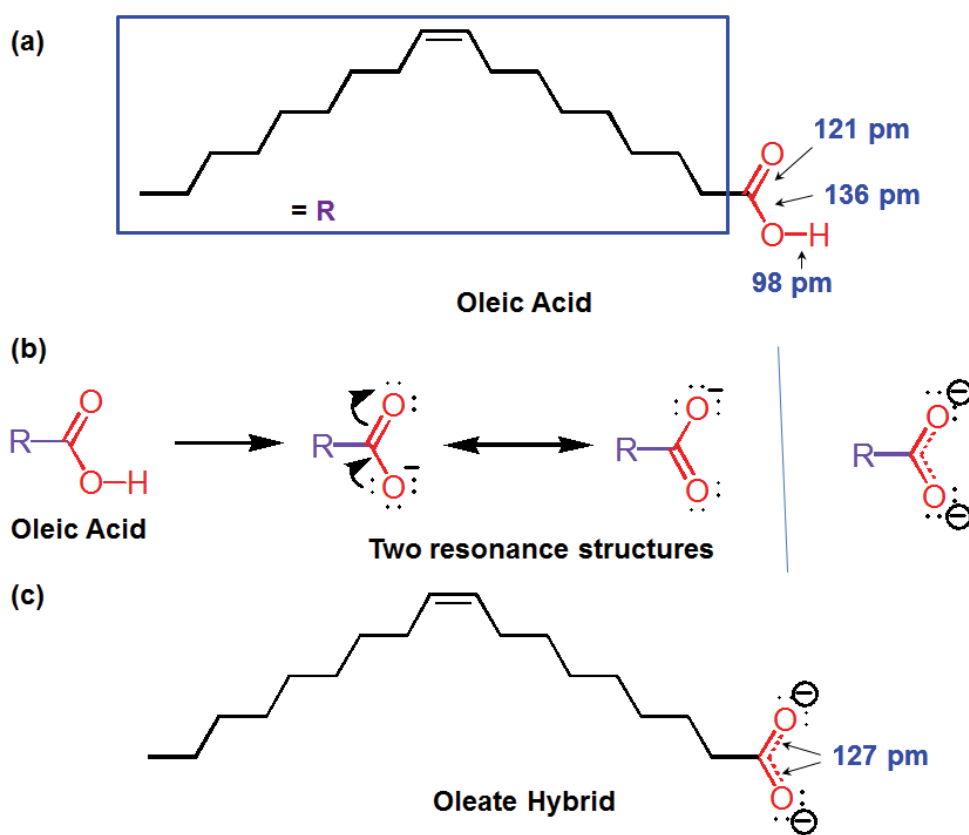
Figure 3-11. The structure of OA. (a). The structure of OA; (b). The resonance structure of OA; (c). The structure of Oleate Hybrid.

On crystal facet of {001}

The distance of two adjacent Y atoms is 5.96 Å, which is larger than the one of two oxygen in a carboxylate. So, a carboxylate cannot reach two Y atoms at the same time. It is acceptable that a carbon-oxygen double bond from a carboxylic acid can form ionic-dipolar interaction with a Y atom. At the same time, OH from OA can form a hydrogen bond with Fluorine near the Y atom. However, normally, the binding strength of a hydrogen bond is much weaker than ion-dipole interaction. So, we predicted that both equal oxygens bond with one Y atom.
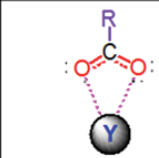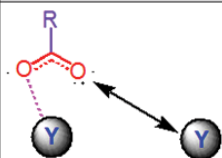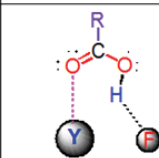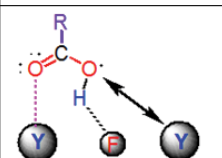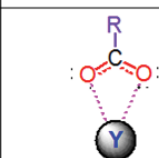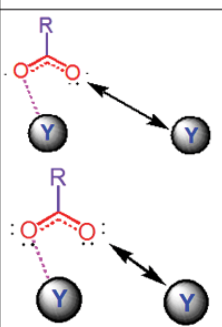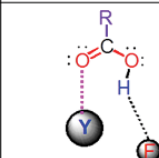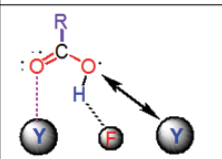
On crystal facet of {100}

Although the distance of two adjust Y atoms is closer than the one of {001}, it is still much larger than the one of two oxygen in a carboxylate. So, a carboxylate still cannot reach two Y atoms at the same time on the {100}. Also, a hydrogen bond could form between OH with Y atom, however, the same as {001}; the binding strength is still smaller than 1:1 binding. So, we also predicted that both equal oxygens bond with one Y atom on the crystal facet {100}.

Compared with bond energies, we considered most of OA⁻ on the surface is binding mode 1 and 5 in **Table 3-2**.

Table 3-1. All Predicted Binding Modes of OA on the surface of β-NaYF₄.

Number	Crystal Surface Plant	Molecular Structure	Binding Mode	Model
1	001	Oleate Hybrid	One Y atom	
2	001	Oleate Hybrid	Two Y atom	
3	001	Oleic Acid	One Y atom	
4	001	Oleic Acid	Two Y atom	
5	100	Oleate Hybrid	One Y atom	
6	100	Oleate Hybrid	Two Y atom	
7	100	Oleic Acid	One Y atom	
8	100	Oleic Acid	Two Y atom	

Table 3-2. Summary of Binding Modes of OA on the surface of the β-NaYF₄ crystal.
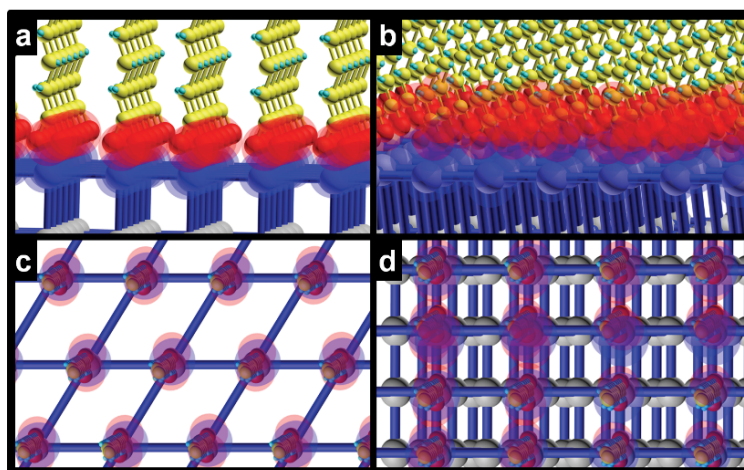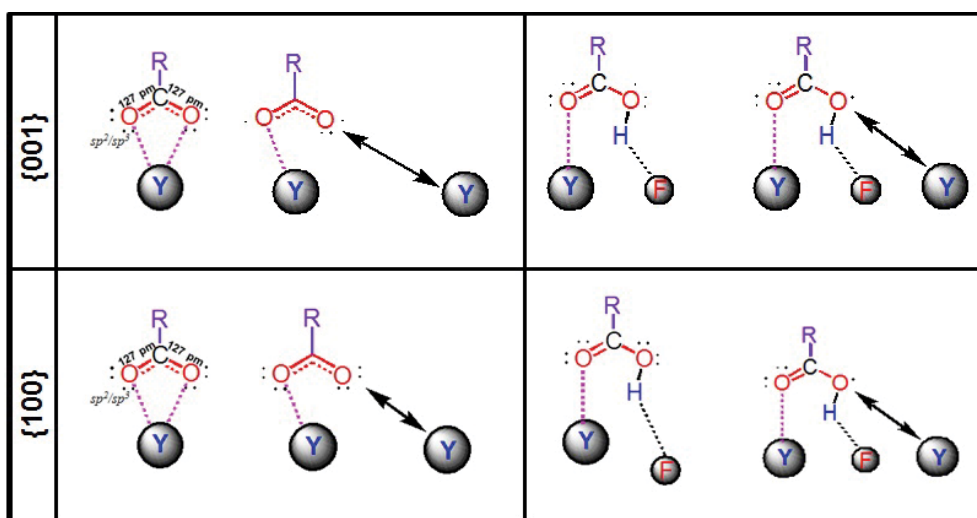
Figure 3-12. Crystallographic analysis of both OA-UCNPs: the side view (a) and top view (c) of {001} in OA-UCNPs; the side view (b) and top view (d) of {100} in OA-UCNPs.

Figure 3-12 shows these three dimensional (3D) images of OA binding models on the surface of UCNPs. In the side view of {001} facet (**Figure 3-12a**), both oxygens in carboxylate bond with positively charged Y atoms by ion-dipole interaction. The binding ration between OAs and Y atoms is 1:1 which is shown in top view of {001} facet (**Figure 3-12c**). On the other facet, {100} also shows the same binding behaviour between OAs and Y atoms (**Figure 3-12b** and **Figure 3-12d**).

3.3.3 Calculation of Coverage of OA on the Surface of OA-UCNPs.

According to the binding mode above, the OA molecules process 1:1 binding with Yttrium atoms on the surface of UCNPs.

So, the coverage of OA on the surface of UCNP (**Equation 3-1**) is

$$\boldsymbol{Coverage\ rate} = \frac{the\ amount\ of\ OA\ molecules}{the\ amount\ of\ Yttrium\ atoms\ on\ the\ surface\ of\ UCNPs}\%\quad\textbf{(3-1)}$$

The weight loss of OA-UCNPs shows the percentage of OA molecules, so the mass of OA can be calculated. Besides, the number of Yttrium atoms is based on the size of UCNPs, which is measured from TEM image. The process of calculation is displayed below.

The **total volume** of all UCNPs (V_u) (**Equation 3-2**) is

$$V_u = \frac{m_u}{\rho_u}\quad\textbf{(3-2)}$$

where the density of UCNP (ρ_u) is 4.2 g/cm³(Liu et al. 2013), m_u is the mass of UCNPs from TGA.

The volume of a single particle (V_s) (**Equation 3-3**) is

$$V_s = \frac{3\sqrt{3}}{2}d^2h\quad\textbf{(3-3)}$$

where d is the length of nanoparticle size on {001}, h is the height of a {100} crystal face of a nanoparticle (**Figure 3-13**).
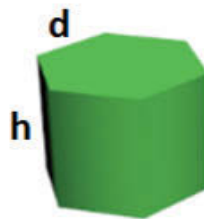
Figure 3-13. The model of a hexagonal UCNP.

The numbers of nanoparticle (*N*) (**Equation 3-4**) is

$$N = \frac{V_u}{V_s} = \frac{m_u/\rho_u}{\frac{3\sqrt{3}}{2}d^2h} = \frac{2m_u}{3\sqrt{3}d^2h\rho_u} \qquad (3\text{-}4)$$

The numbers of Yttrium atom on the surface of nanoparticles

The surface area of single nanoparticle (S_S) (**Equation 3-5**) is

$$S_S = 3\sqrt{3}d^2 + 6hd \qquad (3\text{-}5)$$

where d is the length of nanoparticle size on {001}, h is the height of a {100} crystal face of a nanoparticle.

The occupied area of a Y atom on {001} (**Equation 3-6**) or {100} (**Equation 3-7**) crystal plate is

$$S_{\{001\}} = \frac{\sqrt{3}}{2}a^2 \qquad (3\text{-}6)$$

$$S_{\{100\}} = ab \qquad (3\text{-}7)$$

where a and b are the distance between two atoms in different crystal plates, which is shown in **Figure 3-13**.

The surface numbers of Y atoms (N_S) on a nanoparticle (**Equation 3-8**) is

$$N_S = \frac{6d^2}{a^2} + \frac{6hd}{ab} = \frac{6d^2b + 6ahd}{a^2b} \qquad (3\text{-}8)$$

The amount of Y atoms (N_Y) (**Equation 3-9**) is

$$N_Y = N_S \times N = \frac{2m_u}{3\sqrt{3}d^2h\rho_u} \times \frac{6d^2b + 6ahd}{a^2b} = \frac{4dm_u(db+ah)}{\sqrt{3}d^2h\rho_u a^2b} \qquad (3\text{-}9)$$

The amount of OA molecules (N_{OA}) (**Equation 3-10**) is

$$N_{OA} = n_{OA} \times N_A = \frac{m_{OA}}{M_{OA}} \times N_A \qquad (3\text{-}10)$$

The coverage rate of OA on the surface of UCNP (**Equation 3-11**) is

$$Coverage\ rate = \frac{N_{OA}}{N_Y} = \frac{\sqrt{3}d^2 h\rho_u a^2 bm_{OA}N_A}{4dm_u(db+ah)M_{OA}} \qquad \text{(3-11)}$$

So, the coverage of OA-UCNPs is 54.6%.

3.4 Conclusions

The OA-UCNPs, we synthesised, are stabilised by OA molecule. Both equal oxygen atoms from the terminal of OA form ionic-dipolar interaction with one Y atom from β-NaYF$_4$ surface. Also, the binding mode of both crystal face are the same, and the coverage of OA on the surface is 54.6%. This chapter is significant for ligand exchange and further conjugation. By comparing the different binding behaviour between OA and other molecules, we can investigate if we can replace the molecule with OA and binding efficiency.

4 Self-Assembly Induced Molecular Conjugation of Cyclodextrin-Stabilized Upconversion Nanoparticles for Increasing the Biocompatibility of Anti-Cancer Drug

I, Yulong Sun, raised the whole project, designed all the details of the experiments in this chapter, modified the surface of UCNPs, and did the test for all samples.

I, Yulong Sun, acknowledge Dr Joshua Chou and Mr Baoming Wang for cell culture and biological analysis, Dr Wenjing Zhang for the synthesis of OA-UCNPs, Mr Guochen Bao for modification of CDs.

4.1 Introduction

In **Chapter 2**, we introduced the development of modification and conjugation approaches on the surface of UCNPs in the last two decades (Muhr et al. 2014; Sedlmeier & Gorris 2015; Wang & Liu 2009). Generally, there are two main approaches to ligand exchange: one-step ligand exchange and two-step ligand exchange. In the two-step ligand-exchanged modification, the surface OA molecules have to be removed first by a mild acid and then modify targeted molecules with functional groups for further conjugation in the second step (Kong et al. 2017). The exchanged modifications usually use either the organic molecules processing stronger binding strength with Y atoms on the surface of UCNPs (Lu et al. 2015) or polymer molecules (Duong et al. 2018) with electronic rich functional groups. Both methods can convert OA-UCNPs with hydrophilic surfaces. However, these ligand exchanging methods could not keep nanoparticles in a stable condition, or the tough exchanging conditions could alter the particle morphologies or properties of UCNPs, even damage and dissolve UCNPs.

In this Chapter, we propose a novel one-step ligand-exchanged method to modify a series of macrocycles, including CDs (Uekama, Hirayama & Irie 1998) and CB[n]s (Lagona et al. 2005), on the surface of UCNPs. According to ion-dipole (see Section 1.2.1 in **Chapter 1**) and host-guest interaction (see Section 1.4 in **Chapter 1**), macrocycles can not only stabilize the UCNP surface to keep the properties and but also provide numerous binding sites for further biomolecular conjugations. We firstly chose five typical molecules of CDs to investigate the binding behaviour between CDs and UCNPs surfaces: carboxylic-α-CD sodium salt (α-CD-COONa), carboxylic-β-CD sodium salt (β-CD-COONa), carboxylic-γ-CD sodium salt (γ-CD-COONa), sulfonic-β-CD sodium salt (β-CD-SO$_3$Na), and phosphoric-β-CD sodium salt (β-CD-PO$_3$Na$_2$). The structures of these CDs are shown in **Figure 4-1**. It can be seen that the selected CDs are in varied sizes (from α-CD to γ-CD) and with different functional groups (carboxylate, sulphated,

and phosphate), though all the selected host CDs molecules process hydrophilic external surfaces and hydrophobic cavities. (Uekama, Hirayama & Irie 1998). Additionally, CDs consist of different numbers of sugar units to create a cone shape, which not only is a healthy "food" but also increase bioavailability and stabilize unstable materials. (Uekama, Hirayama & Irie 1998) The properties of CDs have been discussed in Section 1.4.2.2 of **Chapter 1**.

CDs can convert UCNPs from hydrophobic into hydrophilic efficiently. Meanwhile, CDs can provide a large number of cavities as binding sites for different types of guest molecules (e.g., dye, anti-cancer drugs, biomolecules, and nanoparticles) on the surface of UCNPs. (Hu, Tang & Chu 2014; Uekama, Hirayama & Irie 1998; Yang, Yuan, et al. 2014) Thereafter, the further conjugations of biomolecules such as protein, or antibody, were based on host-guest interaction (see Section 1.4 of **Chapter 1**); no more organic reaction was needed for further conjugations (**Figure 4-2**). The related guest molecule at lease follow one of the binding conditions to bind on the surface of CD-modified UCNPs (CD-UCNPs) (Cao, Villalonga & Fragoso 2005):

(1) the guest molecule can form ion-dipole interaction with host molecule or/and

(2) hydrophobic effect for inserting the cavity.

In brief, both steps were based on supramolecular interactions. Between the surface of UCNPs and CDs was based on ion-dipole interaction (see Section 1.2.1 in **Chapter 1**). The further conjugations were based on the hydrophobic effect or/and dipole-dipole interaction (**Figure 4-2**).
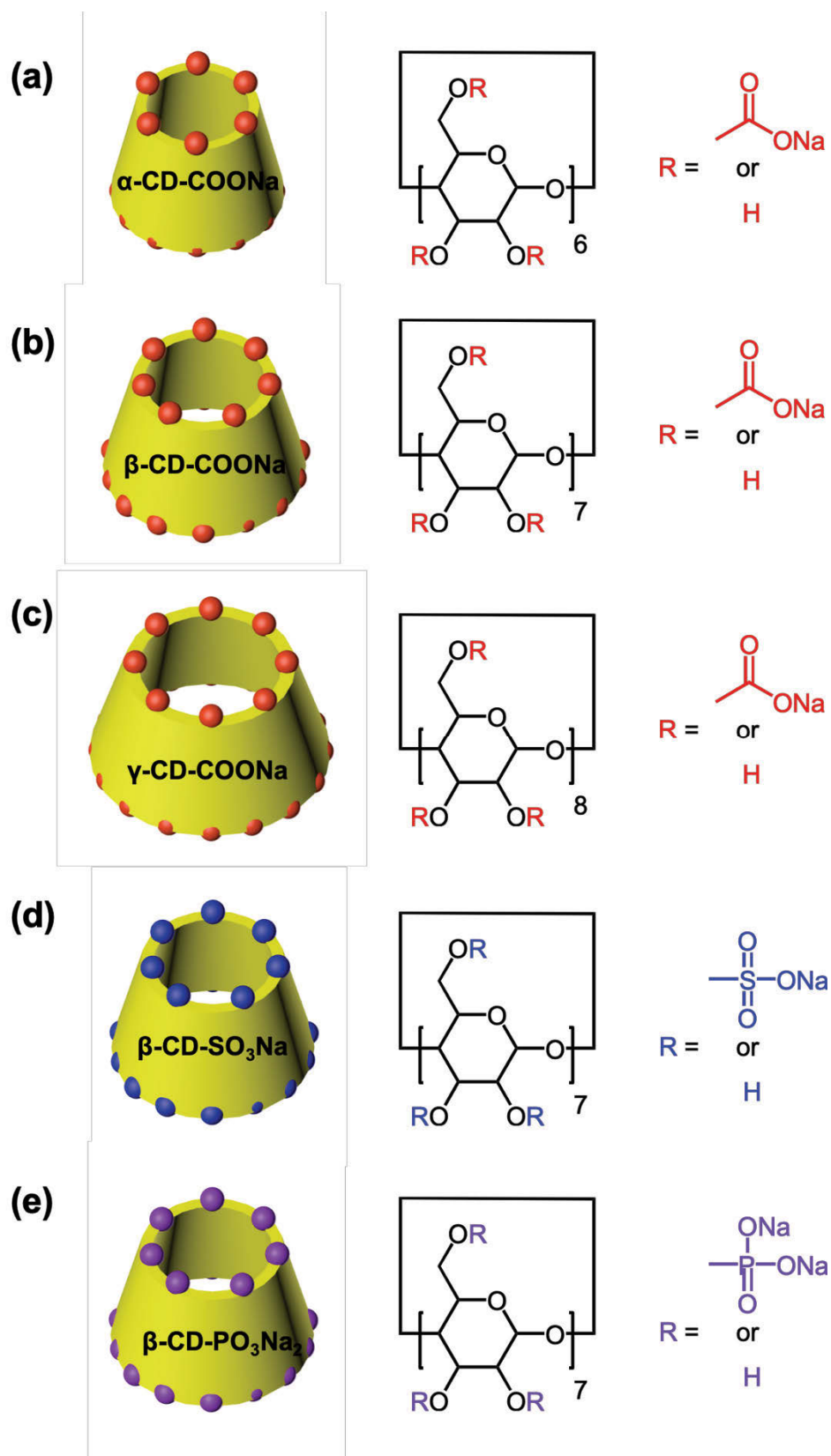
Figure 4-1. The structures of functional CDs mentioned in this chapter: (a) α-CD-COONa, (b) β-CD-COONa, (c) γ-CD-COONa, (d) β-CD-SO₃Na, and (e) β-CD-PO₃Na₂.
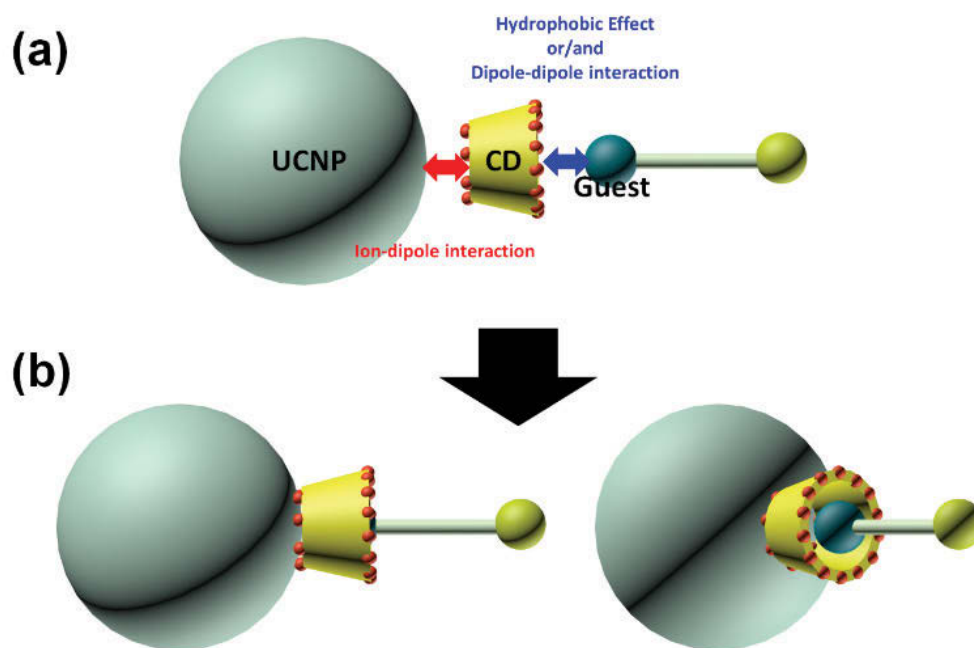
Figure 4-2. (a) The mechanism of the surface modification of CD-UCNPs and molecular conjugation with host-guest interactions. (b) The two side views of the conjugation structure.

4.2 Experimental Section

4.2.1 Materials

α-CD, β-CD, γ-CD, β-CD-SO$_3$Na, β-CD-PO$_3$Na$_2$, methyl sulfoxide (DMSO), thiazolyl blue tetrazolium bromide (MTT), monochloroacetic acid, were purchased from Sigma-Aldrich. NaOH, HCl, MeOH were purchased from ChemSupply. Doxorubicin hydrochlorate (DOX) was purchased from Beijing Huafeng United Technology Co., Ltd. All of the chemicals were used as received. Unless otherwise noted, all reactions were performed under nitrogen atmosphere and in dry solvents.

4.2.2 Methods

4.2.2.1 Absorption spectra

The absorption spectra, except for release experiments, were obtained by UV-*vis* spectroscopy using a Cary 60 UV-vis from Agilent. The testing method was "Scan". The detection wavelength was 498 nm. The scan control chose "Simply". The release experiments were collected by a NanoDrop 2000 spectrophotometers from Thermo Fisher. The detection wavelength was 498 nm. The operating temperature was room temperature (25 °C).

4.2.2.2 DLS

The particle sizes of the surface modified UCNPs with CDs molecules in aqueous solution were characterized using a Zetasizer Nano instrument. All the samples were tested in MQ water. Each experiment scans three times; each time collects automatic numbers. The operating temperature was 25 °C.

4.2.2.3 Photo Luminescent Emission Spectra.

The emission spectra were collected using the instrument which shown in **Figure 3-3** of **Chapter 3**. The range of wavelength was from 400 nm to 900 nm.

4.2.2.4 FT-IT Spectra.

The FT-IR spectra were carried out by a Nicolet 6700 spectrometer with ATR method. The range of all the data was collected from 4000 cm^{-1} to 500 cm^{-1}. The cumulative number was 64 scans.

4.2.2.5 ITC

The binding constants were tested by a Nano ITC (low volume) of TA Instruments. The cell composition was made of 24K gold, which active volume was 190 μL. During the

test, the volume of cell solution was 300 μL. The syringe volume was 50 μL. The injection volume of each time was 2.5 μL, the first injection was 1 μL. The speed of stirring was 300 rpm. The operating temperature was 25 °C.

4.2.2.6 TEM imaging

The TEM images were collected on a FEI-Tecnai T20 instrument, employing an accelerating voltage of 200 kV.

4.2.2.7 NMR Spectra

The NMR spectra were collected by a 500 MHz Agilent instrument. The operating temperature was 25 °C.

4.2.2.8 TGA and DTGA

TGA and DTGA were carried on a Simultaneous TG-DTA instrument S600 with a heating program consisting of a heating rate of 10 K/min from 373.15 K to 923.15 K under N_2 (120 mL/min).

4.2.2.9 Raman Spectra

The Raman Spectra were collected by using a Renishaw Raman Spectrometer. The wavelength of the laser was 785 nm.

4.2.3 Synthesis and Preparation

4.2.3.1 Synthesis of CDs-COONa

Carboxylic acid modified CDs are synthesized following a literature procedure with a few of modifications (Wang et al. 2016).

- **Synthesis of α-CD-COONa**

The synthetic process is shown in **Figure 4-3**. α-CD (2.0 g) was added to NaOH (25% v/v, 10 mL) aqueous solution. Then 16.3% monochloroacetic acid solution (16.3 %, 6 mL) was added dropwise into the mixture over 15 min at room temperature. After dropwise, the mixture was heated up to 60 °C for 4 h. After cooling to room temperature, the pH of the solution was adjusted (pH 6–7) by using 10% HCl, then sufficient MeOH was added to precipitate the product. The white solid was collected after filtration and dried under vacuum at 45 °C for 3 days to give the final α-CD-COONa. The compound was characterized by NMR Spectra, FT-IR Spectra, and Raman Spectra.

Figure 4-3. The synthesis of α-CD-COONa.

- **Synthesis of β-CD-COONa**

The synthetic process is shown in **Figure 4-4**. β-CD (2.0 g) was added to NaOH (25% v/v, 10 mL) aqueous solution. Then 16.3% monochloroacetic acid solution (16.3 %, 6 mL) was added dropwise into the mixture over 15 min at room temperature. After dropwise, the mixture was heated up to 60 °C for 4 h. After cooling to room temperature, the pH of the solution was adjusted (pH 6–7) by using 10% HCl, then sufficient MeOH was added to precipitate the product. The white solid was collected after filtration and dried under vacuum at 45 °C for 3 days to give the final β-CD-COONa. The compound was characterized by NMR Spectra, FT-IR Spectra, and Raman Spectra.

Figure 4-4. The synthesis of β-CD-COONa.

- **Synthesis of γ-CD-COONa**

The synthesis of γ-CD-COONa was based on the literature procedure with few modifications (**Figure 4-5**). γ-CD (2.0 g) was added to NaOH (25% v/v, 10 mL) aqueous solution. Then 16.3% monochloroacetic acid solution (16.3 %, 6 mL) was added dropwise into the mixture over 15 min at room temperature. After dropwise, the mixture was heated up to 60 °C for 4 h. After cooling to room temperature, the pH of the solution was adjusted (pH 6–7) by using 10% HCl, then sufficient MeOH was added to precipitate the product. The white solid was collected after filtration and dried under vacuum at 45 °C for 3 days to give the final γ-CD-COONa. The compound was characterized by NMR Spectra, FT-IR Spectra, and Raman Spectra.
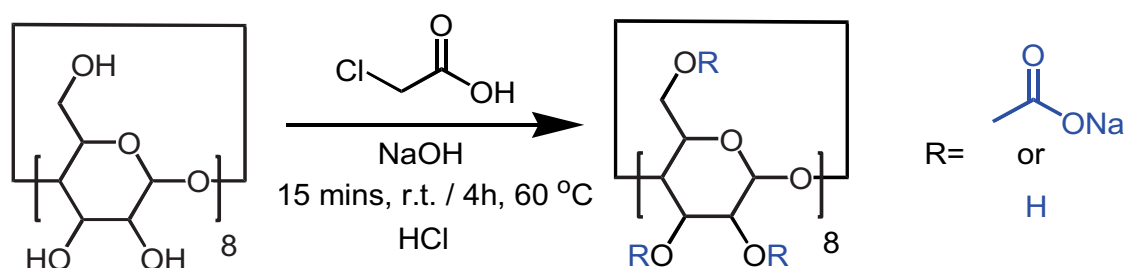
Figure 4-5. The synthesis of γ-CD-COONa.

4.2.3.2 Synthesis of Macrocycles-Modified UCNPs

Generally, the macrocycle stabilized UCNPs were synthesized according to the modified method (Lu et al. 2015). 10 μL of 10 mg/mL UCNP solution was added to 100 μL of chloroform and then mixed with 300 μL of an aqueous solution containing macrocycles

(2 mM). After 12 h incubation on a mixer, the water layer was transferred and then centrifuged at 13 000 rpm for 5 min. Then, the participate was dispersed and centrifuged in water to remove extra macrocyclic molecules. The wash step was repeated at least three times. In this chapter, several types of CDs (**Figure 4-1**) were used to synthesise CD-UCNPs.

4.2.3.3 Drug Loading and Release Experiments

- **Loading**

Loading of macrocycle-stabilized UCNPs (20 mg) with DOX was carried out by socking nanoparticles in an aqueous solution of DOX (0.5 mM in H_2O, 5 mL) for 5 h at room temperature. The precipitate, DOX-loaded CD-UCNPs, (CD-UCNPs-DOX) was centrifuged and redispersed water for release experiments.

- **Controlled release experiments**

Controlled release experiments were carried out at different temperature values. The CD-UCNPs-DOX (5 mg) were dispersed in 500 μL of H_2O and dialyzed against their corresponding buffer solutions (4.5 mL) in capped beakers under stirring at 25 °C and 37 °C. At every designated interval, the solutions (2 μL) in the beaker were taken out for absorption test by using a nanodrop at a wavelength of 498 nm. The concentration of DOX released from the materials was expressed as a percentage of the total DOX available and plotted as a function of time. The cumulative DOX release was calculated through the equation below:

$$\text{Cumulative DOX release (\%)} = M_t/M_\infty \times 100\%$$

where M_t is the amount of drug (DOX) released from materials at time t and M_∞ is the amount of drug released from the materials at time infinity.

4.2.4 Cytotoxicity of CD-UCNPs

In vitro cytotoxicity of materials and the bioavailability of anti-cancer drug-loaded materials were measured by performing MTT assays on the fibroblast L929 and the human cervical cancer HeLa cells. Cells were seeded into a 96-well cell culture plate at 1×10^5/well at 37 °C and 5% CO_2 for 24 h. Different concentrations of CD-UCNPs (25, 50, 100, 200 and 400 µg/mL, diluted in media) were then added to the wells. The cells were subsequently incubated for 24 h at 37 °C under 5% CO_2. After that, MTT (20 µL; 5 mg/mL) was added to each well, and the plate was incubated for an additional 4 h at 37 °C under 5% CO_2. 200 µL DMSO was added to each well after removing media. The optical density OD570 value (Abs.) of each well was measured using a multifunction microplate reader. The following formula was used to calculate the inhibition of cell growth (**Equation 4-1**).

Equation 4-1. The calculation of cell viability in cytotoxicity of CD-UCNPs.

$$\text{Cell Viability (\%)} = \frac{\text{Abs. value of treatment group}}{\text{Abs. value of control group}} \times 100\%$$

4.2.5 Bioavailability of CD-UCNPs-DOX

The same method was shown in Section 4.2.5. Only different concentrations of DOX (4, 8, 12, and 16 µg, diluted in media) were then added to the wells.

4.3 Results and Discussion

4.3.1 Structure Characterizations of CDs-COONa

The structure of CDs-COONa in this chapter was shown in **Figure 4-6**. In NMR spectra (**Figure 4-7 ~ Figure 4-12**), the location of H-1 is between two oxygen atoms, which shows the specific position in NMR (5.0 ppm ~ 5.2 ppm). After modified with

carboxylate, parts of H-1 shift to a higher position (5.2 ppm ~ 5.4 ppm) because of the effect from carboxylate. In addition, another specific chemical shift from carboxylate is found in ^{13}C NMR spectra, which further proves the existence of carboxylate.
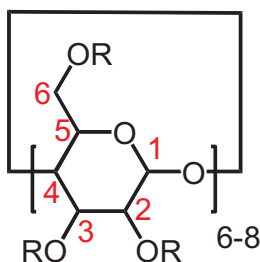
Figure 4-6. The basic structure of CDs and the numbers of protons. (R = H or carboxylate)
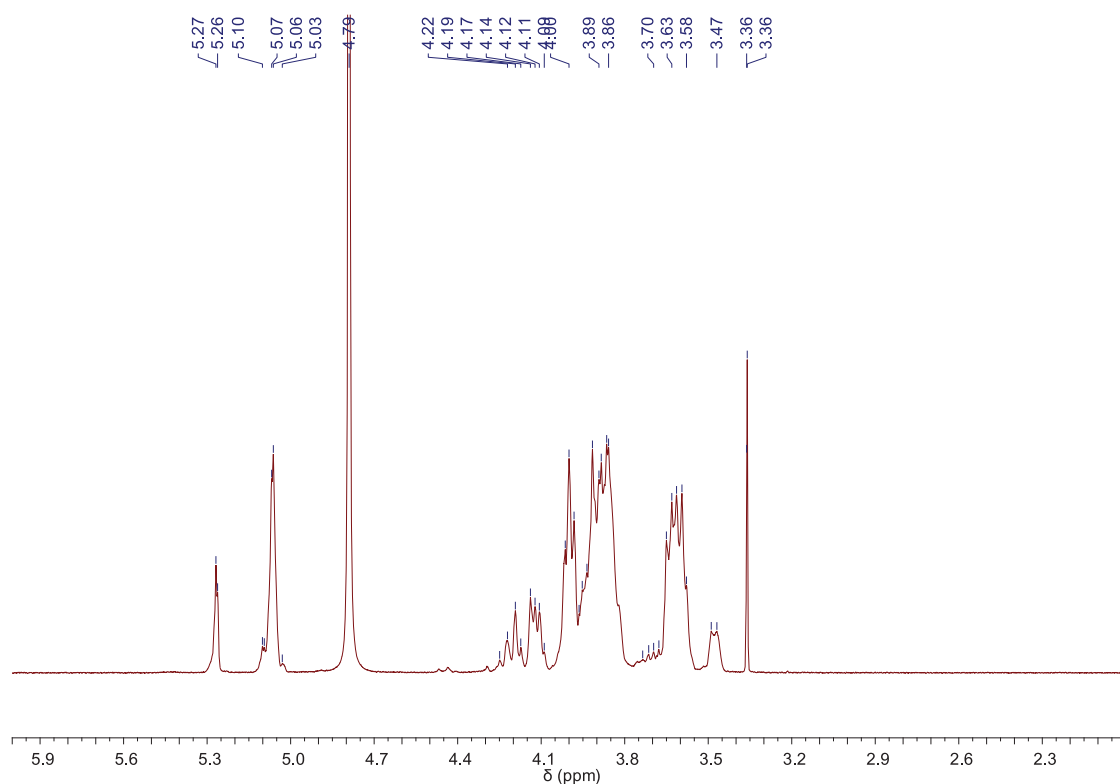
Figure 4-7. ^{1}H NMR spectrum of α-CD-COONa in D$_2$O at 25 ºC (500 MHz).
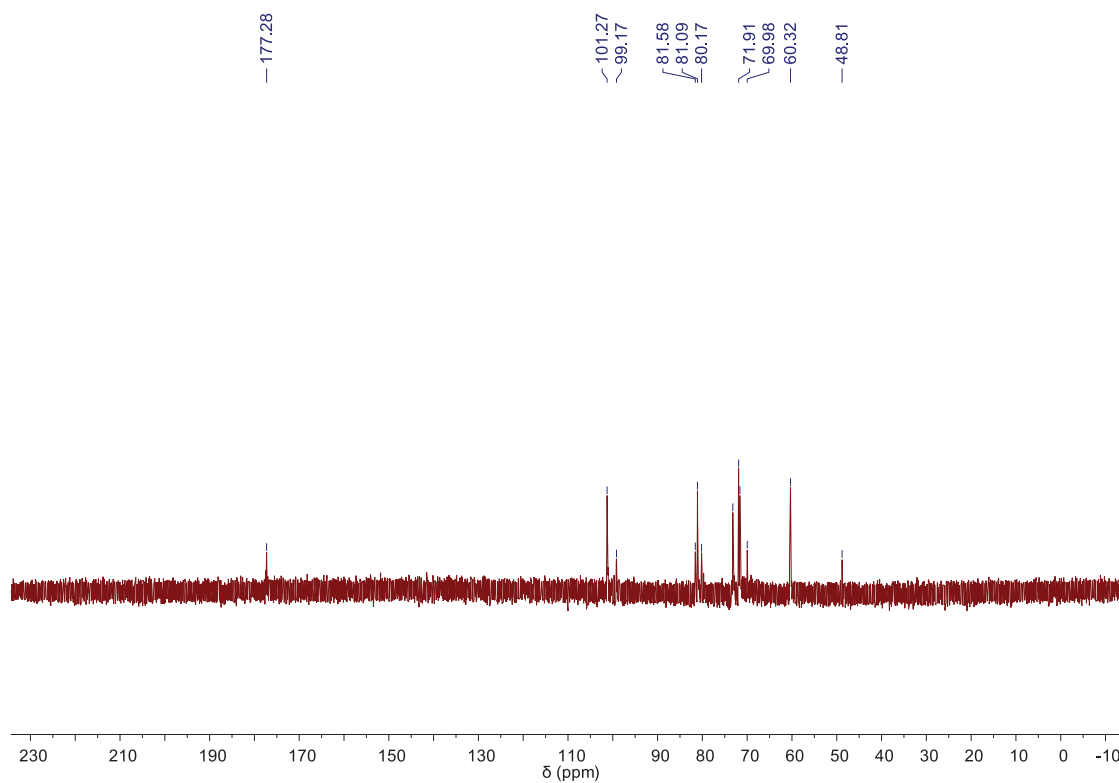
Figure 4-8. ^{13}C NMR spectrum of α-CD-COONa in D$_2$O at 25 °C (125 MHz).
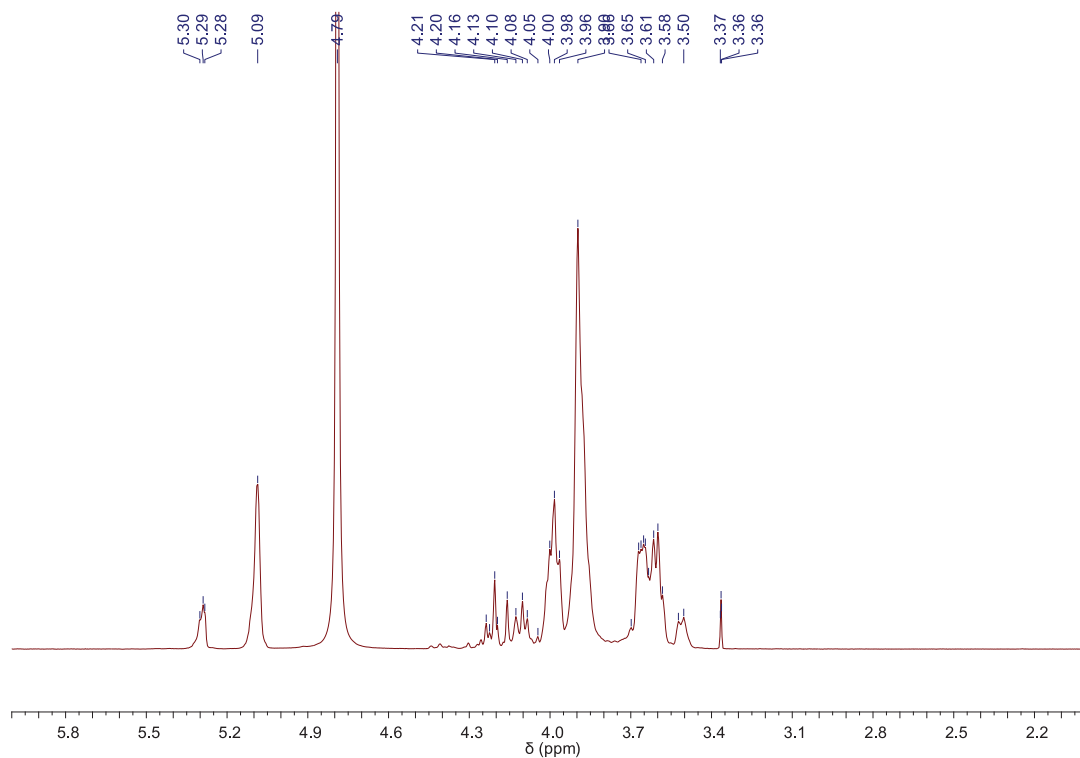
Figure 4-9. ^{1}H NMR spectrum of β-CD-COONa in D$_2$O at 25 °C (500 MHz).
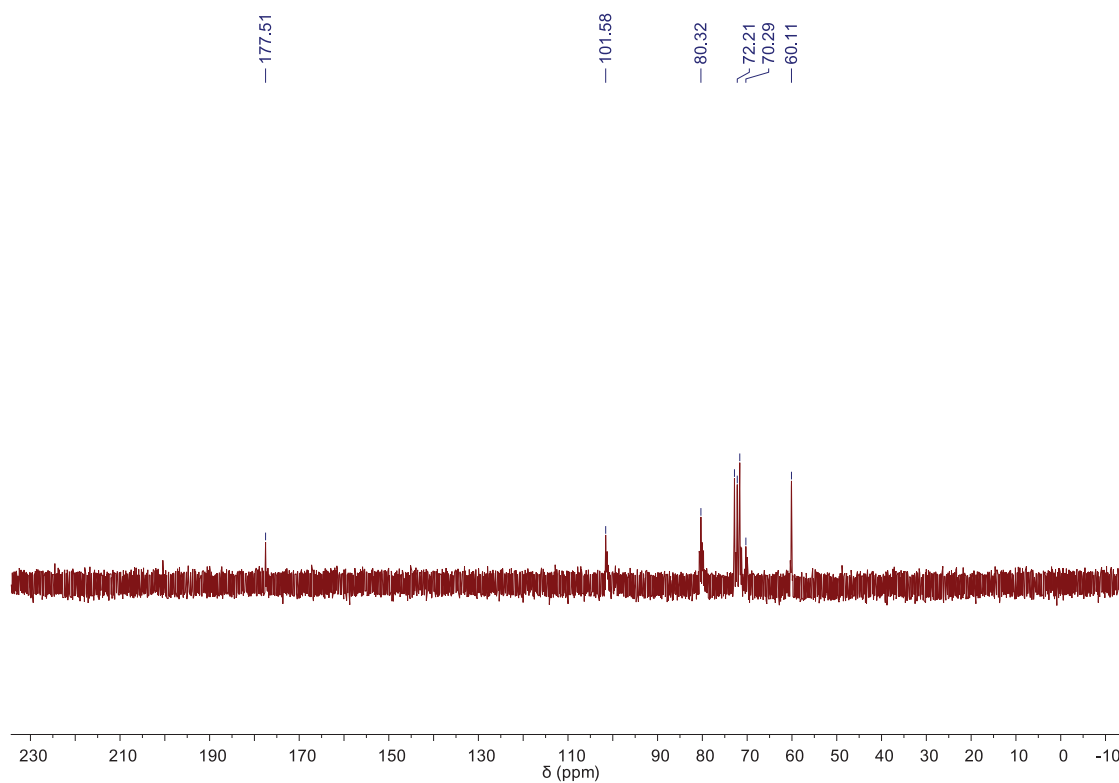
Figure 4-10. ^{13}C NMR spectrum of β-CD-COONa in D₂O at 25 °C (125 MHz).
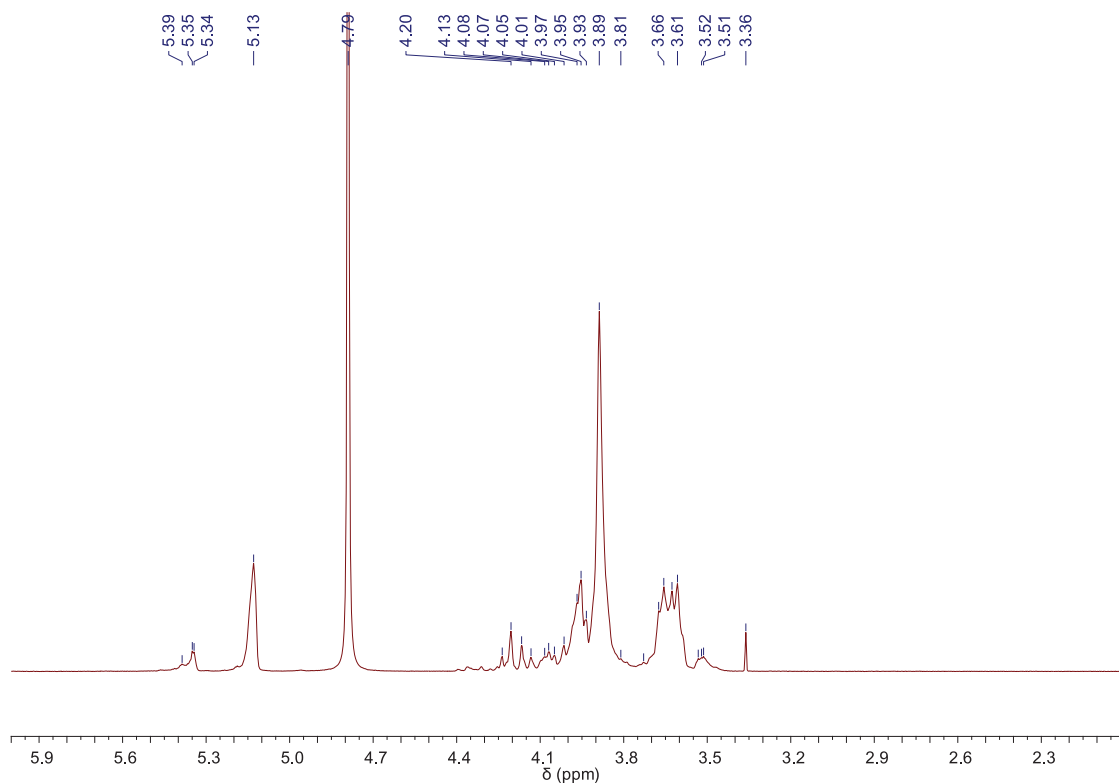
Figure 4-11. ^{1}H NMR spectrum of γ-CD-COONa in D₂O at 25 °C (500 MHz).
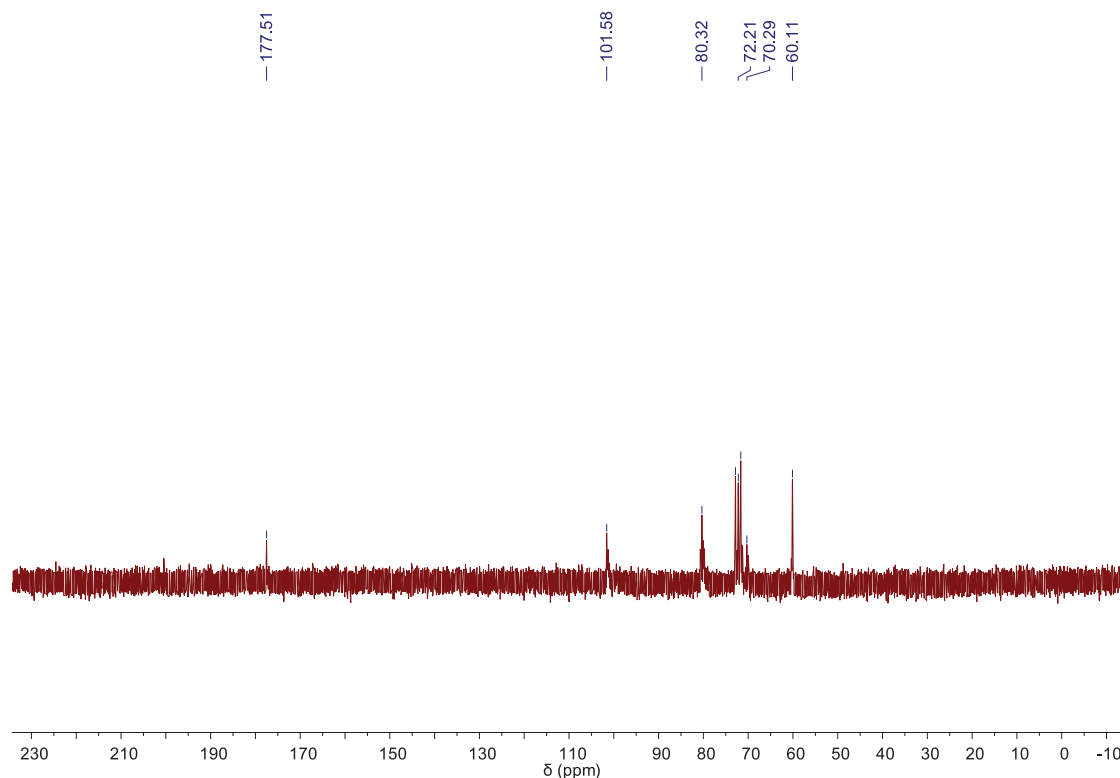
Figure 4-12. ^{13}C NMR spectrum of γ-CD-COONa in D$_2$O at 25 °C (125 MHz).

Compared with natural CDs, new chemical bonds were formed after modifying carboxylate onto the molecules, which is confirmed using Raman spectra and FT-IR spectra. In **Figure 4-13**, Raman spectra showed the carbon-oxygen double bonds in the spectra located at 1700 cm^{-1} for all the three CDs after carboxylate modification. In addition, the carbon-oxygen bonds in the cycles are shown at 490 cm^{-1} (=CH-OH in plane def) which can be attributed to the alcohols. After carboxylic modifications, parts of these alcohols are functioned as carboxylic acid, the ratio of the peak reduced. In FT-IR spectra (**Figure 4-14)**, the sharp peaks of v_{asym} (CO$_2^-$) stretching of carboxylic acid sodium salts are displayed in 1594 cm^{-1}(α-CD-COONa), 1593 cm^{-1} (β-CD-COONa), and 1592 cm^{-1} (γ-CD-COONa), respectively. These also confirm that carboxylate groups are successfully modified on these CDs. Another evidence of successful modification was based on the temperature change of weight loss in TGA (**Figure 4-15**). The weight loss

temperature in natural CDs was about 320 °C ~ 330 °C. After modified with carboxylate

groups, the temperatures were shifted around 300 °C.
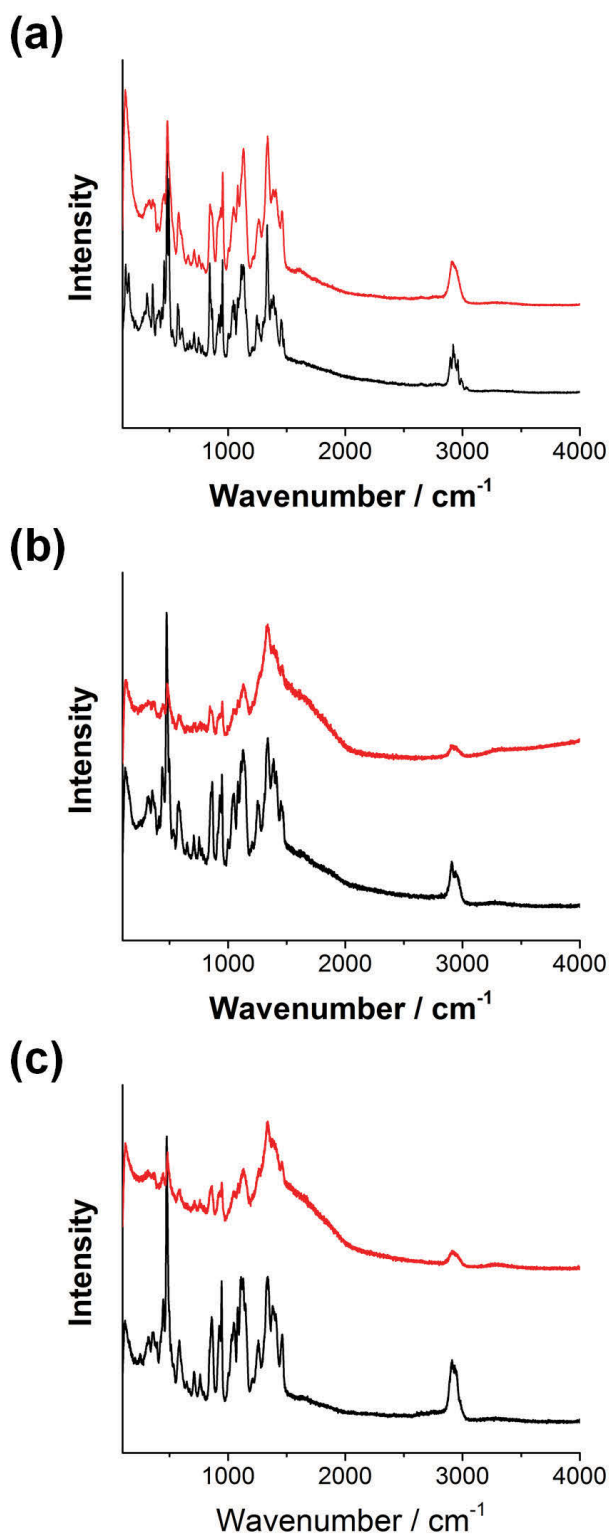
**Figure 4-13. Raman spectra: (a). α-CD (black) and α-CD-COONa (red); (b). β-CD
(black) and β-CD-COONa (red); (c). γ-CD (black) and γ-CD-COONa (red).**
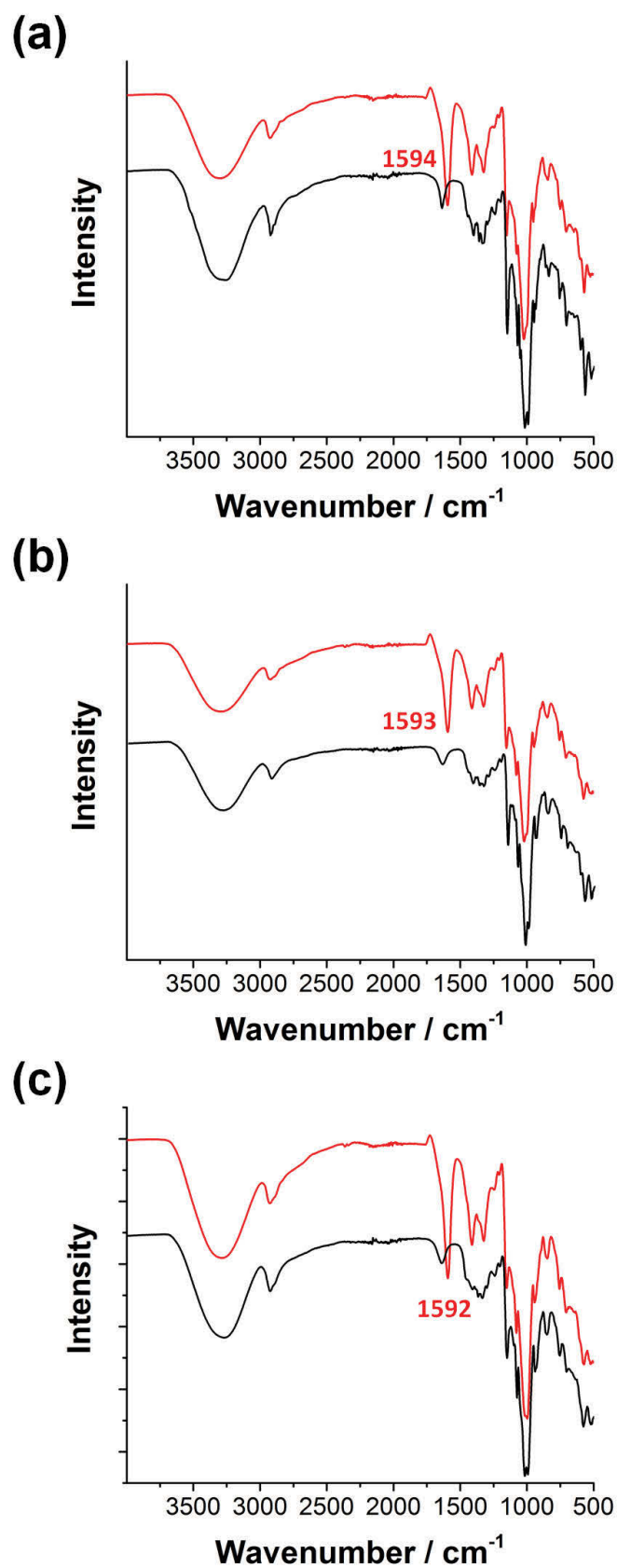
Figure 4-14. FT-IR spectra: (a). α-CD (black) and α-CD-COONa (red); (b). β-CD (black) and β-CD-COONa (red); (c). γ-CD (black) and γ-CD-COONa (red).
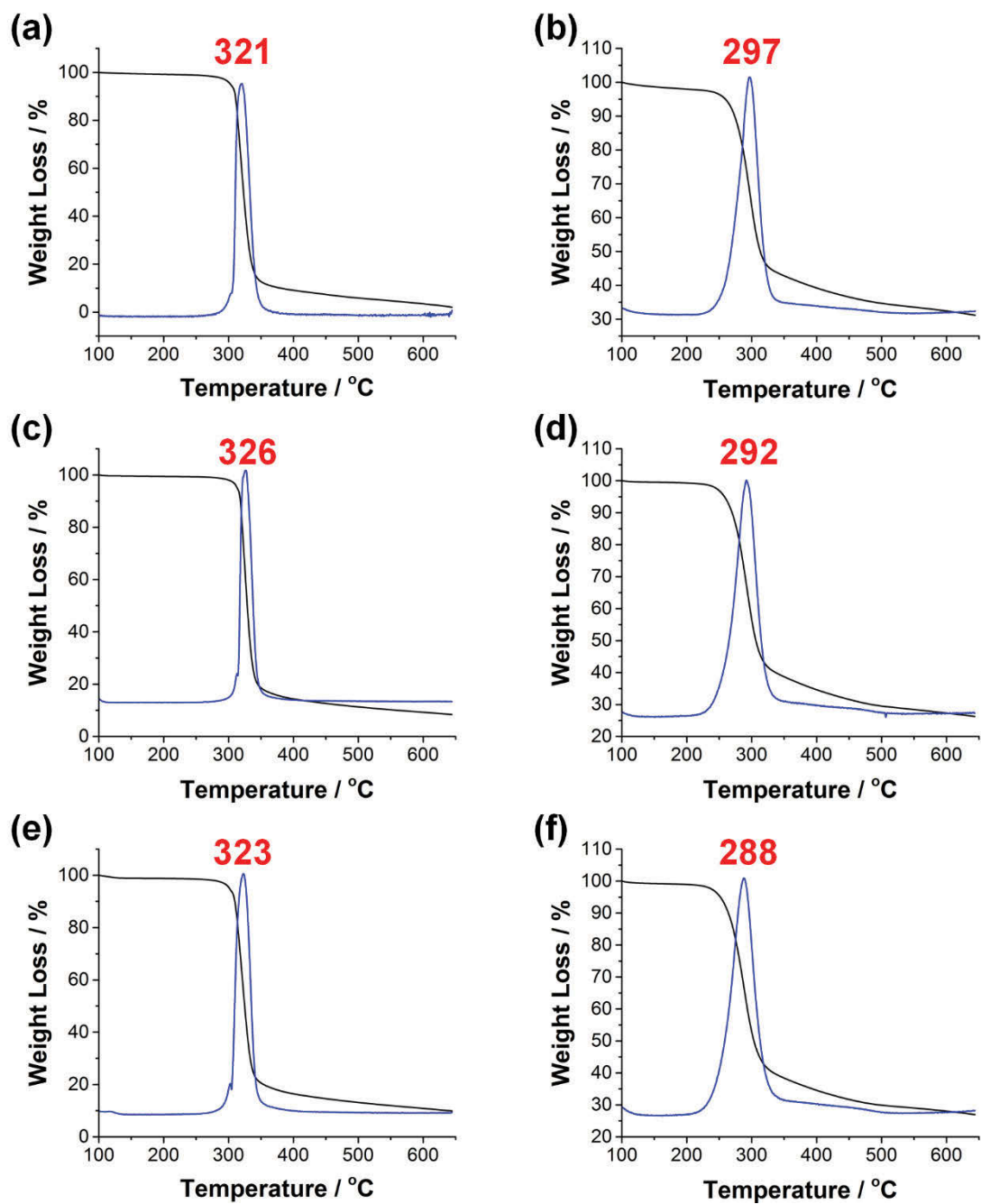
Figure 4-15. TGA and DTGA curves of (a) α-CD, (b) β-CD, (c) γ-CD, (d) α-CD-COONa, (e) β-CD-COONa, and (f) γ-CD-COONa.

4.3.2 Binding Behaviour of Organically Functional Groups

4.3.2.1 Multiple Binding of CDs

According to the calculation of binding constants (see Section 1.3.2 in **Chapter 1**), the equation of multiple binding constant (K_t) is shown in **Equation 4-2**.

Equation 4-2. The binding constant of multiple binding.

$$K_t = k_1 \times k_2 \times \dots \dots \times k_n$$

All the CDs that we chose have at least six functional groups on one side, so the binding constants will be much higher than OA (one carboxylate) on the original surface. Additionally, all the CDs in this chapter processed the multiple binding mode, which greatly increased the binding ability (**Equation 4-2**).

4.3.2.2 Binding Behaviour of Sulfonic Group

In order to investigate the binding behaviour of sulfonic group onto the surfaces of UCNPs, sodium dodecyl sulphate (SDS) was used as a simple model to modify onto UCNPs instead of β-CD-SO$_3$Na, because of the similar binding manner of β-CD-SO$_3$Na and SDS to the surface of UCNPs via SO$_3^-$ and Y atom. In this way, we can easily predict the binding behaviour between β-CD-SO$_3$Na and UCNP surface.

The surface modification of SDS onto UCNPs were carried out by FT-IR for both OA-UCNPs and free SDS (**Figure 4-16**). For organic sulphate esters (SDS), (Chihara 1960) two very strong absorptions are shown at 1247 cm^{-1} and 1216 cm^{-1} (**Figure 4-16**). They are asymmetric stretching vibration of SO$_3$, which was very stable and hardly affected by the substituent presence. This is a very typical identification of sulphate ester. After modified on the surface of UCNPs, the absorption of $_{vs}$ (SO$_3$) shifted to a higher frequency (1261 cm^{-1} and 1210 cm^{-1}) due to electron effect. In addition, when SDS bonded with Y atom, these S-O bonds are equalized because of conjugated effect. Therefore, the intensity

of the second asymmetric stretching vibration of SO$_3$ at 1210 cm^{-1} decreases due to the

increasing symmetry of anchor group. The intensity of SO$_3$ symmetric stretching

vibration is also getting weaker because of the symmetry of sulphate. At the same time,

the S-O-C stretching vibration shifted from 822 cm^{-1} to 800 cm^{-1}. These shifts indicate

that these positions of bands are influenced by the Y atom. According to the FT-IR

spectra, we predicted the binding mode of SDS on the surface of UCNPs and shown in

Figure 4-17.
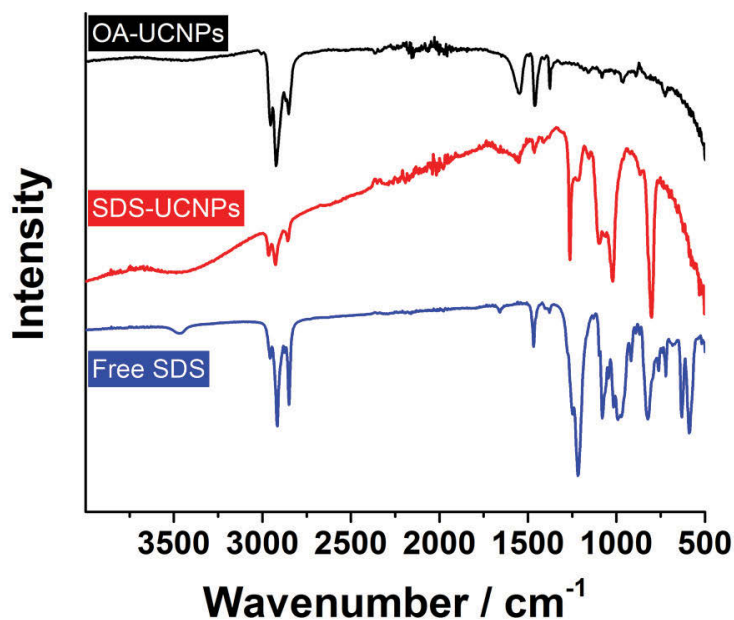
Figure 4-16. The FT-IR Spectra of free SDS (blue), SDS-UCNPs (red), and OA-UCNPs (black).
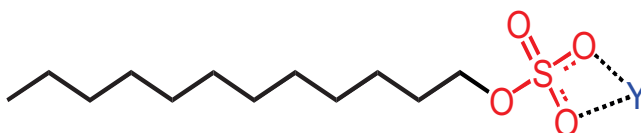
Figure 4-17. The binding prediction of sulphate with Y atom from UCNP surface.

4.3.2.3 Binding Behaviour of Phosphoric Group

The molecular structure of sodium dodecyl phosphate (SDP) from the surface of UCNPs is shown in **Figure 4-18**. In free SDP, a strong peak at 1069 cm^{-1} is the stretching of the P-O bond. The P-O stretching from P-O-C is located at 823 cm^{-1} and 719 cm^{-1}. Another peak at 1466 cm^{-1} shows the C-O stretching from the P-O-C bond. After modified on the surface of UCNPs, the spectrum is similar with the free SDP; it means SDP has already modified on the surface of UCNP successfully. Besides, the peak at 1466 cm^{-1} changed to a low position, which is because the electrons moved to the terminal of the molecule for attaching on the surface of UCNPs. In addition, except for this peak, other peaks reduced, which mean the O here does not form any direct interaction with the surface of UCNPs. Another evidence of modification is several peaks appeared 1700 cm^{-1} to 1600 cm^{-1}, which are from the P-O-M bonds. The predicted binding mode is shown in **Figure 4-19**.
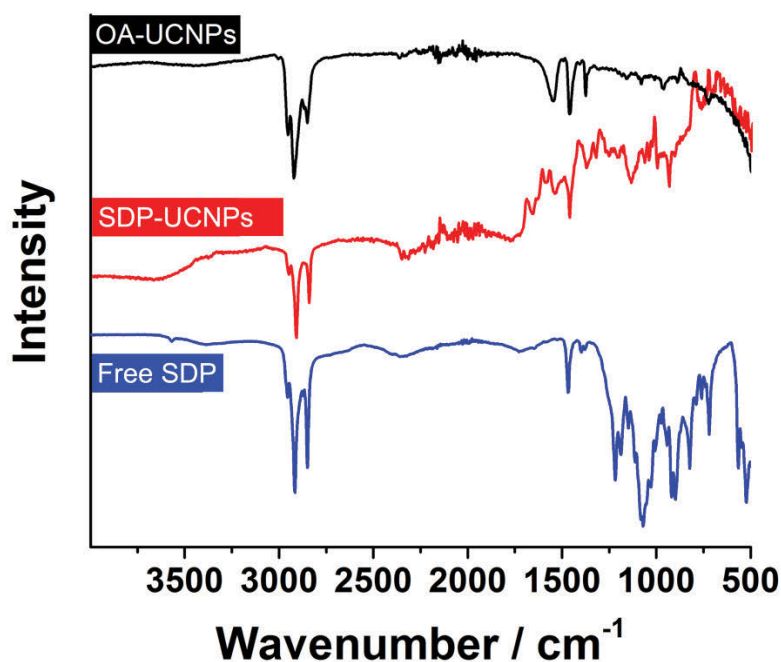
Figure 4-18. The FT-IR Spectra of free SDP (blue), SDP-UCNPs (red), and OA-UCNPs (black).
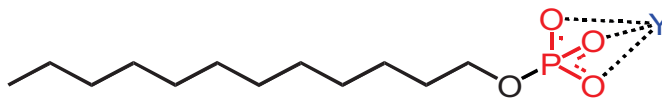
Figure 4-19. The binding prediction of SDP with Y atom from UCNP surface.

4.3.3 Morphology of CD-UCNPs

The sizes of CD-UCNPs were characterized using TEM and DLS. From the TEM (**Figure 4-20**), the size of spherical OA-UCNPs was around 25 nm (**Figure 4-20f**). After modified with different kinds of CDs, these particles still kept in the same size and shape.
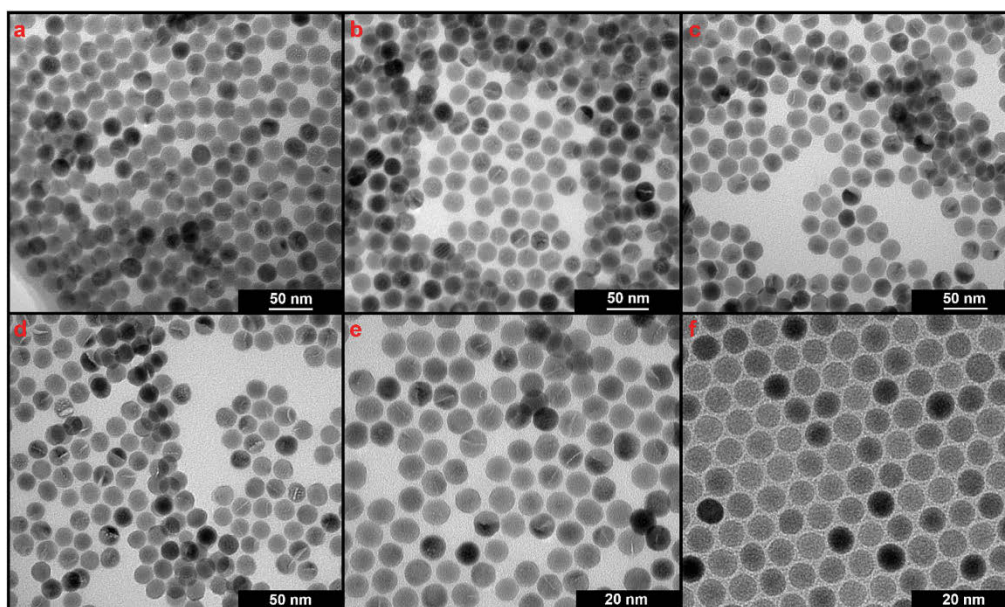
Figure 4-20. TEM images of (a) α-CD-COONa-UCNP, (b) β-CD-COONa-UCNP, (c) γ-CD-COONa-UCNP, (d) β-CD-SO₃Na-UCNP, (e) β-CD-PO₃Na₂-UCNP and (f)OA-UCNP.

The DLS results in **Figure 4-21** showed the size distribution of OA-UCNPs in cyclohexane is around 22 nm, very close to the TEM image (**Figure 4-20f**). While the **Figure 4-21** exhibits the size distributions of CD-UCNPs in water (55 nm) is much larger than the sizes in TEM, which is due to the hydraulic size of CD-UCNPs in aqueous

solution. Because the DLS measured the hydraulic diameter of the nanoparticles surrounded with water molecules rather than the actual size. The DLS results would be different for the same batch nanoparticles when they are in a different solvent and with various surface modifications. Furthermore, the TEM images in **Figure 4-20** shows the excellent dispersity of the CD-UCNPs.

The sizes of CD-UCNPs-DOX are also tested by DLS (**Figure 4-21**). The results show after loading DOX; these nanoparticles still keep similar hydraulic sizes with CD-UCNPs.
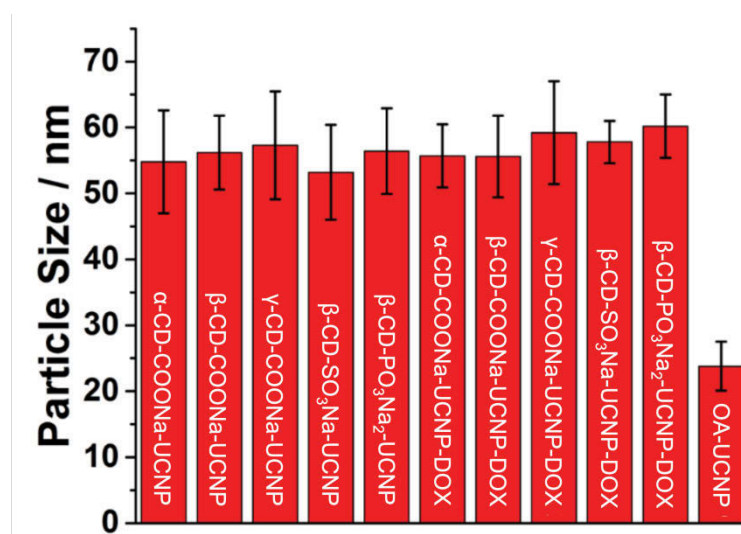
Figure 4-21. Particle sizes (DLS) of α-CD-COONa-UCNP (in water), β-CD-COONa-UCNP (in water), γ-CD-COONa-UCNP (in water), β-CD-SO₃Na-UCNP (in water), β-CD-PO₃Na₂-UCNP (in water), α-CD-COONa-UCNP-DOX (in water), β-CD-COONa-UCNP-DOX (in water), γ-CD-COONa-UCNP-DOX (in water), β-CD-SO₃Na-UCNP-DOX (in water), β-CD-PO₃Na₂-UCNP-DOX (in water), and OA-UCNP (in cyclohexane).

4.3.4 Surface modifications of UCNPs

In Raman Spectra, there are a library of typical chemical bond stretching between Ln ions with oxygens from functional groups. (Ahmad, Prakash & Nagarajan 2012) **Figure 4-22** (α-CD-COONa-UCNP, β-CD-COONa-UCNP, and γ-CD-COONa-UCNP) and **Figure 4-**

23 (β-CD-SO$_3$Na-UCNP and β-CD-PO$_3$Na$_2$-UCNP) show a very strong and broad peak formed around 400 cm^{-1} from CD-UCNPs. It can be proved that varied kinds of Ln-O bonds are formed after functionalized with CDs.
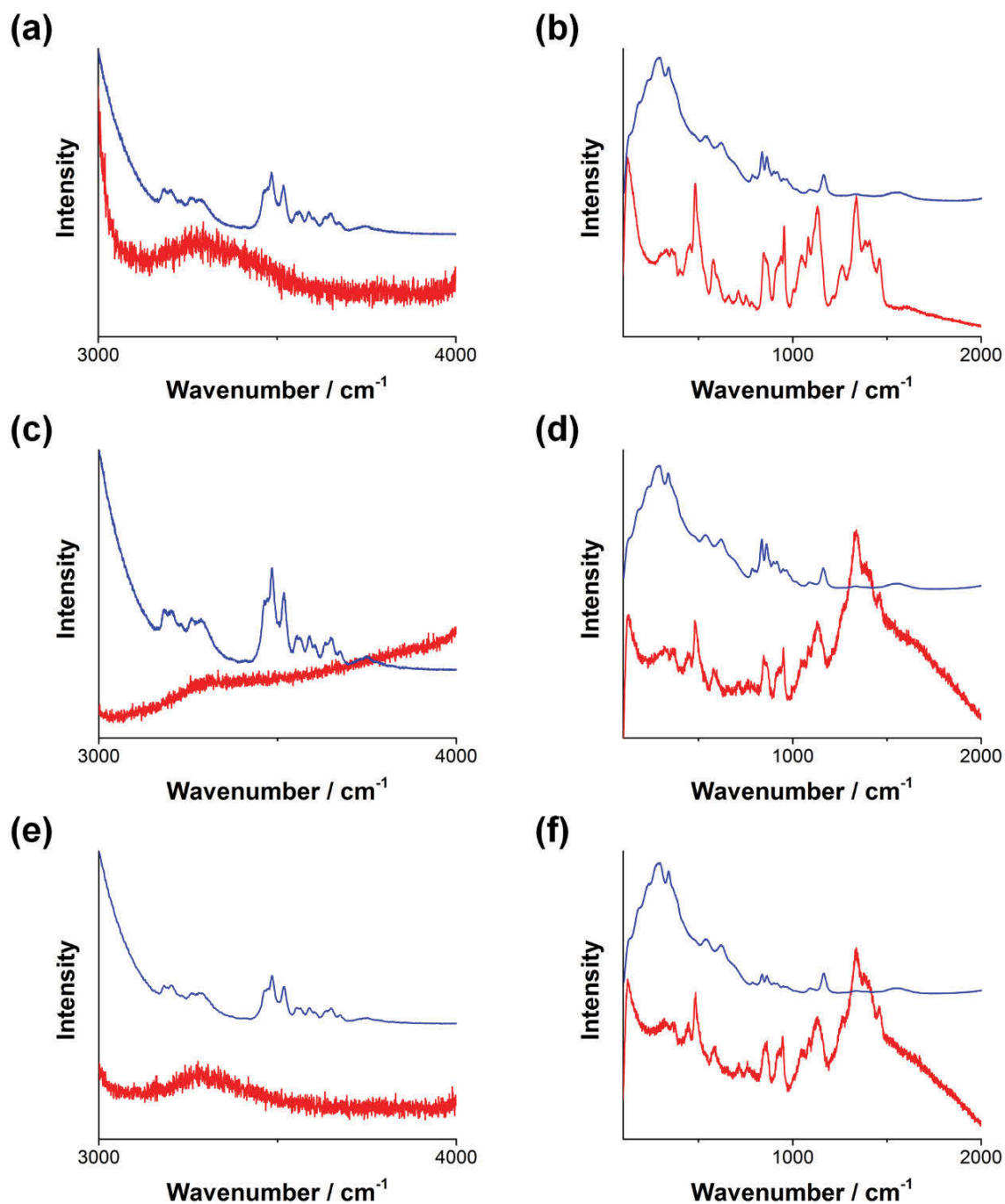
Figure 4-22. Raman spectra of CDs-COONa (red) and CD-COONa-UCNPs (blue). (a, b) α-CD-COONa and α-CD-COONa-UCNP, (c, d) β-CD-COONa and β-CD-COONa-UCNP, (e, f) γ-CD-COONa and γ-CD-COONa-UCNP.
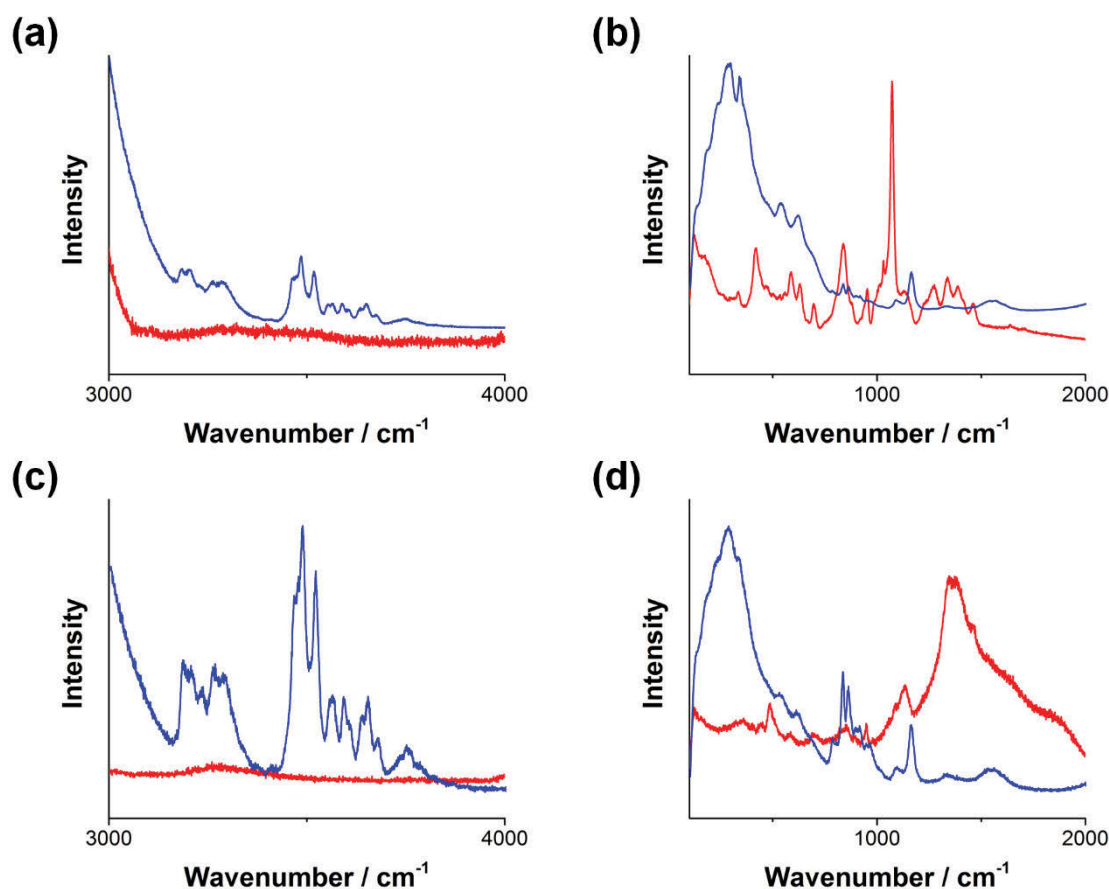
Figure 4-23. Raman spectra of (a, b) β-CD-SO$_3$Na (red) and β-CD-SO$_3$Na-UCNP (blue), (c, d) β-CD-PO$_3$Na$_2$ (red) and β-CD-PO$_3$Na$_2$-UCNP (blue).

In FT-IR spectrum of OA-UCNP, the v_{st} (C=O) stretching is split into two peaks, and they shifted to 1547 cm^{-1} (asymmetric) to 1461 cm^{-1} (symmetric), respectively (**Figure 3-7** in **Chapter 3**). After exchanging with CD-COONa (**Figure 4-24**), the asymmetric stretching of C=O switches to about 1590 cm^{-1}. Also, the symmetric stretching of C=O moves to the lower wavenumbers, and further is splatted into two peaks at ~1410 cm^{-1} and ~1320 cm^{-1}. The spectra of CD-UCNPs match the ones of free CD-COONa. So, FT-IR spectra also exhibit that CDs-COONa are successfully modified on the surfaces of UCNPs.
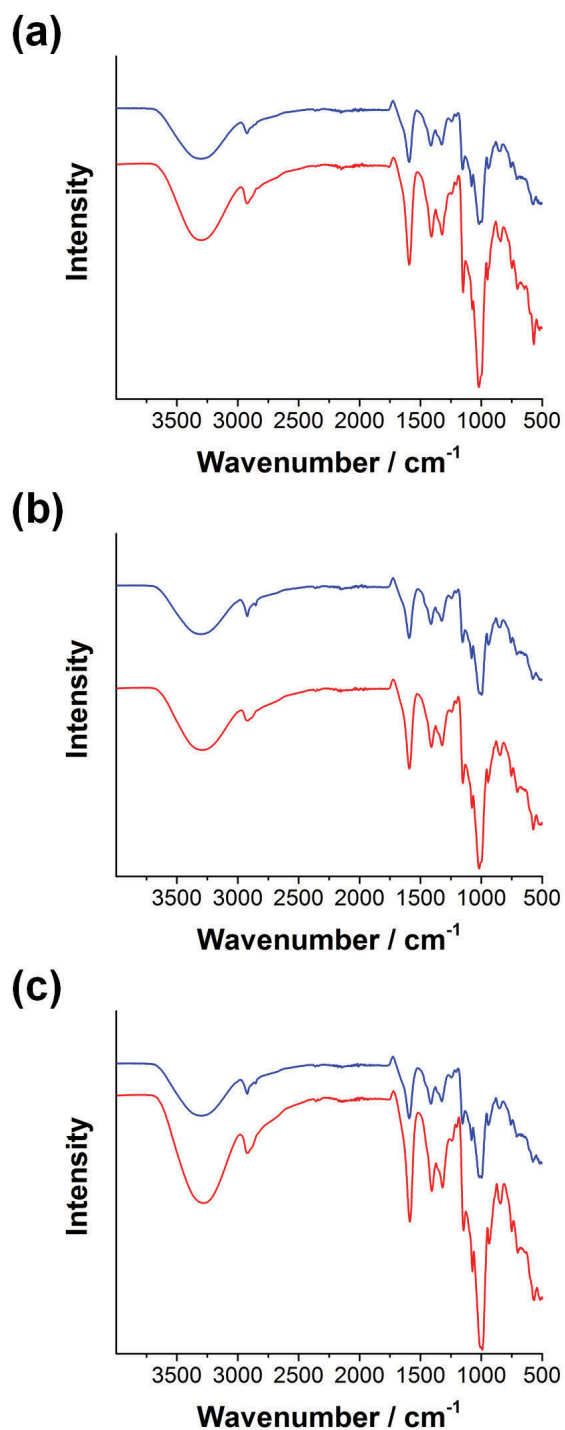
Figure 4-24. FT-IR spectra of (a) α-CD-COONa (red) and α-CD-COONa-UCNP (blue), (b) β-CD-COONa (red) and β-CD-COONa-UCNP (blue), (c) γ-CD-COONa (red) and γ-CD-COONa-UCNP (blue).

After exchanging with β-CD-SO$_3$Na, a new bond forms between –SO$_3^-$ and Ln ioins on the surfaces of UCNPs. So, a peak of $v_{s\ asym}$ SO$_3$ stretching is shown from 1250 cm^{-1} to

1140 cm^{-1}. In **Figure 4-25a**, the peaks locates at 1234 cm^{-1}, which suggests that β-CD-SO$_3$Na has been successfully modified on the surface of UCNPs. Before binding on the surface of UCNPs (**Figure 4-25b**), β-CD-PO$_3$Na$_2$ shows a typical broad stretching at 1023 cm^{-1}, which includes asymmetric and symmetric stretching of PO$_3^{2-}$. After binding on the surface of UCNPs, the v_{st} (PO$_3^{2-}$) stretching is split into two peaks, and they shift to 1100 cm^{-1} (asymmetric) to 1023 cm^{-1} (symmetric), respectively (**Figure 4-25b**).
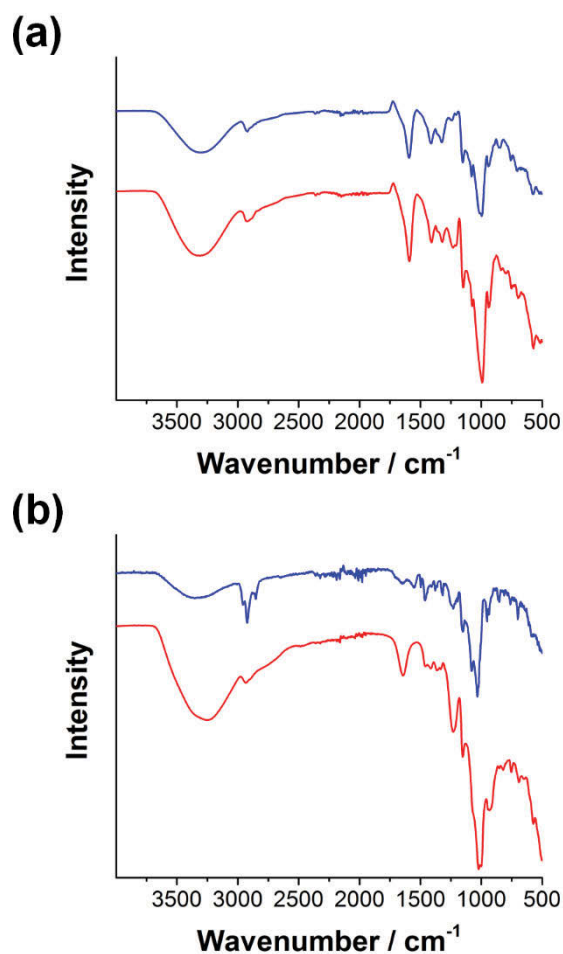
Figure 4-25. FT-IR spectra of (a) β-CD-SO$_3$Na (red) and β-CD-SO$_3$Na-UCNP (blue), (b) β-CD-PO$_3$Na$_2$ (red) and β-CD-PO$_3$Na$_2$-UCNP (blue).

TGA curves of CDs-COONa and CD-COONa-UCNPs are shown in **Figure 4-26** and **Figure 4-27**. Compared with the TGA of OA-UCNPs (**Figure 3-9** in **Chapter 3**), all the weight loss temperature change to the same as the CDs after exchanging with CDs. Besides, the CDs took 7%~9% of the total weight. According to the weight loss, the

coverages of CDs are calculated and displayed in **Table 4-1**, according to the method

shown in Section 3.3.3 in **Chapter 3**.
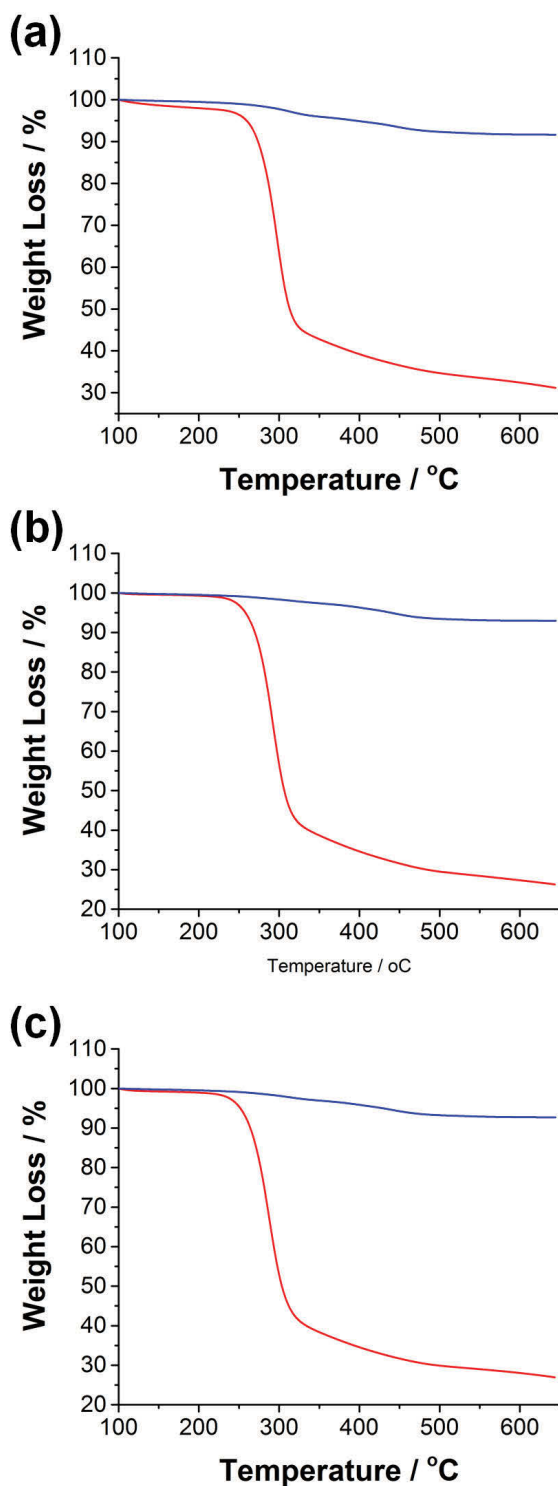
**Figure 4-26. TGA curves of (a) α-CD-COONa (red) and α-CD-COONa-UCNP
(blue), (b) β-CD-COONa (red) and β-CD-COONa-UCNP (blue), (c) γ-CD-COONa
(red) and γ-CD-COONa-UCNP (blue).**
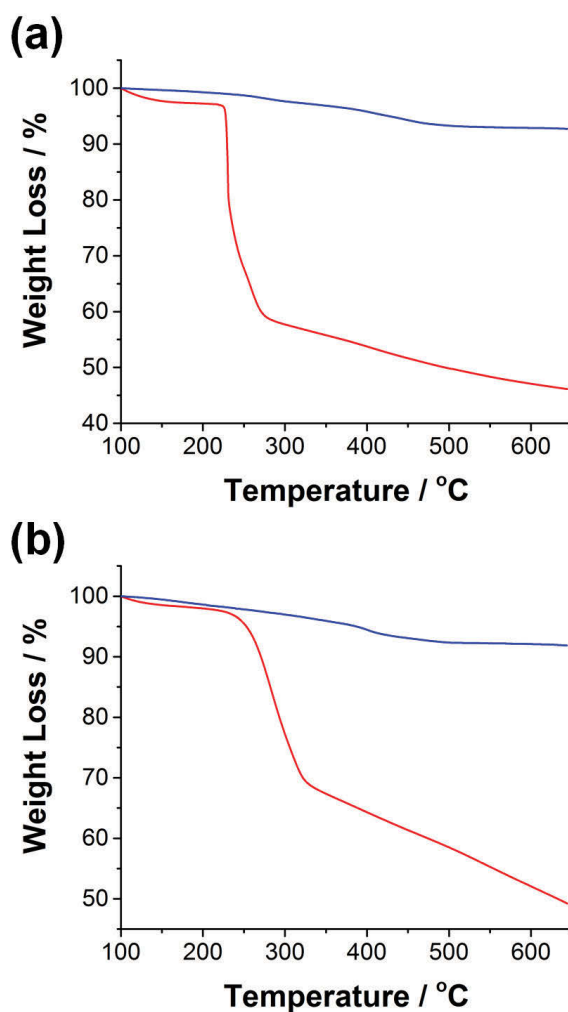
Figure 4-27. TGA curves of (a) β-CD-SO₃Na (red) and β-CD-SO₃Na-UCNP (blue), (b) β-CD-PO₃Na₂ (red) and β-CD-PO₃Na₂-UCNP (blue).

Table 4-1. The coverage of CDs on the surface of UCNPs.

Sample Name	Coverage on the UCNP surface (%)
α-CD-COONa-UCNP	52.64
β-CD-COONa-UCNP	55.26
γ-CD-COONa-UCNP	58.45
β-CD-SO₃Na-UCNP	55.62
β-CD-PO₃Na₂-UCNP	54.99

The binding abilities of different kinds of CDs with DOX were carried out by ITC. Because α-CD hardly binds with DOX, only four kinds of CDs were applied for the investigation in binding behaivour, which are shown in **Figure 4-28** ~ **Figure 4-31**. At the same time, the summary of binding constants and energy is shown in **Table 4-2**. The results show β-CD-SO$_3$Na processes the highest binding strength with DOX.
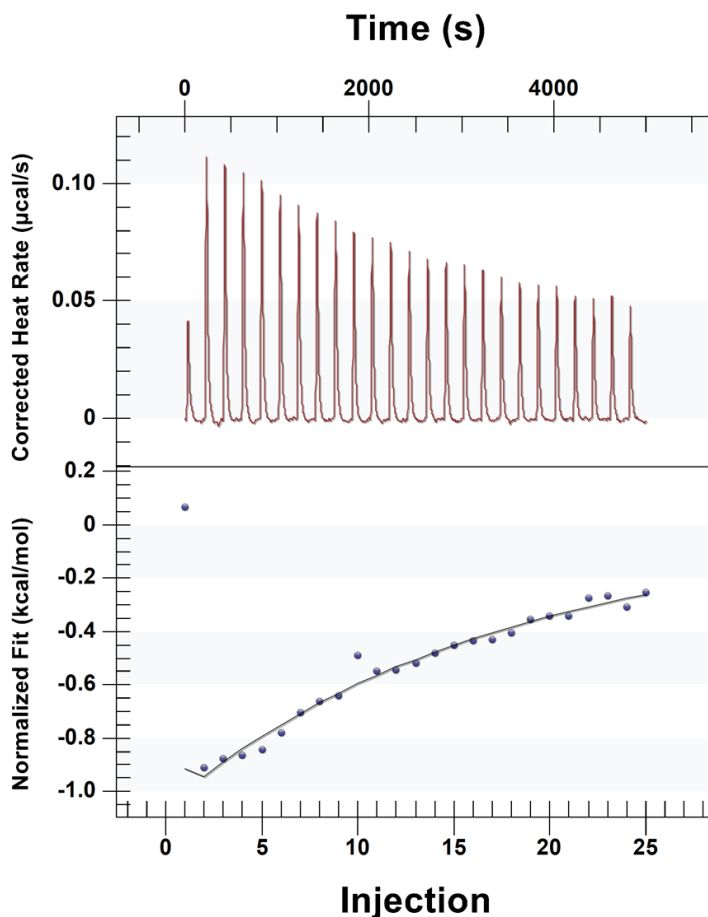
Figure 4-28. ITC measurements: (a). the complexation reaction of β-CD-COONa (1 mM) with DOX (0.5 mmol/L) for each injection during a calorimetric titration at 25 ºC. Top: raw ITC data for 25 sequential injections (2 μL per injection) of β-CD-COONa solution (1 mmol/L) into DOX solution (0.5 mmol/L). Bottom: Net heat effects obtained by subtracting the dilution heat from the reaction heat, fitted by "independence" model. (b) The dilution heat of β-CD-COONa in H$_2$O at 25 ºC. Top: raw ITC data for 25 sequential injections (2 μL per injection) of β-CD-COONa

solution (1 mmol/L) into H₂O. Bottom: Heat effects of the dilution with β-CD-

COONa (1 mmol/L) for each injection during a calorimetric titration at 25 ºC.

Figure 4-29. ITC measurements: (a). The complexation reaction of γ-CD-COONa (1

mM) with DOX (0.5 mmol/L) for each injection during a calorimetric titration at 25

ºC. Top: raw ITC data for 25 sequential injections (2 µL per injection) of γ-CD-

COONa solution (1 mmol/L) into DOX solution (0.5 mmol/L). Bottom: Net heat

effects obtained by subtracting the dilution heat from the reaction heat, fitted by

"independence" model. (b) The dilution heat of γ-CD-COONa in H₂O at 25 ºC. Top:

raw ITC data for 25 sequential injections (2 µL per injection) of γ-CD-COONa

solution (1 mmol/L) into H₂O. Bottom: Heat effects of the dilution with γ-CD-

COONa (1 mmol/L) for each injection during a calorimetric titration at 25 ºC.

Figure 4-30. ITC measurements: (a). The complexation reaction of β-CD-SO₃Na (1 mM) with DOX (0.5 mmol/L) for each injection during a calorimetric titration at 25 °C. Top: raw ITC data for 25 sequential injection (2 μL per injection) of β-CD-SO₃Na solution (1 mmol/L) into DOX solution (0.5 mmol/L). Bottom: Net heat effects obtained by subtracting the dilution heat from the reaction heat, fitted by "independence" model. (b) The dilution heat of β-CD-SO₃Na in H₂O at 25 °C. Top: raw ITC data for 25 sequential injections (2 μL per injection) of β-CD-SO₃Na solution (1 mmol/L) into H₂O. Bottom: Heat effects of the dilution with β-CD-SO₃Na (1 mmol/L) for each injection during a calorimetric titration at 25 °C.
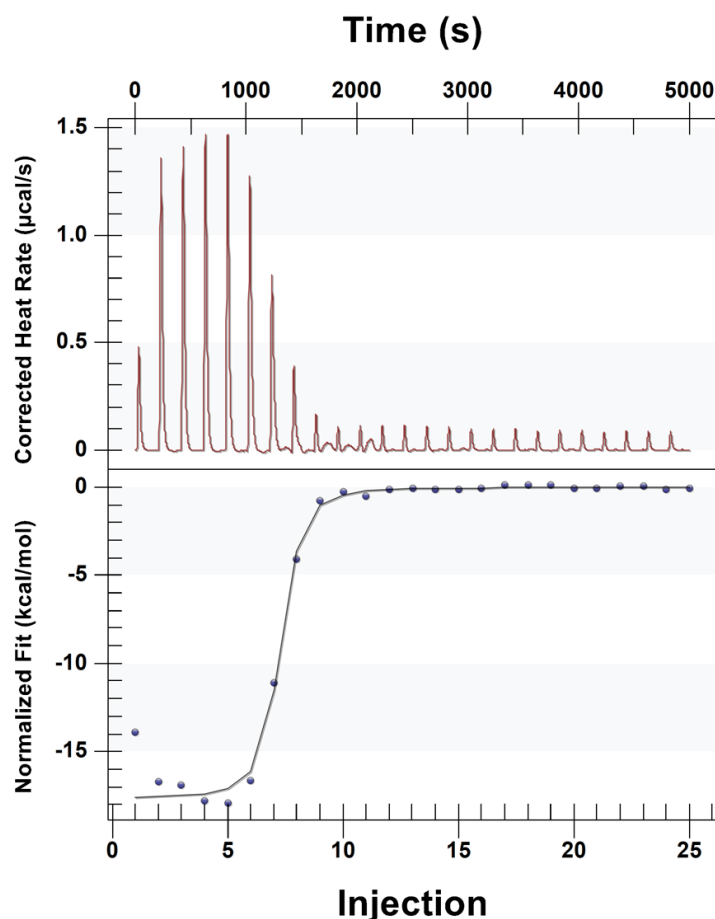
Figure 4-31. ITC measurements: (a). The complexation reaction of β-CD-PO$_3$Na$_2$ (1 mM) with DOX (0.5 mmol/L) for each injection during a calorimetric titration at 25 ℃. Top: raw ITC data for 25 sequential injection (2 μL per injection) of β-CD-PO$_3$Na$_2$ solution (1 mmol/L) into DOX solution (0.5 mmol/L). Bottom: Net heat effects obtained by subtracting the dilution heat from the reaction heat, fitted by "independence" model. (b) The dilution heat of β-CD-PO$_3$Na$_2$ in H$_2$O at 25 ℃. Top: raw ITC data for 25 sequential injections (2 μL per injection) of β-CD-PO$_3$Na$_2$ solution (1 mmol/L) into H$_2$O. Bottom: Heat effects of the dilution with β-CD-PO$_3$Na$_2$ (1 mmol/L) for each injection during a calorimetric titration at 25 ℃.

Table 4-2. The summary of binding constants of CD-UCNPs with DOX

Sample Name	K_a [M^{-1}]	ΔH^o [kcal / mol]	$T\Delta S^o$ [kcal / mol]	ΔG^o [kcal / mol]
α-CD-COONa	--	--	--	--
β-CD-COONa	5.389×10^3	-4.99	0.101	-5.091
γ-CD-COONa	1.446×10^4	-8.388	-2.712	-5.675
β-CD-SO$_3$Na	5.825×10^7	-61.25	50.65	-10.59
β-CD-PO$_3$Na$_2$	5.232×10^6	-17.67	-8.504	-9.166

4.3.5 Drug Delivery Study

We understand that the process of loading DOX is carried out based on host-guest interactions, which has no new chemical bonds formed in this stage. Therefore, there is no significant difference between before and after loading in Raman and FT-IR spectra (**Figure 4-32**, **Figure 4-33**, and **Figure 4-34**).
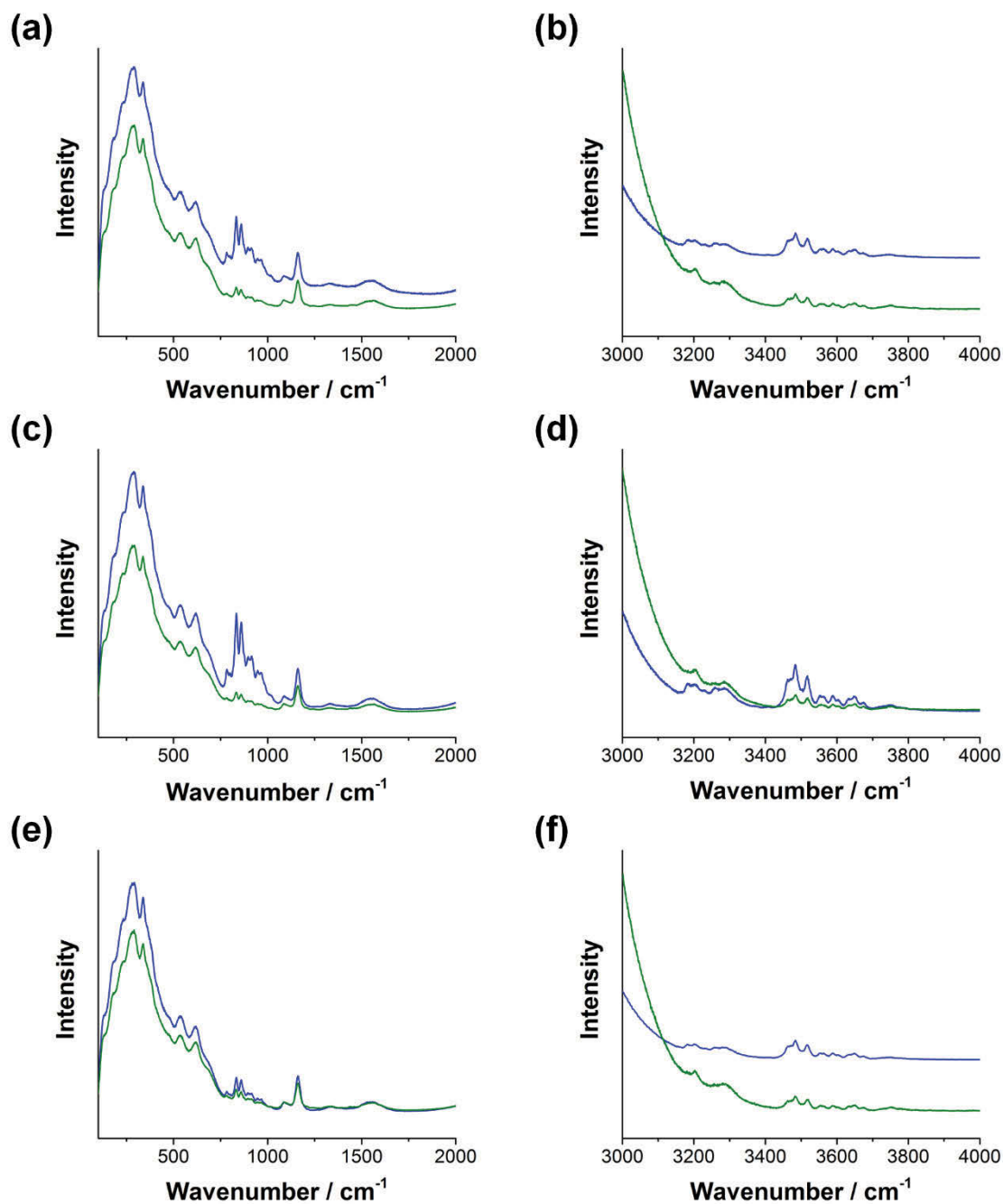
Figure 4-32.Raman spectra of (a) α-CD-COONa-UCNP and α-CD-COONa-UCNP-DOX, (b) β-CD-COONa-UCNP and β-CD-COONa-UCNP-DOX, (c) γ-CD-COONa-UCNP and γ-CD-COONa-UCNP-DOX.
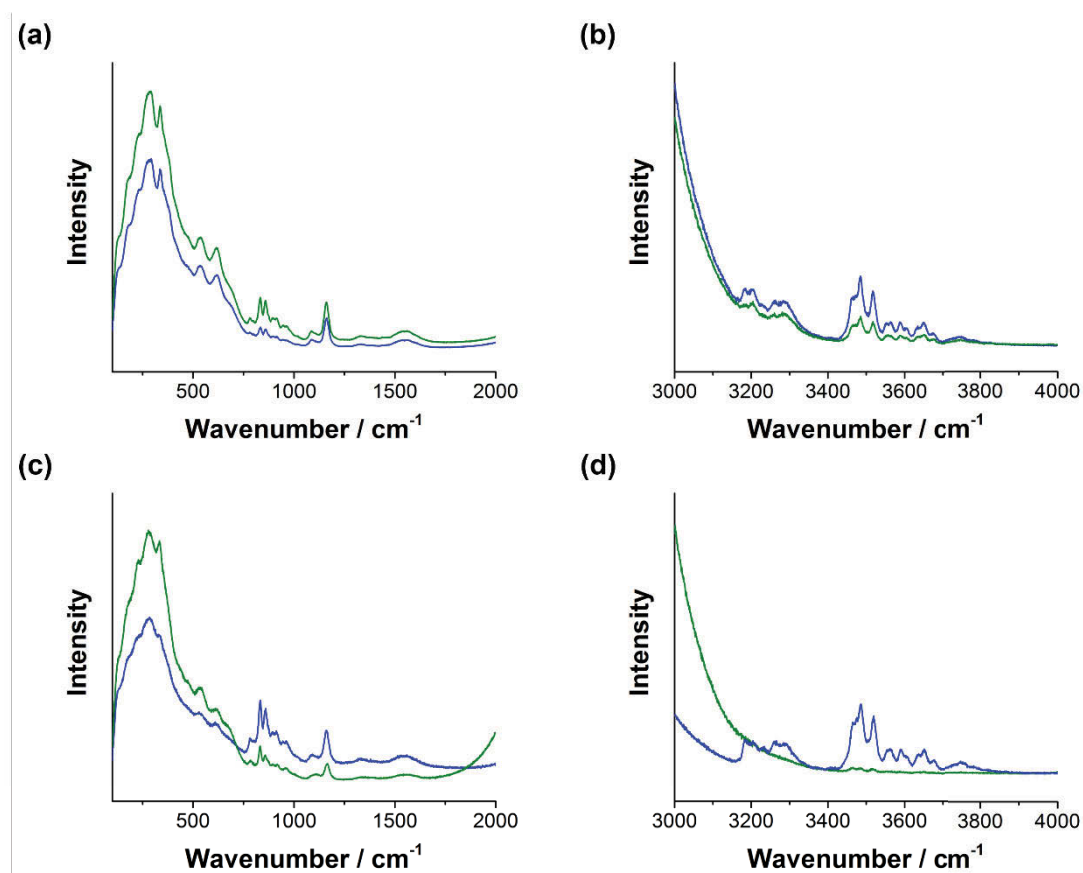
Figure 4-33. Raman spectra of (a,b) β-CD-SO₃Na-UCNP and β-CD-SO₃Na-UCNP-DOX, (c,d) β-CD-PO₃Na₂-UCNP and β-CD-PO₃Na₂-UCNP-DOX.
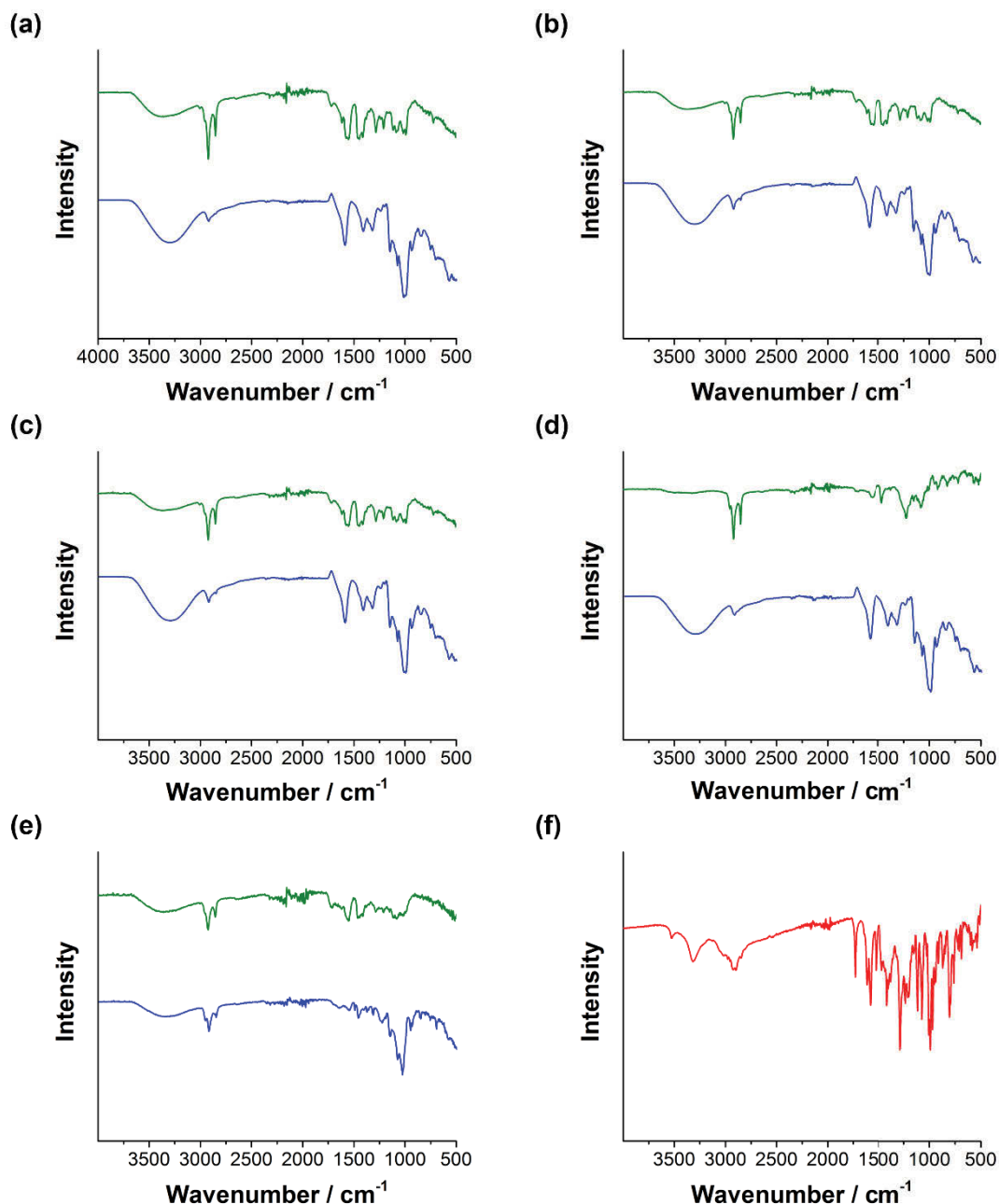
Figure 4-34. FT-IR spectra of (a) α-CD-COONa-UCNP and α-CD-COONa-UCNP-DOX, (b) β-CD-COONa-UCNP and β-CD-COONa-UCNP-DOX, (c) γ-CD-COONa-UCNP and γ-CD-COONa-UCNP-DOX, (d) β-CD-SO$_3$Na-UCNP and β-CD-SO$_3$Na-UCNP-DOX, (e) β-CD-PO$_3$Na$_2$-UCNP and β-CD-PO$_3$Na$_2$-UCNP-DOX, and (f) DOX.

The amount of relative drug loading was detected by UV-vis spectra. We tested the absorption of loading solution and compared the difference from before and after loading.

The comparable loading property is shown in **Figure 4-35**. The sample of β-CD-SO₃Na showed the highest loading amount, but α-CD-COONa only can load 20 % DOX of the one in β-CD-SO₃Na. This result also agrees with the binding constants which were carried out by ITC. It shows that the higher binding ability could offer a high loading property.
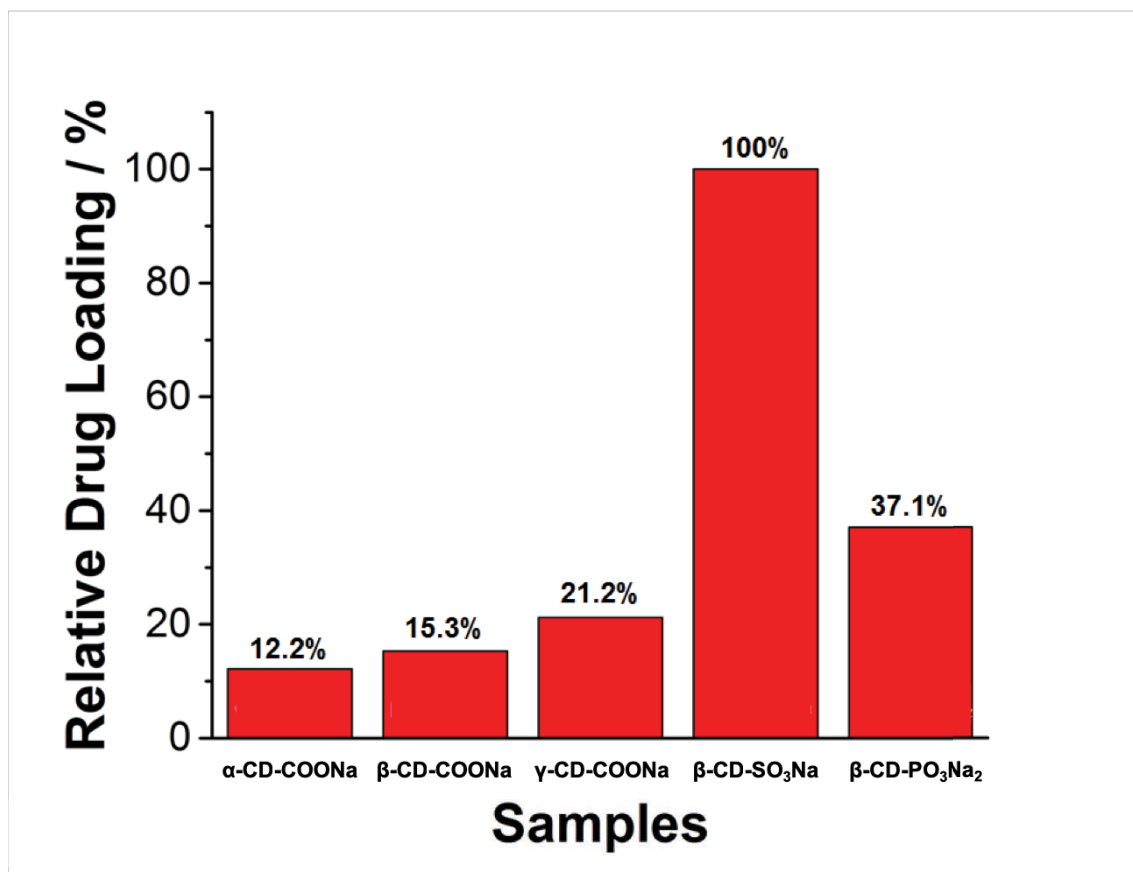
Figure 4-35. UV-vis spectra of (a) α-CD-COONa-UCNP-DOX, (b) β-CD-COONa-UCNP-DOX, (c) γ-CD-COONa-UCNP-DOX, (d) β-CD-SO₃Na-UCNP-DOX, and (e) β-CD-PO₃Na₂-UCNP-DOX.

The emission spectra of CD-COONa-UCNPs and CD-COONa-UCNPs-DOX are shown in **Figure 4-36** and **Figure 4-37**. Before loading DOX, these spectra show three peaks at 520 nm, 540 nm, and 650 nm. The colour of emission is green. After forming the host-guest interaction between DOX molecules and the surface CDs, the ratio of green emission and red emission changed. The red emission is getting stronger than green emission to set the colour of emission to red. At the same time, there is another peak

appearing at 800 nm. The phenomenon proves FRET has been formed between UCNPs and DOX by host-guest interactions. It also confirms that DOX molecules have been successfully bound on the surface of UCNPs.
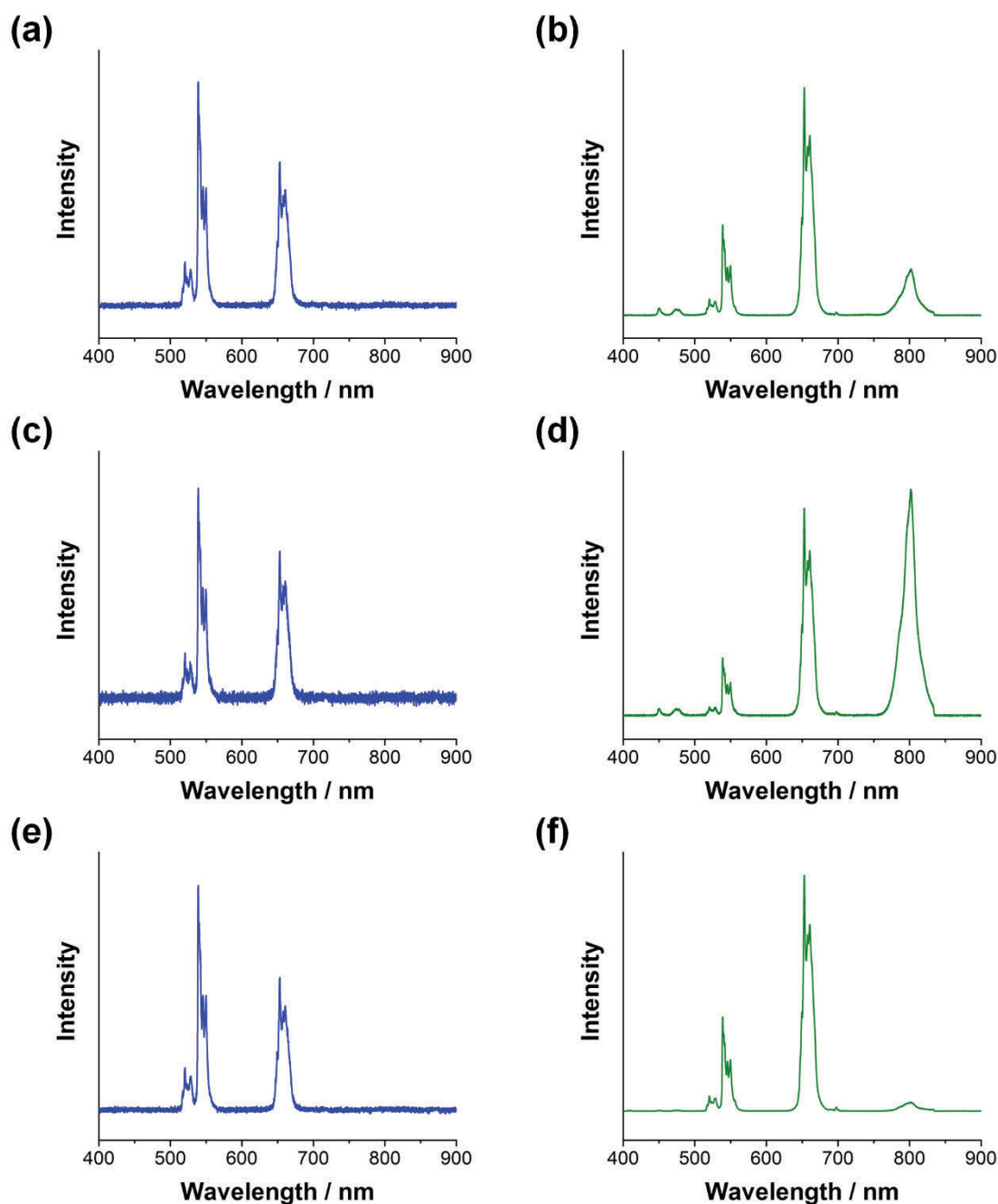
Figure 4-36. Emission spectra of (a) α-CD-COONa-UCNP, (b) α-CD-COONa-UCNP-DOX, (c) β-CD-COONa-UCNP, (d) β-CD-COONa-UCNP-DOX, (e) γ-CD-COONa-UCNP, and (f) γ-CD-COONa-UCNP-DOX.
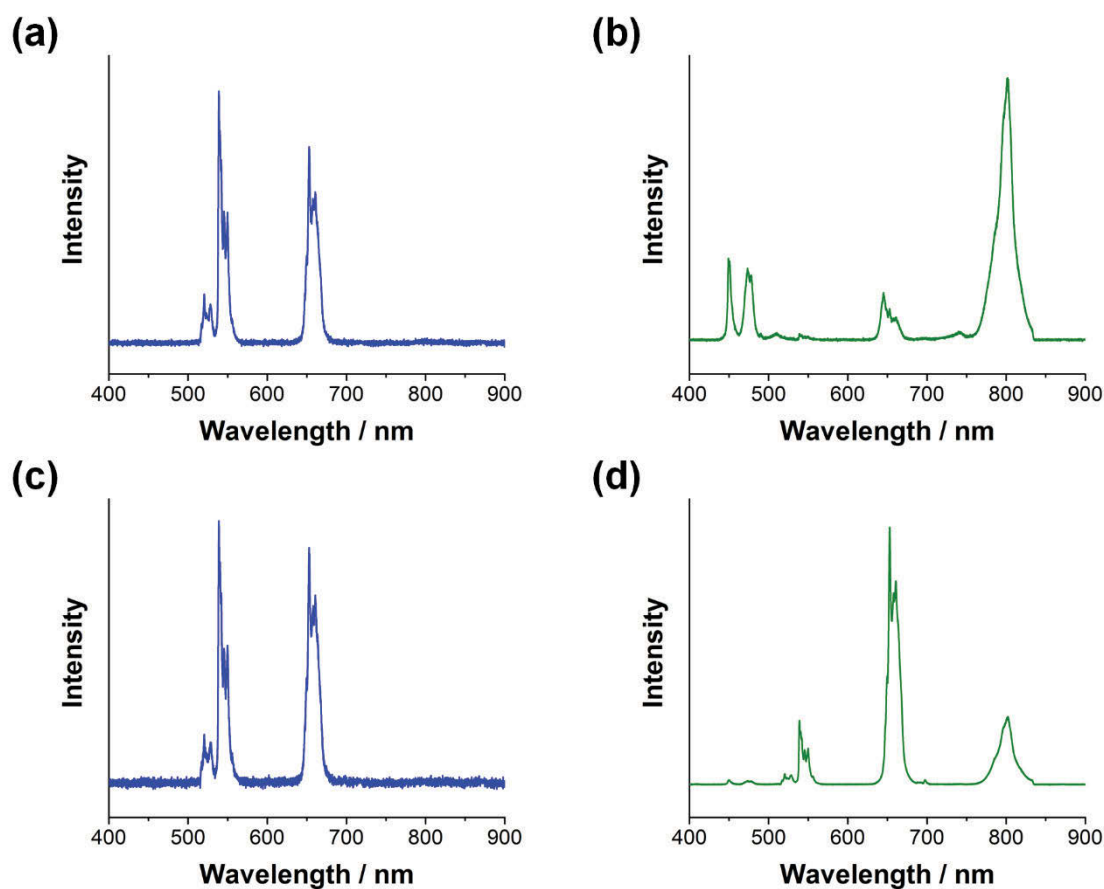
Figure 4-37. Emission spectra of (a) β-CD-SO₃Na-UCNP, (b) β-CD-SO₃Na-UCNP-DOX, (c) β-CD-PO₃Na₂-UCNP, and (d) β-CD-PO₃Na₂-UCNP-DOX.

The TGA curves of CD-COONa-UCNPs and CD-COONa-UCNPs-DOX were shown in **Figure 4-38** and **Figure 4-39**. All of the weight losses are collected from 100 to 650 °C because all the organic parts of the samples have been removed at 650 °C. Compared the weight loss before and after loading DOX, the amount of DOX loading in the samples can be calculated and displayed in **Table 5-3**.
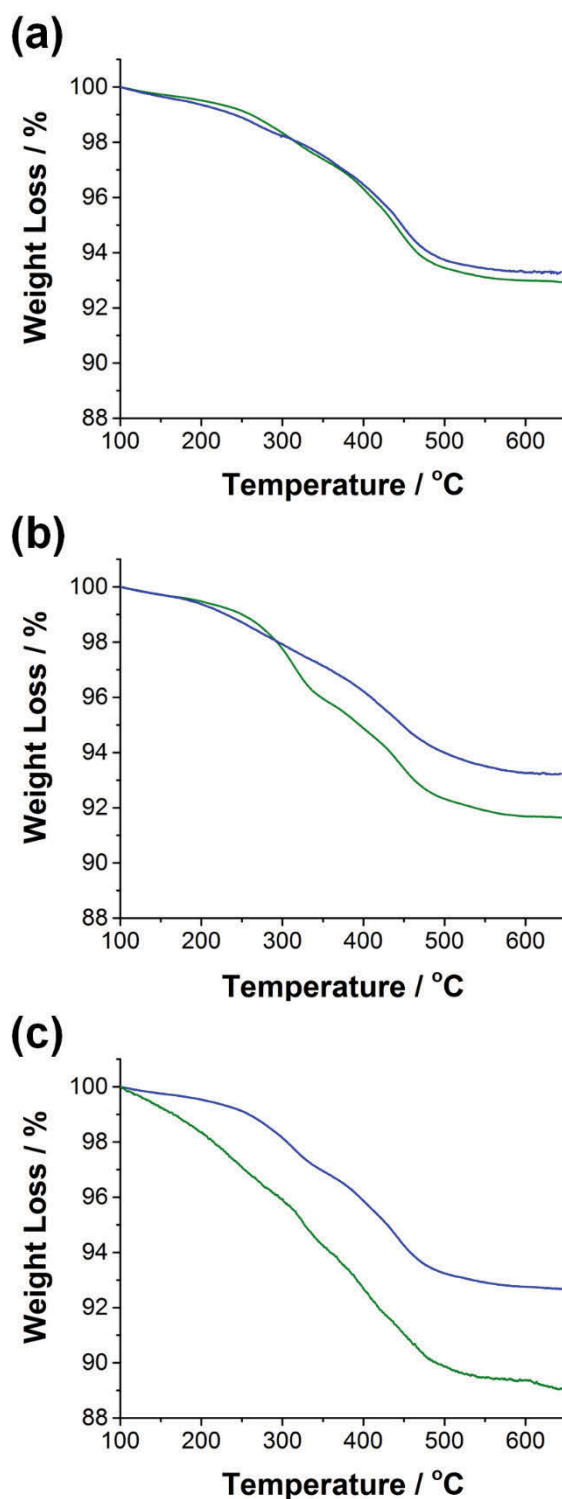
Figure 4-38. TGA curves of (a) α-CD-COONa-UCNP and α-CD-COONa-UCNP-DOX, (b) β-CD-COONa-UCNP and β-CD-COONa-UCNP-DOX, and (c) γ-CD-COONa-UCNP and γ-CD-COONa-UCNP-DOX.
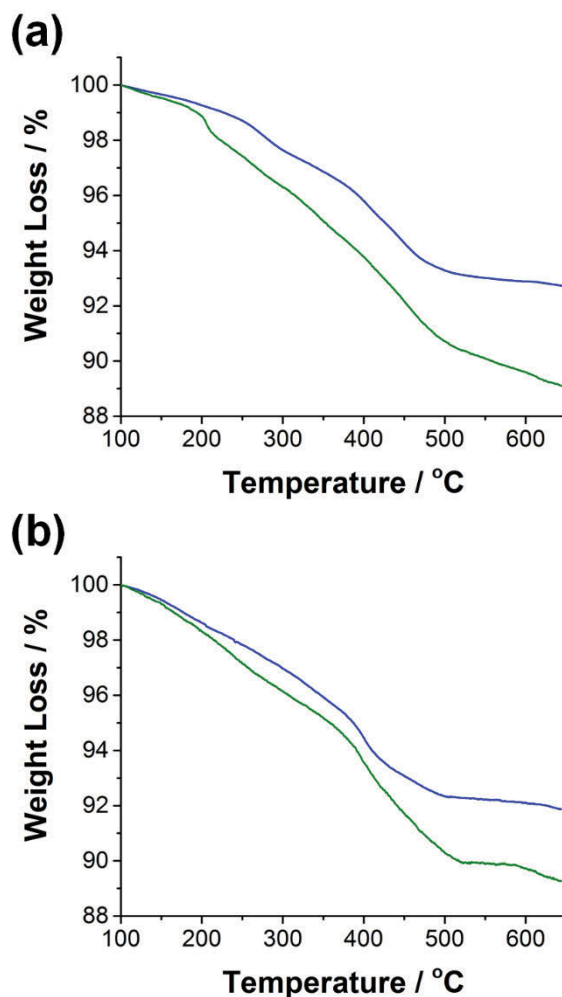
Figure 4-39. TGA curves of (a) β-CD-SO₃Na-UCNP and β-CD-SO₃Na-UCNP-DOX, and (b) β-CD-PO₃Na₂-UCNP and β-CD-PO₃Na₂-UCNP-DOX.

According to the loading amount, γ-CD-COONa-UCNP and β-CD-SO₃Na-UCNP show the excellent binding properties. Because smaller α-CD could not form the host-guest interaction with DOX, only a few DOX molecules could attach on the surface of UCNPs without any specific binding. The result matches the binding constants from the ITC, which further proves higher binding can load more DOX molecules on the surface of UCNPs. All the details are shown in **Table 4-3**.

Table 4-3. Weight loss of CD-UCNPs before and after loading DOX and the loading efficiency.

Sample Names	Before Loading	After Loading	DOX Loading Amount
α-CD-COONa-UCNP	93.31%	92.94%	0.37%
β-CD-COONa-UCNP	93.24%	91.64%	1.60%
γ-CD-COONa-UCNP	92.68%	89.08%	3.60%
β-CD-SO$_3$Na-UCNP	92.73%	89.10%	3.63%
β-CD-PO$_3$Na$_2$-UCNP	91.87%	89.27%	2.60%

4.3.6 Drug Release Studies.

The drug release behaviour from CD-UCNPs was carried out at different temperatures: room temperature (25 °C) and 37 °C (**Figure 4-40 ~ Figure 4-41**). The mechanism of the binding drug on the surface of nanoparticles was based on host-guest interaction (more details in **Chapter 1**). The hydrophobic part of DOX can insert into the cavities of CDs (Neacsu 2018; Soriano et al. 2018). However, the temperature could influence the binding strength, because the binding is thermodynamic (Bouteiller 2011; Fuller et al. 2013; Lin, Li & Li 2012; Munkhbat et al. 2016). The higher the temperature is, the weaker the binding constant is. These samples are located into constant temperature shaker. The DOX concentrations in these samples are investigated by UV-*vis* absorption spectra. After 24h, only less than 10 % of DOX molecules release from UCNPs. It proves the strong binding between DOX and CDs on the surface of nanoparticles. Although DOX molecules are attached to the surface of nanoparticles, the biological ability is still available (Saraswathy & Gong 2014; Wang, Li, et al. 2015). So UCNPs can easily take

DOX into the cell without pre-release. After coming into the cell, UCNPs can even track

them in the cell.
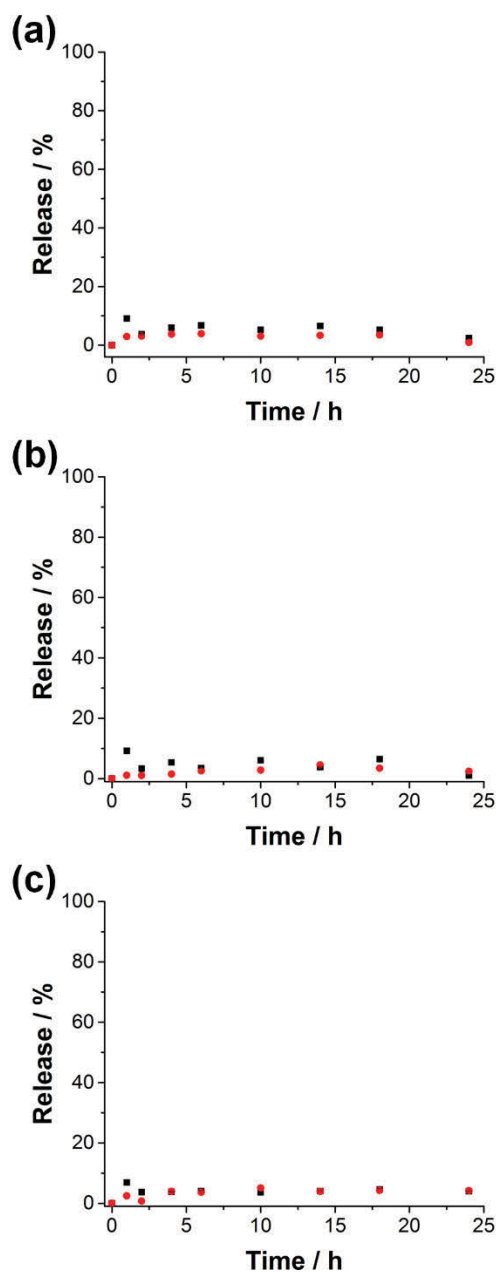
Figure 4-40. Release profiles of DOX from (a) α-CD-COONa-UCNP-DOX, (b) β-CD-COONa-UCNP-DOX, and (c) γ-CD-COONa-UCNP-DOX. The DOX concentration in the solution is carried out by UV-vis spectra and monitored via NanoDrop 2000. The detection wavelength is 498 nm.
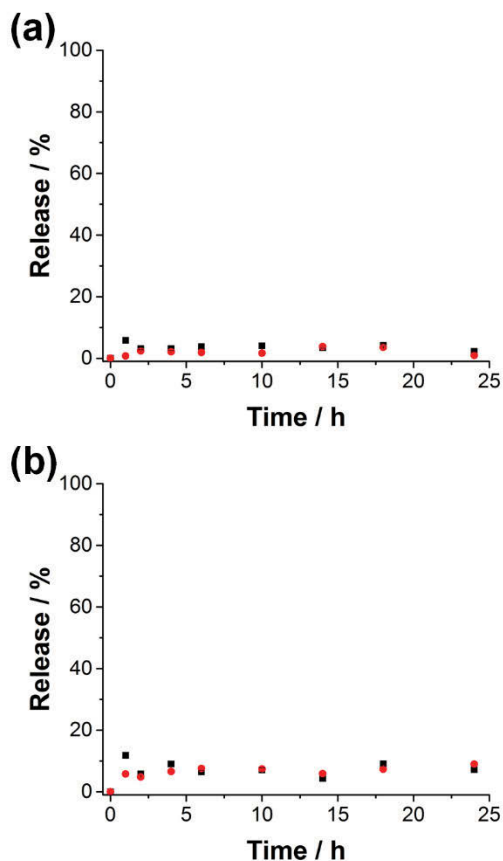
Figure 4-41. Release profiles of DOX from (a) β-CD-SO₃Na-UCNP-DOX, and (b) β-CD-PO₃Na₂-UCNP-DOX. The DOX concentrations in the solutions of these samples are monitored by UV-vis spectra *via* NanoDrop 2000. The detection wavelength is 498 nm.

4.3.7 Cytotoxicity

Figure 4-42 showed that the cell viability decreased with an increasing concentration of CD-UCNPs. Although at a very high level (400 μg/mL), cells still kept good viability (more than 70%). It means that CD-UCNPs process excellent biocompatibility and suitable for disease detection in the future.
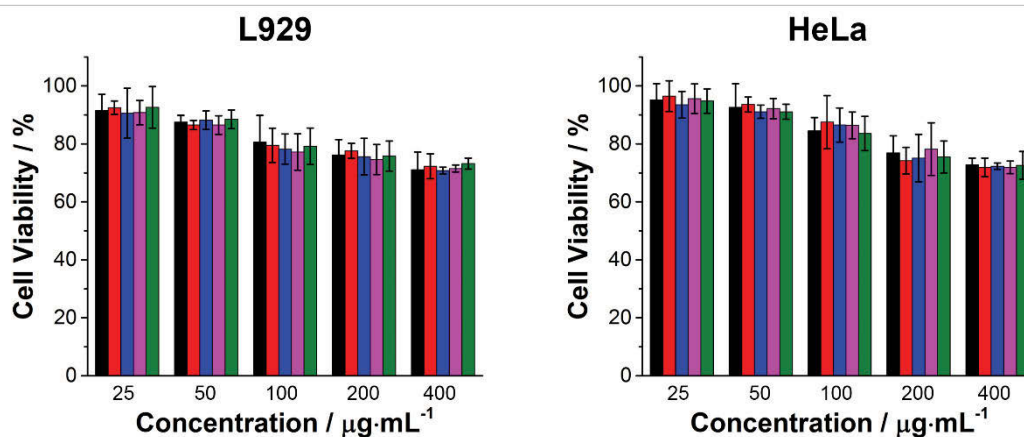
Figure 4-42. *In vitro* **cell-growth inhibition assay for L929 cell line (A) and HaLA cell line (B) obtained by adding α-CD-COONa-UCNP (black), β-CD-COONa-UCNP (red), γ-CD-COONa-UCNP (blue), β-CD-SO₃Na-UCNP (pink), and β-CD-PO₄Na₂-UCNP (green).**

4.3.8 Bioavailability of DOX.

When the drug molecules approach the cell, the first step is to cross the cell membrane. The common method is Passive Diffusion which depends on the drug's concentration differences and hydrophilicity. Compared with the cross method of drug molecules, nanoparticles show several advantages of getting into a cell. First of all, nanoparticle could prefer sticking on the surface of cancer cells because of the EPR effect. Besides, the cell surface can form clathrin, which can easily uptake these nanoparticles into the cell. By using host-guest interactions, we conjugated DOX on the surface of UCNPs. The DOX on the surface will come into the cell at the same time during the endocytosis and semi-endocytosis of nanoparticles. More DOX molecules will come into the cell to increase the bioavailability of DOX.

To determine whether the CD-UCNPs are able to transport the anticancer drugs into the cancer cells and also increase therapeutic actions, a solution of CD-UCNPs-DOX in the cell culture medium has been used to cultivate L929 (**Figure 4-43a**) and HeLa cells

(**Figure 4-43b**). An MTT assay was used for quantitative testing of the viability of cells for CD-UCNPs-DOX. The cell viability decreased with an increasing concentration of DOX. **Figure 4-43** showed CD-UCNPs were fully biocompetitive at the concentration of 16 μg/mL. Compared with pure DOX solution, the CD-UCNPs-DOX showed a higher bioavailability of DOX. Because the materials brought more DOX molecules into the cells.
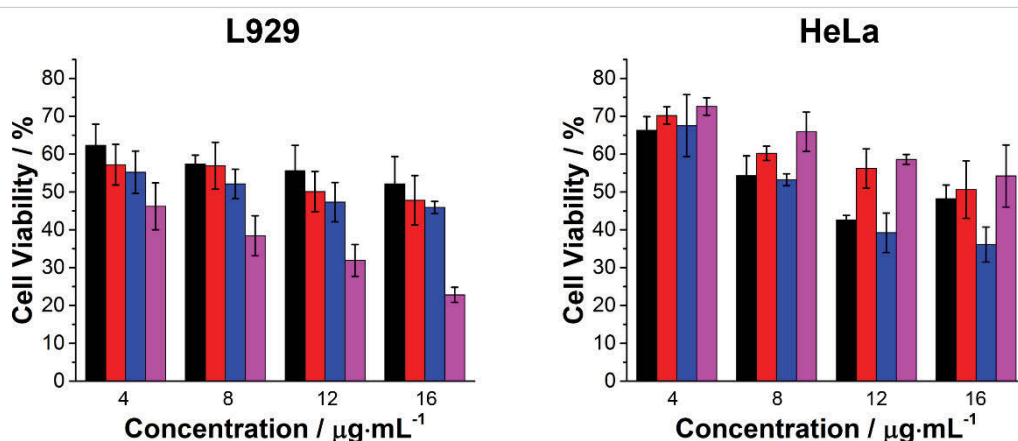
Figure 4-43. *In vitro* **cell-growth inhibition assay for L929 cell line (A) and HeLA cell line (B) obtained by adding γ-CD-COONa-UCNP-DOX (black), β-CD-SO₃Na-UCNP-DOX (red), β-CD-PO₄Na₂-UCNP-DOX (blue) and DOX (pink).**

4.4 Conclusions

In summary, hydrophobic OA stabilized UCNPs have been successfully converted into hydrophilic surface *via* one-step ligand exchange with CDs. Five types of functional CDs were chosen and used according to the binding behaviour of different organic functional groups and the arrangement of functional groups in a molecule. Due to the different structure size and chemical groups, these results show different types of binding behaviour. Furtherly, the conjugation is investigated by using DOX molecules as an example in this chapter. Because of different binding constants between DOX with different CDs, γ-CD-COONa, β-CD-SO₃Na, β-CD-PO₃Na₂ modified UCNPs show the

excellent binding behaviours. However, it doesn't mean that α-CD-COONa and β-CD-COONa modified UCNPs do not process the good binding ability. If the model drug is smaller molecules, they could show better binding ability than others. More importantly, we test the toxicity of these materials and the bioavailability of DOX after binding on the surface of nanoparticles. These results show that these materials we synthesized process low toxicity and enhance the bioavailability of DOX.

5 SELF-ASSEMBLY INDUCED PROTEIN CONJUGATION OF UPCONVERSION NANOPARTICLES FOR CELL TARGET IMAGING

This chapter is based on the research described in the following publication:

Chem. Commun. **2018**, *54*, 3851-3854.

5.1 Introduction

In this chapter, we report another macrocyclic integrated approach to convert the hydrophobicity of UCNPs (OA-UCNPs) into hydrophilic by interfacial ligand-exchange (**Figure 5-1**). The conjugation method is also based on the host-guest self-assembly. Cucurbit[7]uril (CB[7]) has been chosen in this chapter as the host molecule to efficiently replace the surfactant molecules of OA (Barrow et al. 2015; Lagona et al. 2005; Masson et al. 2012) and form CB[7] stabilized UCNPs (CB-UCNPs). The glycoluril molecular structure (**Figure 5-1**) in CB[7] forms the circular wall frame of the ring, and the seven ketones with high electronegativity sit on the top and bottom of the ring structure to form the molecular host structure (Kim et al. 2000). This unique structure renders CB[7] to easily entirely replace OA due to the C=O of the urea functional group that can form resonance delocalized of N lone pair electrons to form polar interactions on both edges of the CB[7] molecular ring. Either one of these edges can undergo selective self-assembly on the surface of UCNP as indicated in **Figure 5-1**. The molecular architecture of CB[7] comprises a hydrophobic host-environment which allow for host-gest recognition of non-polar guest molecules such as adamantane. This approach can achieve successful ligand-exchange without acid washing. The same as CDs in **Chapter 4**, one of the main benefits of using CB[7] over polymer molecules is that it can avoid particle aggregation. Moreover, this will allow for selective and controlled self-assembly of biomolecules onto the surface of UCNP *via* the CB[7] host-guest inclusion of a specific non-polar guest appended-molecule such as adamantane (**Figure 5-1**) without the need of an organic reaction. This modular approach to the construction of bioconjugated UCNPs can overcome the difficulty often encountered with the attachment of biomolecules and allows for a broad range of structural biomolecules that can be applied.(Barrow et al. 2015) As the cavity of CB[7] is directly perpendicular to the particle surface (Frances-Soriano, Gonzalez-Bejar & Perez-Prieto 2015), during self-

assembly, the biomolecules will align and radiate outward on the surface of UCNP due to the positive surface charge.

As mentioned above, the water-soluble CB-UCNPs provide numbers of cavities which can bind with biomolecules by supramolecular host-guest self-assembly. Most of the biomolecules can assemble on the CB-UCNPs as long as the molecule has

1) a positive charge portion (charge transfer with upper ketones) and/or

2) a hydrophobic portion (hydrophobic interaction with hydrophobic cavities).(Urbach & Ramalingam 2011)

If the biomolecule lacked both of the required properties, or if its active sites are neither positive nor hydrophobic, then the biomolecules can be modified by simple organic reactions which will allow it to bind into the cavities.
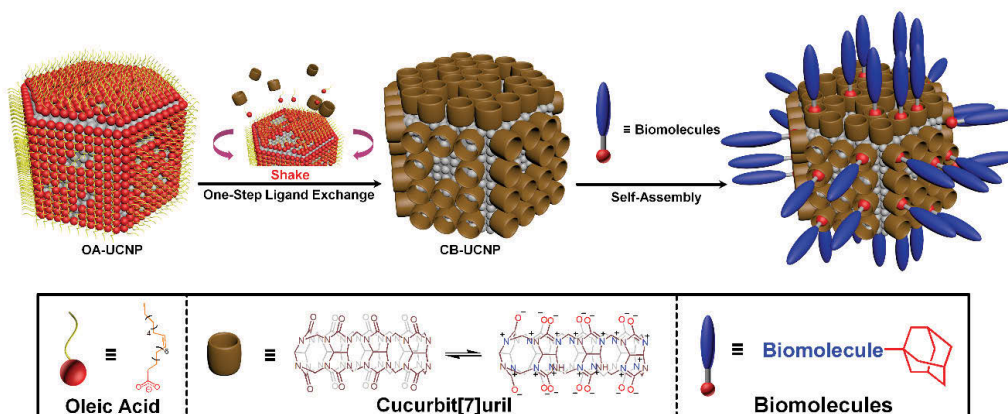
Figure 5-1. CB[7]-based one-step hydrophilic ligand exchange approach without reaction conjugation by host-guest self-assembly.

5.2 Experimental Section

5.2.1 Materials

All the chemicals and reagents: 1-adamantanecarboxylic acid, 2-(4-Amidinophenyl)-6-indolecarbamidine dihydrochloride (DAPI), 3,4-dihydroxylydrocinnamic acid, BCA

Assay Kit, Bovine Serum Albumin (BSA), Dulbecco's Modified Eagle's Medium - high glucose (DMEM), EtOH, Fetal Bovine Serum (FBS), Immunoglobulin G (IgG), DMSO, MES buffer, N-(3-Dimethylaminopropyl)-N′-ethylcarbodiimide hydrochloride (EDC), Paraformaldehyde, PBS buffer, Phalloidin-Fluorescein Isothiocyanate Labelled (Phalloidin-FITC), MTT, Thulium (III) Chloride, Tetrahydrofuran (THF), Triton^{TM} X-100, NaOH were purchased from Sigma-Aldrich & Chem Supply and used as received. Unless otherwise noted, all reactions were performed under nitrogen atmosphere and in dry solvents. CB[7] was synthesised according to a procedure reported by Day (Day et al. 2001) and Kim (Kim et al. 2000). The purification process of CB[7] is shown in **Figure 5-2** after synthesis.
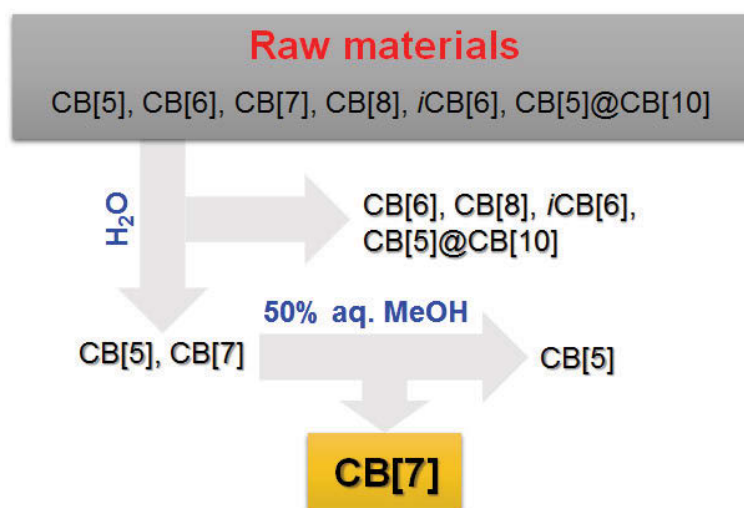
Figure 5-2. Purification of CB[7].

5.2.2 Methods

5.2.2.1 TEM images

TEM images were collected on an FEI-Tecnai T20 instrument, employing an accelerating voltage of 200 kV.

5.2.2.2 FT-IR Spectra

FT-IR spectra were recorded on a Nicolet 6700 spectrometer (ATR Method).

5.2.2.3 TGA and DTGA

TGA was carried on a Simultaneous TG-DTA instrument S600 with a heating program
consisting of a heating rate of 10 K/min from 373.15K to 1273.15 K under N_2.

5.2.2.4 NMR Spectra

NMR Spectra were recorded on an Agilent 500 MHz NMR spectrometer.

5.2.2.5 XRD

XRD measurements were carried out using a Bruker D8 Discover diffractometer. The
radiation source was copper ($K\alpha = 1.39225$ Å).

5.2.2.6 Particle size

Particle size (DLS) was obtained using Zetasizer Nano.

5.2.2.7 XPS

XPS was tested by Thermo ESCALAB250Xi X-ray photoelectron spectrometer. The scan
number of XPS is 20 times, and the spot size is 500 μm.

5.2.2.8 Emission Spectra

Emission Spectra were carried out by our set-up instrument, which is shown in **Figure 3-
3** of **Chapter 3**.

5.2.2.9 BCA test

The concentration of protein was examined by BCA Protein Assay Kit.

5.2.3 Synthesis and Preparation

5.2.3.1 Synthesis of UCNPs (NaYF4: 20% Yb, 2% Er).

The user-friendly synthesis method of the OA-UCNPs (NaYF$_4$: 20%Yb^{3+} / 2% Er^{3+}) was shown in **Chpater 3**.

5.2.3.2 One-Step Ligand Exchange Synthesis of CB-UCNPs.

The CB-UCNPs were synthesized according to the modified method (CD-UCNPs) in **Chapter 4**.

5.2.3.3 Preparation of Direct Carboxyl-Modified UCNPs (UCNPs-COOH).

The UCNPs-COOH were synthesised according to the research article of Tan (Liu et al. 2015). 3,4-dihydroxylydrocinnamic acid (50 mg) was dissolved in 5 mL of THF and mixed with the solution of OA-UCNPs (15 mg, in 2 mL of THF). The reaction was incubated for 5 h at 50 °C. After the reaction, 200 μL of NaOH solution (0.5 mol/L) was added into the mixture to obtain the precipitate, which was collected by centrifuge and redispersed in H$_2$O.

5.2.3.4 EDC amide Coupling of IgG with UCNPs-COOH.

UCNPs-COOH, (100 μg) was dispersed in 500 μL of H$_2$O. Meanwhile, 1.0 mg IgG powder was dissolved in 500 μL of MES buffer and mixed with UCNPs-COOH solution. Then, EDC (2.5 mg) was added to the mixture. The reaction was stirred at 4 °C overnight. The sample was collected by centrifuge (13,000 rpm, 30 min). The precipitate was washed with H$_2$O.

5.2.3.5 Protein (IgG) Modification.

- **Synthesis of Sodium 1-adamantanecarboxylate (SA)**
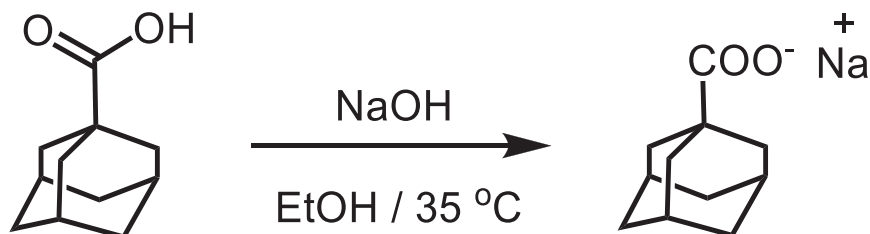
Figure 5-3. Synthesis of SA.

200 mg of 1-adamantanecarboxylic acid was dissolved in EtOH (5 mL), and 44.4 mg of NaOH was dissolved in EtOH (5 mL). Both two EtOH solutions were mixed and stirred at 35 °C overnight. The solvent was removed by vacuum to get white powder. The yield is 95.5 %. ^{1}H NMR (500 MHz, 25 °C, D$_2$O) δ 1.57 (q, 6H), 1.67 (d, 6H), 1.84 (s, 3H). ^{13}C NMR (125 MHz, 25 °C, D$_2$O) δ 30.72, 38.86, 42.12, 44.80, 190.96. FT-IR (ATR): 2901, 2847, 1540, 1450, 1400, 760, 677 cm^{-1}. These spectra are shown in **Figure 5-4 ~ Figure 5-6**.
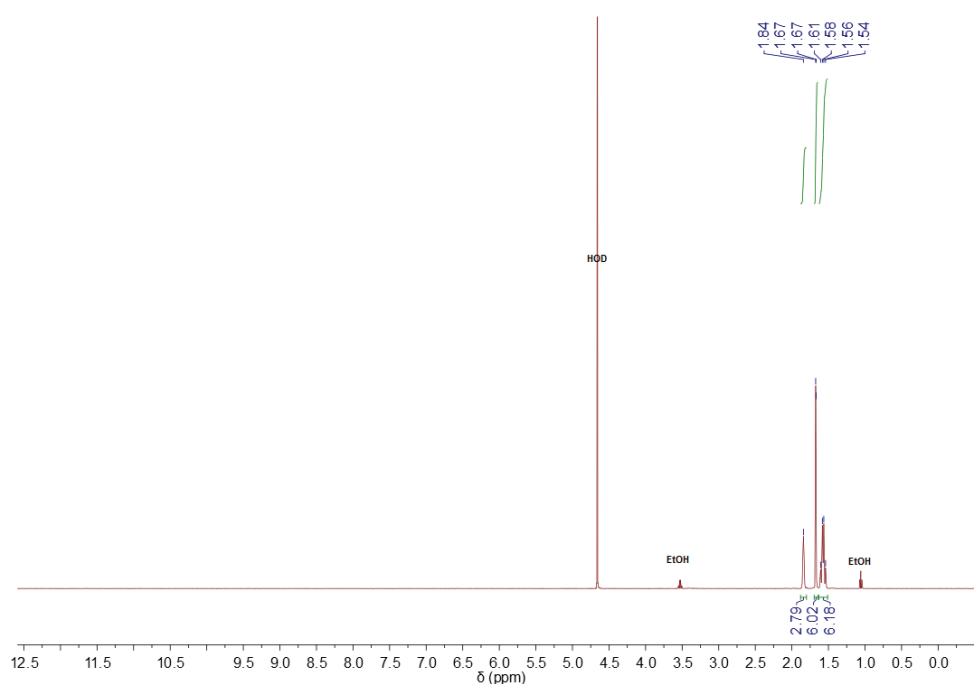
Figure 5-4. ^{1}H NMR spectrum of SA in D$_2$O at 25ºC (500 MHz).
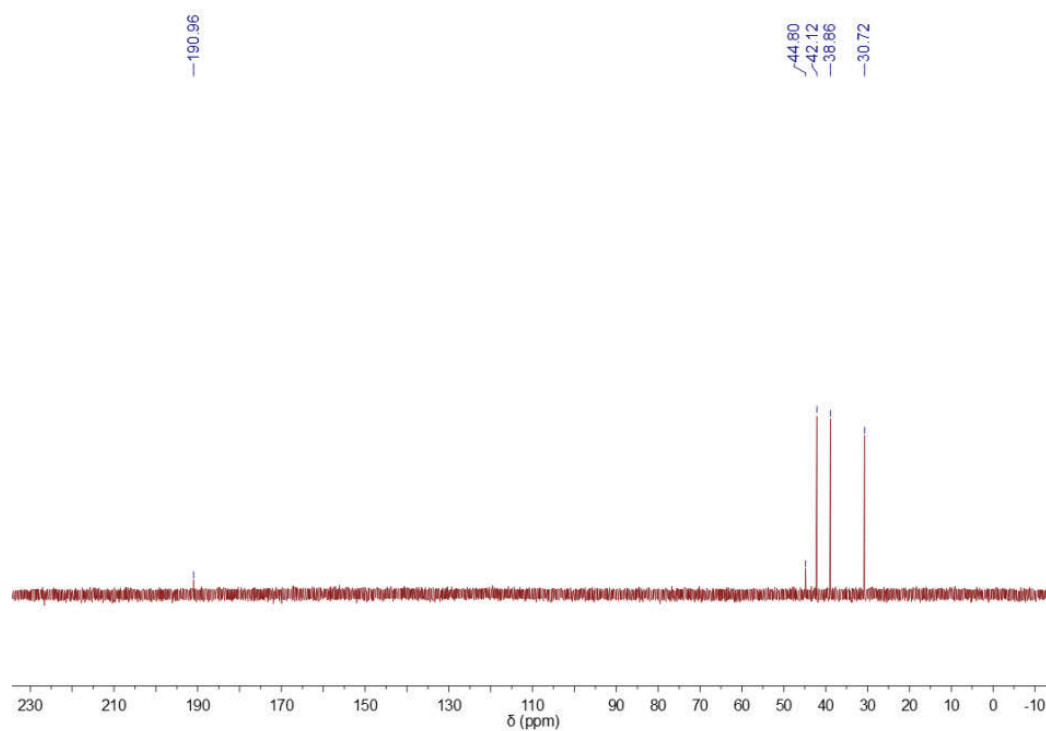
Figure 5-5. ^{13}C NMR spectrum of SA in D$_2$O at 25°C (125 MHz).
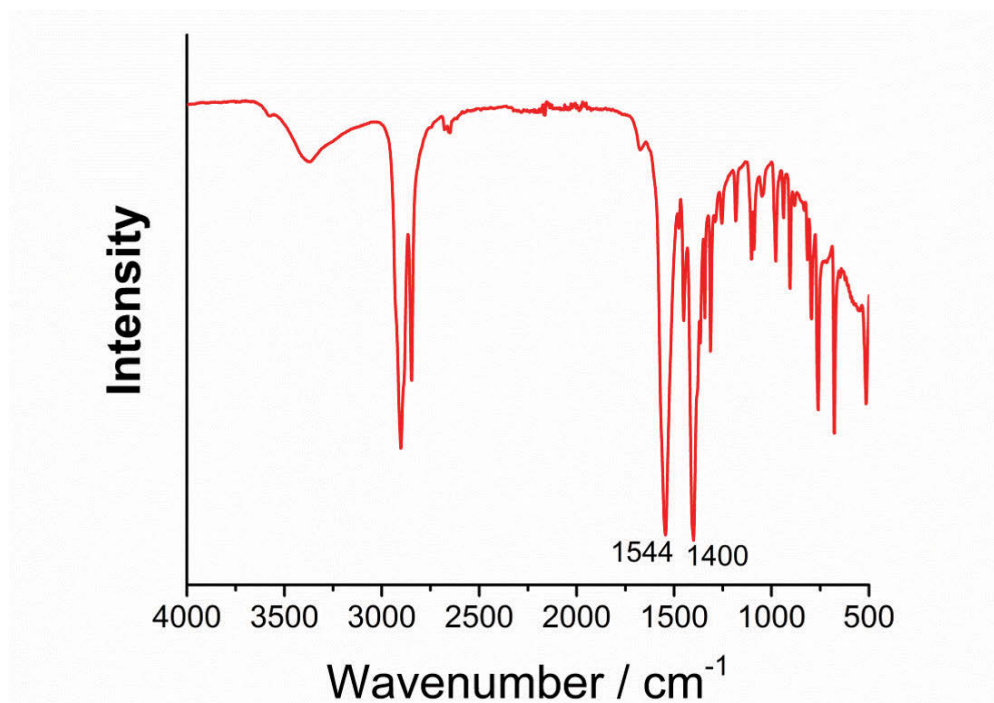
Figure 5-6. FT-IT spectrum of SA.

- **Synthesis of N-1-adamantanecarboxyl-IgG (IgG-ADC).**

The procedure for the synthesis of IgG-ADC is according to the modified process of Fragoso's report (Fragoso et al. 2002) (**Figure 5-7**). The mixture including 1 mg IgG powder (Mw = 150,000), 5 mg of SA and 2.5 mg of EDC was dissolved in 5 mL of 50 mM PBS buffer (pH 6). The reaction was stirred overnight at 4-5 °C. The solution was concentrated and separated by a centrifugal filter. Due to the high concentration of SA and EDC, few positions, like lysine residues, may also be modified with ADC.
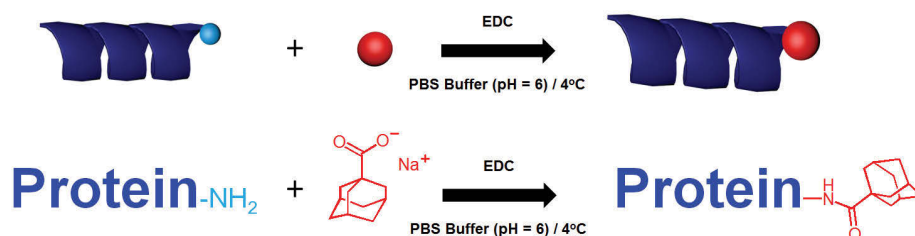
Figure 5-7. Synthesis of 1-adamantanecarboxylate-modified IgG.

5.2.3.6 Self-assembly of IgG-ADC on the surface of CB-UCNPs (CB-UCNP@IgG-ADC).

The mixture of CB-UCNP (0.1 mg) and IgG-ADC (1 mg) was incubated in a suitable buffer and stirred at 4 °C for 24h. The mixture was centrifuged at 14,000 rpm for 5 mins at 4°C. The participates were washed with the same buffer and centrifuged again. The sample was dispersed in a buffer for further test.

5.2.3.7 Conjugation Amount Test.

The protein concentration of CB-UCNP@IgG-ADC was tested according to the protocol from Thermo Scientific.

https://www.thermofisher.com/order/catalog/product/23225

5.2.3.8 Conjugation Rate of Self-Assembly.

The process of self-assembly is shown above. The samples were collected at the different time pots. The concentration of protein at various times was tested by BCA protein concentration test. https://www.thermofisher.com/order/catalog/product/23225

5.2.4 Cell Study

5.2.4.1 Cytotoxicity

In vitro cytotoxicity was measured by performing MTT assays on the human cervical cancer HeLa cells. Cells were seeded into a 96-well cell culture plate at 1×10^5/well at 37 °C and 5% CO_2 for 24 h. Different concentrations of CB-UCNPs (25, 50, 100, 200 and 400 µg/mL, diluted in DMEM) were then added to the wells. The cells were subsequently incubated for 24 h at 37 °C under 5% CO_2. After that, MTT (20 µL; 5 mg/mL) was added to each well, and the plate was incubated for an additional 4 h at 37 °C under 5% CO_2. 200 µL DMSO was added to each well after removing media. The optical density OD570 value (Abs.) of each well was measured using a multifunction microplate reader. The following formula was used to calculate the inhibition of cell growth: Cell Viability (%) = (mean of Abs. value of treatment group/mean Abs. value of control) ×100%.

5.2.4.2 Cell culture and immunostaining

The sample we chose for cell imaging is $NaYF_4$: 20% Yb, 0.5% Tm. The synthetic process is similar to the process of $NaYF_4$: 20% Yb, 2% Er. Human cervical cancer HeLa cells were cultured with DMEM supplemented with 10% FBS in a humidified incubator at 37 °C where the CO_2 level was kept constant at 5%. To do immunostaining, 1×10^4 HeLa cells were seeded in a confocal dish and were fixed with 4% paraformaldehyde for 15 minutes at room temperature after washing three times with PBS buffer for 5 minutes per wash. Washing cells with PBS three times, cells were permeabilised for 10 minutes

with PBS containing 0.1% Triton X-100. The cells were then washed three times with PBS and blocked with 1% BSA in PBS for 1h at room temperature. After that, cells were washed three times with PBS and incubated in the diluted primary antibody in 1% BSA in PBS (1:500) in a humidified chamber overnight at 4℃. After three washes with PBS, cells were incubated with the diluted second antibody conjugates with UCNPs at room temperature. DAPI was used to stain nuclear for 24h at room temperature after three washes with PBS. After that, FITC conjugates of phalloidin were diluted with PBS (1:50) and used to label actin filaments in HeLa cells for 20 minutes at room temperature. Washing cell with PBS three times, the sample was used for immunofluorescent imaging.

5.2.4.3 Fluorescence imaging

All single cell imaging in confocal dishes were performed on Olympus IX 83 confocal microscopy. Samples were imaged with 20X objective lens. The DAPI and FITC conjugates of phalloidin were excited with 405 nm laser and 473 nm laser in the confocal microscopy. UCNPs on the cells were excited with 980 nm laser in a wide field with another light path which was inserted into the confocal microscopy. The images of cell and UCNPs were merged with our program.

5.3 Results and Discussion

5.3.1 Materials Characterizations

TGA and DTGA curves were used for verifying the attachment of CB[7] molecules to the surface of UCNPs (**Figure 5-8**) and for determining the best ligand-exchange concentration of CB[7] (**Figure 5-8** and **Figure 5-9**). Detection range for weight loss was between 100 ℃ to 600 ℃, and all the samples showed weight loss below 180 ℃ resulting from the physical loss of free water. In **Figure 5-8**, the loss of 5.7% of the weight from 100 ℃ to 450 ℃ in OA-UCNPs was due to the removal of the OA on the surface of the

UCNPs. However, the weight loss of CB-UCNPs shifted from 400 °C to 550 °C. To determine the optimal concentration of CB[7] for preparing CB-UCNPs, TGA and DTGA result from samples with different concentrations of CB[7] are displayed in **Figure 5-8** and **Figure 5-9**. The weight losses from 350 °C to 550 °C of CB-UCNP with ligand-exchanged with 2 mM, 5 mM and 10 mM concentrations are 24.4%, 49.2% and 65.0 %, respectively. As already shown in **Figure 5-9**, after CB[7] attached to the surface of UCNP, the derivate weight loss peak moves to the higher temperature as free molecules. **Figure 5-9** showed all the main peaks of CB-UCNPs (2 mM, 5 mM, and 10 mM) shift to 488 °C, 491 °C, and 498 °C, respectively. It means that CB[7] molecules were stabilized on the surface of UCNPs. However, another peak in both 5 mM and 10 mM samples was identified at the same position of free CB[7], which proved many free CB[7]s still exist in the system. This will affect the self-assembly behaviour in subsequent experiments, so the 2 mM concentration was selected for all samples in the test of TEM, XPS, FT-IR.
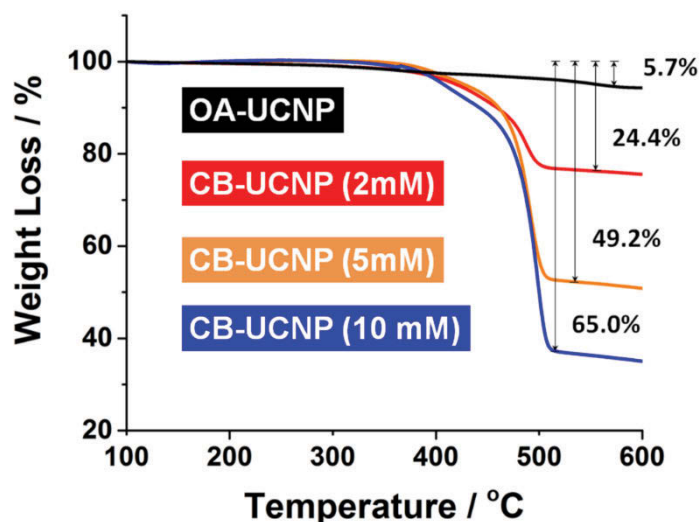
Figure 5-8. TGA curve of CB-UCNP with different concentrations of CB[7], 2 mM (red), 5 mM (orange), 10 mM (blue), compared with OA-UCNP (black).
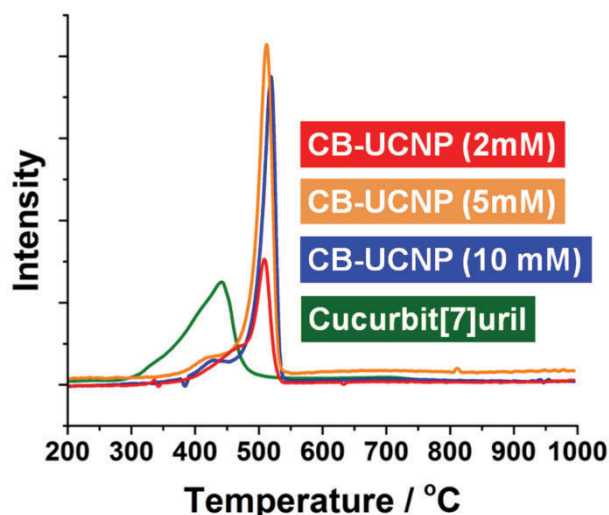
Figure 5-9. DTGA curves of free CB[7] and CB-UCNPs with different concentrations of CB[7], 2 mM (red), 5 mM (orange), 10 mM (blue).

The TEM image of CB-UCNP (**Figure 5-10b**) exhibits a hexagonal morphology, consistent monodispersity and homogeneous size, which is the same as OA-UCNP (**Figure 5-10a**). The image illustrates that one-step ligand exchange retains the morphology of UCNP. The average size of nanoparticles is around 37 nm before and after ligand exchange, according to the distribution of OA-UCNPs and CB-UCNPs which were calculated and displayed in **Figure 5-10c** and **Figure 5-10d**.
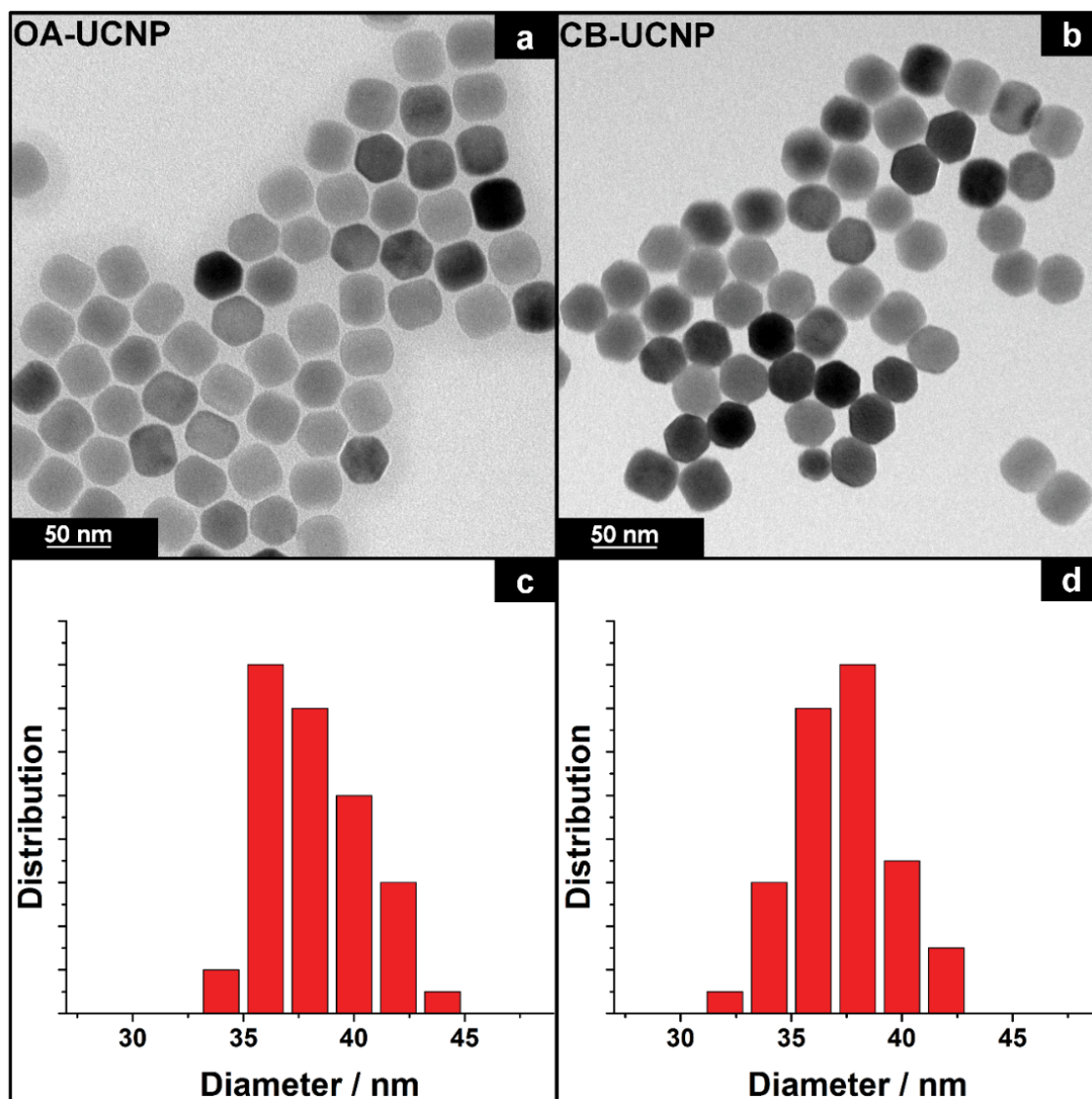
Figure 5-10. The TEM image of (a) OA-UCNPs and (b) CB-UCNPs. The size distribution of (c) OA-UCNPs and (d) CB-UCNPs.

DLS was used to calculate the average size of OA-UCNPs in cyclohexane and CB-UCNPs in water. The average particle size of OA-UCNPs in cyclohexane (**Figure 5-11a**) is ca. 37 nm. The size distribution generated by DLS is a number distribution. After exchanged with CB[7], the average particle effective size of CB-UCNPs was ca. 78 nm (**Figure 5-11b**). It is understandable because the DLS measures the hydraulic diameter of the nanoparticles rather than the actual size. The DLS results would be different for the same batch nanoparticles when they are in a different solvent and with different surface modifications.
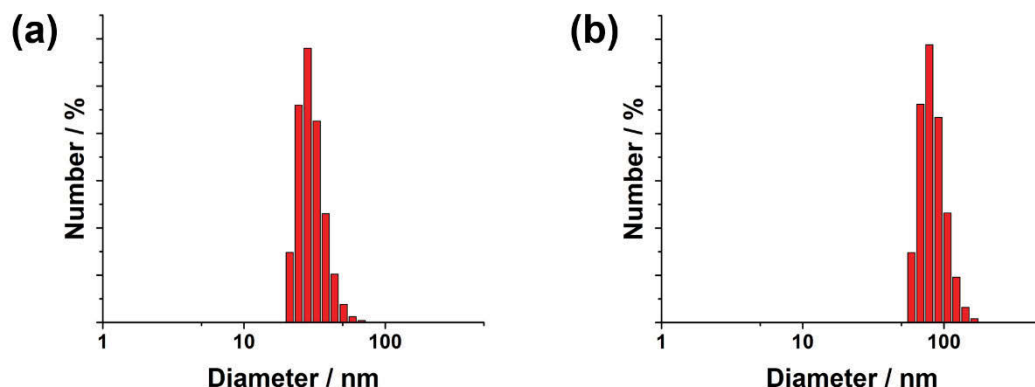
Figure 5-11. The size of OA-UCNPs in cyclohexane (a) and CB-UCNPs in water (b).

Figure 5-12 showed the XRD patterns of CB[7] modified β-NaYF$_4$ nanocrystals co-doped with 2% Er^{3+} and 20 % Yb^{3+} (CB-UCNPs), with the standard XRD patterns of hexagonal phase NaYF$_4$ (JCPDS: 00-016-0334) and NaYbF$_4$ (JCPDS: 00-027-1427). Compared with XRD of OA-UCNP (**Chapter 3**), the XRD Patterns of CB-UCNPs still kept the hexagonal phase after ligand exchange.
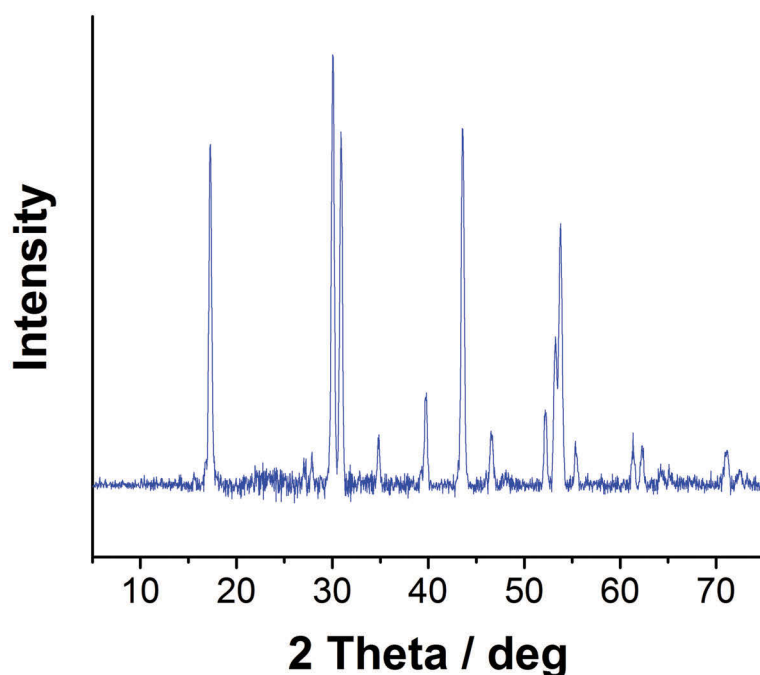
Figure 5-12. The XRD pattern of CB-UCNPs (β-NaYF$_4$: 2%Er^{3+} / 20%Yb^{3+} @CB[7]).

Figure 5-13 shows the XPS to determine the surface properties. Compared with the XPS of OA-UCNPs (blue in **Figure 5-13**), the nitrogen (N 1s) from the glycoluril units in CB[7] was identified in CB-UCNP (green in **Figure 5-13**).

In the O1s region, **Figure 5-14** showed that there are two kinds of oxygens on the surface. However, CB[7] molecule is symmetry, all of the oxygens should be the same. Therefore, it further proves that the CB[7] modified on the surface of UCNPs, because parts of molecules moved to another position.
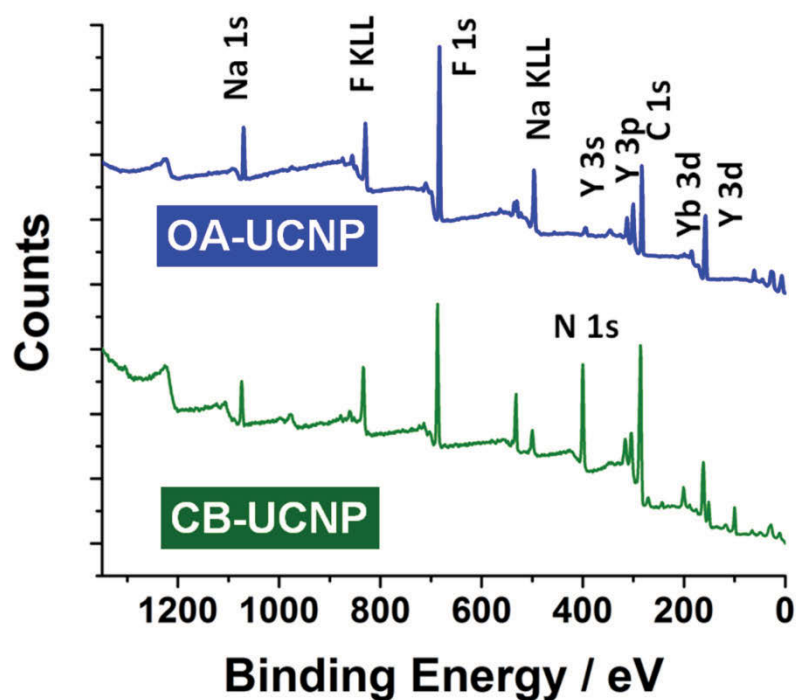
Figure 5-13. XPS Spectra of OA-UCNPs (blue) and CB-UCNPs (green, 2 mM).
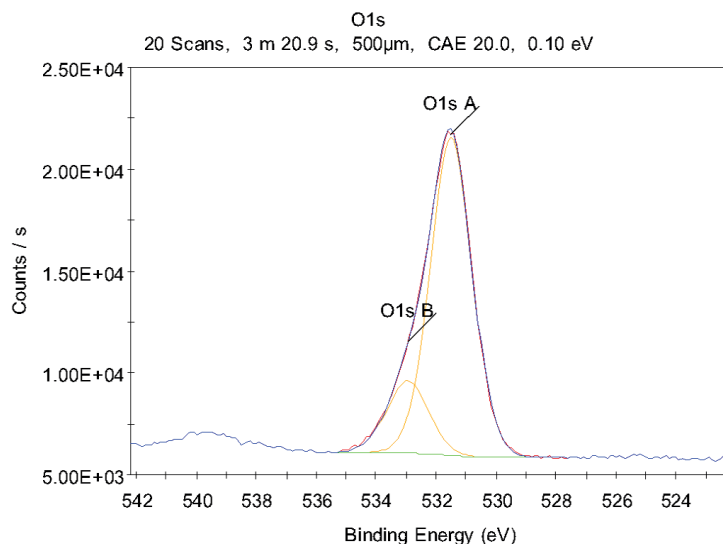
Figure 5-14. XPS Spectrum (O1s) of CB-UCNPs.

In the C1s region, there are three kinds of carbon in free CB[7] after modified on the surface of the nanoparticle (**Figure 5-15**), these peaks were split, because of the effect from the surface of UCNPs.
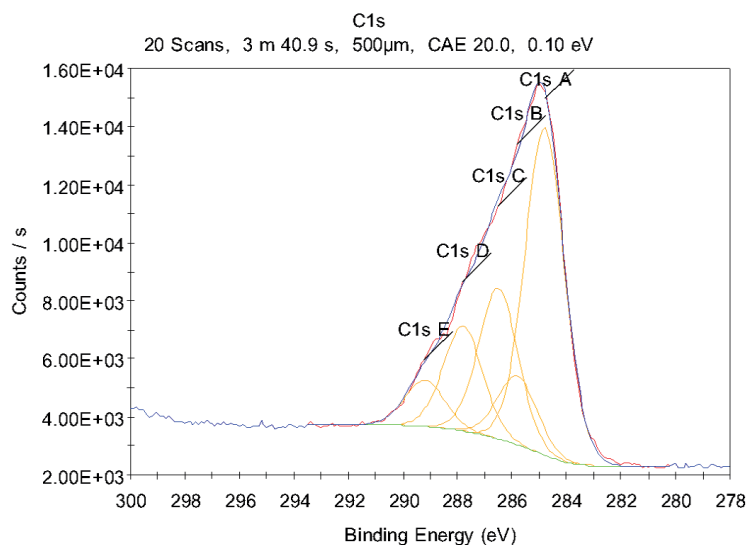
Figure 5-15. XPS Spectrum (C1s) of CB-UCNPs.

After exchanged with CB[7], nitrogen was found as a new element from CB[7] on the surface. In addition, the only one peak from free CB[7] was also split because of the surface of UCNPs.(**Figure 5-16**)
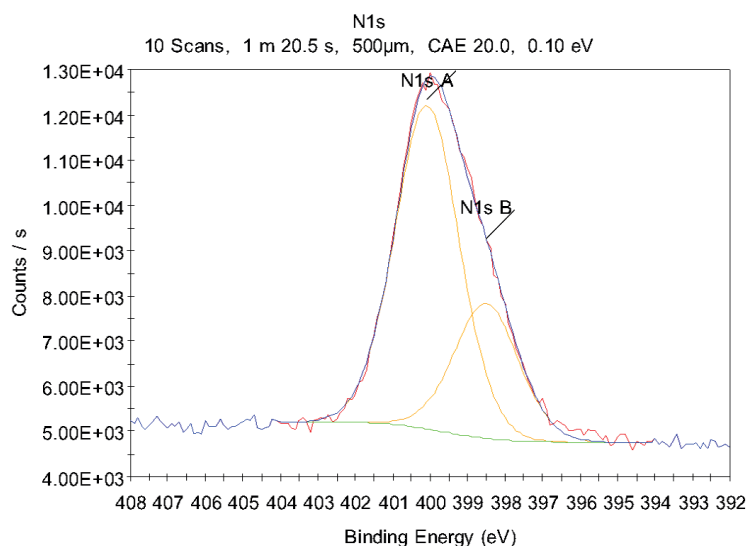
Figure 5-16. XPS Spectrum (N1s) of CB-UCNP.

The emission of CB[7] modified NaYF$_4$ nanocrystal co-doped with 20% Yb and 2% Er was shown in **Figure 5-17**.
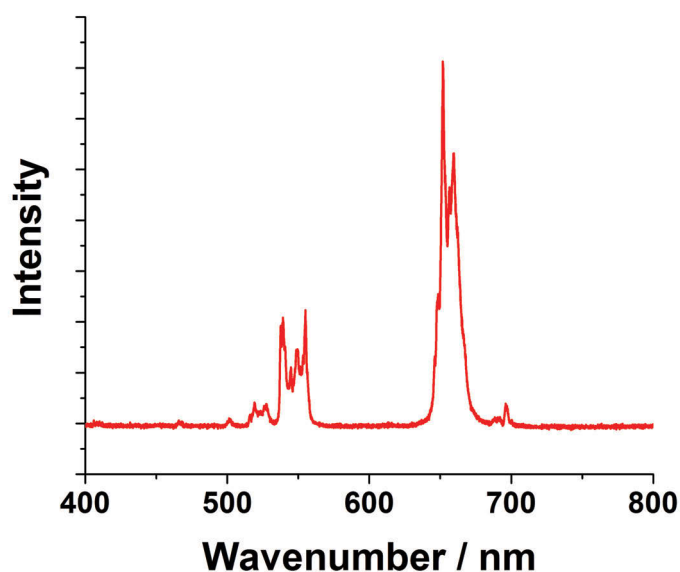
 Figure 5-17. The emission spectrum of CB[7]-functional NaYF$_4$ nanocrystal co-doped with 20% Yb and 2% Er (CB-UCNPs).

^{1}H NMR of CB-UCNPs was shown in **Figure 5-18**. It also proves that CB[7] had already entirely replaced OA from the surface of OA-UCNPs in **Chapter 3**.
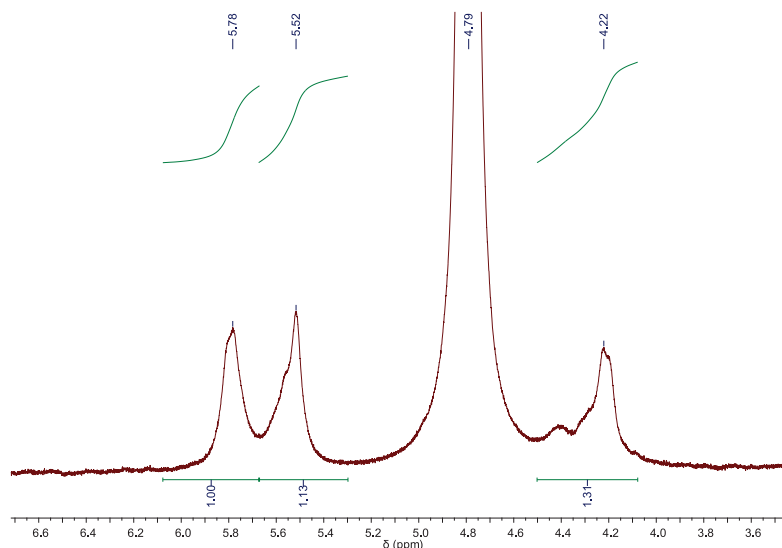
Figure 5-18. ^{1}H NMR Spectrum of CB-UCNPs in D$_2$O at 25 ^{o}C.

FT-IR spectroscopy was also used to investigate the surface of UCNPs. **Figure 5-19** shows the stretching vibration of the carbonyl group in free OA molecules at 1708 cm^{-1}. After being stabilized on the surface of UCNP, the absorption peak shifted and appeared as two bands: at 1547 cm^{-1} (the asymmetric stretching vibration of carbonyl group) and 1461 cm^{-1} (the symmetric stretching vibration of carbonyl group). This indicates that all the acidic terminal groups of OA are carboxylate (-COO-) rather than carboxylic acid (-COOH).It further reinforces our calculation of the optimized binding modes on the surface of UCNPs. After OA was exchanged with CB[7], the stretching vibration of C-H (~3005 cm^{-1}) in *sp^2* carbon of OA was completely absent, proving that the OA on the surface of UCNP has been completely removed. This is further reinforced by the presence of a strong and sharp carbonyl stretching vibration at 1730 cm^{-1}. This band was identified to be the asymmetric stretching vibration of CB[7] (C=O) which was shifted to higher values (~ 15 cm^{-1}) when bound to the surface of UCNP. These changes corroborated the interaction of the CB[7] with the UCNP surface through the carbonyl groups. The higher values suggest a further deviation from the planarity of the carbonyl bond compared with the N–C–N plane when the CB[7] is anchored to the nanoparticle surface which can attribute to a less effective interaction of CB[7] with the surface of the nanoparticle.
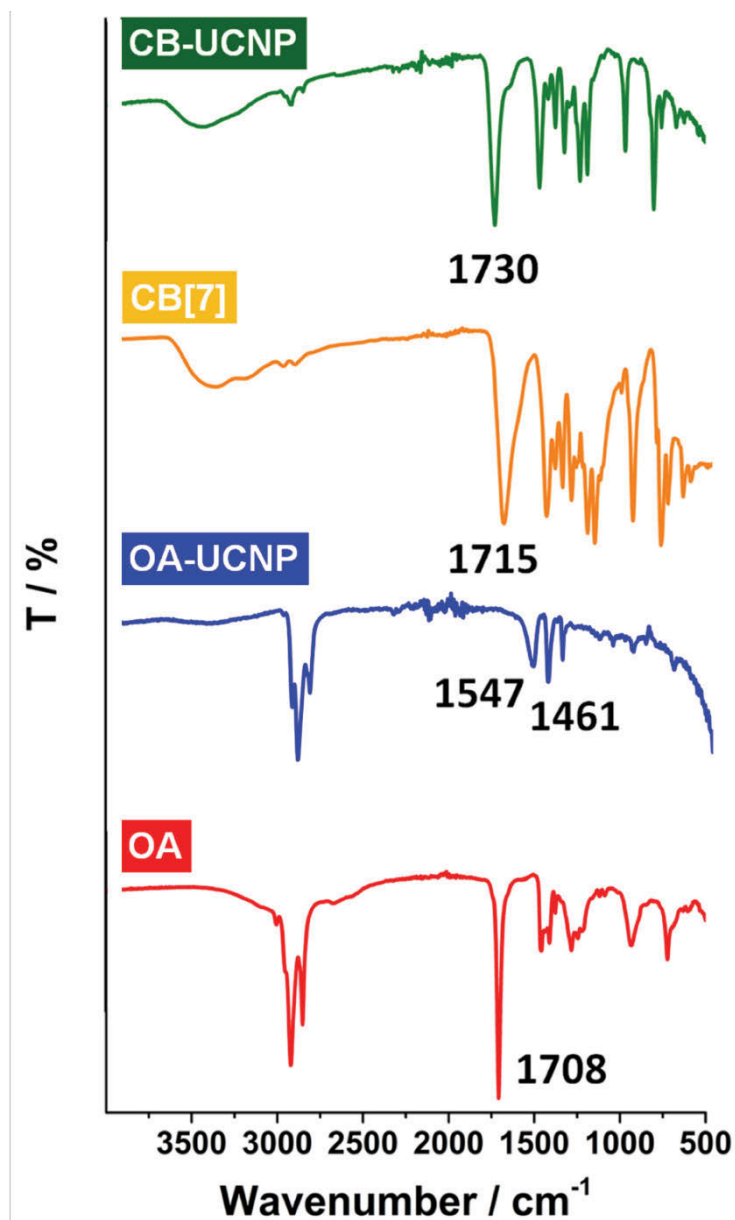
Figure 5-19. FT-IR Spectra: free OA (red), OA-UCNP (blue), free CB[7] (orange) and CB-UCNPs (green, 2 mM).

5.3.2 Binding Behaviours

To evaluate the efficiency of replacement and the binding behaviour of CB-UCNPs, we calculate the binding site and mode of OA-UCNPs (**Chapter 3**) and CB-UCNPs *via* crystallographic analysis. The crystal structure of NaYF$_4$ Based UCNPs is shown in **Chapter 3.**

5.3.2.1 Binding mode of CB[7] on the surface of UCNPs.

The structure of CB[7] is shown in **Figure 5-20**. Both sides of CB[7] have seven ketones, which form a substantial π electronic cloud. Therefore, CB[7] processes very high binding with NaYF$_4$ crystal surface because of charge transfer interactions. The binding mode of CB[7] on the surface of the NaYF$_4$ crystal is shown in **Figure 5-21**.

According to the previous reference(Moeller et al. 1965), the binding constant (log K) of a carboxylic acid with Y atom is from 1.97 to 1.42. About CB-UCNPs, seven ketones from CB[7] bind with three Y atoms. It means more than two ketones share one Y atom. In this situation, the binding constant (log K) of two ketones with one Y atom is 7.19. In addition, the multiple binding sites of CB[7] with Y atoms can increase the binding constant. Therefore, the binding constant of CB[7] with Y atom is much higher than OA.
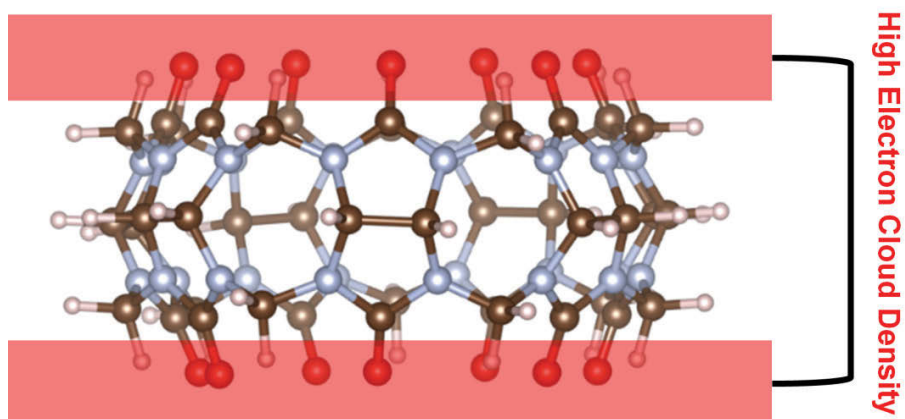
Figure 5-20. The structure of CB[7].
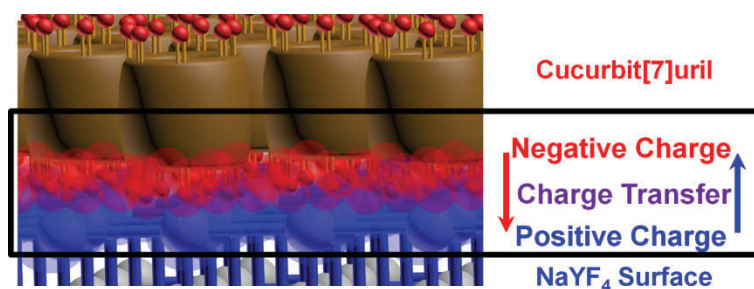
Figure 5-21. The binding mechanism of CB[7] on the surface of NaYF$_4$.

In comparison to the binding mechanics of OA-UCNPs (**Chapter 3**), there is strong charge interaction between the negatively charged edge of CB[7] molecules to the positively charged surface of UCNP. The array of negatively charged oxygen atoms that are aligned to the edges of the CB[7] molecules contribute to the binding, (**Figure 5-22**). Therefore, the binding of CB[7] was calculated to be much stronger than that found between OA and UCNP.
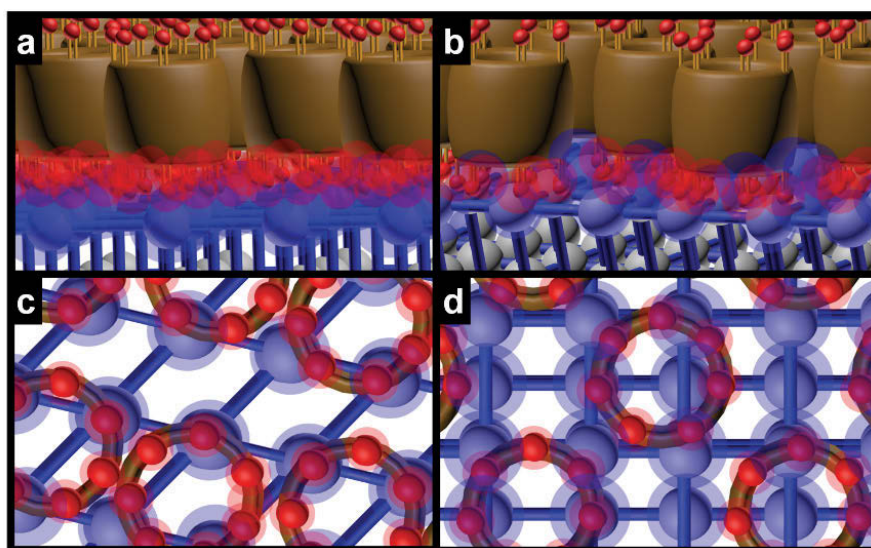
Figure 5-22. Crystallographic analysis of CB-UCNPs: the side view (e) and top view (g) of {001} in CB-UCNPs; the side view (f) and top view (h) of {100} in CB-UCNPs.

5.3.2.2 Quantitative Binding Amount of CB[7] on the surface of UCNPs.

According to the binding mode of CB[7] on the surface of UCNPs, we found each CB[7] molecule can occupy three Yttrium atoms. Therefore, the coverage of CB[7] on the surface of UCNPs is

$$Coverage\ rate = \frac{3 \times the\ amount\ of\ CB\ molecules}{the\ amount\ of\ Yttrium\ atoms\ on\ the\ surface\ of\ UCNPs}\%$$

The process of calculation of CB-UCNPs is similar to the OA one above.

The coverage of OA-UCNPs is 50.1%.

5.3.2.3 The Mechanism and efficiency of one-step ligand exchange modification.

Before exchanged on the surface of OA-UCNPs, the ligands followed dynamic equilibrium according to chemical kinetics. The rate ($K_{falling\ off}$) of molecular falling off from the surface is almost equal to the rate ($K_{binding}$) of molecular binding on the surface at the same time. Both of the rates are practically equal.

$$K_{falling\ off} = K_{binding}$$

After at least 12h shaking, all of the nanoparticles were extracted from cyclohexane layer (**Figure 5-23**). These emission spectra before and after exchange are shown in **Figure 5-24**.

Figure 5-23. Comparison of visible emission between the cyclohexane layer before (a) and after (b) ligand exchange with CB[7] solution under 980 nm laser.
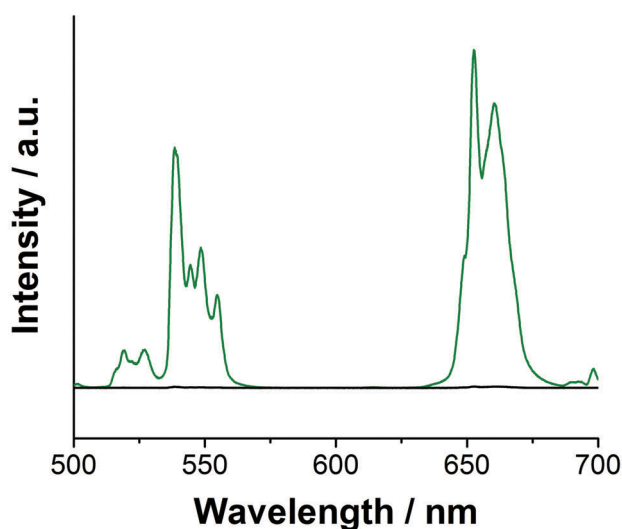
Figure 5-24. The emission spectra of cyclohexane layer: before exchange (green) and after the exchange (black) under 980 nm laser.

5.3.2.4 The Mechanism of Self-assembly.

CB[7] molecules have a non-polar cavity and two polar portals. The fixed negative charge is formed on both sides. Typically, the guests of CB[7] have one of the following properties at least: i). positive charge; ii). hydrophobic; iii). the fitting size.

The amino acids have to bind with CB[7], because of the charge transfer between the cationic amino group and negative portals. The binding constants and test conditions of amino acids were shown in **Figure 5-25** and **Table 5-1**, which values are from 10^1 M^{-1} to 10^6 M^{-1}.(Bailey et al. 2008; Cong et al. 2006; Liu et al. 2005; Rekharsky et al. 2007) However, the highest binding of amino acid (Phe) is still much lower than 1-adamantanecarboxylic acid (3.23×10^8 M^{-1}). According to selective binding theory,(Harada et al. 2011) CB[7] will choose 1-adamantanecarbpxylic acid rather than amino acids in general proteins.
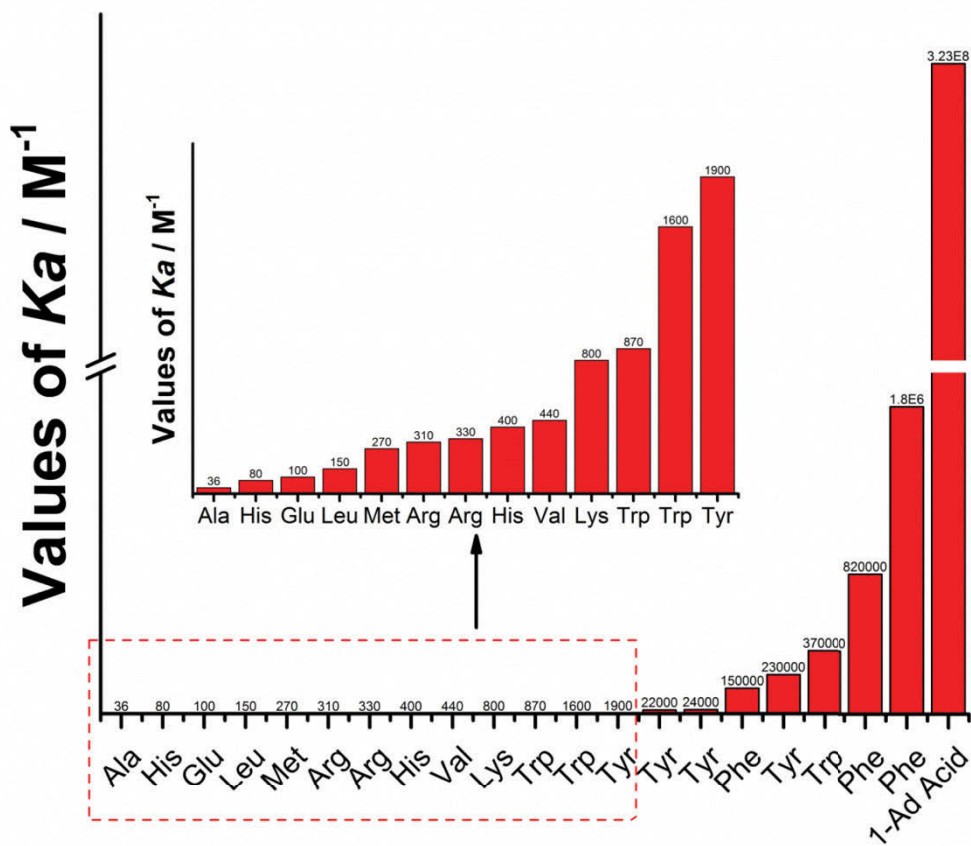
Figure 5-25. Binding contrasts of amino acids and 1-admantanecarboxylic acid with CB[7].

Table 5-1. Binding constants of amino acids and 1-adamantanecarboxylic acid with CB[7].

Guest molecule	K_a (M^{-1})	Method	Conditions	Ref.
Ala	3.6×10	UV titration		(Cong et al. 2006)
His	8.0×10	UV titration		(Cong et al. 2006)
Glu	1.0×10^2	UV titration		(Cong et al. 2006)
Leu	1.5×10^2	UV titration		(Cong et al. 2006)
Met	2.7×10^2	UV titration		(Cong et al. 2006)

Arg	3.1×10^2	Fluorescence titration	10 mM NH₄OAc, pH = 6, 25°C	(Bailey et al. 2008)
Arg	3.3×10^2	ITC	10 mM NH₄OAc, pH = 6, 30°C	(Bailey et al. 2008)
His	4.0×10^2	Fluorescence titration	10 mM NH₄OAc, pH = 6, 25°C	(Bailey et al. 2008)
Val	4.4×10^2	UV titration		(Cao, Villalonga & Fragoso 2005)
Lys	8.0×10^2	ITC	10 mM NH₄OAc, pH = 6, 30°C	(Bailey et al. 2008)
Lys	8.7×10^2	Fluorescence titration	10 mM NH₄OAc, pH = 6, 25°C	(Bailey et al. 2008)
Trp	1.6×10^3	Fluorescence titration	10 mM NH₄OAc, pH = 6, 25°C	(Bailey et al. 2008)
Trp	1.9×10^3	ITC	10 mM NH₄OAc, pH = 6, 30°C	(Bailey et al. 2008)
Tyr	2.2×10^4	ITC	10 mM NH₄OAc, pH = 6, 30°C	(Bailey et al. 2008)
Tyr	2.4×10^4	Fluorescence titration	10 mM NH₄OAc, pH = 6, 25°C	(Bailey et al. 2008)
Tyr	2.3×10^5	UV titration		(Cong et al. 2006)
Trp	3.7×10^5	UV titration		(Cong et al. 2006)
Phe	1.5×10^5	NMR titration	Water, 25 °C	(Liu et al. 2005)
Phe	8.2×10^5	UV titration		(Cong et al. 2006)
Phe	1.8×10^6	ITC	Water, 25 °C	(Rekharsky et al. 2007)
1-Ad Acid	3.23×10^8	NMR		(Liu et al. 2005)

Compared with EDC amide coupling, self-assembly has shown several advantages in bio-conjugation. (Fragoso et al. 2002) Self-assembly is based on intermolecular forces without requiring any organic reaction for conjugation (Lagona et al. 2005). When CB-UCNP was mixed with guest molecules, the guest molecules were shown to undergo host-guest recognition and then attached into the CB-UCNP cavities. Although there is no formation of covalent bond in the process, however, the binding strength is sufficiently strong to form a stable assembly on the surface of the nanoparticles. (Corma et al. 2007) The binding mechanism is shown in **Figure 5-26**.
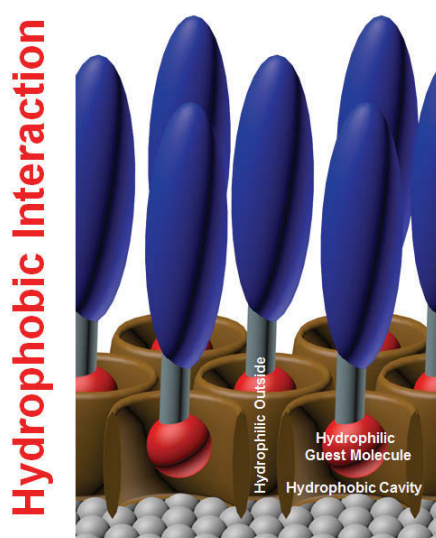
Figure 5-26. Binding Model of Self-Assembly.

Most biological conjugations utilize EDC amide coupling because of the mild reaction conditions.(Totaro et al. 2016) However, the strong positive surface charge of the nanoparticle impedes the reaction process. It is therefore difficult for the biomolecules to get close to the nanoparticle surface due the repulsive force created by the positive charge of the nanoparticle surface. The positive charge could also attract the conjugated molecules to bind directly to the surface resulting in the misalignment of the assembly or even changing the conformation of the biomolecules (Sperling & Parak 2010). To investigate the binding behaviour of the CB-UCNP, IgG conjugate was chosen for this

study. The IgG was coupled with a high binding molecule, 1-adamantane acid, at the N-terminus of the protein via an amide coupling reaction. This creates a biomolecule that contains a small guest-molecule, ADC, which strategically appended at the N-terminus of the protein to form IgG-ADC. The ADC moiety is designed to anchor to the surface of CB-UCNP via the host-guest inclusion complex. This structural design would reduce the undesired interactions of the biomolecules with each other or to the surface of UCNP. This approach would encourage the self-assembly of the biomolecules in an organized fashion.

5.3.2.5 Conjugation Amount Test.

The IgG-ADC would be expected to self-assemble on the surface of CB-UCNPs to form CB-UCNP@IgG-ADC after mixing with the CB-UCNP solution. In comparison to the EDC binding that used 10 times more of IgG concentration than IgG-ADC, the binding efficiency of self-assembly of IgG-ADC is more than twice as that of EDC amide coupling (**Figure 5-27**).
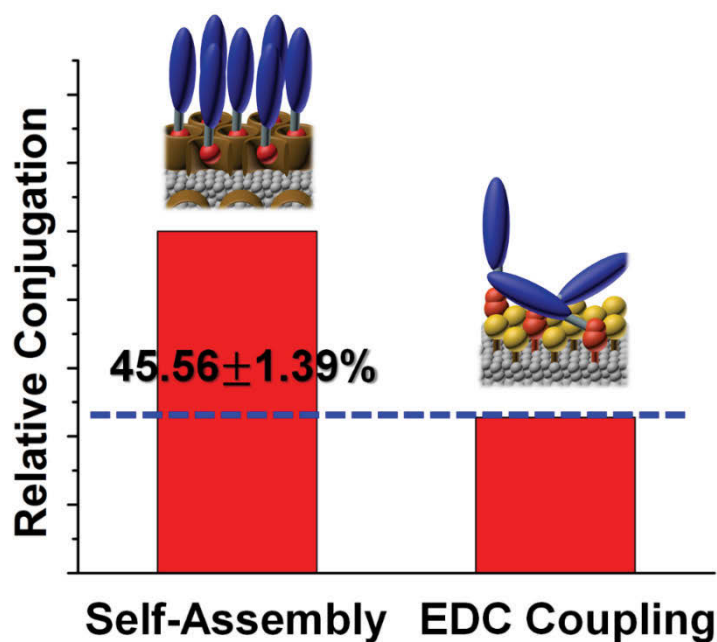
Figure 5-27. Conjugation amount of functional groups on the surface of CB-UCNPs and OA-UCNPs.

5.3.2.6 Conjugation Availability.

- **Conjugation Availability of CB-UCNPs.**

The number of CB[7] ($N_{CB[7]}$) on the surface is

$$N_{CB[7]} = \frac{m_{CB[7]}}{M_{CB[7]}} N_A$$

where $m_{CB[7]}$ is the weight of CB[7] in CB-UCNPs, was tested by TGA, $M_{CB[7]}$ is molecular weight of CB[7], N_A is Avogadro's constant.

The number of IgG (N_{IgG}) on the surface is

$$N_{IgG} = \frac{m_{IgG}}{M_{IgG}} N_A$$

where m_{IgG} is the weight of IgG in CB-UCNP@IgG-ADC, was tested by BCA protein concentration test, $M_{IgG\text{-}ADC}$ is the molecular weight of IgG, N_A is Avogadro's constant.

So, the conjugation availability is

$$conjugation\ availability = \frac{N_{IgG}}{N_{CB[7]}} \times 100\%$$

We calculated the conjugation availability of CB-UCNPs with IgG is 7.5%.

- **Conjugation Availability of UCNPs-COOH.**

The same as CB-UCNPs, the conjugation availability of UCNPs-COOH is

$$\boldsymbol{conjugation\ availability = \frac{N_{IgG}}{N_{COOH}} \times 100\%}$$

We calculated the conjugation availability of CB-UCNPs with IgG is 1.7%.

The accessibility of CB-UCNPs for bioconjugation was also assessed. The binding efficiency was found to be four times higher than EDC coupling method (**Figure 5-28**).
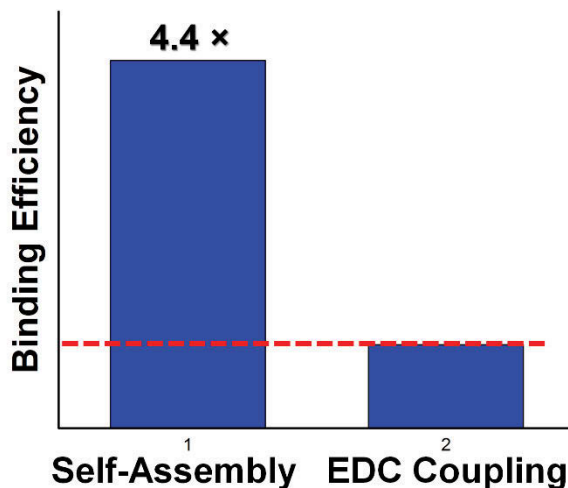
Figure 5-28. Conjugation availability of functional groups on the surface of CB-UCNPs and OA-UCNPs.

5.3.2.7 Conjugation Rate of Self-Assembly

The binding rate of self-assembly was also evaluated by allowing the IgG-ADC to interact with CB-UCNPs at different mixing times. At each time point, the resulting CB-UCNP@IgG-ADC was collected for analysis. The half-life time of IgG-ADC binding to CB-UCNP is about 30 minutes (**Figure 5-29**).
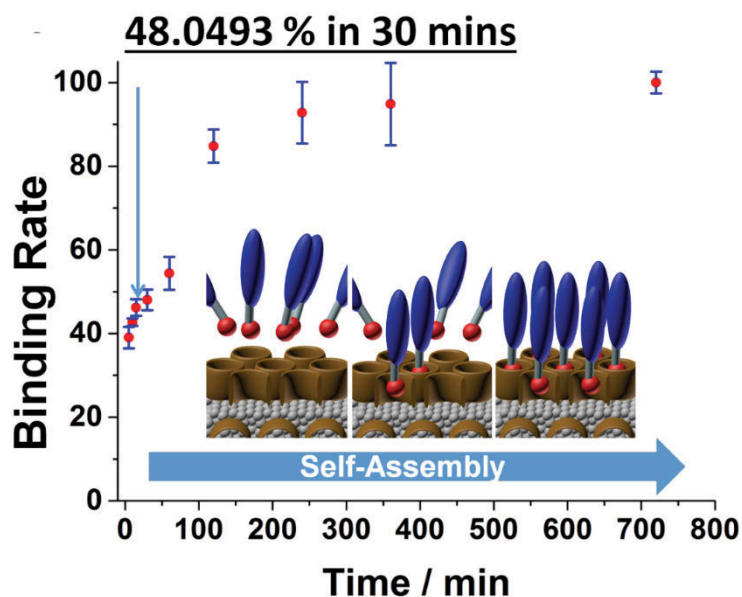
Figure 5-29. Binding rate of IgG-ADC on the surface of CB-UCNPs and OA-UCNPs.

5.3.2.8 The Shelf-Life of Self-Assembly Conjugation.

Two experiments to investigate the shelf-life of the self-assembled conjugation system were carried out. (1) The emission stability of self-assembled CB-UCNP@IgG-ADC system, and (2) the binding stability of IgG in the self-assembled system. After the self-assembly, the CB-UCNP@IgG-ADC was kept at 4 °C, and the emission spectrum was measured for a varied time from 0 h to 192 h (8 d). The half-life of conjugation is about 7 d (ca. 167 h). We also measured the free IgG amount in solution using BCA method after the conjugation of IgG. After 8 d, only 6.6% IgG was shown in the solution indicating the disassembly at a very slow rate. (**Table 6-2**, **Table 6-3, Figure 6-31 and Figure 6-32**) The difference between **Table 6-2** and **Table 6-3** can be explained because UCNPs can precipitate or hydrolyze even if IgG is still on their surface. In any case, the data of **Table 6-2** is more relevant for the overall stability.

Table 5-2. The emission stability of CB-UCNP@IgG-ADC

Time	The Emission Percentage
12 h	$(99.0\pm0.82)\%$
24 h	$(94.2\pm0.42)\%$
48 h	$(86.3\pm1.32)\%$
72 h	$(75.3\pm1.79)\%$
96 h	$(65.4\pm2.06)\%$
120 h	$(58.2\pm1.56)\%$
144 h	$(54.9\pm0.96)\%$
168 h	$(51.5\pm2.52)\%$
192 h	$(48.6\pm2.10)\%$
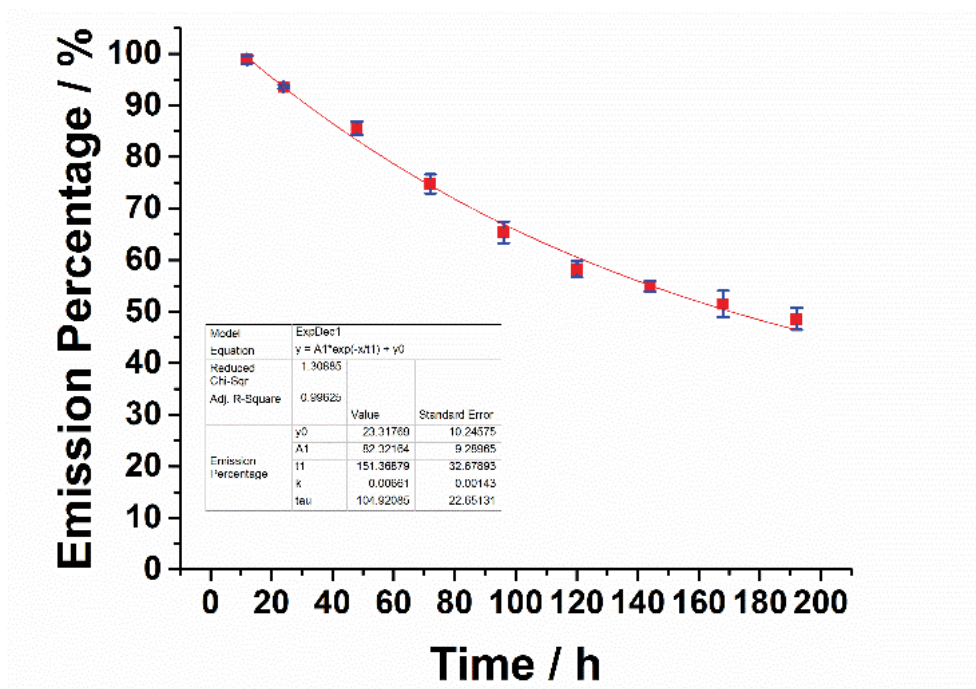
Figure 5-30. The emission stability of CB-UCNP@IgG-ADC.

Table 5-3. Free IgG percentage in media

Time	Percentage of Free IgG
12 h	(0.2±0.16)%
24 h	(1.6±0.78)%
48 h	(3.7±0.44)%
72 h	(4.3±0.83)%
96 h	(4.6±0.55)%
120 h	(5.2±0.43)%
144 h	(5.9±0.89)%
168 h	(6.2±1.25)%
192 h	(6.6±1.15)%
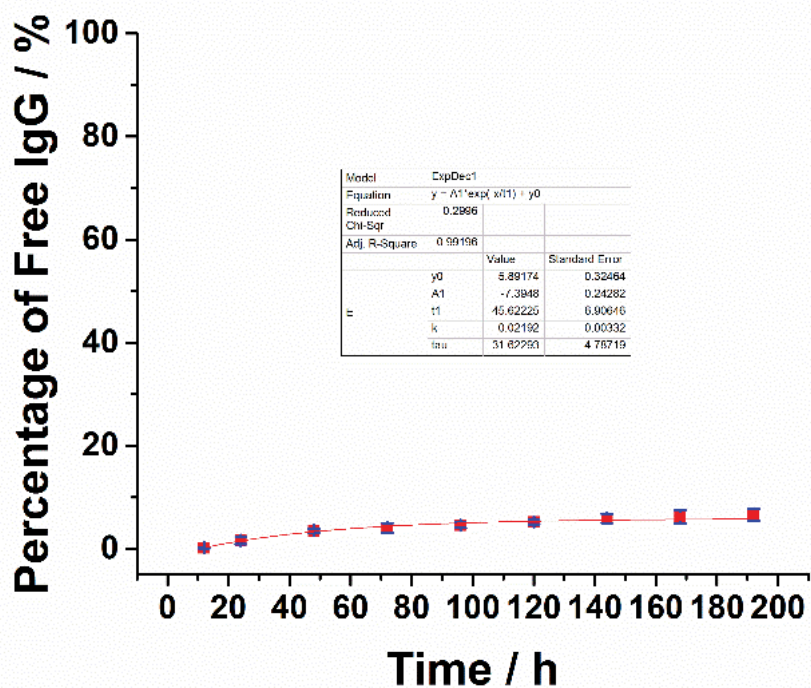
Figure 5-31. Free IgG percentage in media.

5.3.3 *in vitro* Cell Study

5.3.3.1 Cytotoxicity.

To display the targeting behaviour of CB-UCUPs@IgG-ADC, cytotoxicity by MTT assay with HeLa cell line has shown that the nanoparticles to be biocompatible. **Figure 5-32** shows that the cell viability decreased with an increasing concentration of CB-UCNPs. Although at a very high level (400 µg/mL), cells still kept good viability (more than 70%). It means that CB-UCNPs processed excellent biocompatibility and suitable for disease detection in the future.
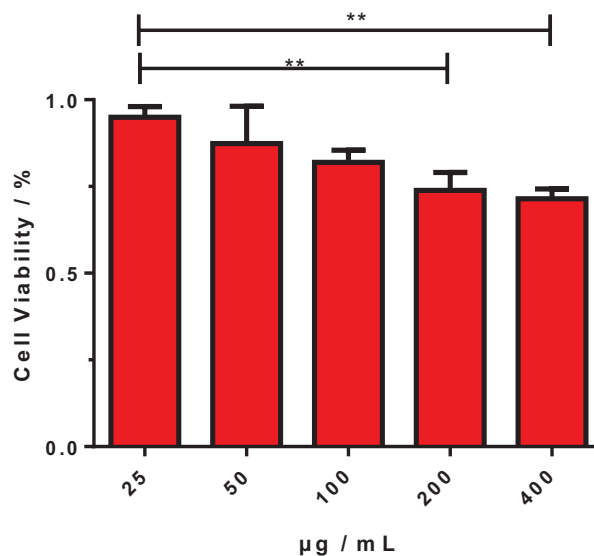
Figure 5-32. *In vitro* **cell-growth inhibition assay for HeLa cancer cell line obtained by adding different concentrations of CB-UCNPs.**

5.3.3.2 Fluorescence Imaging.

To demonstrate the biological specificity of the CB-UCNP nanoparticles, E-cadherin IgG bound to CB-UCNP was tested by immunofluorescent imaging at 980nm. From **Figure 5-33** it is clear that the E-cadherin IgG bound CB-UCNP was able to target the E-cadherin transmembrane protein of the HeLa cells. One of the key limitations of this study lies in the spot size limit of the 980nm sensor which can only detect an area between 3-5μm (**Figure 5-34**).
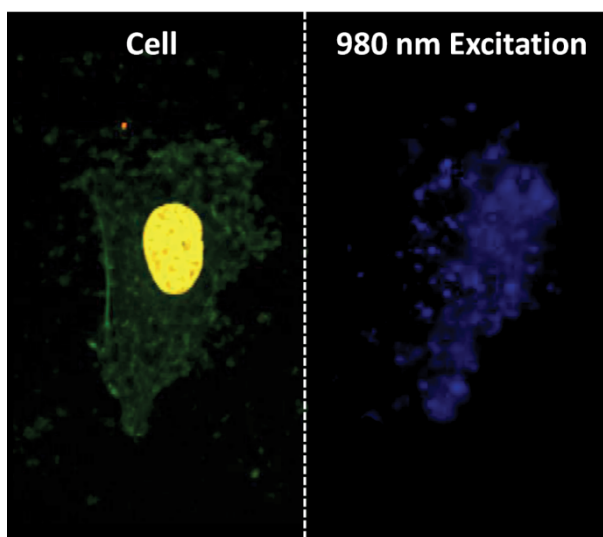
Figure 5-33. Cell imaging of CB-UCNP@IgG-ADC targeting on the surface of HeLa cells. Phalloidin-FITC stains the framework of the cell, DAPI stains nucleus, we pseudo blue colour to yellow for easier visualization.
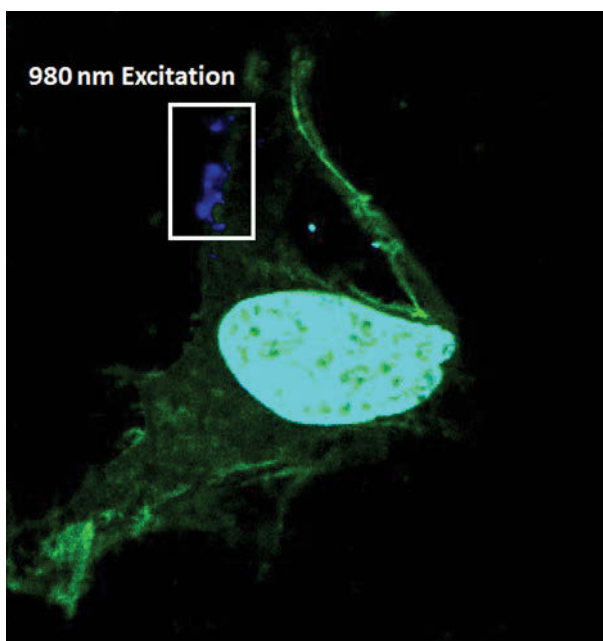
Figure 5-34. The cell imaging of CB-UCNP@IgG-ADC attached on the surface of HeLa cell.

5.4 Conclusions

In conclusion, CB[7] has shown to have dual roles in both an efficient ligand exchange process and supramolecular conjugation of biomolecules. It converts UCNPs from a hydrophobic surface into a hydrophilic surface and creates an array of specific anchor points for the attachment of biomolecules via host-guest inclusion. This offers an advance in simplicity, stability, and high yield, compared with EDC bioconjugation. The binding behaviour of CB–UCNPs to a selected biomolecule, e.g., IgG antibodies, shows the advantages of this approach in binding capability, availability, conjugation rate and cell targeting. The scope of the applications of CB–UCNPs in the field of bioconjugation to create molecular tools that can be used in early disease detection would be wide and significant.

6 SELF-ASSEMBLY INDUCED FLUORESCENCE RESONANCE ENERGY TRANSFER SYSTEM BASED ON UPCONVERSION NANOPARTICLES WITH GOLD NANOPARTICLES

This chapter introduced a supramolecular competitive controlled FRET system based on UCNPs with AuNPs. By using host-guest interaction, CB-UCNPs and L-phenylalanine (L-Phe) reduced AuNPs (L-Phe-AuNPs) self-assemble to form a pair of FRET.

6.1 Introduction

In the last two chapters, macrocycle-stabilized UCNPs were used to conjugate organic small molecules (e.g., anti-cancer drug in **Chapter 4**) and bio-macromolecule (e.g., protein in **Chapter 5**) by supramolecular host-guest interaction for anti-cancer therapy and cell imaging. Here, we used the same system in **Chapter 5**, CB-UCNP, to conjugate inorganic nanoparticle rather than organic molecules. The controllable system is a good model for investigating the effect of distance between two kinds of nanoparticles. This chapter combines FRET and supramolecular competitive binding to achieve the controlled interaction between two types of nanoparticles.

FRET, as one of the most critical spectroscopic phenomenon, has been broadly used in the area of nanomedicine, biosensing, analysis, and clinical application (Jiang & Zhang 2010). The mechanism of phenomenon describes an energy transfer from an excited donor to an acceptor by dipole-dipole coupling. More importantly, FRET is a susceptible technology based on near-field communication, the effective radius of interaction is much smaller than the wavelength of light emitted. So the technology is widely used for the substance detection of near-field interaction between molecules. In the last decade, to enhance FRET efficiency and sensitivity, many nanoparticles are included as new both donors and acceptors to replace the traditional organic molecules, such as QDs (Qiu, Shu & Tang 2017), AuNPs (Abadeer et al. 2014), carbon dots (Liu, Duan, et al. 2017) and UCNPs (Chen et al. 2017).

During connecting two kinds of nanoparticles, choosing an effective method is another challenge in energy transfer. So, much effort has been made to look for new linking ways for pushing nanoparticles closer, such as chemical reactions (e.g., EDC coupling), molecular interaction (e.g., charge transfer, π-π stacking, hydrophobic effect), template, and biological binding (e.g., DNA fold or cut) (Sedlmeier & Gorris 2015). In our design, we used a host-guest self-assembly interaction to push an AuNP into a near field of a

UCNP. We modified host molecules, CB[7], on the surface of UCNPs (Sun et al. 2018). At the same time, we synthesized AuNPs with the reduction of amino acid (e.g., L-Phe) (Nayak & Shin 2006). L-Phe can form a stable interaction with CB[7], because of the hydrophobic effect and charge transfer. After the phenyl part of L-Phe came into the cavity of CB[7], the distance between AuNPs and UCNPs is around 1 nm. AuNPs can quench the emission of UCNPs went into the near field of UCNPs and formed the FRET pair.

Compared with many other approaches, we process a significant advantage that is we can also separate the nanoparticles by supramolecular competitive binding, which is a common phenomenon in nature (Yang, Yuan, et al. 2014). Typically, a model molecule with a high binding constant over L-Phe can easily replace AuNPs to decrease the FRET due to the increasing distance between UCNPs and AuNPs. In order to show the detection phenomenon, we choose a model molecule, amantadine hydrochloride (Ad), as a detective model molecule to investigate the effect of detection. The entire process of quenching to recovery is shown in **Figure 6-1**.

6.2 Experimental Section

6.2.1 Materials

$YCl_3 \cdot 6H_2O$, $YbCl_3 \cdot 6H_2O$, $ErCl_3 \cdot 6H_2O$, OA, ODE, chloroauric acid ($HAuCl_4$), L-Phe, Ad, were purchased from Sigma-Aldrich & Chem Supply and used as received. Unless otherwise noted, all reactions were performed under nitrogen atmosphere and in dry solvents. CB[7] was synthesized according to a procedure reported by Day (Day et al. 2001) and Kim (Kim et al. 2000). The synthetic process of CB[7] is shown in **Chapter 5**.
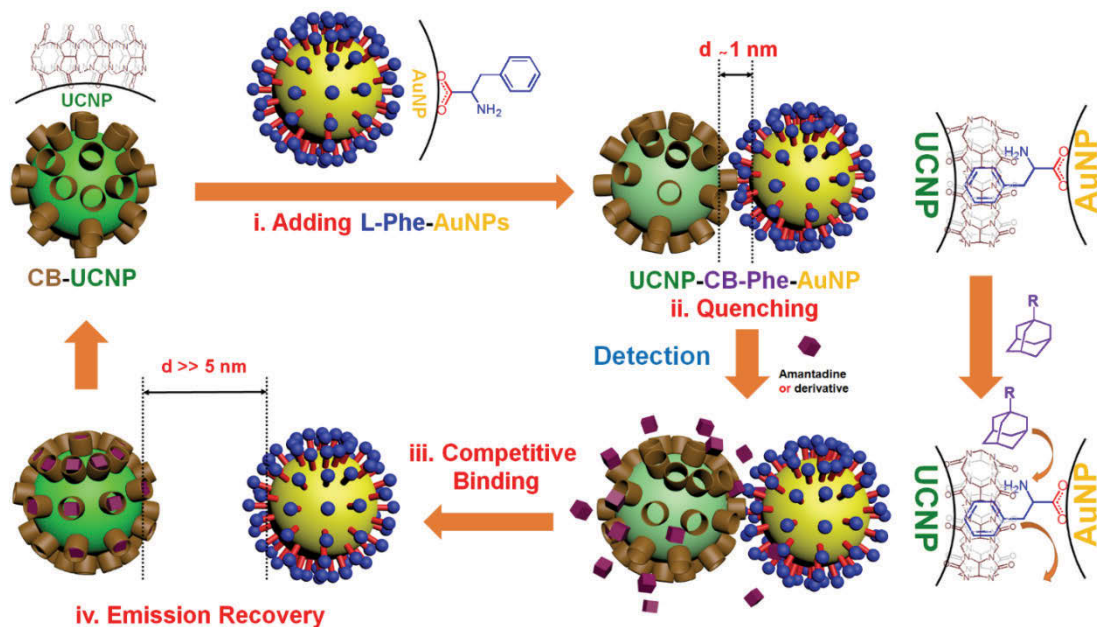
Figure 6-1. The process and mechanism of the controllable FRET system. i. Adding the L-Phe-AuNPs and mixing with CB-UCNPs; ii. CB-UCNP and L-Phe-AuNP form a FRET pair with supramolecular host-guest interaction. AuNPs quench the emission of UCNPs because the distance between the two types of nanoparticles is around 1 nm; iii. Competitive binding step: a kind of higher binding guest molecules (compared with L-Phe, such as Ad and derivatives) can replace and occupy the cavities of CB[7] on the surface of UCNPs due to the competitive binding; (iv). After higher binding molecules (Ad and derivatives) form the complex with CB[7] from the surface of CB-UCNPs, L-Phe-AuNPs are getting free again. The distance between a CB-UCNP and an L-Phe-AuNP is larger than 5 nm, and the emission of CB-UCNPs is recovered.

6.2.2 Methods

6.2.2.1 TEM images

TEM images were collected on an FEI-Tecnai T20 instrument, employing an accelerating voltage of 200 kV. The size distribution of nanoparticles is calculated by image J.

6.2.2.2 DLS

Hydration particle sizes are carried out by DLS on a Zetasizer Nano.

6.2.2.3 FT-IR spectra

FT-IR spectra were recorded on a Nicolet 6700 spectrometer (ATR Method).

6.2.2.4 Emission Spectra

The Emission Spectra were carried out by our set-up instrument.

6.2.2.5 ITC

The binding constants of host-guest interactions are tested by ITC.

6.2.2.6 Raman Spectra

The Raman Spectra were collected by using a Renishaw Raman Spectrometer. The wavelength of the laser was 785 nm.

6.2.3 Synthesis and Preparation

6.2.3.1 Synthesis of UCNPs (NaYF$_4$: 20% Yb, 2% Er)

The user-friendly synthesis method of OA-UCNPs (NaYF$_4$: 20%Yb^{3+} / 2% Er^{3+}) was modified from a previous report (Lu et al. 2015). The whole procedure is described in **Chapter 3**.

6.2.3.2 Synthesis of L-Phe-AuNPs

90 mL of a 1×10^{-4} mol/L aqueous solution of HAuCl$_4$ was reduced by treatment with 10
ml of 1×10^{-3} mol/L concentrated aqueous solution of L-Phe under the boiling condition
to yield stable AuNPs in water. The reduction of the metal ions to yield AuNPs was
evident by the appearance of a ruby red colour. The colloidal gold solution was subjected
to centrifugation (10,000 rpm, 5 min) and the resulting pellet was washed with copious
amounts of deionized water to remove any uncoordinated L-Phe molecules. The colloidal
gold solution was characterized by TEM, FT-IR, Raman, DLS.

6.2.3.3 Synthesis of CB-UCNPs

The method of ligand exchange from OA-UCNP to CB-UCNP is shown in **Chapter 4**.

6.2.4 Self-Assembly and Competitive Binding

6.2.4.1 Self-assembly of CB-UCNP and L-Phe-AuNP

The solution of CB-UCNP was added into the solution of L-Phe-AuNP. The mixture was
sonicated for 15 mins, then shake for an hour. After the sufficient mixing, the sample was
used for all the test without any further steps.

6.2.4.2 Competitive binding experiment

An excess of Ad molecules was added into the self-assembly solution. The mixture was
sonicated and stirred for an hour or 12 hours. The emission was tested directly without
any further steps.

6.3 Results and Discussion

6.3.1 Design and Mechanism of FRET system

6.3.1.1 Preparation and design of materials

The mechanisms of the typical synthesis of UCNPs have been discussed in **Chapter 1**. In this chapter, we used the co-precipitation method to synthesize the UCNPs, which is shown in **Figure 6-2**. The CB[7] molecules replace the original OA molecules on the surface of as-made UCNPs to obtain the hydrophilic UCNPs with host molecules (CB-UCNPs).
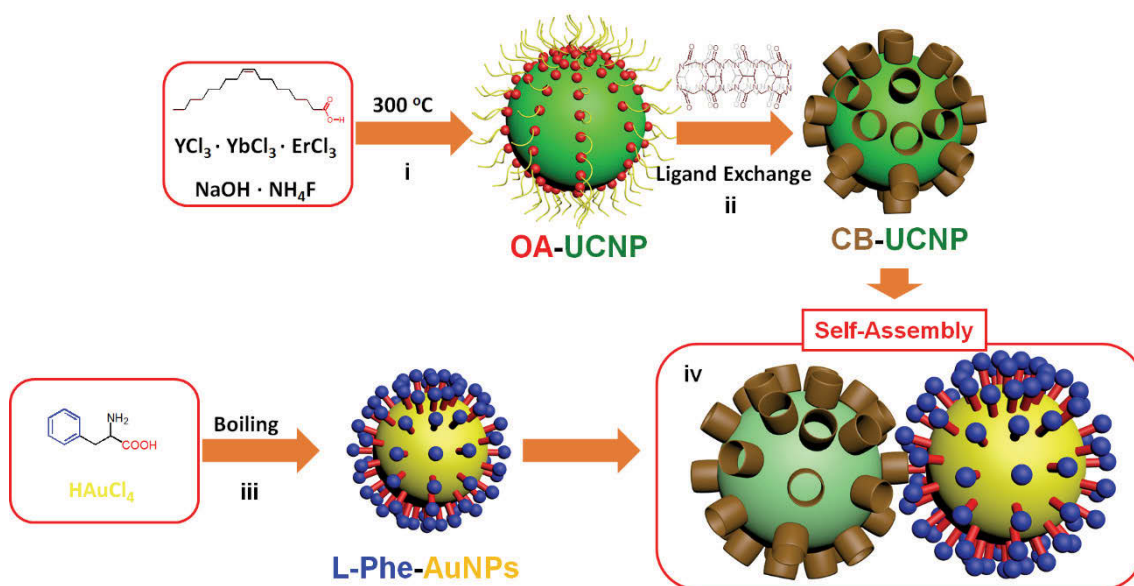
Figure 6-2. The synthesis of the detection system: i. the synthesis of OA-UCNPs; ii. the preparation of CB-UCNPs by ligand-exchange; iii. the synthesis of L-Phe-AuNPs; iv. self-assembly for forming the detection system.

The synthetic method of L-Phe-AuNPs is through a reduction of aqueous chloroaurate ions directly by L-Phe, which is according to a modified method from Nimai's report (Nayak & Shin 2006). The surface L-Phe molecules have benzene and a positive amine, which can form a hydrophobic effect and ion-dipole interactions with the host molecules

on the surface of UCNPs. Therefore, the self-assembly occurs between CB-UCNPs and L-Phe-AuNPs (**Figure 6-2**).

6.3.1.2 Investigation of energy state.

A successful FRET needs two conditions: (1). the absorption of energy acceptor can overlap the emission of energy donor; (2). two kinds of nanoparticles are close enough (< 5 nm). In **Figure 6-3**, we show the overlap between the absorption of L-Phe-AuNPs (blue curve) and the emission of CB-UCNPs. It means the both CB-UCNPs and AuNPs process the similar energy state. The electron can easily transfer from UCNP to AuNPs when they are close enough.
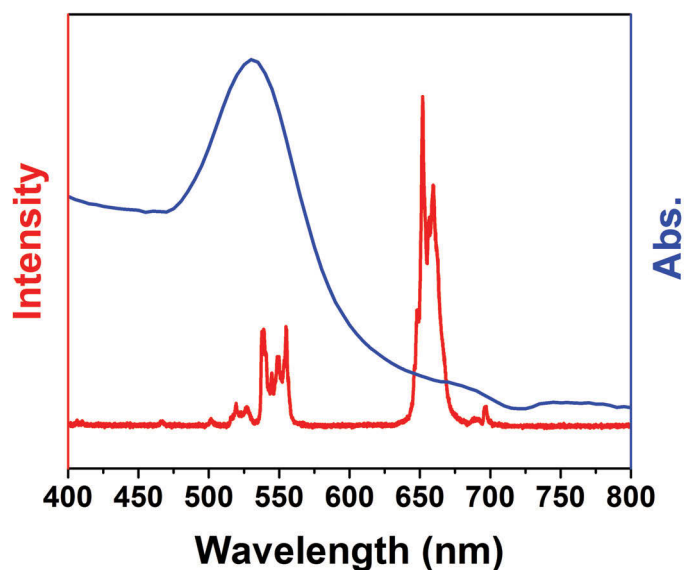
Figure 6-3. The mechanism of FRET between CB-UCNPs and L-Phe-AuNPs.

6.3.1.3 The distance of CB-UCNPs and L-Phe-AuNPs

The interaction between CB-UCNP and L-Phe-AuNP is based on the hydrophobic effect of the cavity of CB[7] with L-Phe molecule. To reduce the entropy, L-Phe molecule will insert into the cavity of CB[7], the distance between two kinds of nanoparticles will be the same as the complex size.

The molecular structures of CB[7], L-Phe, and Ad in **Figure 6-4**. After forming the complex with L-Phe and Ad respectively, the distances between two binding sites are ca. 1.21 nm and ca. 1.14 nm. When a AuNPs is connected with a UCNP by host-guest interaction, the distance between two types of nanoparticles will also keep at the same size to form the FRET pair (**Figure 6-1**).

Therefore, this design meets both conditions of the FRET, and electron theoretically can transfer from UCNPs to AuNPs.
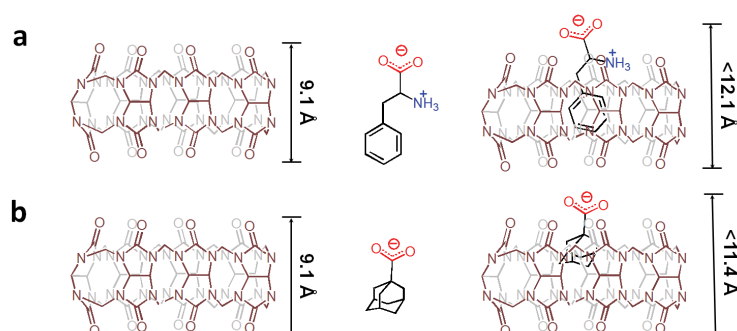
Figure 6-4. The calculation of the size of the complexes: a. the complex of CB[7] and L-Phe; b. The complex of CB[7] and Ad.

6.3.2 Binding Behaviour

To achieve the host-guest interaction and competitive binding between two different kinds of guest molecules. Firstly, we gave the binding modes of CB[7] with both guest molecules, respectively. Then, by comparing the binding constants, we investigate the competitive binding can occur between two types of guest molecules.

6.3.2.1 Binding mode

The binding structure is shown in **Figure 6-4**. In both complexes, there are two types of supramolecular interactions in both host-guest interactions. One is the hydrophobic effect between the cavity of CB[7] and benzene or adamantane; the other is the ion-dipole interaction between ketone edges with a partly positive anime group.

6.3.2.2 Binding constants

ITC is one of the most sensitive methods available for measuring the host-guest complex interactions. The instrument characteristics include very high sensitivity, rapid calorimetric response, and fast thermal equilibration. The convenient software is available for instrument operation, data collection, data reduction, and deconvolution to obtain least-squares estimates of binding parameters n, enthalpy and entropy changes ($\Delta H°$ and $\Delta S°$) and the complex association constants (K_a). In the ITC experiments, the CB[7] solution was placed in the reaction cell, and the guest solutions (L-Phe or Ad) were then injected into the cell. The binding isotherm data were fitted by "independence" model. All the net heat effects are obtained by subtracting the dilution heat from the reaction heat.
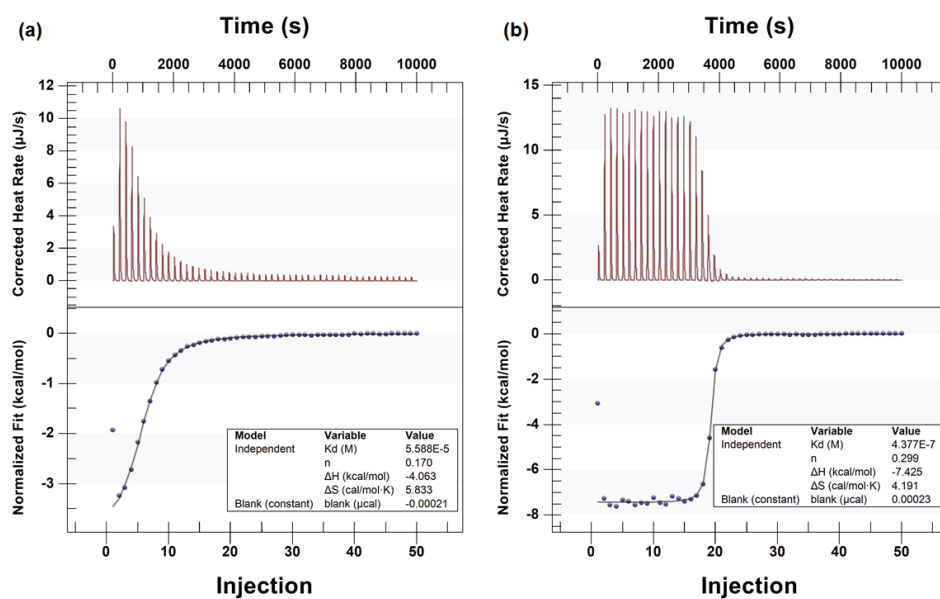
Figure 6-5. ITC measurements (a). the complexation reaction of CB[7] (2 mmol/L) with L-Phe (20 mmol/L) for each injection during a calorimetric titration at 25 ºC. Top: raw ITC data for 50 sequential injections (1 µL per injection) of L-Phe solution (20 mmol/L) into CB[7] solution (2 mmol/L). Bottom: Net heat effects obtained by subtracting the dilution heat from the reaction heat, fitted by "independence" model. (b). the complexation reaction of CB[7] (2 mmol/L) with Ad (10 mmol/L) for

each injection during a calorimetric titration at 25 °C. Top: raw ITC data for 50

sequential injections (1 μL per injection) of Ad solution (10 mmol/L) into CB[7]

solution (2 mmol/L). Bottom: Net heat effects obtained by subtracting the dilution

heat from the reaction heat, fitted by "independence" model. The K_d of the

complexation of CB[7] with L-Phe is 5.588 × 10^{-5} M, the one of CB[7] with Ad is

4.377 × 10^{-7} M.
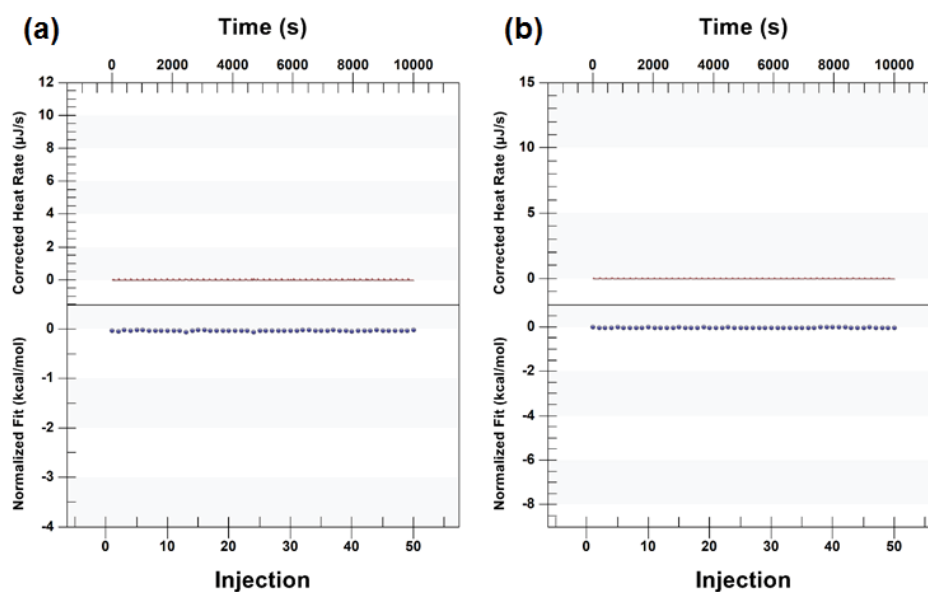
**Figure 6-6. The dilution heat of L-Phe in PBS buffer (pH = 7.4) at 25 °C. Top: raw

ITC data for 50 sequential injections (1 μL per injection) of L-Phe solution (20

mmol/L) into PBS buffer (pH=7.4).** Bottom: Heat effects of the dilution with L-Phe (20

mmol/L) for each injection during a calorimetric titration at 25 °C. **The dilution heat of Ad in

PBS buffer (pH = 7.4) at 25 °C. Top: raw ITC data for 50 sequential injections (1 μL

per injection) of Ad solution (10 mmol/L) into PBS buffer (pH=7.4).** Bottom: Heat

effects of the dilution with Ad (10 mmol/L) for each injection during a calorimetric titration at 25 °C.

The summary of binding constants of Ad and L-Phe is shown in **Table 6-1**. The binding

of Ad with CB[7] is about 100 times than the one of L-Phe. It proves that the formation

of CB[7] with Ad is much easier than L-Phe. It also shows that Ad could replace the L-

Phe to form the complex with CB[7].

Table 6-1. The complex stability constant (K_a) and thermodynamic parameters for the 1:1 inclusion complexation of CB[7] with L-Phe/Ad in PBS buffer (pH=7.4) at 25 °C.

Sample Name	K_a (M^{-1})	ΔH^o (kcal / mol)	$T\Delta S^o$ (kcal / mol)	ΔG^o (kcal / mol)
CB[7] / L-Phe	1.789×10^4	-4.063	-1.738	-5.802
CB[7] / Ad	2.284×10^6	-7.425	-1.250	-8.675

6.3.2.3 Competitive Binding

Competitive binding is a common phenomenon in nature. Typically, there are two types of competitive binding: (a) Inhibition and (b) Replacement, which are shown in **Figure 6-7**. In the "inhibition" mode, guest molecule A block the binding site first, then guest molecule B hardly bind on the host molecules because there are no more binding sites for guest molecule B. In this situation, the size of molecule A is larger than the one of molecule B. The binding sites are totally blocked. Another possible reason is the binding constants of molecules B is weaker or similar with guest molecule A. There is no enough strength replacing the binded molecules. In the "replacement" mode, guest molecule C is bonded with the host molecule. When adding a much higher binding constant molecule D, molecule C is replaced by molecule D.

According to the ITC results, the **K_a** of Ad with CB[7] is much higher than the one of L-Phe. It means Ad can easily replace L-Phe to form a new inclusion by competitive binding ("Replacement").
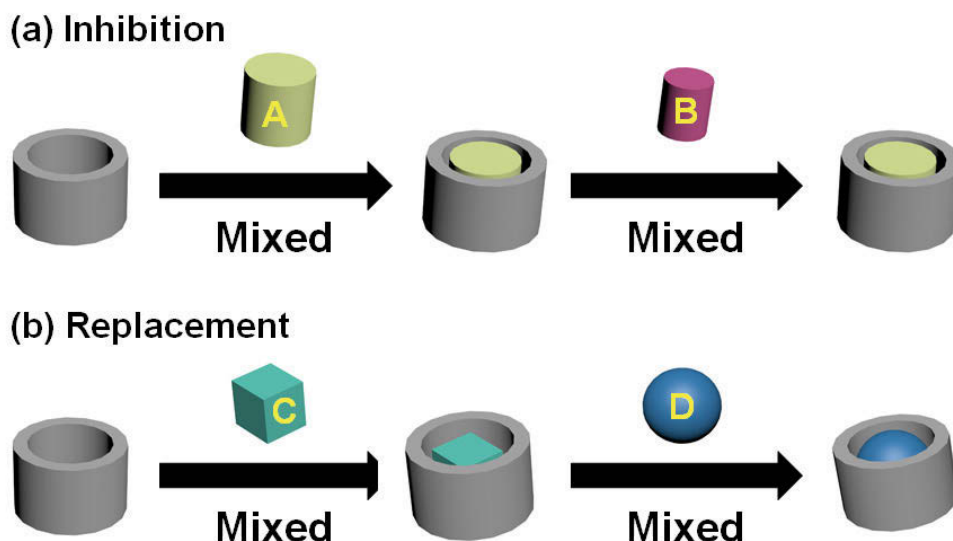
Figure 6-7. Two types of competitive binding modes: (a) inhibition and (b) replacement.

6.3.3 Materials Characterization

6.3.3.1 Morphological Analysis

The morphological characterizations of CB-UCNPs and L-Phe-AuNPs are investigated by TEM (**Figure 6-8**). It shows the TEM image of CB-UCNPs processes a uniform spherical in shape. The average size of CB-UCNPs is ca. 23 nm in diameter. **Figure 6-8b** also shows the TEM image of L-Phe-AuNPs which also processes a good monodispersed with the diameter of 30 nm. The size distributions of CB-UCNPs and L-Phe-AuNPs are shown in **Figure 6-9**. The size range of CB-UCNPs is from 22 nm to 25 nm. The one of L-Phe-AuNPs is 26 nm to 40 nm. It proves both nanoparticles we synthesized to have a homogeneous size. The self-assembly in solution was tested by DLS. Before mixed together, the hydration sizes of CB-UCNPs and L-Phe-AuNPs are about 82 nm and 38 nm, respecicity. The size is sharply increased to 1000 nm, after a mix of both nanoparticles (**Figure 6-10**).
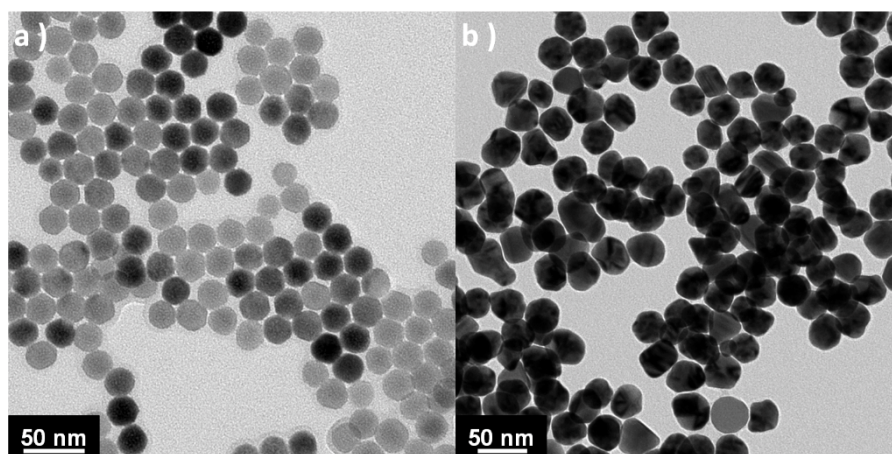
Figure 6-8. TEM images of (a) CB-UCNPs and (b) L-Phe-AuNPs.
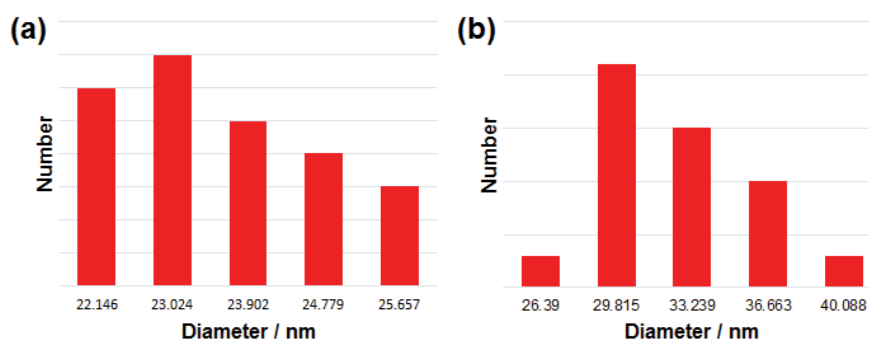
Figure 6-9. The size distributions of (a) CB-UCNPs and (b) L-Phe-AuNPs.
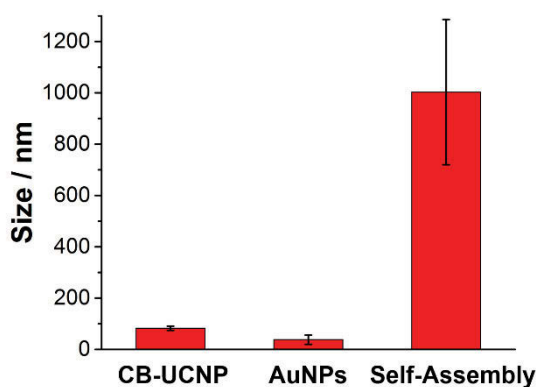
Figure 6-10. The hydration size of (a) CB-UCNPs, (b) L-Phe-AuNPs, and (3) self-assembly of CB-UCNPs and L-Phe-AuNPs.

6.3.3.2 Surface Characterizations

In **Figure 6-11**, FT-IR and Raman spectra give some significate evidence to investigate the surface of nanoparticles. **Figure 6-11a** shows the FT-IR spectra of L-Phe molecules and L-Phe-AuNPs. Compared with L-Phe's spectrum, two peaks which located at 1621 cm^{-1} and 1557 cm^{-1} are both the asymmetric stretching vibration of carboxylate and skeletal vibration from phenyl rings. The symmetric stretching vibration of carboxylate occurs at 1408 cm^{-1}. A broad peak from 1223 cm^{-1} to 1002 cm^{-1} includes the asymmetric/symmetric stretching vibrations from CH_2 group and the deformation vibration of C-H bond on the phenyl rings. Another deformation vibration of C-H bond on the phenyl rings is shown from 848 cm^{-1} to 641 cm^{-1}. All the peaks of AuNPs prove that we have successfully synthesized L-Phe-AuNPs.

The FT-IR spectra of CB[7] and CB-UCNPs are shown in **Figure 6-11b**. According to **Chapter 5**, the FT-IR spectrum of CB-UCNPs is similar with CB[7] molecules, and the shift of C=O bond further proves CB[7]s have been attached on the surface of UCNPs.

Figure 6-11c shows there is no new chemical bond in both self-assembly and competitive binding because both processes are based on supramolecular interaction In Raman Spectra (**Figure 6-11d**), L-Phe-AuNPs show the peak at 1580 cm^{-1}, which is from the symmetric stretching vibration of carboxylate. After self-assembled with CB-UCNPs, the asymmetric stretching vibration of N-C-N bond from CB[7] is obviously found in 1300 cm^{-1}.
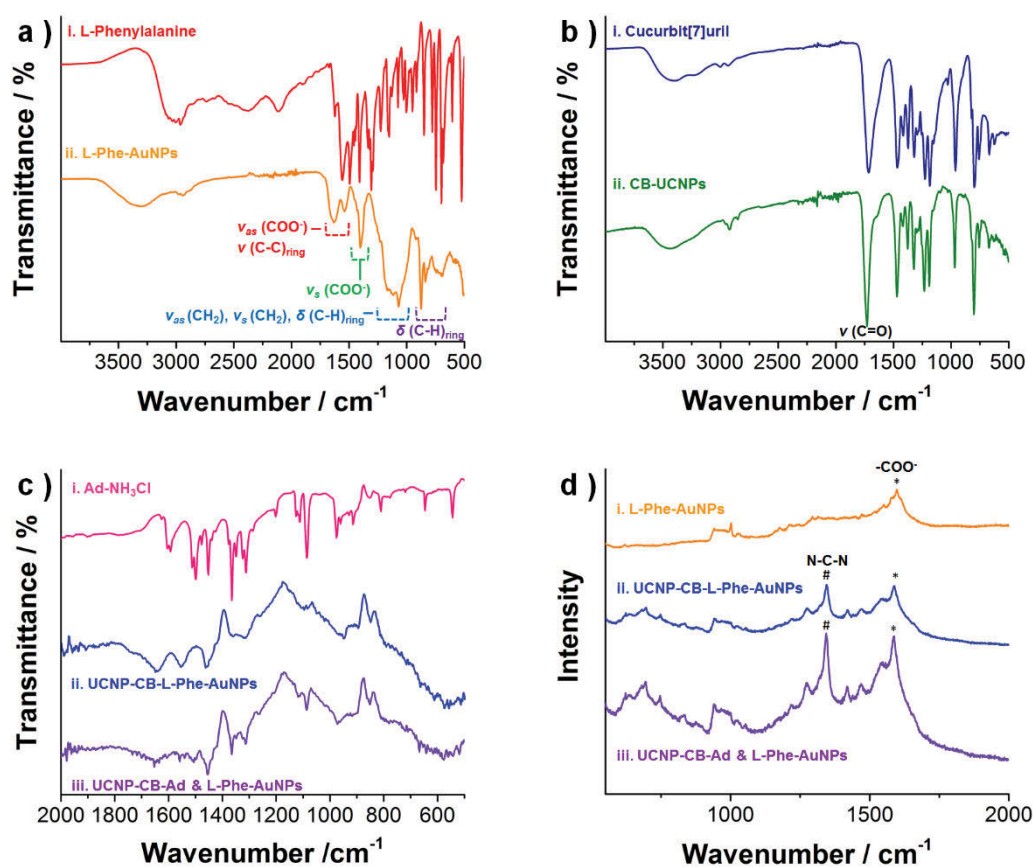
Figure 6-11. The structure characterizations. FT-IR Spectra: a) *i.* **L-Phe molecules;** *ii.* **L-Phe-AuNPs; b)** *i.* **CB[7] molecules;** *ii.* **CB-UCNPs; c)** *i.* **1-Aminoadamantane hydrochloride (Ad-NH₃Cl);** *ii.* **CB-UCNP self-assembled with L-Phe-AuNPs (UCNP-CB-L-Phe-AuNPs);** *iii.* **Adding Ad-NH₃Cl into the Self-assembled System (UCNP-CB-Ad & L-Phe-AuNPs). d) Raman Spectra:** *i.* **L-Phe-AuNPs;** *ii.* **CB-UCNP self-assembled with L-Phe-AuNPs (UCNP-CB-L-Phe-AuNPs);** *iii.* **Adding Ad-NH₃Cl into the Self-assembled System (UCNP-CB-Ad & L-Phe-AuNPs).**

6.3.4 Emission Study

6.3.4.1 The calculation of nanoparticles' concentrations

- **The concentration of L-Phe-AuNPs**

The concentration of L-Phe AuNPs is calculated by the method from Fernig e.t.c. (Haiss et al. 2007), which is based on the data of ε_{450} in different sizes of nanoparticles.

According to:

$$c = \frac{A_{450}}{\varepsilon_{450}}$$

From the TEM image, we can collect the average diameter of AuNPs, which is 34 nm. From the database, we can find $\varepsilon450$ is 2.93×10^9 $M^{-1}cm^{-1}$.

For example:

if A_{450}=0.3476,

c=1.19×10^{-10} mol/L.

- **The concentration of CB-UCNPs**

The calculation method is shown in **Chapter 3**.

6.3.4.2 Emission Quenching Study

Figure 6-12a showed the emission quenching results of the same amount of UCNPs with different concentrations of AuNPs. With the increasing concentration of AuNPs, the FRET effect induced emission quenching was getting stronger and stronger. Only one-fifth of the number of UCNPs, AuNPs absorb most all the emission from UCNPs, which is displayed in **Figure 6-12b**.
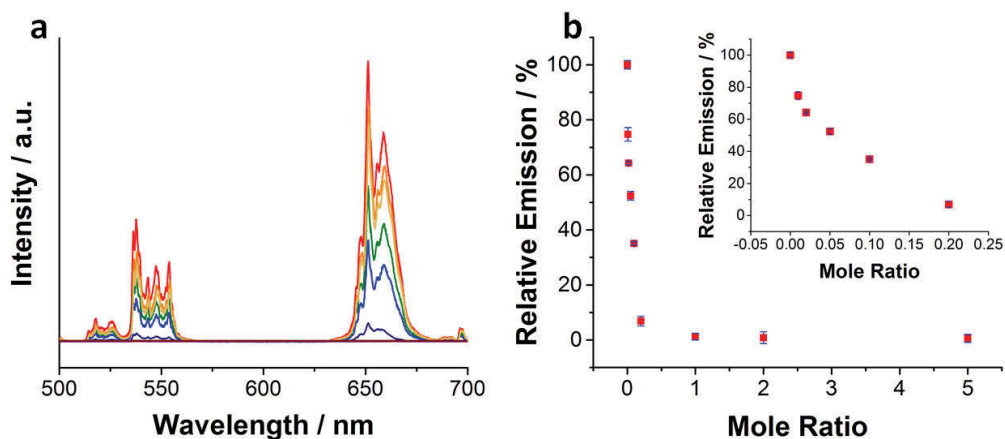
Figure 6-12. The quenching experiment between AuNPs with UCNPs. (a). Emission spectra of UCNPs binding with different concentrations of AuNPs; (b). The curve of the quenching ratio of UCNPs with varying concentrations of AuNPs.

6.3.5 Competitive Binding Study

In this chapter, we used the "replacement" mode to achieve the competitive replacing. After adding a higher binding constant molecule (Ad), the AuNPs were replaced by Ad molecules. The distance of AuNPs and UCNPs were According to the binding constants' tests, the binding constant of Ad is much higher than L-Phe, Ad could break the interaction between AuNPs and UCNPs. After adding an excess of Ad molecules, a certain recovery can be discovered by emission spectra (**Figure 6-13**). In the mole ratio at 0.01 and 0.02, the emission of UCNPs was fully recovered. But the partial recovery was found after increasing the ratio of AuNPs. At this stage, the more recovery will be found after extending the time. When the ratio reached 0.2, a slight increase is shown because the concentration of AuNPs is too high and a network will be formed after adding more AuNPs. In the network, each UCNP will bind several AuNPs, at the same time, each AuNP is also surrounded by several UCNPs. The binding constants between two particles are extremely increased because of the multiple bindings. Therefore, Ad

molecules are very hard to replace the AuNPs from the surface of UCNPs. Besides, when the concentration of AuNPs increases, the replacement is getting weaker in this stage.
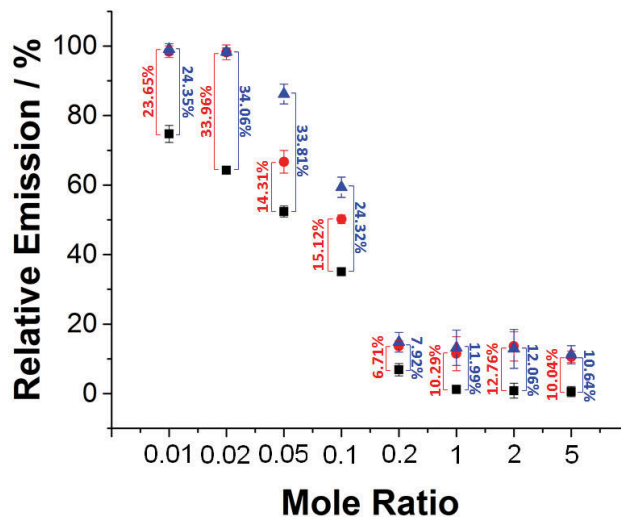
Figure 6-13. The emission recovery of UCNPs with adding Ad molecules: the emission for 1 h mixed (red) and 12 h mixed (blue). Mole Ratio is AuNPs /UCNPs.

6.4 Conclusion

In conclusion, a supramolecular host-guest interaction induced FRET system is achieved between UCNPs and AuNPs. More importantly, the FRET system can break by supramolecular competitive binding. In this system, guest-modified AuNPs are tied on the surface of host-stabilized UCNPs to quench the emission by supramolecular host-guest interaction. Due to the differences in binding constants, higher binding molecules (e.g., Ad in this chapter) can always break the interactions between host molecules from UCNPs with lower binding molecules from the Au surface. The recovery of emission of UCNPs can be widely used for the molecular detection.

7 CONCLUSION

CONCLUSION

This work combined supramolecular chemistry and UCNPs, raised a novel method for UCNP surface modification by using macrocycles (i.e., CDs and CB[7]). These surface macrocycles not only brought UCNPs from hydrophobic into hydrophilic but also provided numerous cavities which can bind a library of molecules or materials (**Chapter 6**) on the surface of UCNPs for further applications. We choose three typical models: (1) DOX (**Chapter 4**), (2) IgG protein (**Chapter 5**), and (3) AuNPs (**Chapter 6**) for testing the binding ability. All of these results showed great potential in the areas of biological and physical science.

Several significant questions have been solved in this work:

1. The binding mode of OA on the surface of UCNPs was determined (**Chapter 3**). We listed and compared all the predicted binding modes of OA on different UCNP crystal faces. Also, combining the experimental data, we confirmed the binding mode of OA on both crystal faces are the same. Both O atoms in an OA molecule are equal and bond with one Y atom from UCNP surface.

2. A one-step efficient surface modification method was achieved by using macrocycles.

   Several typical kinds of macrocycles (CDs and CB[7]) were used and replaced the original OA molecules out of the surface. More importantly, these macrocycles have shown to have dual roles in both an efficient ligand exchange process and supramolecular conjugation of biomolecules. They converted UCNPs from a hydrophobic surface into a hydrophilic surface and created an array of specific anchor points for the further attachment *via* supramolecular host-guest interactions.

3. Several typical macrocycle-stabilized UCNPs were successfully applied with organic molecules, biomolecules, and inorganic nanoparticles.

In the binding with an organic molecule (**Chapter 4**), these results showed CD-UCNPs could bind with different types of drugs according to the molecular size and also process low toxicity and enhance the bioavailability of drugs.

In the binding with biomolecules (**Chapter 5**), CB-UCNP offered an advance in simplicity, stability, and high yield, compared with EDC bioconjugation. The binding behaviour of CB-UCNPs to a selected biomolecule, e.g., IgG antibodies, showed the advantages of this approach in binding capability, availability, conjugation rate and cell targeting. The scope of the applications of CB-UCNPs in the field of bioconjugation to create molecular tools that can be used in early disease detection would be wide and significant.

In the binding with inorganic materials (**Chapter 6**), a FRET system between AuNPs and UCNPs has been designed for the detection of model molecules. By controlling the distance between AuNPs and UCNPs, the emission of UCNPs can be controlled. A recovery system was also achieved by supramolecular competitive binding.

8 REFERENCES

Abadeer, N.S., Brennan, M.R., Wilson, W.L. & Murphy, C.J. 2014, 'Distance and plasmon wavelength dependent fluorescence of molecules bound to silica-coated gold nanorods', *ACS Nano*, vol. 8, no. 8, pp. 8392–406.

Ahmad, S., Prakash, G.V. & Nagarajan, R. 2012, 'Hexagonally Ordered KLaF4 Host: Phase-Controlled Synthesis and Luminescence Studies', *Inorganic Chemistry*, vol. 51, no. 23, pp. 12748–54.

Bailey, D.M., Hennig, A., Uzunova, V.D. & Nau, W.M. 2008, 'Supramolecular tandem enzyme assays for multiparameter sensor arrays and enantiomeric excess determination of amino acids', *Chemistry – A European Journal*, vol. 14, no. 20, pp. 6069–77.

Bao, L.Y., You, H.L., Wang, L.M., Li, L., Qiao, R., Zhang, Y., Zhong, Y.J., Xiong, Y.J. & Li, Z.Q. 2014, 'Self-assembly of LaF$_3$:Yb,Er/Tm nanoplates into colloidal spheres and tailoring their upconversion emissions with fluorescent dyes', *Journal of Materials Chemistry C*, vol. 2, no. 42, pp. 8949–55.

Barrow, S.J., Kasera, S., Rowland, M.J., Del Barrio, J. & Scherman, O.A. 2015, 'Cucurbituril-based molecular recognition', *Chemical Reviews*, vol. 115, no. 22, pp. 12320–406.

Bogdan, N., Vetrone, F., Roy, R. & Capobianco, J.A. 2010, 'Carbohydrate-coated lanthanide-doped upconverting nanoparticles for lectin recognition', *Journal of Materials Chemistry*, vol. 20, no. 35, pp. 7543–50.

Bouteiller, L. 2011, 'Supramolecular chemistry in material science', *Actualite Chimique*, no. 348-49, pp. 54–6.

Boyer, J.C., Manseau, M.P., Murray, J.I. & van Veggel, F. 2010, 'Surface modification of upconverting NaYF$_4$ nanoparticles with PEG-phosphate ligands for NIR (800

nm) biolabeling within the biological window', *Langmuir*, vol. 26, no. 2, pp. 1157–64.

Cai, H.J., Shen, T.L., Kirillov, A.M., Zhang, Y., Shan, C.F., Li, X., Liu, W.S. & Tang, Y. 2017, 'Self-assembled upconversion nanoparticle clusters for NIR-controlled drug release and synergistic therapy after conjugation with gold nanoparticles', *Inorganic Chemistry*, vol. 56, no. 9, pp. 5295–304.

Cao, R., Villalonga, R. & Fragoso, A. 2005, 'Towards nanomedicine with a supramolecular approach: a review', *IEE Proceedings – Nanobiotechnology*, vol. 152, no. 5, pp. 159–64.

Cao, T.Y., Yang, T.S., Gao, Y., Yang, Y., Hu, H. & Li, F.Y. 2010, 'Water-soluble NaYF4:Yb/Erupconversion nanophosphors: Synthesis, characteristics and application in bioimaging', *Inorganic Chemistry Communications*, vol. 13, no. 3, pp. 392–4.

Cao, T.Y., Yang, Y., Gao, Y.A., Zhou, J., Li, Z.Q. & Li, F.Y. 2011, 'High-quality water-soluble and surface-functionalized upconversion nanocrystals as luminescent probes for bioimaging', *Biomaterials*, vol. 32, no. 11, pp. 2959–68.

Cen, Y., Wu, Y.M., Kong, X.J., Wu, S., Yu, R.Q. & Chu, X. 2014, 'Phospholipid-modified upconversion nanoprobe for ratiometric fluorescence detection and imaging of phospholipase D in cell lysate and in living cells', *Analytical Chemistry*, vol. 86, no. 14, pp. 7119–27.

Chen, D.-X., Sun, Y.-L., Zhang, Y., Cui, J.-Y., Shen, F.-Z. & Yang, Y.-W. 2013, 'Supramolecular self-assembly and photophysical properties of pillar[5]arene-stabilized CdTe quantum dots mediated by viologens', *RSC Advances*, vol. 3, no. 17, p. 5765–8.

Chen, G.J., Jaskula-Sztul, R., Esquibel, C.R., Lou, I., Zheng, Q.F., Dammalapati, A., Harrison, A., Eliceiri, K.W., Tang, W.P., Chen, H. & Gong, S.Q. 2017, 'Neuroendocrine Tumor-Targeted Upconversion Nanoparticle-Based Micelles for Simultaneous NIR-Controlled Combination Chemotherapy and Photodynamic Therapy, and Fluorescence Imaging', *Advanced Functional Materials*, vol. 27, no. 8, pp. 1604671.

Chen, Y.H., Duong, H.T.T., Wen, S.H., Mi, C., Zhou, Y.Z., Shimoni, O., Valenzuela, S.M. & Jin, D.Y. 2018, 'Exonuclease III-assisted upconversion resonance energy transfer in a wash-free suspension DNA assay', *Analytical Chemistry*, vol. 90, no. 1, pp. 663–8.

Chen, Z.G., Chen, H.L., Hu, H., Yu, M.X., Li, F.Y., Zhang, Q., Zhou, Z.G., Yi, T. & Huang, C.H. 2008, 'Versatile synthesis strategy for carboxylic acid-functionalized upconverting nanophosphors as biological labels', *Journal of the American Chemical Society*, vol. 130, no. 10, pp. 3023–9.

Cheng, E., Yin, W., Bai, S., Qiao, R., Zhong, Y. & Li, Z. 2015, 'Synthesis of vis/NIR-driven hybrid photocatalysts by electrostatic assembly of NaYF$_4$:Yb, Tm nanocrystals on g-C$_3$N$_4$ nanosheets', *Materials Letters*, vol. 146, pp. 87–90.

Chihara, G. 1960, 'Medical and biochemical application of infrared spectroscopy. V. : infrared absorption spectra of organic sulfate esters. (1).', *Chemical and Pharmaceutical Bulletin*, vol. 8, no. 11, pp. 988–94.

Ciesielski, A., Haar, S., El Gemayel, M., Yang, H.F., Clough, J., Melinte, G., Gobbi, M., Orgiu, E., Nardi, M.V., Ligorio, G., Palermo, V., Koch, N., Ersen, O., Casiraghi, C. & Samori, P. 2014, 'Harnessing the liquid-phase exfoliation of graphene using aliphatic compounds: a supramolecular approach', *Angewandte Chemie International Edition*, vol. 53, no. 39, pp. 10355–61.

Ciesielski, A. & Samori, P. 2016, 'Supramolecular approaches to graphene: from self-assembly to molecule-assisted liquid-phase exfoliation', *Advanced Materials*, vol. 28, no. 29, pp. 6030–51.

Cong, H., Tao, L.-L., Yu, Y.-H., Yang, F., Du, Y., Xue, S.-F. & Tao, Z. 2006, 'Molecular recognition of aminoacid by cucurbiturils', *Acta Chimica Sinica*, vol. 64, no. 10, pp. 989–96.

Corma, A., Garcia, H., Montes-Navajas, P., Primo, A., Calvino, J.J. & Trasobares, S. 2007, 'Gold nanoparticles in organic capsules: a supramolecular assembly of gold nanoparticles and cucurbituril', *Chemistry – A European Journal*, vol. 13, no. 22, pp. 6359–64.

Cram, D.J. 1986, 'Preorganization – from solvents to spherands', *Angewandte Chemie International Edition*, vol. 25, no. 12, pp. 1039–57.

Cram, D. J. & Cram, J. M. 1978, 'Design of complexes between synthetic hosts and organic guests', *Accounts of Chemical Research*, vol. 11, no. 1, pp. 8–14.

Darani, M.K., Bastani, S., Ghahari, M. & Kardar, P. 2015, 'An experimental design approach for hydrothermal synthesis of $NaYF_4$: Yb^{3+}, Tm^{3+} upconversion microcrystal: UV emission optimization', *Optical Materials*, vol. 49, pp. 255–65.

Day, A., Arnold, A.P., Blanch, R.J. & Snushall, B. 2001, 'Controlling factors in the synthesis of cucurbituril and its homologues', *Journal of Organic Chemistry*, vol. 66, no. 24, pp. 8094–100.

Dong, B.A., Xu, S., Sun, J.A., Bi, S., Li, D., Bai, X., Wang, Y., Wang, L.P. & Song, H.W. 2011, 'Multifunctional $NaYF_4$: Yb^{3+}, Er^{3+}@Agcore/shell nanocomposites: integration of upconversion imaging and photothermal therapy', *Journal of Materials Chemistry*, vol. 21, no. 17, pp. 6193–200.

Dorokhin, D., Hsu, S.H., Tomczak, N., Reinhoudt, D.N., Huskens, J., Velders, A.H. & Vancso, G.J. 2010, 'Fabrication and luminescence of designer surface patterns with beta-cyclodextrin functionalized quantum dots via multivalent supramolecular coupling', *ACS Nano*, vol. 4, no. 1, pp. 137–42.

Duong, H.T.T., Chen, Y.H., Tawfik, S.A., Wen, S.H., Parviz, M., Shimoni, O. & Jin, D.Y. 2018, 'Systematic investigation of functional ligands for colloidal stable upconversion nanoparticles', *RSC Advances*, vol. 8, no. 9, pp. 4842–9.

Engel, S., Moller, N., Stricker, L., Peterlechner, M. & Ravoo, B.J. 2018, 'A modular system for the design of stimuli-responsive multifunctional nanoparticle aggregates by use of host-guest chemistry', *Small*, vol. 14, no. 16, pp. 1704287.

Erbas-Cakmak, S., Fielden, S.D.P., Karaca, U., Leigh, D.A., McTernan, C.T., Tetlow, D.J. & Wilson, M.R.. 2017, 'Rotary and linear molecular motors driven by pulses of a chemical fuel', *Science*, vol. 358, no. 6361, pp. 340–343.

Esipova, T.V., Ye, X.C., Collins, J.E., Sakadzic, S., Mandeville, E.T., Murray, C.B. & Vinogradov, S.A. 2012, 'Dendritic upconverting nanoparticles enable in vivo multiphoton microscopy with low-power continuous wave sources', *Proceedings of the National Academy of Sciences of the United States of America*, vol. 109, no. 51, pp. 20826–31.

Fan, X.P., Pi, D.B., Wang, F., Qiu, J.R. & Wang, M.Q. 2006, 'Hydrothermal synthesis and luminescence behavior of lanthanide-doped GdF3 nanoparticles', *IEEE Transactions on Nanotechnology*, vol. 5, no. 2, pp. 123–8.

Feu, K.S., de Assis, F.F., Nagendra, S. & Pilli, R.A. 2017, 'The Nobel Prize in Chemistry 2016: Molecular Machines', *Quimica Nova*, vol. 40, no. 1, pp. 113–23.

Fragoso, A., Caballero, J., Almirall, E., Villalonga, R. & Cao, R. 2002, 'Immobilization of adamantane-modified cytochrome c at electrode surfaces through supramolecular interactions', *Langmuir*, vol. 18, no. 13, pp. 5051–4.

Frances-Soriano, L., Gonzalez-Bejar, M. & Perez-Prieto, J. 2015, 'Cucurbit[n]uril-capped upconversion nanoparticles as highly emissive scaffolds for energy acceptors', *Nanoscale*, vol. 7, no. 12, pp. 5140–6.

Fuller, J.M., Raghupathi, K.R., Ramireddy, R.R., Subrahmanyam, A.V., Yesilyurt, V. & Thayumanavan, S. 2013, 'Temperature-sensitive transitions below LCST in amphiphilic dendritic assemblies: host-guest implications', *Journal of the American Chemical Society*, vol. 135, no. 24, pp. 8947–54.

Ge, J.M., Zhang, B., Lv, L.B., Wang, H.H., Ye, T.N., Wei, X., Su, J., Wang, K.X., Li, X.H. & Chen, J.S. 2015, 'Constructing holey graphene monoliths via supramolecular assembly: Enriching nitrogen heteroatoms up to the theoretical limit for hydrogen evolution reaction', *Nano Energy*, vol. 15, pp. 567–75.

Gil-Ramírez, G., Leigh, D.A. & Stephens, A.J. 2015, 'Catenanes: Fifty years of molecular links', *Angewandte Chemie International Edition*, vol. 54, no. 21, pp. 6110–6150.

Gonzalez-Bejar, M., Liras, M., Frances-Soriano, L., Voliani, V., Herranz-Perez, V., Duran-Moreno, M., Garcia-Verdugo, J.M., Alarcon, E.I., Scaiano, J.C. & Perez-Prieto, J. 2014, 'NIR excitation of upconversion nanohybrids containing a surface grafted Bodipy induces oxygen-mediated cancer cell death', *Journal of Materials Chemistry B*, vol. 2, no. 28, pp. 4554–63.

Goodman, C. 2007, 'Jean-Marie Lehn', *Nature Chemical Biology*, vol. 3, no. 11, pp. 685.

Greybush, N.J., Saboktakin, M., Ye, X., Giovampaola, C.D., Oh, S.J., Berry, N.E., Engheta, N., Murray, C.B. & Kagan, C.R. 2014, 'Plasmon-enhanced upconversion

luminescence in single nanophosphor-nanorod heterodimers formed through template-assisted self-assembly', *ACS Nano*, vol. 8, no. 9, pp. 9482–91.

Haar, S., Ciesielski, A., Clough, J., Yang, H.F., Mazzaro, R., Richard, F., Conti, S., Merstorf, N., Cecchini, M., Morandi, V., Casiraghi, C. & Samori, P. 2015, 'A supramolecular strategy to leverage the liquid-phase exfoliation of graphene in the presence of surfactants: unraveling the role of the length of fatty acids', *Small*, vol. 11, no. 14, pp. 1691–702.

Haiss, W., Thanh, N.T.K., Aveyard, J. & Fernig, D.G. 2007, 'Determination of size and concentration of gold nanoparticles from UV-Vis spectra', *Analytical Chemistry*, vol. 79, no. 11, pp. 4215–21.

Hallett, J.P. & Welton, T. 2011, 'Room-temperature ionic liquids: solvents for synthesis and catalysis. 2', *Chemical Reviews*, vol. 111, no. 5, pp. 3508–3576.

Harada, A., Kobayashi, R., Takashima, Y., Hashidzume, A. & Yamaguchi, H. 2011, 'Macroscopic self-assembly through molecular recognition', *Nature Chemistry*, vol. 3, no. 1, pp. 34–7.

Hawthorne, M.F. 2001, 'Obituary: Donald J. Cram (1919-2001)', *Nature*, vol. 412, no. 6848, pp. 696.

Hazarika, P., Ceyhan, B. & Niemeyer, C.M. 2004, 'Reversible switching of DNA-gold nanoparticle aggregation', *Angewandte Chemie International Edition*, vol. 43, no. 47, pp. 6469–71.

He, L., Feng, L.Z., Cheng, L., Liu, Y.M., Li, Z.W., Peng, R., Li, Y.G., Guo, L. & Liu, Z. 2013, 'Multilayer dual-polymer-coated upconversion nanoparticles for multimodal imaging and serum-enhanced gene delivery', *ACS Applied Materials & Interfaces*, vol. 5, no. 20, pp. 10381–8.

Hirsch, A.K. 2015, 'Supramolecular chemistry ... and beyond', *Angewandte Chemie International Edition*, vol. 54, no. 38, pp. 11013–4.

Hu, H., Xiong, L.Q., Zhou, J., Li, F.Y., Cao, T.Y. & Huang, C.H. 2009, 'Multimodal-luminescence core-shell nanocomposites for targeted imaging of tumor cells', *Chemistry – A European Journal*, vol. 15, no. 14, pp. 3577–84.

Hu, H., Yu, M.X., Li, F.Y., Chen, Z.G., Gao, X., Xiong, L.Q. & Huang, C.H. 2008, 'Facile epoxidation strategy for producing amphiphilic up-converting rare-earth nanophosphors as biological labels', *Chemistry of Materials*, vol. 20, no. 22, pp. 7003–9.

Hu, Q.D., Tang, G.P. & Chu, P.K. 2014, 'Cyclodextrin-based host-guest supramolecular nanoparticles for delivery: from design to applications', *Accounts of Chemical Research*, vol. 47, no. 7, pp. 2017–25.

Huang, P., Zheng, W., Zhou, S.Y., Tu, D.T., Chen, Z., Zhu, H.M., Li, R.F., Ma, E., Huang, M.D. & Chen, X.Y. 2014, 'Lanthanide-doped LiLuF$_4$ upconversion nanoprobes for the detection of disease biomarkers', *Angewandte Chemie International Edition*, vol. 53, no. 5, pp. 1252–7.

Idris, N.M., Jayakumar, M.K., Bansal, A. & Zhang, Y. 2015, 'Upconversion nanoparticles as versatile light nanotransducers for photoactivation applications', *Chemical Society Reviews*, vol. 44, no. 6, pp. 1449–78.

Izatt, R.M. 2007, 'Charles J. Pedersen: Innovator in macrocyclic chemistry and co-recipient of the 1987 Nobel Prize in Chemistry', *Chemical Society Reviews*, vol. 36, no. 2, pp. 143–7.

Izatt, R.M. 2017, 'Charles J. Pedersen's legacy to chemistry', *Chemical Society Reviews*, vol. 46, no. 9, pp. 2380–4.

Jayaraman, N. 2017, '2016 Nobel Prize in Chemistry conferring molecular machines as engines of creativity', *Resonance-Journal of Science Education*, vol. 22, no. 9, pp. 835–45.

Jeffrey, G.A. (1997) *An Introduction to Hydrogen Bonding,* Oxford University Press, USA.

Jiang, M., Kurvits, J.A., Lu, Y., Nurmikko, A.V. & Zia, R. 2015, 'Reusable inorganic templates for electrostatic self-assembly of individual quantum dots, nanodiamonds, and lanthanide-doped nanoparticles', *Nano Letters*, vol. 15, no. 8, pp. 5010–6.

Jiang, S. & Zhang, Y. 2010, 'Upconversion nanoparticle-based FRET system for study of siRNA in live cells', *Langmuir*, vol. 26, no. 9, pp. 6689–94.

Jiang, T., Qin, W.P. & Zhou, J. 2016, 'Hydrothermal synthesis and aspect ratio dependent upconversion luminescence of $NaYF_4$:Yb^{3+}/Er^{3+} microcrystals', *Journal of Nanoscience and Nanotechnology*, vol. 16, no. 4, pp. 3806–10.

Jin, B., Lin, M., Zong, Y., Wan, M., Xu, F., Duan, Z. & Lu, T. 2015, 'Microbubble embedded with upconversion nanoparticles as a bimodal contrast agent for fluorescence and ultrasound imaging', *Nanotechnology*, vol. 26, no. 34, pp. 345601.

Jing, B., Chen, X., Wang, X.D., Zhao, Y.R. & Qiu, H.Y. 2008, 'Sol-gel-sol transition of gold nanoparticle-based supramolecular hydrogels induced by cyclodextrin inclusion', *ChemPhysChem*, vol. 9, no. 2, pp. 249–52.

Johnson, N.J.J., Sangeetha, N.M., Boyer, J.C. & van Veggel, F. 2010, 'Facile ligand-exchange with polyvinylpyrrolidone and subsequent silica coating of hydrophobic upconverting beta-$NaYF_4$:Yb^{3+}/Er^{3+} nanoparticles', *Nanoscale*, vol. 2, no. 5, pp. 771–7.

Kaminker, R., Lahav, M., Motiei, L., Vartanian, M., Popovitz-Biro, R., Iron, M.A. & van der Boom, M.E. 2010, 'Molecular structure-function relations of the optical properties and dimensions of gold nanoparticle assemblies', *Angewandte Chemie International Edition*, vol. 49, no. 7, pp. 1218–21.

Kim, J., Jung, I.-S., Kim, S.-Y., Lee, E., Kang, J.-K., Sakamoto, S., Yamaguchi, K. & Kim, K. 2000, 'New cucurbituril homologues: syntheses, isolation, characterization, and X-ray crystal structures of Cucurbit[n]uril (n = 5, 7, and 8)', *Journal of the American Chemical Society*, vol. 122, no. 3, pp. 540–1.

Kong, W., Sun, T., Chen, B., Chen, X., Ai, F., Zhu, X., Li, M., Zhang, W., Zhu, G. & Wang, F. 2017, 'A general strategy for ligand exchange on upconversion nanoparticles', *Inorganic Chemistry*, vol. 56, no. 2, pp. 872–7.

Lagona, J., Mukhopadhyay, P., Chakrabarti, S. & Isaacs, L. 2005, 'The Cucurbit[n]uril family', *Angewandte Chemie International Edition*, vol. 44, no. 31, pp. 4844–70.

Lehn, J.-M. 1995, *Supramolecular Chemistry: concepts and perspectives*, Weinheim, FRG: Wiley-VCH Verlag GmbH & Co. KGaA.

Li, C.X., Yang, J., Quan, Z.W., Yang, P.P., Kong, D.Y. & Lin, J. 2007, 'Different microstructures of ss-NaYF4 fabricated by hydrothermal process: Effects of pH values and fluoride sources', *Chemistry of Materials*, vol. 19, no. 20, pp. 4933–42.

Li, H., Chen, D.X., Sun, Y.L., Zheng, Y.B., Tan, L.L., Weiss, P.S. & Yang, Y.W. 2013, 'Viologen-mediated assembly of and sensing with carboxylatopillar[5]arene-modified gold nanoparticles', *Journal of the American Chemical Society*, vol. 135, no. 4, pp. 1570–6.

Li, S., Ye, S., Chen, X., Liu, T.H., Guo, Z. & Wang, D.P. 2017, 'OH- ions-controlled synthesis and upconversion luminescence properties of $NaYF_4:Yb^{3+},Er^{3+}$

nanhaiyouyocrystals via oleic acid-assisted hydrothermal process', *Journal of Rare Earths*, vol. 35, no. 8, pp. 753–60.

Lin, Y.W., Li, L.F. & Li, G.W. 2012, 'Preparation and properties of temperature and pH sensitive chitosan supramolecular gel based on host-guest interaction of Cucurbit[8]uril', *Acta Chimica Sinica*, vol. 70, no. 21, pp. 2246–50.

Liras, M., Gonzalez-Bejar, M., Peinado, E., Frances-Soriano, L., Perez-Prieto, J., Quijada-Garrido, I. & Garcia, O. 2014, 'Thin amphiphilic polymer-capped upconversion nanoparticles: enhanced emission and thermoresponsive properties', *Chemistry of Materials*, vol. 26, no. 13, pp. 4014–22.

Liu, B., Li, C.X., Yang, D.M., Hou, Z.Y., Ma, P.A., Cheng, Z.Y., Lian, H.Z., Huang, S.S. & Lin, J. 2014, 'Upconversion-luminescent core/mesoporous-silica-shell structured beta-NaYF$_4$:Yb^{3+},Er^{3+}@SiO$_2$@mSiO$_2$ composite nanospheres: fabrication and drug-storage/release properties', *European Journal of Inorganic Chemistry*, vol. 2014, no. 11, pp. 1906–13.

Liu, B.X., Tan, H.L. & Chen, Y. 2013, 'Upconversion nanoparticle-based fluorescence resonance energy transfer assay for Cr(III) ions in urine', *Analytica Chimica Acta*, vol. 761, pp. 178–85.

Liu, D.M., Xu, X.X., Du, Y., Qin, X., Zhang, Y.H., Ma, C.S., Wen, S.H., Ren, W., Goldys, E.M., Piper, J.A., Dou, S.X., Liu, X.G. & Jin, D.Y. 2016, 'Three-dimensional controlled growth of monodisperse sub-50 nm heterogeneous nanocrystals', *Nature Communications*, vol. 7, pp. 10254.

Liu, H.C., Xu, C.T., Dumlupinar, G., Jensen, O.B., Andersen, P.E. & Andersson-Engels, S. 2013, 'Deep tissue optical imaging of upconverting nanoparticles enabled by exploiting higher intrinsic quantum yield through use of millisecond single pulse excitation with high peak power', *Nanoscale*, vol. 5, no. 20, pp. 10034–40.

Liu, J.H., Chen, G.S. & Jiang, M. 2011, 'Supramolecular hybrid hydrogels from noncovalently functionalized graphene with block copolymers', *Macromolecules*, vol. 44, no. 19, pp. 7682–91.

Liu, Q., Li, C., Yang, T., Yi, T. & Li, F. 2010, '"Drawing" upconversion nanophosphors into water through host-guest interaction', *Chemical Communications (Cambridge)*, vol. 46, no. 30, pp. 5551–3.

Liu, S., Ruspic, C., Mukhopadhyay, P., Chakrabarti, S., Zavalij, P.Y. & Isaacs, L. 2005, 'The Cucurbit[n]uril family: prime components for self-sorting systems', *Journal of the American Chemical Society*, vol. 127, no. 45, pp. 15959–67.

Liu, X.M., Zhao, J.W., Sun, Y.J., Song, K., Yu, Y., Du, C.A., Kong, X.G. & Zhang, H. 2009, 'Ionothermal synthesis of hexagonal-phase $NaYF4:Yb^{3+},Er^{3+}/Tm^{3+}$ upconversion nanophosphors', *Chemical Communications*, no. 43, pp. 6628–30.

Liu, X.X., Ni, Y.R., Zhu, C., Fang, L., Kou, J.H., Lu, C.H. & Xu, Z.Z. 2016, 'Controllable self-assembly of $NaREF_4$ upconversion nanoparticles and their distinctive fluorescence properties', *Nanotechnology*, vol. 27, no. 29, pp. 295605.

Liu, Y., Lu, Y., Yang, X., Zheng, X., Wen, S., Wang, F., Vidal, X., Zhao, J., Liu, D., Zhou, Z., Ma, C., Zhou, J., Piper, J.A., Xi, P. & Jin, D. 2017, 'Amplified stimulated emission in upconversion nanoparticles for super-resolution nanoscopy', *Nature*, vol. 543, no. 7644, pp. 229–33.

Liu, Y., Purich, D.L., Wu, C., Wu, Y., Chen, T., Cui, C., Zhang, L., Cansiz, S., Hou, W., Wang, Y., Yang, S. & Tan, W. 2015, 'Ionic functionalization of hydrophobic colloidal nanoparticles to form ionic nanoparticles with enzymelike properties', *Journal of the American Chemical Society*, vol. 137, no. 47, pp. 14952–8.

Liu, Y.H., Duan, W.X., Song, W., Liu, J.J., Ren, C.L., Wu, J., Liu, D. & Chen, H.L. 2017, 'Red emission B, N, S-co-doped carbon dots for colorimetric and fluorescent dual

mode detection of Fe^{3+} ions in complex biological fluids and living cells', *ACS Applied Materials & Interfaces*, vol. 9, no. 14, pp. 12663–72.

Liu, Z., Sun, L.N., Li, F.Y., Liu, Q., Shi, L.Y., Zhang, D.S., Yuan, S., Liu, T. & Qiu, Y.N. 2011, 'One-pot self-assembly of multifunctional mesoporous nanoprobes with magnetic nanoparticles and hydrophobic upconversion nanocrystals', *Journal of Materials Chemistry*, vol. 21, no. 44, pp. 17615–8.

Lu, J., Chen, Y., Liu, D., Ren, W., Lu, Y., Shi, Y., Piper, J., Paulsen, I. & Jin, D. 2015, 'One-step protein conjugation to upconversion nanoparticles', *Analytical Chemistry*, vol. 87, no. 20, pp. 10406–13.

Lv, Y., Yue, L., Li, Q., Shao, B.Y., Zhao, S., Wang, H.T., Wu, S.J. & Wang, Z.P. 2018, 'Recyclable (Fe_3O_4-$NaYF_4$:Yb,Tm)@TiO_2 nanocomposites with near-infrared enhanced photocatalytic activity', *Dalton Transactions*, vol. 47, no. 5, pp. 1666–73.

Mai, H.-X., Zhang, Y.-W., Sun, L.-D. & Yan, C.-H. 2007, 'Size- and phase-controlled synthesis of monodisperse $NaYF_4$:Yb,Er nanocrystals from a unique delayed nucleation pathway monitored with upconversion spectroscopy', *The Journal of Physical Chemistry C*, vol. 111, no. 37, pp. 13730–9.

Masson, E., Ling, X., Joseph, R., Kyeremeh-Mensah, L. & Lu, X. 2012, 'Cucurbituril chemistry: a tale of supramolecular success', *RSC Advances*, vol. 2, no. 4, pp. 1213–47.

Medintz, I.L., Sapsford, K.E., Konnert, J.H., Chatterji, A., Lin, T.W., Johnson, J.E. & Mattoussi, H. 2005, 'Decoration of discretely immobilized cowpea mosaic virus with luminescent quantum dots', *Langmuir*, vol. 21, no. 12, pp. 5501–10.

Moeller, T., Martin, D.F., Thompson, L.C., Rerrús, R., Feistel, G.R. & Randail, W.J. 1965, 'The coordination chemistry of Yttrium and the rare earth metal ions', *Chemical Reviews*, vol. 65, no. 1, pp. 1–50.

Muhr, V., Wilhelm, S., Hirsch, T. & Wolfbeis, O.S. 2014, 'Upconversion nanoparticles: from hydrophobic to hydrophilic surfaces', *Accounts of Chemical Research*, vol. 47, no. 12, pp. 3481–93.

Munkhbat, O., Garzoni, M., Raghupathi, K.R., Pavan, G.M. & Thayumanavan, S. 2016, 'Role of aromatic interactions in temperature-sensitive amphiphilic supramolecular assemblies', *Langmuir*, vol. 32, no. 12, pp. 2874–81.

Naccache, R., Vetrone, F., Mahalingam, V., Cuccia, L.A. & Capobianco, J.A. 2009, 'Controlled synthesis and water dispersibility of hexagonal phase $NaGdF_4$:Ho^{3+}/Yb^{3+} nanoparticles', *Chemistry of Materials*, vol. 21, no. 4, pp. 717–23.

Nayak, N.C. & Shin, K. 2006, 'Synthesis of L-phenylalanine stabilized gold nanoparticles and their thermal stability', *Journal of Nanoscience and Nanotechnology*, vol. 6, no. 11, pp. 3512–6.

Neacsu, A. 2018, 'Physicochemical investigation of the complexation between gamma-cyclodextrin and doxorubicin in solution and in solid state', *Thermochimica Acta*, vol. 661, pp. 51–8.

Nguyen, P.D., Cong, V.T., Baek, C. & Min, J. 2016, 'Self-assembly of an upconverting nanocomplex and its application to turn-on detection of metalloproteinase-9 in living cells', *Nanotechnology*, vol. 27, no. 40, pp. 405101.

Ni, D.L., Zhang, J.W., Bu, W.B., Xing, H.Y., Han, F., Xiao, Q.F., Yao, Z.W., Chen, F., He, Q.J., Liu, J.N., Zhang, S.J., Fan, W.P., Zhou, L.P., Peng, W.J. & Shi, J.L. 2014, 'Dual-targeting upconversion nanoprobes across the Blood-Brain Barrier

for magnetic resonance/fluorescence imaging of intracranial glioblastoma', *ACS Nano*, vol. 8, no. 2, pp. 1231–42.

Niemeyer, C.M., Ceyhan, B. & Hazarika, P. 2003, 'Oligofunctional DNA-gold nanoparticle conjugates', *Angewandte Chemie International Edition*, vol. 42, no. 46, pp. 5766–70.

Nyk, M., Kumar, R., Ohulchanskyy, T.Y., Bergey, E.J. & Prasad, P.N. 2008, 'High contrast in vitro and in vivo photoluminescence bioimaging using near infrared to near infrared up-conversion in TM^{3+} and Yb^{3+} doped fluoride nanophosphors', *Nano Letters*, vol. 8, no. 11, pp. 3834–8.

Ogoshi, T., Kanai, S., Fujinami, S., Yamagishi, T. & Nakamoto, Y. 2008, 'para-bridged symmetrical Pillar[5]arenes: their Lewis Acid catalyzed synthesis and host–guest property', *Journal of the American Chemical Society*, vol. 130, no. 15, pp. 5022–3.

Pedersen, C.J. 1967, 'Cyclic polyethers and their complexes with metal salts', *Journal of the American Chemical Society*, vol. 89, no. 26, pp. 7017–36.

Qi, Z.H., Bharate, P., Lai, C.H., Ziem, B., Bottcher, C., Schulz, A., Beckert, F., Hatting, B., Mulhaupt, R., Seeberger, P.H. & Haag, R. 2015, 'Multivalency at interfaces: supramolecular carbohydrate-functionalized graphene derivatives for bacterial capture, release, and disinfection', *Nano Letters*, vol. 15, no. 9, pp. 6051–7.

Qiu, P.Y., Sun, R.J., Gao, G., Chen, B., Zhang, C.L., Yin, T., Zhang, J.P., Fang, S. & Cui, D.X. 2015, 'Hydrothermal targeted-explosion synthesis of hollow/porous upconversion nano- and microcrystals with potential for luminescent displays and biological imaging', *ChemNanoMat*, vol. 1, no. 2, pp. 128–34.

Qiu, X.C., Zhu, X.J., Xu, M., Yuan, W., Feng, W. & Li, F.Y. 2017, 'Hybrid nanoclusters for near-infrared to near-infrared upconverted persistent luminescence bioimaging', *ACS Applied Materials & Interfaces*, vol. 9, no. 38, pp. 32583–90.

Qiu, Z.L., Shu, J. & Tang, D.P. 2017, 'Bioresponsive release system for visual fluorescence detection of carcinoembryonic antigen from mesoporous silica nanocontainers mediated optical color on quantum dot-enzyme-impregnated paper', *Analytical Chemistry*, vol. 89, no. 9, pp. 5152–60.

Rekharsky, M.V., Mori, T., Yang, C., Ko, Y.H., Selvapalam, N., Kim, H., Sobransingh, D., Kaifer, A.E., Liu, S., Isaacs, L., Chen, W., Moghaddam, S., Gilson, M.K., Kim, K. & Inoue, Y. 2007, 'A synthetic host-guest system achieves avidin-biotin affinity by overcoming enthalpy-entropy compensation', *Proceedings of the National Academy of Sciences of the United States of America*, vol. 104, no. 52, pp. 20737–42.

Samanta, S.K., Subrahmanyam, K.S., Bhattacharya, S. & Rao, C.N.R. 2012, 'Composites of graphene and other nanocarbons with organogelators assembled through supramolecular interactions', *Chemistry – A European Journal*, vol. 18, no. 10, pp. 2890–901.

Saraswathy, M. & Gong, S.Q. 2014, 'Recent developments in the co-delivery of siRNA and small molecule anticancer drugs for cancer treatment', *Materials Today*, vol. 17, no. 6, pp. 298–306.

Sedlmeier, A. & Gorris, H.H. 2015, 'Surface modification and characterization of photon-upconverting nanoparticles for bioanalytical applications', *Chemical Society Reviews*, vol. 44, no. 6, pp. 1526–60.

Shen, J., Chen, G.Y., Vu, A.M., Fan, W., Bilsel, O.S., Chang, C.C. & Han, G. 2013, 'Engineering the upconversion nanoparticle excitation wavelength: cascade

sensitization of tri-doped upconversion colloidal nanoparticles at 800 nm', *Advanced Optical Materials*, vol. 1, no. 9, pp. 644–50.

Shen, J., Zhao, L. & Han, G. 2013, 'Lanthanide-doped upconverting luminescent nanoparticle platforms for optical imaging-guided drug delivery and therapy', *Advanced Drug Delivery Reviews*, vol. 65, no. 5, pp. 744–55.

Sherman, J.C. 2007, 'Donald J. Cram', *Chemical Society Reviews*, vol. 36, no. 2, pp. 148–50.

Song, K., Wei, L., Ma, X.F., Li, J.H., Mei, T. & Wang, J.Y. 2017, 'Construction of upconversion photonic films with enhanced luminescence via self-assembly of monodispersed hexagonal-phase NaYF$_4$:Yb, Er nanoplates', *Materials Express*, vol. 7, no. 4, pp. 324–8.

Soriano, M.L., Carrillo-Carrion, C., Ruiz-Palomero, C. & Valcarcel, M. 2018, 'Cyclodextrin-modified nanodiamond for the sensitive fluorometric determination of doxorubicin in urine based on its differential affinity towards beta/gamma-cyclodextrins', *Microchimica Acta*, vol. 185, no. 2, pp. 115.

Sperling, R.A. & Parak, W.J. 2010, 'Surface modification, functionalization and bioconjugation of colloidal inorganic nanoparticles', *Philosophical Transactions of the Royal Socitey A Mathematical Physical Engineering Sciences*, vol. 368, no. 1915, pp. 1333–83.

Steed, J.W. & Atwood, J.L. 2009, *Supramolecular Chemistry*. 2nd edn. Chichester, UK: John Wiley & Sons, Ltd.

Sudheendra, L., Ortalan, V., Dey, S., Browning, N.D. & Kennedy, I.M. 2011, 'Plasmonic enhanced emissions from cubic NaYF$_4$:Yb: Er/Tm nanophosphors', *Chemistry of Materials*, vol. 23, no. 11, pp. 2987–93.

Sun, M., Xu, L., Ma, W., Wu, X., Kuang, H., Wang, L. & Xu, C. 2016, 'Hierarchical plasmonic nanorods and upconversion core-satellite nanoassemblies for multimodal imaging-guided combination phototherapy', *Advanced Materials*, vol. 28, no. 5, pp. 898–904.

Sun, Y., Zhang, W., Wang, B., Xu, X., Chou, J., Shimoni, O., Ung, A.T. & Jin, D. 2018, 'A supramolecular self-assembly strategy for upconversion nanoparticle bioconjugation ', *Chemical Communications*, vol. 54, no. 31, pp. 3851–4.

Svec, J., Necas, M. & Sindelar, V. 2010, 'Bambus[6]uril', *Angewandte Chemie International Edition*, vol. 49, no. 13, pp. 2378–81.

Tang, K.T. & Toennies, J.P. 2010, 'Johannes Diderik van der Waals: A pioneer in the molecular sciences and Nobel Prize winner in 1910', *Angewandte Chemie International Edition*, vol. 49, no. 50, pp. 9574–9.

Tang, X.M., Liu, H.X., Zou, B.H., Tian, D.B. & Huang, H. 2012, 'A fishnet electrochemical Hg^{2+} sensing strategy based on gold nanoparticle-bioconjugate and thymine-Hg^{2+}-thymine coordination chemistry', *Analyst*, vol. 137, no. 2, pp. 309–11.

Totaro, K.A., Liao, X.L., Bhattacharya, K., Finneman, J.I., Sperry, J.B., Massa, M.A., Thorn, J., Ho, S.V. & Pentelute, B.L. 2016, 'Systematic investigation of EDC/sNHS-mediated bioconjugation reactions for carboxylated peptide substrates', *Bioconjugate Chemistry*, vol. 27, no. 4, pp. 994–1004.

Uekama, K., Hirayama, F. & Irie, T. 1998, 'Cyclodextrin drug carrier systems', *Chemical Reviews*, vol. 98, no. 5, pp. 2045–76.

Urbach, A.R. & Ramalingam, V. 2011, 'Molecular recognition of amino acids, peptides, and proteins by Cucurbit[n]uril receptors', *Israel Journal of Chemistry*, vol. 51, no. 5-6, pp. 664–78.

Valderrama, J.O. 2010, 'The legacy of Johannes Diderik van der Waals, a hundred years after his Nobel Prize for physics', *Journal of Supercritical Fluids*, vol. 55, no. 2, pp. 415–20.

Voliani, V., Gonzalez-Bejar, M., Herranz-Perez, V., Duran-Moreno, M., Signore, G., Garcia-Verdugo, J.M. & Perez-Prieto, J. 2013, 'Orthogonal functionalisation of upconverting $NaYF_4$ nanocrystals', *Chemistry – A European Journal*, vol. 19, no. 40, pp. 13538–46.

Wang, A., Jin, W., Chen, E., Zhou, J., Zhou, L. & Wei, S. 2016, 'Drug delivery function of carboxymethyl-beta-cyclodextrin modified upconversion nanoparticles for adamantine phthalocyanine and their NIR-triggered cancer treatment', *Dalton Transactions*, vol. 45, no. 9, pp. 3853–62.

Wang, C., Cheng, L., Liu, Y., Wang, X., Ma, X., Deng, Z., Li, Y. & Liu, Z. 2013, 'Imaging-guided pH-sensitive photodynamic therapy using charge reversible upconversion nanoparticles under near-infrared light', *Advanced Functional Materials*, vol. 23, no. 24, pp. 3077–86.

Wang, C.L., Li, B., Niu, W.F., Hong, S.S., Saif, B., Wang, S.B., Dong, C. & Shuang, S.M. 2015, 'beta-Cyclodextrin modified graphene oxide-magnetic nanocomposite for targeted delivery and pH-sensitive release of stereoisomeric anti-cancer drugs', *RSC Advances*, vol. 5, no. 108, pp. 89299–308.

Wang, C.L., Li, X.M. & Zhang, F. 2016, 'Bioapplications and biotechnologies of upconversion nanoparticle-based nanosensors', *Analyst*, vol. 141, no. 12, pp. 3601–20.

Wang, C.Y. & Cheng, X.H. 2015, 'Hydrothermal synthesis and upconversion properties of alpha-$NaYF_4$:Yb^{3+}, Er^{3+} nanocrystals using citric acid as chelating ligand and $NaNO_3$ as mineralizer', *Journal of Nanoscience and Nanotechnology*, vol. 15, no. 12, pp. 9656–64.

Wang, F. & Liu, X.G. 2009, 'Recent advances in the chemistry of lanthanide-doped upconversion nanocrystals', *Chemical Society Reviews*, vol. 38, no. 4, pp. 976–89.

Wang, Y., Wang, H., Liu, D., Song, S., Wang, X. & Zhang, H. 2013, 'Graphene oxide covalently grafted upconversion nanoparticles for combined NIR mediated imaging and photothermal/photodynamic cancer therapy', *Biomaterials*, vol. 34, no. 31, pp. 7715–24.

Wang, Y., Wu, Z. & Liu, Z. 2013, 'Upconversion fluorescence resonance energy transfer biosensor with aromatic polymer nanospheres as the lable-free energy acceptor', *Analytical Chemistry*, vol. 85, no. 1, pp. 258–64.

Wang, Y.F., Chen, S., Qiu, L., Wang, K., Wang, H.T., Simon, G.P. & Li, D. 2015, 'Graphene-directed supramolecular assembly of multifunctional polymer hydrogel membranes', *Advanced Functional Materials*, vol. 25, no. 1, pp. 126–33.

Wang, Y.F., Liu, G.Y., Sun, L.D., Xiao, J.W., Zhou, J.C. & Yan, C.H. 2013, 'Nd^{3+}-sensitized upconversion nanophosphors: efficient in vivo bioimaging probes with minimized heating effect', *ACS Nano*, vol. 7, no. 8, pp. 7200–6.

Xia, L., Kong, X.G., Liu, X.M., Tu, L.P., Zhang, Y.L., Chang, Y.L., Liu, K., Shen, D.Z., Zhao, H.Y. & Zhang, H. 2014, 'An upconversion nanoparticle - Zinc phthalocyanine based nanophotosensitizer for photodynamic therapy', *Biomaterials*, vol. 35, no. 13, pp. 4146–56.

Xiong, L.Q., Yang, T.S., Yang, Y., Xu, C.J. & Li, F.Y. 2010, 'Long-term in vivo biodistribution imaging and toxicity of polyacrylic acid-coated upconversion nanophosphors', *Biomaterials*, vol. 31, no. 27, pp. 7078–85.

Xu, S., Zhang, Y.Q., Li, X.P., Zhang, J.S., Sun, J.S., Cheng, L.H. & Chen, B.J. 2017, 'Remarkable fluorescence enhancement of upconversion composite film and its

application on mercury sensing', *Journal of Rare Earths*, vol. 35, no. 5, pp. 460–7.

Yan, B., Boyer, J.C., Habault, D., Branda, N.R. & Zhao, Y. 2012, 'Near infrared light triggered release of biomacromolecules from hydrogels loaded with upconversion nanoparticles', *Journal of the American Chemical Society*, vol. 134, no. 40, pp. 16558–61.

Yang, H., Yuan, B., Zhang, X. & Scherman, O.A. 2014, 'Supramolecular chemistry at interfaces: host-guest interactions for fabricating multifunctional biointerfaces', *Accounts of Chemical Research*, vol. 47, no. 7, pp. 2106–15.

Yang, S., Li, N., Liu, Z., Sha, W., Chen, D., Xu, Q. & Lu, J. 2014, 'Amphiphilic copolymer coated upconversion nanoparticles for near-infrared light-triggered dual anticancer treatment', *Nanoscale*, vol. 6, no. 24, pp. 14903–10.

Yi, G.S. & Chow, G.M. 2006, 'Synthesis of hexagonal-phase $NaYF_4$: Yb,Er and $NaYF_4$: Yb,Tm nanocrystals with efficient up-conversion fluorescence', *Advanced Functional Materials*, vol. 16, no. 18, pp. 2324–9.

Yi, G.S., Sun, B.Q., Yang, F.Z., Chen, D.P., Zhou, Y.X. & Cheng, J. 2002, 'Synthesis and characterization of high-efficiency nanocrystal up-conversion phosphors: Ytterbium and Erbium codoped lanthanum molybdate', *Chemistry of Materials*, vol. 14, no. 7, pp. 2910–4.

Zhang, F., Deng, Y., Shi, Y., Zhang, R. & Zhao, D. 2010, 'Photoluminescence modification in upconversion rare-earth fluoride nanocrystal array constructed photonic crystals', *Journal of Materials Chemistry*, vol. 20, no. 19, p. 3895–900.

Zhang, F., Wan, Y., Yu, T., Zhang, F.Q., Shi, Y.F., Xie, S.H., Li, Y.G., Xu, L., Tu, B. & Zhao, D.Y. 2007, 'Uniform nanostructured arrays of sodium rare-earth fluorides

for highly efficient multicolor upconversion luminescence', *Angewandte Chemie International Edition*, vol. 46, no. 42, pp. 7976–9.

Zhang, H., Li, Y., Ivanov, I.A., Qu, Y., Huang, Y. & Duan, X. 2010, 'Plasmonic modulation of the upconversion fluorescence in NaYF$_4$:Yb/Tm hexaplate nanocrystals using gold nanoparticles or nanoshells', *Angewandte Chemie International Edition*, vol. 49, no. 16, pp. 2865–8.

Zhang, L., August, D.P., Zhong, J., Whitehead, G.F.S., Vitorica-Yrezabal, I.J. & Leigh, D.A. 2018, 'Molecular Trefoil Knot from a Trimeric Circular Helicate', *Journal of the American Chemical Society*, vol. 140, no. 15, pp. 4982–4985.

Zhang, L.M., Mao, L.L., Lu, Z.X., Deng, Y. & He, N.Y. 2016, 'One-step hydrothermal synthesis of butanetetracarboxylic acid-coated NaYF$_4$:Yb^{3+}, Er^{3+} upconversion phosphors with enhancement upconversion luminescence', *Journal of Nanoscience and Nanotechnology*, vol. 16, no. 1, pp. 1220–4.

Zhang, L., Stephens, A.J., Nussbaumer, A.L., Lemonnier, J.-F., Jurček, P., Vitorica-Yrezabal, I.J. & Leigh, D.A. 2018, 'Stereoselective synthesis of a composite knot with nine crossings', *Nature Chemistry*, vol. 10, no. 11, pp. 1083–8.

Zhang, Q.B., Song, K., Zhao, J.W., Kong, X.G., Sun, Y.J., Liu, X.M., Zhang, Y.L., Zeng, Q.H. & Zhang, H. 2009, 'Hexanedioic acid mediated surface-ligand-exchange process for transferring NaYF$_4$:Yb/Er (or Yb/Tm) up-converting nanoparticles from hydrophobic to hydrophilic', *Journal of Colloid and Interface Science*, vol. 336, no. 1, pp. 171–5.

Zhao, J., Wu, J., Xue, J., Zhu, Q. & Ni, W. 2016, 'Au/NaYF$_4$: Yb,Er binary superparticles: synthesis and optical properties', *Israel Journal of Chemistry*, vol. 56, no. 4, pp. 242–8.

Zhao, J.W., Yang, H., Li, J.L., Wang, Y.J. & Wang, X. 2017, 'Fabrication of pH-responsive PLGA(UCNPs/DOX) nanocapsules with upconversion luminescence for drug delivery', *Scientific Reports*, vol. 7. pp. 18014:1–11.

Zhou, B., Shi, B., Jin, D. & Liu, X. 2015, 'Controlling upconversion nanocrystals for emerging applications', *Nature Nanotechnology*, vol. 10, no. 11, pp. 924–36.

Zhou, F., Noor, M.O. & Krull, U.J. 2014, 'Luminescence resonance energy transfer-based nucleic acid hybridization assay on cellulose paper with upconverting phosphor as donors', *Analytical Chemistry*, vol. 86, no. 5, pp. 2719–26.

Zhou, H.P., Xu, C.H., Sun, W. & Yan, C.H. 2009, 'Clean and flexible modification strategy for carboxyl/aldehyde-functionalized upconversion nanoparticles and their optical applications', *Advanced Functional Materials*, vol. 19, no. 24, pp. 3892–900.